EES Catalysis

REVIEW ARTICLE

View Article Online
View Journal | View Issue

Cite this: *EES Catal.*, 2026, 4, 522

Integrated CO_2 capture and conversion: dual-functional materials, mechanisms, and pathways to industrial decarbonization

Mohamed A. Elokl, Ahmed G. Ali, Abdelrahman M. Abdelmohsen, Ahmed A. Taha, Abdelrahman A. Ashour, Salma Elshabrawy and Nageh K. Allam *

Carbon dioxide (CO_2) is both the principal anthropogenic greenhouse gas and a valuable, non-toxic, and abundant C_1 feedstock for sustainable fuel and chemical production. Conventional approaches have typically addressed CO_2 capture and CO_2 conversion as independent processes; however, each remains energy-intensive and economically constrained when implemented in isolation. The emerging concept of integrated CO_2 capture and conversion (ICCC) offers a transformative strategy to simultaneously mitigate CO_2 emissions and synthesize value-added products within a unified system. Unlike the simple sequential coupling of capture and utilization, ICCC demands the synergistic integration of capture media, catalytic interfaces, and reaction environments, requiring interdisciplinary insight spanning materials chemistry, catalysis, and electrochemical engineering. This review critically surveys recent progress in ICCC with a focus on dual-functional materials (DFMs) that enable concurrent CO_2 capture and catalytic conversion. The discussion encompasses a broad range of DFMs, including porous organic polymers, covalent organic frameworks, zeolites, metal–organic frameworks, metal oxides, amines, ionic liquids, deep eutectic solvents, and molten salts. Mainstream CO_2 capture technologies, post-, pre-, and oxy-fuel combustion routes, and associated separation techniques such as absorption, adsorption, membrane filtration, cryogenics, and looping cycles are systematically analyzed through a SWOT framework (strengths, weaknesses, opportunities, and threats) across efficiency, energy, cost, and technology readiness dimensions. By coupling techno-economic evaluation with emerging mechanistic and computational insights, this review identifies viable strategies to bridge the gap between laboratory innovation and industrial deployment. Finally, we outline key research priorities, including the rational design of DFMs, optimization of catalytic interfaces, and integration of AI-driven process control, positioning ICCC as an emerging pathway toward industrial decarbonization and the global clean energy transition, while highlighting fundamental constraints from coupled CO_2 adsorption thermodynamics, transport, and catalytic kinetics that expose critical material-stability and system-integration challenges for large-scale deployment.

Received 8th November 2025,
Accepted 10th February 2026

DOI: 10.1039/d5ey00322a

rsc.li/eescatalysis

Broader context

Carbon dioxide (CO_2) emissions are the primary driver of global climate change, yet CO_2 also represents a vast, renewable carbon resource for producing sustainable fuels and chemicals. Conventional carbon capture and utilization approaches have advanced independently, but their separation limits overall efficiency, scalability, and economic viability. The emerging concept of integrated CO_2 capture and conversion (ICCC) provides a unified route to simultaneously mitigate CO_2 emissions and generate valuable products. By coupling CO_2 adsorption and catalytic transformation within a single system, ICCC redefines how we think about carbon management, from end-of-pipe mitigation to circular resource utilization. This review provides a comprehensive framework linking materials design, catalysis, and process engineering to establish ICCC as a cornerstone of carbon circularity and industrial decarbonization, accelerating the transition toward a net-zero energy future.

Introduction

The rapid increase in atmospheric carbon dioxide (CO_2) concentrations, from less than 300 ppm in the pre-industrial era to

Energy Materials Laboratory (EML), Physics Department, School of Sciences and Engineering, The American University in Cairo, New Cairo 11835, Egypt.
E-mail: nageh.allam@aucegypt.edu

416.47 ppm in 2020 (Earth's CO_2), and further to 422.5 ppm in 2024 (IEA), has intensified the urgent need for engineered solutions to remove carbon from the atmosphere.[1–3] To align with the Paris Agreement's 1.5 °C pathway, the Intergovernmental Panel on Climate Change (IPCC) estimates that global greenhouse gas emissions must peak before 2025 and decline by 43% by 2030 and 84% by 2050.[4] And, as climate change accelerates, the challenges associated with CO_2, such as

Mohamed A. Elokl

Mohamed A. Elokl received his BSc from the Department of Petroleum and Energy Engineering at The American University in Cairo with minors in Economics and Community Development. He is currently a graduate research assistant at the Energy Materials Laboratory (EML), where his research focuses on carbon capture and electrochemical conversion, emphasizing nanostructured catalysts, MOF-based and electrospun nanofiber materials, and biochar-derived composites. Beyond carbon utilization, he has contributed to green hydrogen research through anti-corrosive electrolyzers for seawater electrolysis and Africa's deployment feasibility, alongside carbon capture and storage (CCS) research using reservoir modeling and well placement design. His research integrates rational catalyst design and synthesis with advanced materials characterization, electrochemical interface analysis and modeling, and techno-economic assessment to advance sustainable energy and decarbonization technologies.

Ahmed G. Ali

Ahmed G. Ali is a research and teaching assistant at Ain Shams University and The American University in Cairo, Egypt. He obtained his MSc in Materials Science from the Skolkovo Institute of Science and Technology, Russia. His research focuses on the rational design of advanced materials for sustainable electrochemical energy conversion, including water electrolysis, HER, OER, CO_2 electroreduction, and the development of high-performance electrolyzer architectures and ion-conducting membranes.

Abdelrahman M. Abdelmohsen

Abdelrahman Abdelmohsen is a graduate research assistant at the Energy Materials Laboratory (EML), The American University in Cairo (AUC). His research interests span electrocatalysis, materials science, and electrochemical energy conversion, focusing on the development and electrochemical assessment of functional materials for CO_2 utilization, nitrogen-related electrochemical reactions, and sustainable chemical production. His work integrates materials engineering, advanced electrochemical characterization, and reaction engineering to develop efficient catalysts for energy and environmental applications.

Ahmed A. Taha

Ahmed A. Taha received his PhD in Environmental Science and Engineering from Tongji University, Shanghai, China. He began his career at the Soils, Water and Environment Research Institute (SWERI), Agricultural Research Center (ARC), Egypt, and later conducted research in China at Tongji University, Beijing University of Chemical Technology, and Beijing Forestry University, focusing on nanomaterials, membranes, and catalytic materials for environmental applications. From 2014 to 2017, he contributed to industry–academia collaborations in China on nanotechnology-based water treatment solutions. He returned to academia as an Associate Professor at SWERI, ARC, leading national and international projects. In 2023, he was awarded a Fulbright Postdoctoral Fellowship at the University of Cincinnati, USA, working with Prof. Dionysios D. Dionysiou and Dr Jingjie Wu on MOF- and nanofiber-based catalysts for CO_2 capture and conversion. After returning to Egypt, he cooperated with Prof. Nageh Allam's group at AUC on optimizing nanofiber catalysts for CO_2 electrochemical conversion. His research interests include MOFs, carbon nanomaterials, nanofiber membranes, heterogeneous catalysis for CO_2 mitigation, water treatment, and sustainable energy applications.

atmospheric CO_2 reduction, emissions mitigation, and conversion to carbon-based products, will remain persistent for decades.[5]

Carbon capture, utilization, and storage (CCUS) is widely regarded as a promising mitigation pathway.[6] Furthermore, the International Energy Agency (IEA) Net Zero Emissions scenario necessitates scaling Carbon Capture, Utilization, and Storage (CCUS) capacity from approximately 45 Mt CO_2 per year in 2022 to over 6.0 Gt CO_2 per year by 2050, a more than 100-fold increase required to address heavy industry, power generation, and transport.[7] However, conventional CCUS faces major hurdles: the processes of separation, compression, purification, and storage are highly energy-intensive, with prohibitive economic costs acting as a major barrier.[8,9] Additional concerns include limited geological storage capacity, high monitoring costs, and public resistance due to risks of potential leakage.[10]

Integrated carbon capture and utilization (ICCU), also known as integrated carbon capture and conversion (ICCC),[11] reactive capture of CO_2 (RCC),[12] and carbon capture and recycling (combined CCR),[13] has emerged as a compelling alternative. ICCC eliminates the need for desorption, compression, transportation, and long-term storage by enabling direct CO_2 conversion within absorbents, thereby reducing overall energy consumption and simultaneously lowering atmospheric CO_2 concentrations (Fig. 1).[14] These systems may take the form of integrated cascades or fully *in situ* single-pass processes.

In Aspen Plus–based syngas production TEA,[15] ICCU demonstrated higher energy efficiency (37.1%) compared to CCU (35.4%) for Ca-looping capture coupled with reverse water–gas shift (RWGS) syngas production, reflecting reduced energy consumption per unit product. Comparative syngas TEA shows the total annual cost of ICCU is $867.07 million, corresponding to a total cost of CO of $720.25 per tonne. In contrast, CCU has higher costs, with a total annual cost of $1027.61 million and a total cost of CO of $1004.53 per tonne. Analysis also shows that the ICCU process can produce more CO (1.20 Mt year^{-1}), less purge (0.21 Mt year^{-1}), and less consumption of CaCO3 (0.62 Mt year^{-1}). The Cost of CO_2 Avoided of ICCU (317.11 $ per ton) is much lower than that of CCU (1230.27 $ per ton). Furthermore, in methanation applications, the integrated route requires only one-third of the energy input consumed by the decoupled CCU process, which translates into a 13% reduction in production costs, lowering the price of methane from 962.86 € per ton in the conventional scheme to 837.1 € per ton with ICCU.[16]

Nevertheless, realizing the full extent of these efficiency gains requires a level of process-material integration that is not yet adequately reflected in most existing reviews, which focus on either capture materials or conversion technologies separately. As a result, the current ICCC literature remains fragmented, with limited comprehensive evaluations that bridge material design, process integration, techno-economic analysis, and industrial scalability. Furthermore, there is insufficient comparative assessment of dual-functional materials (DFMs) with respect to structural stability, product selectivity, and durability under realistic flue-gas conditions. Therefore, this review addresses existing gaps by presenting a

Abdelrahman A. Ashour

Abdelrahman Ashour is a Graduate Research Assistant at the Energy Materials Laboratory, The American University in Cairo. His research focuses on developing and evaluating functional materials for electrocatalysis and sustainable energy conversion, with interests in CO_2 utilization, system design, and techno-economic analysis for renewable fuel production.

Salma Elshabrawy

Salma Elshabrawy received her BS (2021) and MS (2024) degrees in Chemical Engineering from Alexandria University, Egypt. She worked as a research assistant under the supervision of Prof. Nageh Allam, at the American University in Cairo, Egypt. The research focused on electrocatalytic CO_2 reduction, and integrated methods of capturing and conversion. She is currently pursuing her PhD in Chemical and Biomolecular Engineering at Rice University, USA, under the supervision of Dr Jason Adams, where her research focuses on kinetic modeling and computational simulation of electrocatalytic reactions.

Nageh K. Allam

Nageh Allam received his PhD in Materials Science and Engineering from Pennsylvania State University. He joined Georgia Institute of Technology as a postdoctoral fellow then Massachusetts Institute of Technology as a Research Scholar. After his postdoctoral tenure, he joined The American University in Cairo, where he is currently a professor of Materials Science and Engineering. His research focuses on the fabrication of well-designed nanostructured materials with composition, size, and shape control for use in energy conversion (Water electrolysis, CO_2 reduction, NH_3 synthesis, Biogas, etc.) and storage (Batteries & Supercapacitors), Capacitive deionization, Electrochemical sensors, Biomaterials, among others. The research comprises both experimental and theoretical activities.

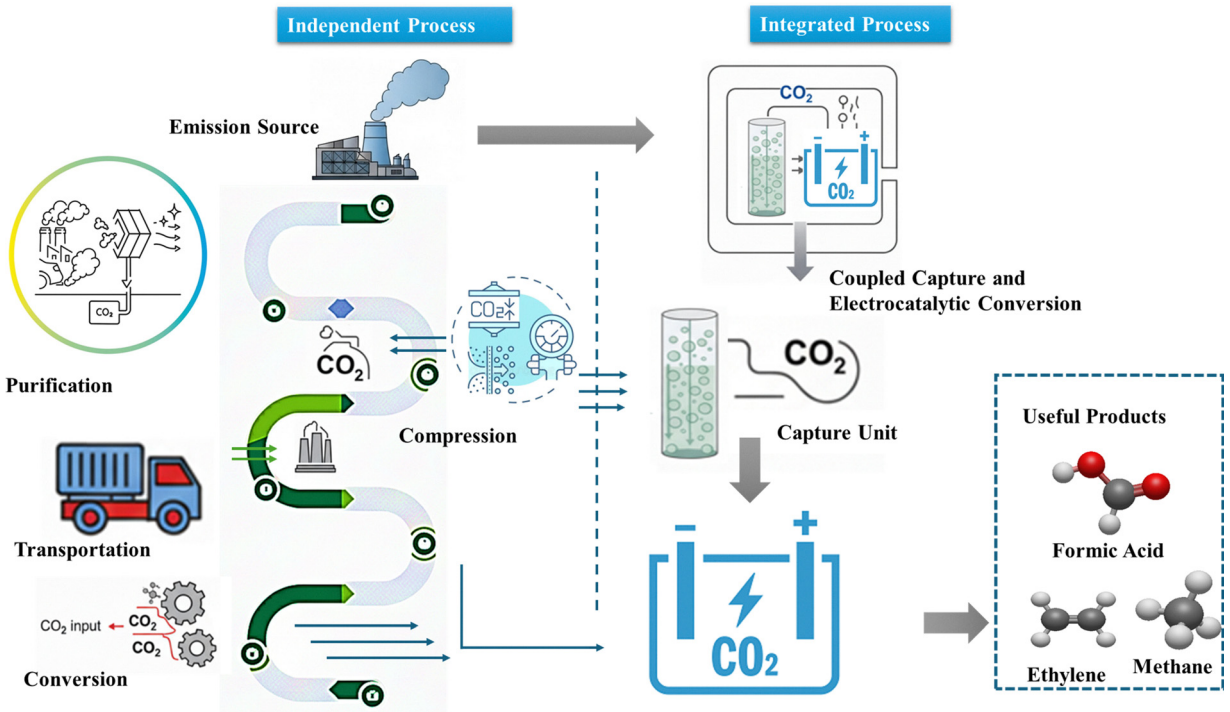

Fig. 1 A schematic comparing two pathways for CO_2 utilization: the conventional multi-step process (independent process) *versus* an integrated approach for direct capture and conversion (integrated process).

state-of-the-art analysis of the Integrated CO_2 Capture and Conversion (ICCC) field, spanning fundamental materials science to process-level techno-economics. Advances in dual-function materials (DFMs) are surveyed, including solid sorbents such as porous organic polymers (POPs), covalent organic frameworks (COFs), metal–organic frameworks (MOFs), zeolites, and metal oxides, as well as liquid solvents such as amines, ionic liquids (ILs), deep eutectic solvents (DESs), and molten salts. In addition, the performance and technology readiness levels (TRLs) of major capture and separation technologies are evaluated, along with the definition of critical performance indicators and the identification of outstanding challenges. As illustrated in (Fig. 2), the workflow of this review provides a structured pathway that connects materials development with carbon capture technologies and separation techniques and further extends to system-level performance indicators and techno-economic assessment, ensuring comprehensive coverage from fundamentals to applications. However, integrating capture and conversion within a single workflow imposes stringent kinetic and thermodynamic constraints: materials must bind CO_2 strongly enough for efficient capture yet release or activate it rapidly at catalytic sites, while mass transport and heat management must be compatible with high turnover frequencies under realistic flue-gas compositions. Therefore, this review places particular emphasis on how capture thermodynamics, diffusion limitations, reaction kinetics, and process synergies co-determine the performance window of integrated ICCC processes and dual-functional materials. Finally, a research roadmap is outlined to accelerate the transition of ICCC from laboratory-scale development to industrial deployment, complemented by a bibliometric analysis that maps development trends, research hotspots, and future directions.

Bibliometric analysis of ICCC research

On July 1, 2025, the research status of ICCC was analyzed and discussed based on the core database of Web of Science, which is a multidisciplinary core journal citation index database for the most relevant academic journals and international conferences. To ensure comprehensive coverage, the following search terms were employed: integrated carbon capture and conversion, integrated CO_2 capture and utilization, ICCC, ICCU, carbon capture and *in situ* conversion, carbon capture and *in situ* utilization, and dual-functional materials. The bibliometric analysis was conducted with VOSviewer software to generate keyword clusters and visualize research trends.[17] Out of 2181 publications, 1336 were published between 2020 and 2025, reflecting the exponential growth in this field. After filtering repetitive terms, 51 keywords appeared more than 45 times among the 9081 retrieved, with dominant themes including flue gas, carbon dioxide capture, electrochemical reduction, absorption, adsorption, and dual-functional materials, all of which align with the primary scope of this review (Fig. 3). The author network revealed 9947 contributing researchers, of whom 30 authors have at least nine publications with one or more citations, underscoring the presence of a growing core community. Geographically, 97 countries have contributed to ICCC research. China leads publication output, mainly through the Chinese Academy of Sciences, followed by the United States, England, and South Korea, highlighting the global and competitive nature of this research domain.

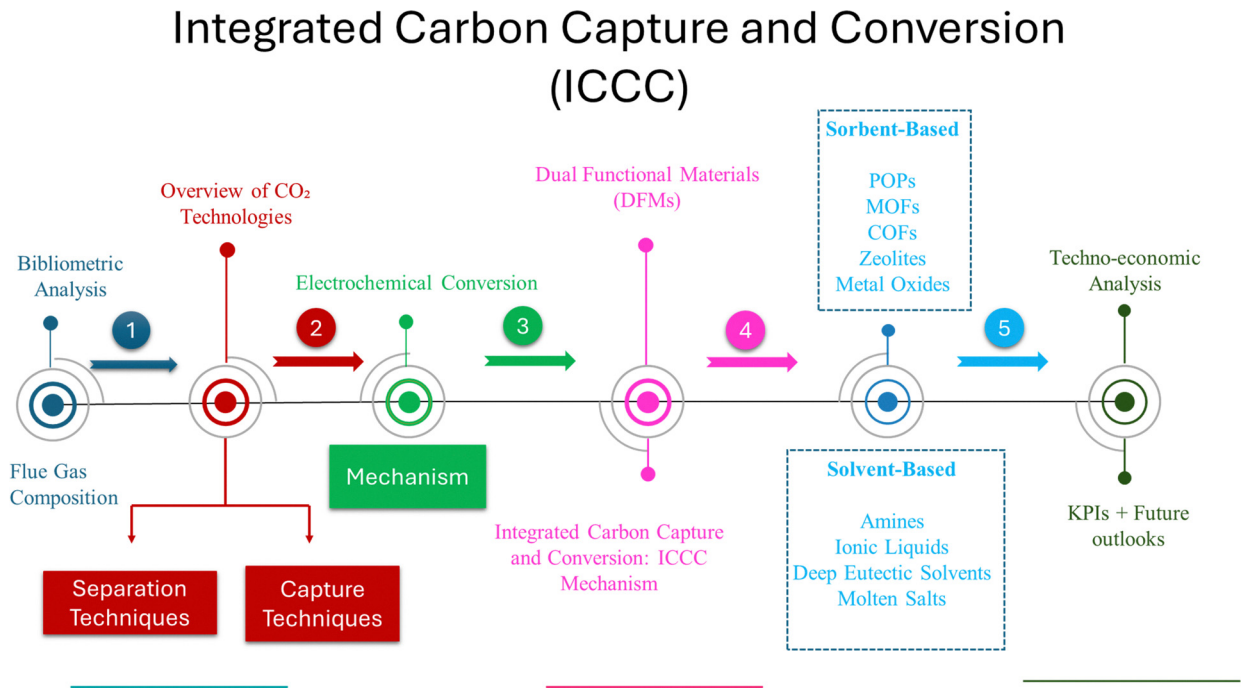

Fig. 2 Schematic overview of the review workflow: materials advances, capture technologies, performance indicators, and techno-economics.

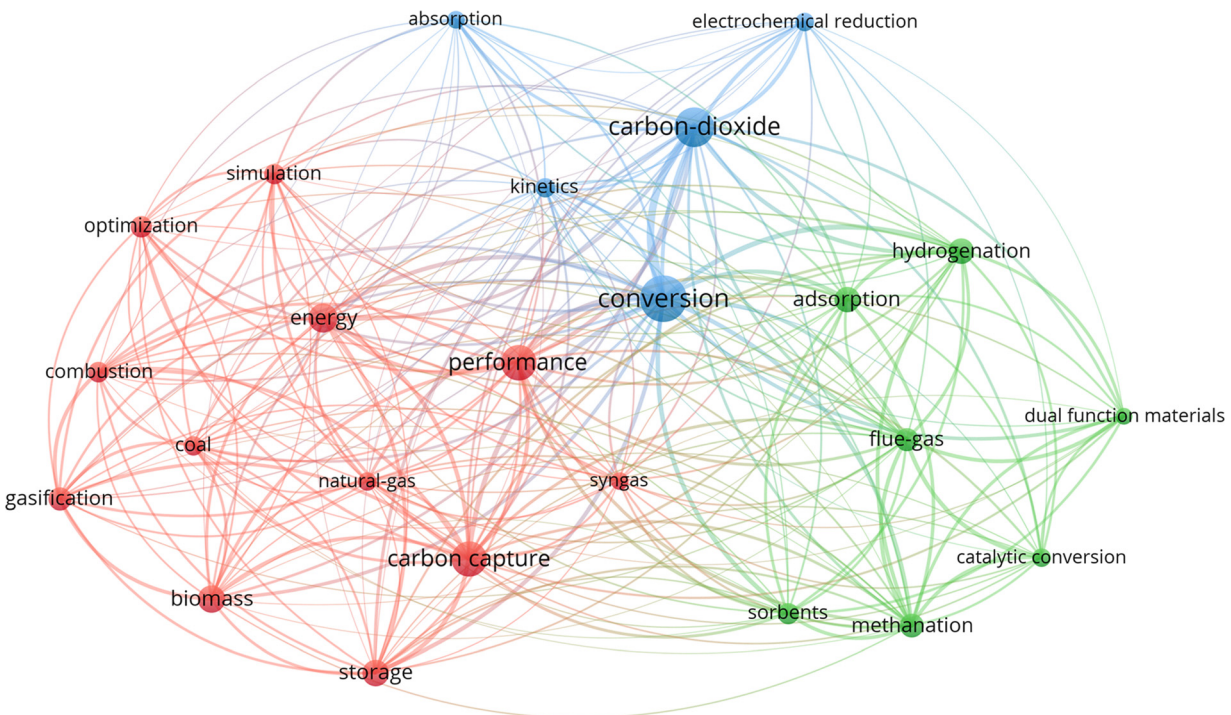

Fig. 3 Bibliometric analysis of keyword co-occurrence in research on integrated carbon capture and conversion. Each node represents a keyword, with its size corresponding to its frequency. The colored clusters group related terms, visually separating the main research sub-themes within the field.

Insight

These bibliometric findings reveal not only the surging momentum of ICCC research but also a shift toward global collaboration, with strong leadership emerging in Asia alongside active contributions from North America and Europe. The clustering of keywords indicates a transition from fundamental CO_2 capture studies toward integrated electrochemical conversion and dual-functional material design. This trend underscores the urgency and relevance of ICCC as a multidisciplinary research frontier that bridges chemistry, materials science, and

engineering, and sets the stage for industrial translation in the coming decade. Beyond mapping existing trends, this bibliometric analysis reveals several critical research gaps that this review addresses. First, some material classes, particularly sorbent materials, remain underexplored under realistic flue-gas conditions. Second, the scarcity of terms related to *in situ*/*operando* characterization (*e.g.*, DRIFTS, ambient-pressure XPS) and kinetic modelling signals a lack of fundamental insight into CO_2 activation at the capture–catalytic interface. Third, the analysis highlights a disconnect between lab-scale innovation and industrial translation, as techno-economic assessments (TEA) and pilot-scale demonstrations (TRL $\geq$ 4) remain negligible in current literature, representing a major bottleneck for industrial translation of ICCC technologies.

Composition of flue gas

The composition of flue gas is a critical factor in determining both the efficiency and cost of CO_2 capture and conversion systems, as CO_2 concentrations vary significantly across power generation and industrial processes[18] (Table 1). For example, flue gases from power plants typically contain 12.6%–14% CO_2, depending on the fuel type, whereas industrial sources such as urea, hydrogen, steel, and cement production can emit streams with CO_2 concentrations approaching 20%. In certain cases, such as ethanol or ethylene production, the exhaust may consist of nearly pure CO_2,[19] while carbon capture costs can differ substantially based on the CO_2 source (Fig. 4). In industries with dilute CO_2 streams, such as power generation, capture is considerably more expensive, with costs ranging from USD 52–86 per ton of CO_2, and levelized costs between USD 50–100 per ton.[20,21] By contrast, processes that emit concentrated CO_2 streams typically incur significantly lower capture costs, on the order of USD 14–32 per ton.[22]

While impurity tolerance is a key differentiator, the fundamental selection between thermocatalytic and electrocatalytic systems rests on their distinct operational requirements and capabilities. Thermocatalytic systems rely on high temperatures (100–500 °C) and elevated pressures (0.1–10 MPa) to drive reaction kinetics, requiring a supply of external molecular hydrogen (H_2) and often hitting thermodynamic equilibrium ceilings that limit conversion

Table 1 Summary of flue gas compositions, CO_2 capture costs, and the levelized cost of CCUS across major industrial sectors

Industrial process	CO_2 concentration in feed (vol%)[19]	Main impurities (vol%)[19]	Capture cost of CO_2 (US$ per ton CO_2)[20]	Levelized cost of CCUS (US$ per ton CO_2)[21]
Power generation (coal-fired)	12.6%–14%	71.4%–74% N_2, 8%–10.8% H_2O, 3%–4.3% O_2, trace SO_x, H_2S, NO_x	52–86	50–100
Hydrogen plant (steam methane reforming)	12%	29% H_2O, 50% H_2, 1% CO	>50	50–80
Cement industry	19%	61% N_2, 13% H_2O, 8% O_2	62–94	60–120
Steel industry (Blast furnace)	20%	56% N_2, 21% CO, 3% H_2	>75	40–100
Natural gas processing	99%[22]	1% H_2O[22]	14–20	15–25
Ammonia production	99%[22]	1% H_2O[22]	19[22]	25–35
Bioethanol (fermentation)	100%	—	32[22]	25–35
Ethylene oxide (vented stream)	100%	—	26[22]	25–35
Air (for reference)	0.04%	78% N_2, 20% O_2, 1% Ar	—	134–342

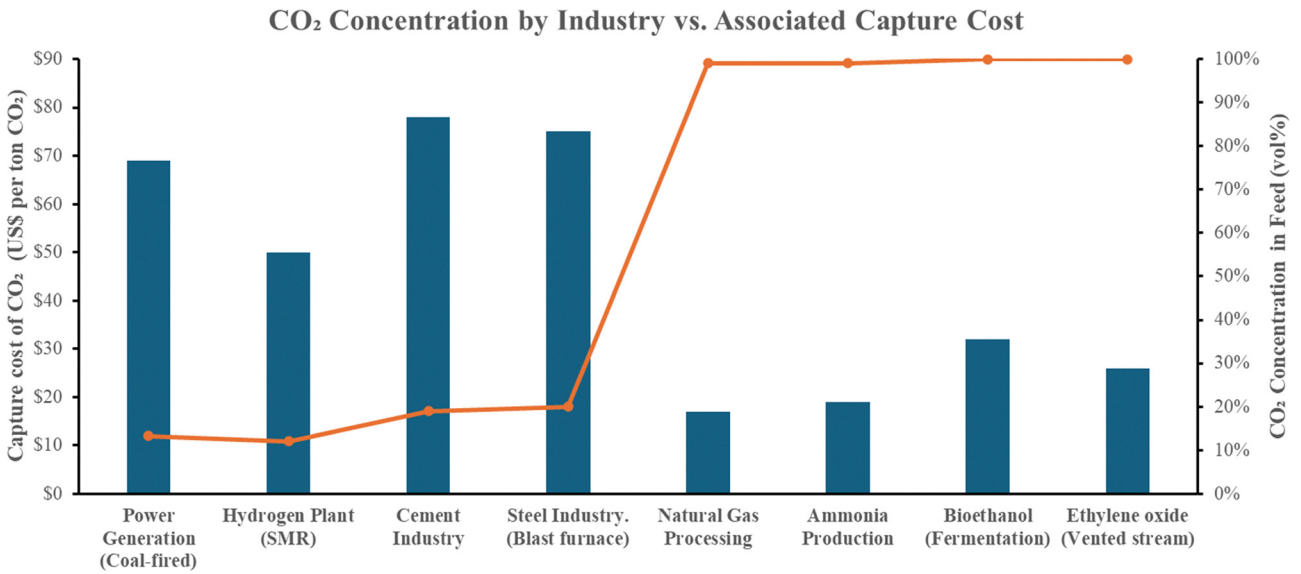

Fig. 4 Variation of CO_2 concentration in flue gas across different industries and impact on capture costs. The plotted data show estimated averages, reflecting the variability documented in the literature for each industrial application.

efficiency; however, electrocatalytic approaches offer a compelling alternative by operating under mild, ambient conditions (<100 °C, <1 MPa).[23] By utilizing renewable electricity and water as a direct proton source, electrocatalysis eliminates the need for energy-intensive hydrogen storage and transport and leverages applied overpotentials to overcome thermodynamic limits, unlocking superior selectivity for valuable multi-carbon (C_{2+}) products like ethylene that are difficult to synthesize thermochemically. However, beyond CO_2 concentration, the stability of ICCC materials is critically compromised by flue gas impurities, which trigger distinct poisoning mechanisms that must be accounted for in reactor design. First, sulfur oxides (SO_x), being stronger acids than CO_2, react irreversibly with basic active sites to form heat-stable salts (sulfates) that survive standard regeneration, leading to permanent pore plugging and progressive capacity decay.[24] Second, nitrogen oxides (NO_x) compete *via* stronger adsorption on Lewis's acid sites (metal oxides, zeolites) and accelerate sorbent degradation through nitration/reduction side reactions, reducing faradaic efficiency.[25] Third, moisture exerts a dual negative effect: it competitively adsorbs on hydrophilic sites, hindering CO_2 uptake, and promotes hydrothermal sintering of dispersed metal nanoparticles during the high-temperature conversion step, effectively deactivating the catalyst.[26] Fourth, oxygen (O_2) selectively oxidizes hydrogenation catalysts (*e.g.*, Ru/Rh) and induces carbonate decomposition in solid DFMs.[27]

Regarding the impact of flue gas impurities on the direct electrochemical CO_2 conversion, Pimlott *et al.* assessed this using a reactive carbon electrolyzer for electrocatalytic (bi)carbonate conversion.[28] They found that flue gas containing sulfur oxides (SO_x), and nitrogen oxides (NO_x) exhibit markedly different impacts on the CO_2 electrolysis: SO_x have minimal impact on CO selectivity, whereas NO_x drastically reduce faradaic efficiency (FECO), from ~60% to <5% at 2000 ppm (Fig. 5a). Besides that, gas-fed CO_2 electrolyzer exhibited a +90% reduction in CO selectivity with 10% oxygen (O_2) in the feed while liquid-fed electrolyzer was unaffected, the same FECO of 65% at 100 mA cm^2 at an O_2-saturated feedstock and O_2-depleted feedstock (Fig. 5b). Thus, both CO_2 concentration and impurity composition must be considered when evaluating the economics and scalability of capture–conversion systems. Accordingly, the following sections will provide a detailed overview of state-of-the-art carbon capture technologies and separation techniques, followed by an in-depth analysis of the electrochemical conversion process.

Overview of CO_2 capture technologies

There are three major approaches for carbon capture: post-combustion,[29] pre-combustion,[30] and oxyfuel combustion.[31] Determining the optimal carbon capture technique is a multi-faceted decision that requires evaluating a variety of technological and economic factors, such as the properties of flue gas, the required gas purity, the costs of plant construction and operation, the availability of commercial expertise, and the process's reliability and flexibility in operation. Thus, a thorough comparison of the three key CO_2 capture technologies for flue gas is summarized in (Table 2) and (Fig. 6).

As shown in (Fig. 7),[32,33] all three CO_2 capture technologies achieve high capture removal efficiency, with post-combustion and pre-combustion at 90% and oxyfuel combustion at over 90%, but they differ in their techno-economic performance. The pre-combustion process exhibits the lowest energy consumption and the most competitive capture cost at 3.35 GJ t^{-1} CO_2 and $34–63 per t CO_2, respectively. In contrast, post-combustion is the least economically favorable, with the highest energy requirement of 4.14 GJ t^{-1} CO_2 and a cost of $46–74 per t CO_2. At a middle ground, oxyfuel Combustion occupies as high energy consumption as Post-Combustion at 4.05 GJ t^{-1} CO_2 but its capture cost remains moderately lower at $52 per t CO_2. Thus, this analysis indicates that, based on these metrics, the economic viability of the three carbon capture technologies

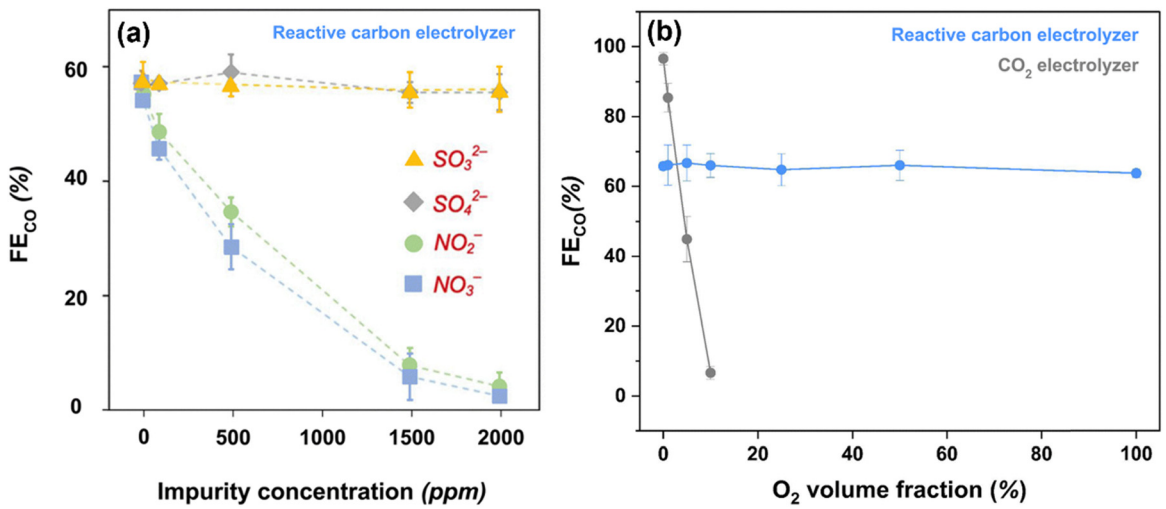

Fig. 5 Effect of flue gas impurities of (a) sulfur oxides (SO_x), nitrogen oxides (NO_x), and (b) oxygen (O_2) on CO selectivity in the direct electrochemical CO_2 electrolysis. Reprinted (adapted) from *Chem. Soc. Rev.*, 2025,**54**, 590–600. Copyright © 2025 the Royal Society of Chemistry.

Table 2 SWOT analysis of CO_2 capture technologies[32,33]

Carbon capture technology	Mechanism	Strengths	Weaknesses/threats	Opportunities
Post combustion	A process involves CO_2 capture from gas streams produced after the combustion of fossil fuels or other carbonaceous materials	– Mature, retrofittable technology. – Higher thermal efficiency *vs.* pre-combustion method. – Additional removal of NOx and SOx emissions	– Low CO_2 concentration reduces efficiency – High flue gas temperatures and volumes cause design challenges – Trace impurities such as NOx and SOx significantly affect the adsorption method – Requires powerful chemical solvents to capture CO_2 at low concentrations – Energy-intensive solvent regeneration	– Research into hybrid systems (*e.g.* membrane-pressure swing adsorption) – Improving pulverized coal systems to reduce emissions – Plant productivity enhancement
Pre combustion	A process transformes fuels into a gasified state to separate the CO_2 before burning the hydrogen-rich fuel like the SMR process	– 38–45% cheaper than post-combustion – 50% less energy for CO_2 separation than post-combustion due to high concentration and partial pressures – Minimal regeneration energy – Low-cost physical solvents	– Heat transfer and efficiency issues due to the high temperature of H_2-rich gas – Extensive supporting systems, such as an air separation unit and flue gas cooling – Complex chemical processes lead to additional plant shutdowns – Higher energy loss than post-combustion for reforming and air separation processes – Requires special non-gaseous feedstocks and NOx control	– Research needed for high-value chemical feedstock production – Flexible hydrogen/electricity production – Syngas as alternative turbine fuel
Oxyfuel combustion	A process involves oxygen rather than air burns fuel to produce flue gas with high CO_2 concentration	– 70–95% less expensive than other carbon capture methods due to lower flue gas volume and higher CO_2 concentration – 60–70% less NO_x emissions than air-fired combustion due to the absence of nitrogen – High-pressure operation reduces compression energy – Preserves high-efficiency steam cycles – Can be retrofitted into existing power plants	– Technology needs validation at a large scale – Pure oxygen combustion challenges due to the high temperatures involved – High capital expenditure and energy consumption costs due to the required larger amounts of oxygen, air separation, and flue gas recirculation costs – High risk of CO_2 leakage	– Research needed for heat-resistant materials and oxygen separation beyond cryogenic distillation – Improvements to reduce economic and efficiency penalties – Multiple fuel compatibility such as biomass and municipal solid waste for carbon neutrality

falls in the sequence: pre-combustion > oxyfuel combustion > post-combustion, especially for high-pressure, high-CO_2-concentration applications like IGCC and hydrogen production.

CO_2 separation techniques

The primary factors to consider when employing ICCC technologies are the CO_2 generation process, the technical readiness level (TRL), the efficiency of CO_2 separation, the economic costs, the environmental impact, which can be assessed through life cycle assessment (LCA) and the potential for CO_2 utilization either on-site or in nearby areas of a facility. And, each CO_2 capture technology applies different separation techniques such as chemical absorption, physical absorption, adsorption, membrane filtration, cryogenic separation, chemical looping combustion, calcium looping, and electroswing, which are summarized in (Table 3)[10,20,32–35] and (Fig. 8).

As Fig. 8 illustrates, among the CO_2 separation techniques, physical absorption stands out as the sole Tier 1 performer, demonstrating a high CO_2 removal efficiency of 93%, coupled with low energy consumption (1.03 GJ per tCO_2) and minimal capture cost (USD 12.38 per tCO_2).[36] In contrast, technologies such as chemical absorption (90%, ~3 GJ per tCO_2, USD 48.07 per tCO_2[36]), membrane filtration (up to 88%, ~2 GJ per tCO_2, USD 36.78 per tCO_2[36]), and calcium looping (89%, 2.8 GJ per tCO_2, USD 32 per tCO_2[37,38]) fall under Tier 2, primarily due to their moderate energy demands and higher capture costs. Meanwhile, chemical looping combustion (96%, 0.95 GJ per tCO_2, USD 59.2 per tCO_2[33]), cryogenic separation (95%, 3.8 GJ per tCO_2, USD 55 per tCO_2[39,40]), and adsorption (90%, 4 GJ per tCO_2, USD 47 per tCO_2[39,40]) are categorized as Tier 3, reflecting a trade-off wherein high capture efficiencies are accompanied by significant energy penalties and costs. It should be noted that all of these values represent averages, which may be influenced by various

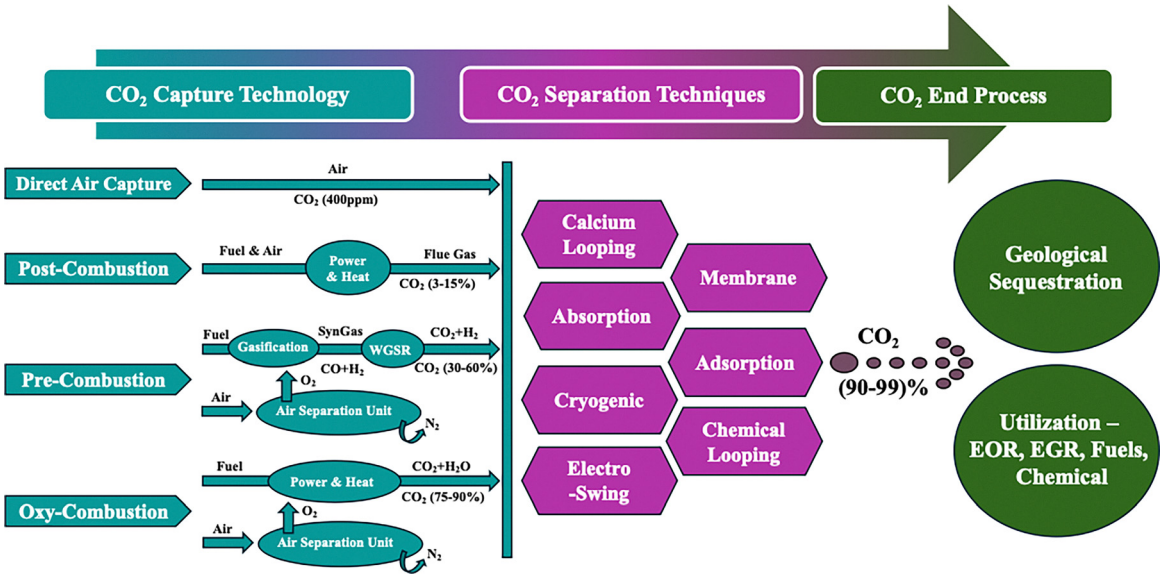

Fig. 6 Process flow of major CO_2 capture technologies, subsequent separation techniques, and the final pathways for either geological sequestration or industrial utilization.

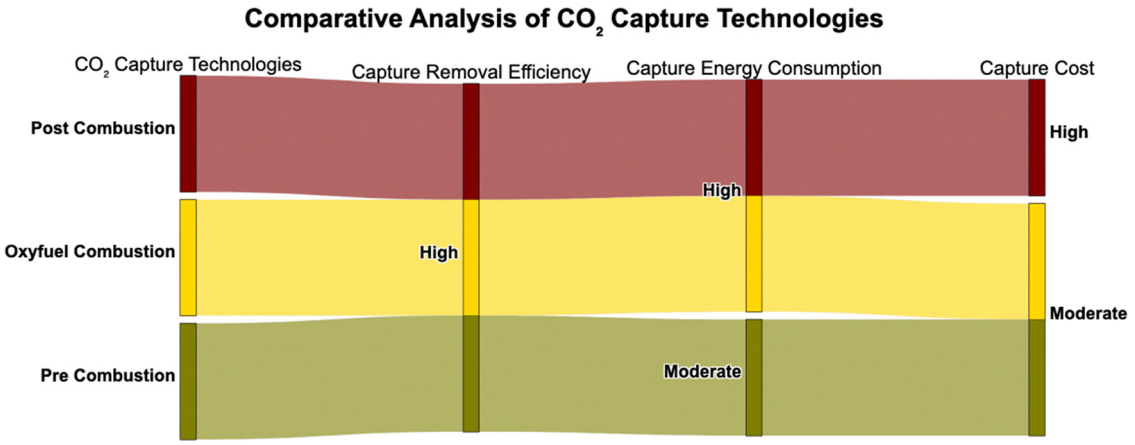

Fig. 7 Sankey diagram comparing three major CO_2 capture methods in terms of capture efficiency, energy consumption, and cost. These pathways illustrate general trends, as actual performance may vary significantly depending on scale, technology maturity, and operating conditions.

factors, including operating temperature and pressure, flue gas composition, properties of the capture agent, scale of deployment, and, most notably, the technology readiness level (TRL), which is addressed subsequently.

Technology readiness level (TRL)

Regarding Technology readiness level (TRL), as defined by the US Government Accountability Office (US GAO), Technology readiness level (TRL) is a nine-level scale system used to assess the maturity of a technology, ranging from the initial observation and reporting of fundamental principles to the successful implementation in mission operations, which was adopted by the Electric Power Research Institute (EPRI) for use with CO_2 processes.[41] Accordingly, TRL spectrum for ICCC can be divided into three phases: the research phase covers TRLs 1–3, the development phase encompasses TRLs 4–6, and the demonstration or deployment phase covers TRLs 7–9. In detail, the stages of technology readiness levels (TRL) begin with the basic principles (TRL 1), progress through application formulation (TRL 2), laboratory-scale development (TRL 3–5), pilot-scale trials (TRL 6), demonstration scale (TRL 7), commercial refinement (TRL 8), and eventually reaching full commercial scale (TRL 9). In (Fig. 9), a comparative overview of the Technology Readiness Levels (TRL) is presented for major CO_2 separation techniques in specific industries.[39,40,42,43] Among these, absorption is the most mature technology and has full commercial deployment among the other separation methods, depending on the type of solvents such as Amine, Selexol, and Rectisol. In contrast, separation techniques like Chemical Looping, Membrane Filtration, and cryogenic separation exhibit lower technology

Table 3 SWOT analysis of CO_2 separation technologies

Separation method	Mechanism	Strengths	Weaknesses/threats	Opportunities
Physical absorption	Absorption of CO_2 in the solvent is governed by its solubility, as defined by Henry's law, with solubility varying in response to temperature and pressure changes like in materials of Selexol and Fluor	– Low energy needed for sorbent regeneration – Low corrosivity and toxicity – More cost-effective at higher CO_2 partial pressures	– Limited operating temperature range; solvent capacity is optimized at lower temperatures to avoid any reduction in the solvent – High capital and operational costs	– Potentially operating at lower temperatures than chemical methods, so less energy consumption and cost
Chemical absorption	Upon interaction with the solvent, CO_2 forms an intermediate through a reversible or irreversible chemical process, which subsequently breaks down, releasing CO_2 upon heating like in materials of amines, ionic liquids, and Phase-change solvents	– Mature technology due to its high absorption capacities, such as amine absorption – High product purity > 99% vol. – Well-suited for retrofit – Effective at low CO_2 partial pressures	– Higher water consumption – Exhaust gases (water, SOx, and NOx) need to be treated – High regeneration energy costs – Requires a large absorber volume	– Further advancements needed for amines and ionic liquids
Adsorption	The flue gas flows over a solid sorbent, where CO_2 is adsorbed, and other gases are allowed to pass, with the desorption of CO_2 occurring through changes in temperature and pressure like in materials of zeolite, metal–organic, framework, activated carbon, and polymeric resins	– Flexibility in operating conditions with low-maintenance operation and Easy installation – Regeneration occurs at lower temperatures, so less heat than absorption methods – Waste biomass or industrial by-products can be used in adsorbent synthesis – The process is reversible through physical adsorption – Adsorbent can be recycled, hence low waste generation	– Sensitive to contaminants like sulfur, and nitrogen oxides, affecting their efficiency – Poor adsorbent durability, resulting in additional costs for frequent material replacements – Challengeable to achieve the optimal operating temperature	– Advances in developing composite adsorbents to have cost-effective, reusable, and non-corrosive sorbents – A wide range of potential sorbent materials exist – Dry gas products can be addressed
Membrane filtration	CO_2 is separated from the main gas stream using a membrane that operates in two ways: the gas separation membrane, which exposes flue gas to the high-pressure side and separates CO_2 on the low-pressure side, and the gas absorption microporous membrane, which enables both gas flow and absorption like in materials of graphene, organic, inorganic, and mixed matrix	– Simple, modular system design for easy adaptation – No regeneration energy required, leading to lower costs – Higher energy efficiency compared to absorption and adsorption methods – Zero waste by-products generated – Continuous separation, offering efficiency over time	– Structural problems under high-pressure conditions lead to instability – Long-term performance degradation due to sensitivity to corrosive gases makes sustained operation challenging – Moderate product purity	– Advances in composite hollow-fiber membranes, mixed matrix membranes, and hybrid membrane-cryogenic processes – Low separation costs and minimal energy requirements might push this technology forward – Minimal footprint, making it ideal for offshore applications – High commercial availability with efficient separation capabilities
Cryogenic separation	CO_2 is separated from a gas mixture through consecutive refrigeration at different condensation temperatures, inducing phase changes only in carbon dioxide based on its dew point or sublimation like in materials of ceramic, glass, and aqueous	– Commercially proven and well-established technology Easily integrated into power stations and other industrial point sources – Energy savings by reducing the need for compression – No chemicals required for the process, making it simpler and more sustainable – Capable of filtering other pollutants, offering additional environmental benefits	– Moisture removal is required from flue gas to prevent ice formation and equipment blockages – Energy-intensive due to the extreme cooling requirements, increasing operational costs – Accumulation of solid CO_2 reduces evaporator or heat exchanger efficiency over time	– High purity of the captured CO_2 raises its economic value for various industrial uses

Table 3 (*continued*)

Separation method	Mechanism	Strengths	Weaknesses/threats	Opportunities
Chemical looping combustion	The combustion process is split into oxidation and reduction phases, each carried out separately, with a solid oxygen carrier being oxidized by air in the first phase and then reduced with a hydrocarbon in the second phase, producing CO_2 and H_2O	– Simple operation, with compatibility for low CO_2 partial pressures – The exhaust stream from the fuel reactor contains CO_2 and water, where CO_2 can be efficiently separated by condensation – The process relies on low-cost oxygen carriers	– Early-stage technology – Fuel needs to be desulfurized to avoid metal sulfide formation – Sensitivity to any air leakage – Retrofitting the system is complex – Costly oxygen production	– Exhaust gas from the air reactor is primarily nitrogen, with no harmful compounds – No need for energy-heavy air separation, as the process yields high concentrations of CO_2
Calcium looping combustion	CO_2 is captured through reversible reactions between CaO and CO_2, known as carbonation and calcination for the respective stages	– Cost-effective raw materials for sorbent synthesis – Ideal technique for retrofitting pulverized coal-fired power plants and enhancing sorption-based hydrogen production	– Rapid decline in limestone (sorbent) capacity after several CO_2 reaction cycles – Environmental concerns relate to limestone mining, waste from Ca-looping, and high operational temperatures – Need for an air separation unit to supply pure oxygen (O_2) for calcination	– Offering a minimal decrease in power plant efficiency, with the potential for further reduction
Electroswing	It operates by using a reversible electric current to either directly charge an electrode for CO_2 adsorption or to manipulate a solution's pH, creating a chemical swing that captures and then releases the gas like in materials of quinones, ferrocenes, and carbon nanotubes	– Ambient operating conditions – Low cost due to the decreasing cost of renewable electricity	– Technology readiness is still at the pilot stage – Low current density due to their inability to operate at high current densities, limited to less than 5 mA cm^{-2} – High energy consumption and cost: to run at higher current densities results in large overpotentials, which lead to a higher energy demand and increase the capital cost	– Developing novel electrode materials to overcome current limitations, *e.g.*, advanced redox-active organics and electrode designs – Further scaling and optimization are needed for commercialization

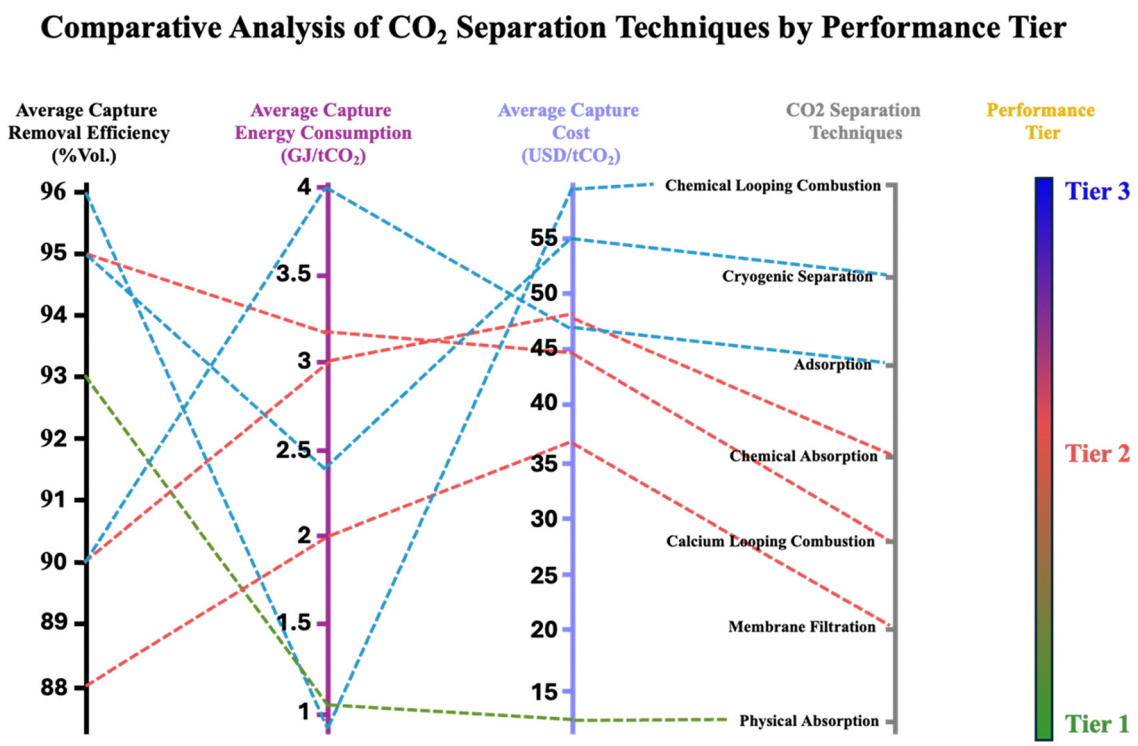

Fig. 8 Parallel coordinates plot comparing seven CO_2 separation methods across three techno-economic indicators: average removal efficiency, energy consumption, and capture cost, color-coded by three performance tiers (Tier 1: green; Tier 2: red; Tier 3: blue). The plotted values are representative benchmarks and an indicative guide from the literature and are subject to variation based on real-world operating conditions.

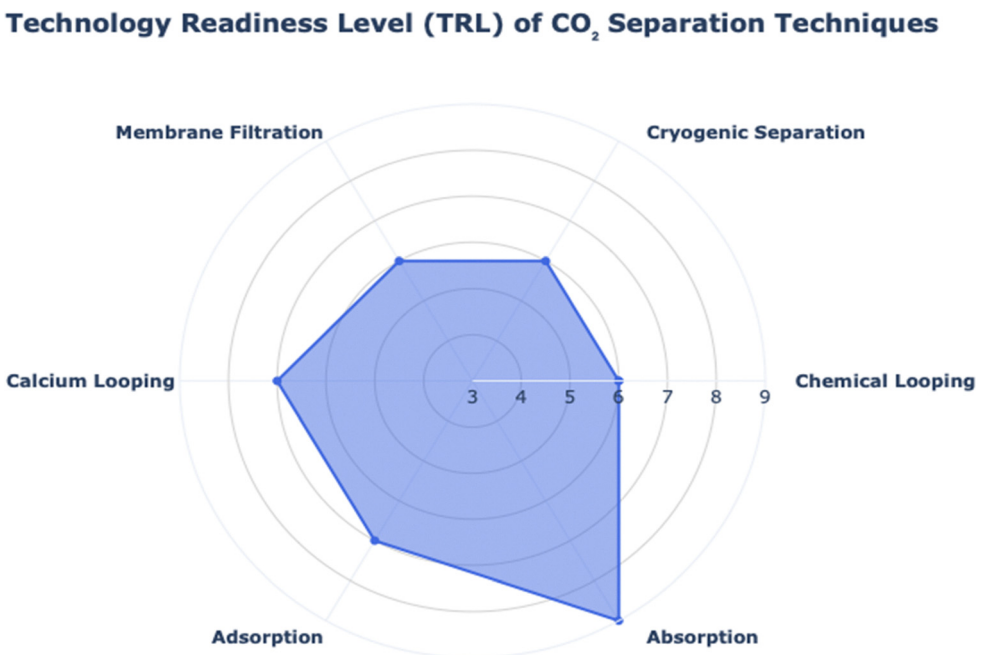

Fig. 9 Comparative TRL assessment for each of across the CO_2 separation techniques. TRLs are dynamic and context-dependent, varying with system design, operating conditions, and demonstration scale, and the values shown correspond to the highest levels reported in the literature for each technique.

maturity (TRL 5-6)[44,45] which reflects their limited operational experience and deployment beyond laboratory or pilot scales. Meanwhile, separation techniques such as adsorption and calcium looping are positioned at intermediate (TRL 6-7),[46] which indicates active development and initial field demonstrations, but not yet full commercial viability. Assessing these TRL levels underscores which CO_2 capture and separation technologies are approaching commercialization, and which still require significant scale-up and

practical field validation since technology maturity significantly impacts both the feasibility and short-term adoption prospects of these carbon capture approaches.

Electrochemical conversion: mechanism

Besides the direct use of CO_2 in several industrial processes such as enhanced oil recovery, urea production, food and beverage, water treatment, and fire retardants, there are several routes to convert CO_2 into commercial products, including thermal, electrochemical, photocatalytic, photosynthetic, biological, copolymerization, and mineralization.[47] While extensive research in academia has focused on developing materials for CO_2 capture from point sources and ambient air, and subsequent conversion to value-added chemicals[48] such as fuel production, like methane,[49] methanol,[50] and formic acid,[51] this review paper primarily emphasizes the electrochemical conversion process.

Among the various CO_2 conversion techniques, electrochemical conversion has multiple advantages, including mild reaction conditions, potential synergy with renewable energy sources, high environmental compatibility, and controllable reaction rate and product selectivity by modulating the applied electrode potential; however, several challenges still need to be addressed such as high energy requirements, durability, environmental impacts and sustainability of certain conversion products, and high thermodynamic and kinetic barriers.[17]

After efficient capture and separation of CO_2 gas, the CO_2 undergoes electrochemical conversion to valuable carbon-based products such as carbon monoxide, ethylene, ethanol, and more through a multi-proton-coupled and multi-electron transfer process.[52] Generally, the electrochemical CO_2RR can be presented as

$$xCO_2 + n(H^+ + e^-) \rightarrow \text{product} + yH_2O$$

Noting that the anodic reaction is the oxygen evolution reaction (OER) while the contemporaneous reduction of H^+ is accompanied by the hydrogen evolution reaction (HER), which should be restricted during the electrolytic reduction of CO_2 by considering the thermodynamics involved in the whole conversion process to get the desired product.[53] Additionally, the electrocatalytic reduction of CO_2 follows a three-part reaction mechanism: electron transfer, electrochemical reaction, and catalytic reaction.[54]

Initially, CO_2 dissolved in the electrolyte gets in contact with the electrode, where it adsorbs onto the catalyst for activation. Secondly, the reduction of adsorbed CO_2 occurs through proton-electron transfer on the catalyst surface, which breaks the C=O bond and requires about 750 kJ per mole as a thermodynamically uphill reaction, forming a new chemical bond (COOH*), where * denotes surface-bound species or vacant catalytically active sites. Subsequently, the reduction products are desorbed from the electrode and diffuse into the response medium, which depends not only on the stability but also on the reduction of COOH*, but also on the catalyst's capacity.

Integrated carbon capture and conversion: ICCC mechanism

Regarding CO_2 capture and conversion from diluted sources, the electrochemical conversion has been operated in three distinct processes: independent, coupled, and integrated.[55] The independent process involves multiple decoupled processes, in which CO_2 capture occurs independently of electrochemical CO_2 conversion, leading to energy losses and costs associated with CO_2 compression, transportation, purification, and release. In the integrated process, it simultaneously exhibits complete integration between the capture and electrochemical conversion of CO_2, directly converting the captured CO_2 at the electrode

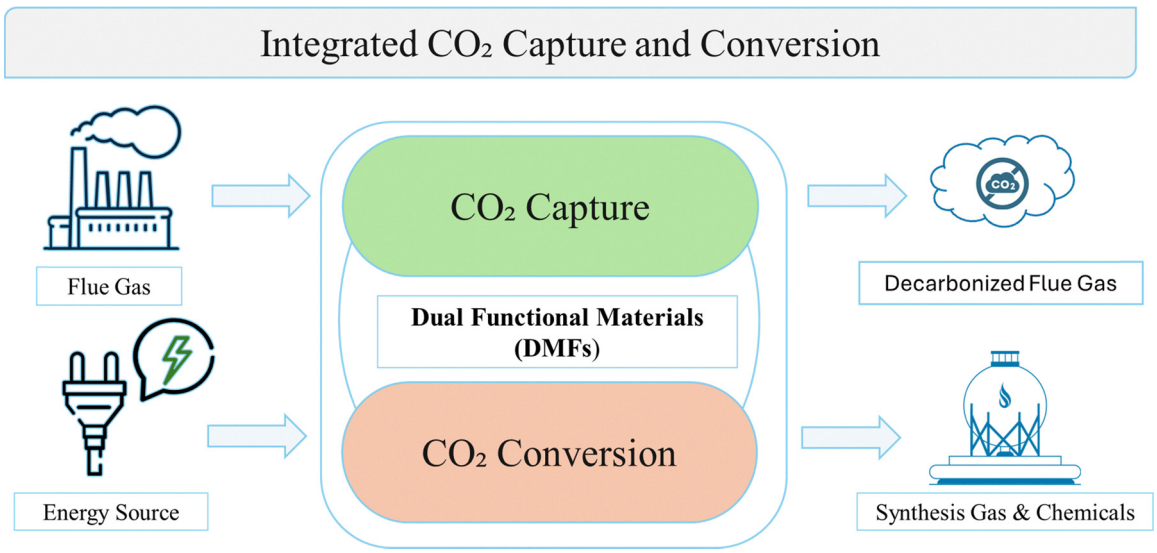

Fig. 10 Conceptual overview of the integrated CO_2 capture and conversion (ICCC) process by using dual functional materials (DFMs).

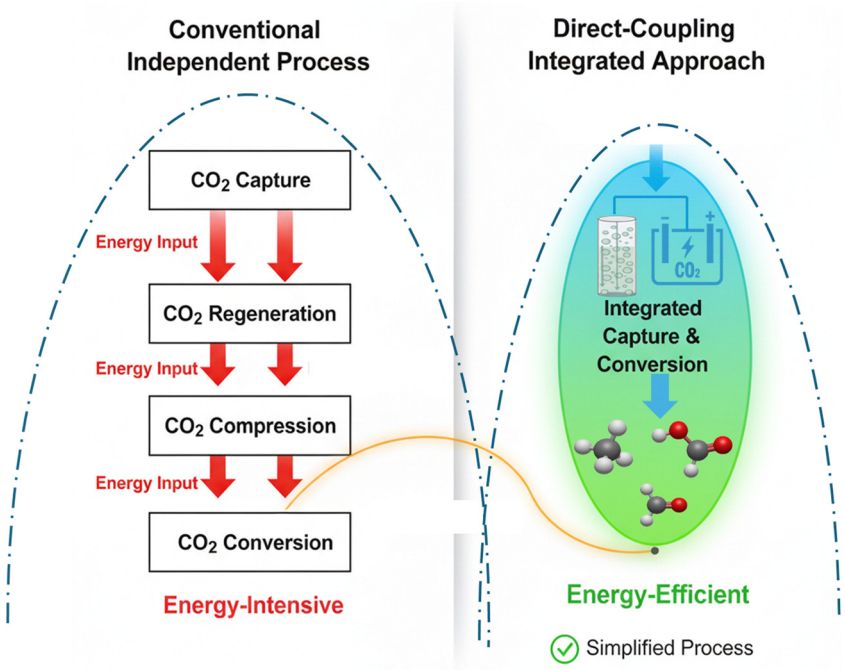

Fig. 11 A conceptual energy diagram contrasting the conventional, energy-intensive independent process *versus* the direct coupling 'integrated' approach of carbon capture and conversion.

surface to the regeneration of the capture media and the production of valuable products, which reduces the complexity and energy consumption of the overall process, as shown in (Fig. 10 and 11). For electrochemical ICCC pathways operated at industrially relevant current densities ($\sim$200–800 mA cm^{-2}), solid oxide and molten carbonate electrolysis systems achieve $>$70–90% energy efficiency, with electricity consumption below $\sim$2.5–3.4 kWh Nm^{-3} CO at $\sim$200 mA cm^{-2} (equivalent to $\sim$2200 kWh t^{-1} CO produced), while maintaining near-unity faradaic efficiencies ($>$99%) at current densities exceeding 750 mA cm^{-2}.[56] Therefore, the integrated process bypasses the CO_2 stripping steps, thereby compensating for capture costs and making commercial deployment economically more feasible. Consequently, the following section will explore dual-functional materials for Integrated Carbon Capture and Conversion (ICCC), with a particular focus on key adsorbent and absorbent materials.

Dual functional materials (DFMs): adsorbents and absorbents materials

As flue gases are characterized by high temperatures (around 373 K), low pressures, and low CO_2 levels (1 atm and 10–15% mol), absorption and adsorption processes are likely the most efficient methods for CO_2 separation under these conditions, with the highest TRL among CO_2 separation methods, which are the primary focus of this review,[57] and the process itself simply illustrated in (Fig. 12). Regarding absorption, it refers to CO_2 dissolving into a solvent with 60–95% CO_2 removal efficiency, where it may either chemically react with the solvent as in chemical solvents such as Amines or be held by weak van der Waals forces as in physical solvents such as Selexol, Fluor, Purisol, and Sulfinol.[58] On the other hand, adsorption method is divided into two types: chemisorption, where covalent bonds are created, and physisorption, where electrostatic and van der Waals forces dominate the interaction, using solid adsorbents such as activated carbon and silicates, with 80–95% CO_2 removal efficiency.[59]

In this context, this timely and thorough review paper summarizes the latest developments of the integrated process progress with an emphasis the following promising dual functional materials: adsorbents such as porous organic polymers (POPs), covalent organic frameworks (COFs), metal–organic frameworks (MOFs), zeolites and absorbents such as amines, ionic liquids, eutectics, and molten salts, the mechanism (Fig. 13).

Sorbent-based CO_2 capture and conversion

This section focuses on solid-phase techniques for CO_2 capture, emphasizing advanced sorbents such as porous organic polymers (POPs), covalent organic frameworks (COFs), zeolites, metal–organic frameworks (MOFs), and metal oxides, and their applications in integrated electrochemical CO_2 capture and conversion systems. This analysis will highlight their advantages, challenges, future outlook, and potential for rapid implementation in carbon-neutral technologies.

Porous polymer materials

Recently, porous materials such as zeolites,[60] porous carbon compounds,[61] and porous polymers[62] have been used in intriguing research advancements in CO_2 recuperation and electrocatalytic reduction (Fig. 14). Because of their finely engineered

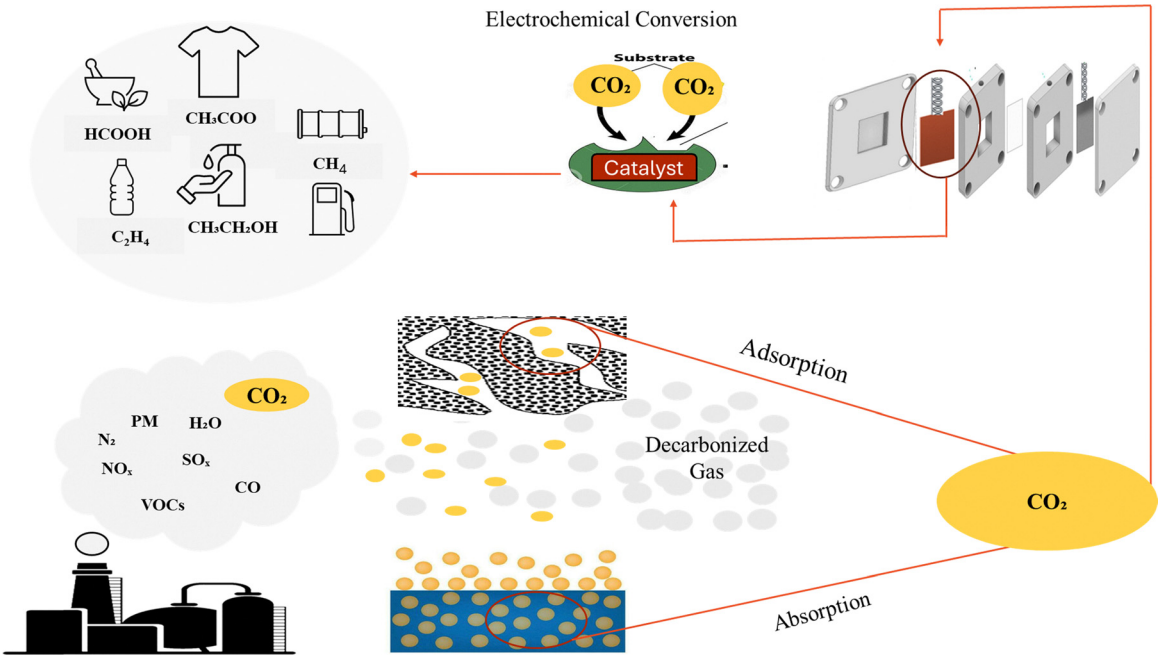

Fig. 12 A schematic of the two-step process involving carbon capture with a sorbent or solvent material, followed by carbon conversion into final products.

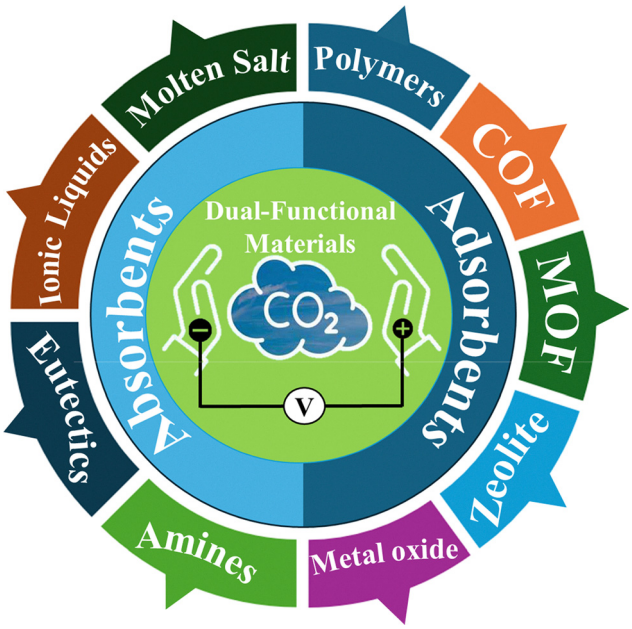

Fig. 13 Examples of the dual-functional materials used in integrated processes, with emphasis on the adsorbents and absorbents highlighted in this review.

active sites, high specific surface area, and controllable porosity, porous polymers stand out among the others.[63,64] There are four primary types of porous polymer materials utilized for CO_2 capture and electrocatalytic reduction, which are nitrogen-containing polymers (N-polymers), covalent organic frameworks (COFs), porous organic polymers (POPs), and porous coordination polymers (PCPs) (Table 4). Numerous synthetic techniques, such as solvothermal, iono-thermal, microwave, mechanochemical, and interfacial synthesis approaches, can be used to create such porous polymeric materials. The most popular preparation technique among them is the solvothermal approach.[65,66] The solvent thermal method's main drawback is that it is not appropriate for large-scale production because the reaction conditions are harsh and the solvent is primarily organic, which will pollute the environment when used in large quantities. However, it can increase synthesis efficiency by switching the solvent. The iono-thermal approach is not appropriate for commercial applications since it is primarily employed for the synthesis of covalent triazine frameworks (CTFs) and requires more stringent reaction conditions than the solvent thermal method.[67] One interesting synthesis technique is the microwave approach, which may efficiently shorten reaction times while preserving porosity.[68] Due to its simplicity, the mechanochemical approach is a suitable green synthesis method since it doesn't use solvents, which prevents contamination of the environment.[69] Three stages are typically involved in the CO_2 reduction reaction (CO_2RR): CO_2 adsorption, electrocatalytic reduction, and desorption. Specifically, a CO_2-saturated electrolyte is created by first dissolving gaseous CO_2 molecules in the solvent. On the electrode surface, the CO_2 dissolved in the solvent then undergoes a reaction. To finish the entire reaction process, the reaction products are finally desorbed off the electrode surface. Defined reaction mechanisms are yet unknown due to the many products and intricate intermediates in the multi-step reactions of CO_2RR. By transferring varying quantities of electrons, CO_2 can experience varying degrees of electrochemical reduction processes, as shown by the reaction equations in the table. The products of these reactions include HCOOH, CH_3OH, CO, CH_4, CH_3COOH, C_2H_4,

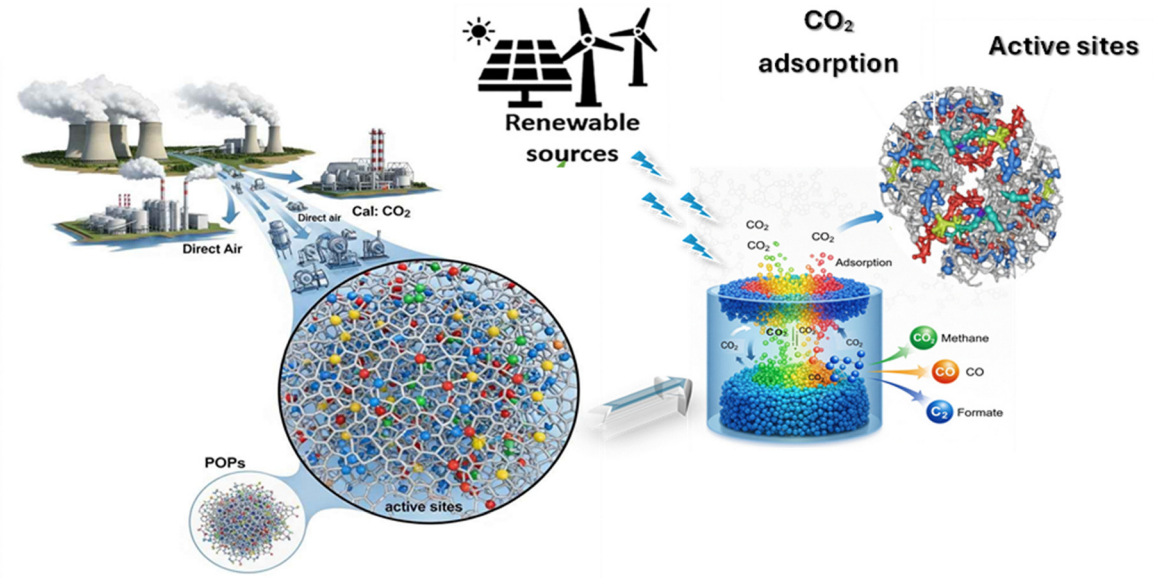

Fig. 14 Graphical abstract of POPs for CO_2 capture and electrocatalytic conversion.

Table 4 Advantages and disadvantages of porous polymer materials for CO_2 capture and electrocatalytic reduction[63]

Materials	Structural features	Advantages	Disadvantages (technical)	Techno-economic barriers
POPs	2D/3D covalent networks from organic polymerization	– Large SSA (up to 3000 $m^2 g^{-1}$)	– Poor microporosity (V_{micro} <50%)	– High monomer cost ($50–200 per kg)
		– Controllable functionality	– Oxidative degradation (+0.8 V)	– Solvothermal scale-up ($ZnCl_2$, 400 °C)
		– Tunable porosity – Good thermal stability (>400 °C)	– Swelling in humid flue gas	– Poor recyclability (30% SSA loss/cycle)
PCPs	Metal ions/clusters + organic linkers (crystalline)	– Ultra-high SSA (>7000 $m^2 g^{-1}$) – Adjustable pore function	– Poor thermal stability (<300 °C) – Hydrolysis in humid flue gas	– Metal salt cost ($100–500 per kg) – Multi-step solvothermal (DMF, 120 °C)
		– High CO_2 capacity (10 mmol g^{-1})	– Metal leaching under bias	– Non-recyclable (framework collapse)
COFs	Crystalline covalent organic frameworks	– Large SSA (4210 $m^2 g^{-1}$) – Abundant active sites (N-doping) – Diverse synthesis routes	– Poor crystallinity control – Hydrolysis (>50% loss @80% RH) – Low conductivity	– High cost ($200–1000 per kg) – Slow crystallization (days–weeks) – Non-recyclable (irreversible hydrolysis)
N-polymers	Nitrogen-functional polymers (± metals)	– Simple preparation – Cost-efficient ($10–50 per kg)	– Poor conductivity (R_{ct} >100 Ω) – Mechanical instability	– Large-scale mixing challenges – Moderate recyclability (50% capacity loss)
		– Adjustable pores	– Low SSA (<500 $m^2 g^{-1}$)	– Limited flue-gas tolerance

CH_3CH_2OH, C_2H_6, and so on. Furthermore, HER on the cathode coincides with the CO_2 decrease.

Porous organic polymers (POPs)

Porous organic polymers (POPs) constitute a category of lightweight, porous network materials characterized by extensive surface areas, adjustable pore sizes, and customizable components and structures. They consist of biological building units linked by covalent bonds. POPs utilized as electrocatalysts have exhibited notable activity and achieved substantial advancements in numerous electrocatalytic reactions, including the hydrogen evolution reaction, oxygen evolution reaction, oxygen reduction reaction, CO_2 reduction reaction, N_2 reduction reaction, nitrate/nitrite reduction reaction, nitrobenzene reduction reaction, hydrogen oxidation reaction, and benzyl alcohol oxidation reaction, owing to their well-maintained structural and compositional attributes. This section presents a comprehensive description of recent advancements in the application of POPs in electrocatalytic CO_2 reduction.[62,70,71] CO_2 reduction reactions (CO_2RRs) are transforming CO_2 molecules into hydrocarbon fuels through sustainable operations. These processes require unique catalytic systems, such as transition-metal dichalcogenides/phosphides, single-atom catalysts, perovskite materials, graphene derivatives, layered double hydroxides, metal oxides, two-dimensional metal-carbonitride and metal-boride layered materials, and POPs, which are recognised for

their physicochemical properties and potential for energy-driven operations.[72]

Physicochemical properties of porous organic polymers

Porous organic polymers (POPs) are regarded as a promising candidate for CO_2RR applications because of their superior stability, adaptability, perpetual porosity, and structural and compositional customization. Researchers have employed heteroatom-rich microporous structures and surface functionalization to increase CO_2RR activity.[62] Porosity tailoring has recently produced cutting-edge POPs materials with surface-active spots that catalyze reactions. Covalent bonds hold organic connections together to form POPs. The ability to tune CO_2 adsorption can be achieved *via* engineering by selectively functionalizing monomers and adding CO_2-philic metallic or nonmetallic sites. Transition-metal ions or nanoparticles can be immobilized on the POP surface to create metallized POPs. POP materials with various organic functional groups also use conjugated architectures to increase catalytic performance.[73–75] It has very good physicochemical features, such as high specific surface areas (up to 3001 $m^2\ g^{-1}$) and tunable pore designs (from microporous to hierarchical) made up of stiff organic building pieces that form covalent networks. They are very stable at high temperatures (up to 800 °C) and resistant to chemicals in severe settings. Fluorination makes them even more water-repellent. Because Lewis's acid–base interactions happen in ultra-micropores, POPs are good at adsorbing gases like CO_2 (up to 6.58 mmol g^{-1} at 273 K). Transition-metal coordination enables electrocatalytic CO_2 reduction, while π-conjugated complexes facilitate modulation of photoluminescence for optoelectronic applications. These materials are light, easy to change once they are made, and can be made into networks that dissolve or do not dissolve. POPs have a reduced density, better chemical stability, and conductivity that may be changed by hybrid topologies.[76]

Classification of porous organic polymers

POPs are crystalline and amorphous equivalents of multidimensional porous materials with large surface areas and adjustable functionality. As shown in (Fig. 15), CMPs, PIMs, HCPs, and PAFs are examples of amorphous POPs, whereas COFs and CTFs are examples of crystalline POPs. Like nanoporous

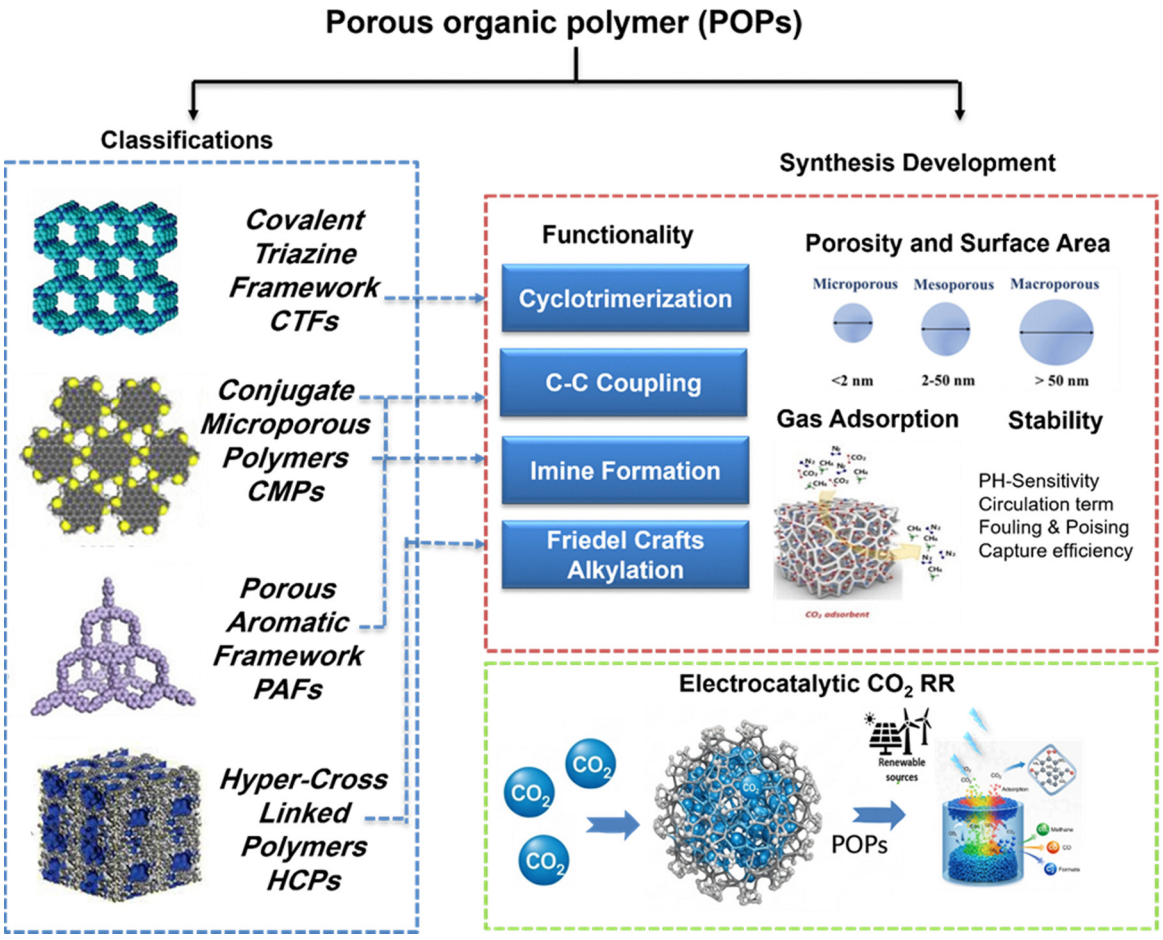

Fig. 15 The classifications, synthesis development and electrocatalytic CO_2 RR of POPs.

materials, POPs are inexpensive, lightweight, adjustable, and have good stability.[77–79] Because of their many chemical reactions and uniform pore widths, they are appropriate for a wide range of applications. With their large specific surface area and adjustable structure, POPs are the primary benefits for CO_2 electrochemical conversion. Examples include PAF-1, with a surface area of 5600 m^2 g^{-1} BET, and 3D COF-103, with a surface area of 4210 m^2 g^{-1} BET.[80,81]

Covalent triazine framework (CTFs)

CTFs have high surface area, a well-defined pore structure, good physicochemical stability, and surface-active sites that can be designed, making them promising functional materials for a range of applications. CTFs offer a flexible framework for heterogeneous catalysis, particularly for CO_2 conversion and adsorption. They are mostly made up of well-defined building pieces that create triazine moieties by covalent bonding. The main synthesis methods for CTF are the Iono-thermal trimerization molten $ZnCl_2$ that yields most functionalized CTF-based products. P_2O_5-catalyst for direct condensation of amide monomers, polycondensation, and superacid-catalyzed trimerization of aromatic nitriles (Fig. 16).[82] There are two types of CTFs: crystalline and amorphous. Since the strong covalent bond (C═N) is highly stable and the synthesis conditions are severe, the majority of reported CTFs are amorphous. However, crystalline CTFs with many highly ordered holes and periodic architecture provide substrate specificity and a better understanding of their basic properties. Recent developments in a range of CTF-based catalysts derived from task-specific nitrile monomers are compiled for CO_2-involved catalytic processes, including CO_2 cycloaddition, CO_2 carboxylation, CO_2 hydrogenation, CO_2 photoreduction, and CO_2 electroreduction. This review emphasizes the structural design and synthesis of common CTFs from a sustainable perspective, as well as the relationship between structure and properties in CO_2 catalysis. Significant opportunities and strategies in this field are examined to develop precisely designed CTFs with superior CO_2-catalytic capability.[83]

CTFs have a nitrogen-rich, electron-deficient structure with their inherent 1,3,5-triazine rings, which results in interesting heteroatom effects such as H-bonding, metal chelation, and π–π interactions. CTFs have an alkaline nature owing to the high nitrogen content, which makes them suitable for base-catalyzed organic reactions. The incorporation of stoichiometric, precisely defined coordination sites into triazine frameworks can enhance their capacity for metal ion complexation, while the meticulous integration of heteroatoms and other functional groups can further broaden their use. CTFs are commonly used as homogenous catalysts and as a pathway for stabilizing metal nanoparticles. They can also be used as precursors of nitrogen-doped porous carbon materials, which can be easily obtained after pyrolysis. The main classifications of CTFs as catalysts and support materials are: metal-free catalysts, supports

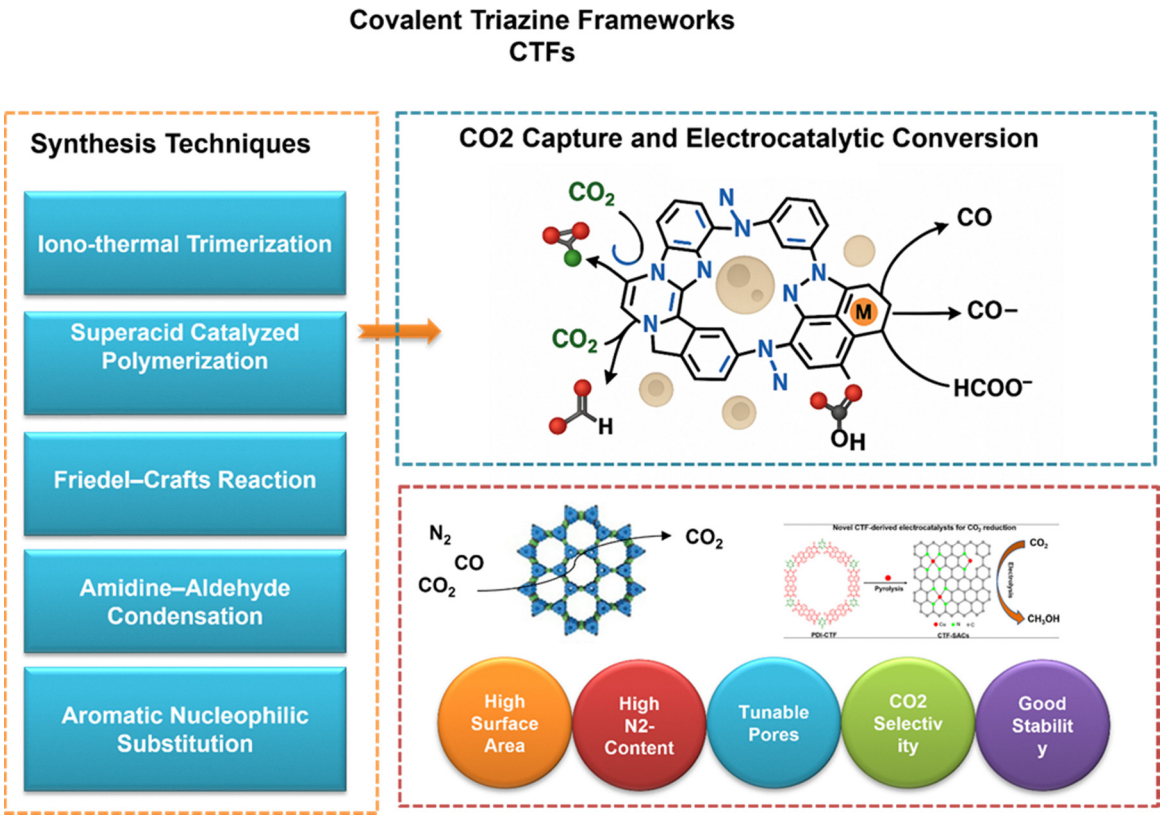

Fig. 16 Schematic illustration of CTFs for CO_2 capture and electrocatalytic reduction.

for solid molecular catalysts, supports for nanoparticulate catalysts, and precursors of N-doped porous carbon materials. The initial method employs CTFs as a primary catalyst to activate CO_2 *via* acid–base interactions; the second method utilizes CTFs as carriers for solid molecular catalysts; the third method involves CTFs as functionalized supports for the stabilization of metal nanoparticles with catalytically active species; and the fourth method utilizes CTFs as precursors for N-doped porous carbon materials through high-temperature pyrolysis.[84,85]

CTFs for CO_2 capture

CTFs are considered exceptionally promising materials for CO_2 capture owing to their physicochemical characteristics, including nitrogen-rich backbones, permanent porosity, great thermal and chemical durability, and adjustable pore architectures as shown in (Table 5). It mainly comprises triazine-based bonds generated through the trimerization of nitrile monomers, resulting in resilient covalent networks that display microporosity and elevated surface areas, generally between 500 and 2500 $m^2\ g^{-1}$.[86] Rational design of carbonaceous frameworks involves the incorporation of heteroatoms, specific functional groups such as amines and pyridine units, as well as metals like Ni, Co, and Cu, with customized pore size distributions to augment CO_2 adsorption capacity and selectivity for electroreduction into value-added products. CTFs possess advantages over MOFs as they do not depend on metal sites for CO_2 adsorption. The elevated density of nitrogen sites facilitates robust dipole-quadrupole interactions with CO_2 molecules, rendering them particularly effective for low-pressure CO_2 collection.[86,87] A pyridine-rich CTF demonstrates a CO_2 absorption of 4.2 mmol g^{-1} at 1 bar and 273 K, whereas the functionalization of CTFs with ionic liquids, urea, or amine groups improves CO_2 adsorption capabilities in flue gas conditions and humid settings. The integration of CTFs with metal single atom sites, such as Ni and Co, creates coordinated binding sites for CO_2, facilitating adsorption and selective reduction while ensuring good chemical stability and renderability. CTFs exhibit competitive CO_2/N_2 selectivity and substantial working capacity, alongside strong cycling performance throughout numerous adsorption/desorption cycles.[86,88] The CO_2 adsorption capacity at low pressures is a crucial factor in assessing porous materials for post-combustion carbon capture, where selective CO_2 separation is vital. In this regime, CO_2 absorption is governed more by the intensity of CO_2 interactions with the pores and active sites than by the surface area of the material. CTFs with micropores smaller than 1 nm are highly efficient for CO_2 adsorption, since their pore size roughly aligns with the molecular diameter of CO_2 (0.36 nm), hence improving adsorption efficacy. For instance, PHCTF-1a, PHCTF-4, and PHCTF-6 exhibit variations in porosity: PHCTF-4 and PHCTF-6 exhibit a greater surface area as determined by BET, although they possess smaller micropore volume fractions (V_{micro}/V_{total} = 58% and 39%, respectively) in contrast to PHCTF-1a (79%). Notwithstanding the substantial surface area of PHCTF-4 (52.4 $cm^3\ g^{-1}$) and PHCTF-6 (51.9 $cm^3\ g^{-1}$), their CO_2 uptake was comparable to that of PHCTF-1a (51.9 $cm^3\ g^{-1}$), underscoring the pivotal influence of micropore structure beyond surface area alone. The rational design of homogeneous or ultra-microporous CTFs is a viable approach for enhancing CO_2 collection at low pressures.[89,90] In addition to the microporosity design and extensive surface area, the incorporation of polar functional groups into the framework markedly improves CO_2 affinity by reinforcing dipole-quadrupole interactions. For instance, FCTF-1 and FCTF-1-600, characterized by polar C–F linkages, demonstrated elevated heat of adsorption (Q_{st}) and improved CO_2 binding relative to CTF-1 and its thermally treated derivative, CTF-1-600. The nitrile groups in CTF-1-600 were more effective for CO_2 binding than the triazine nitrogen sites in CTF-1. Nitrogen doping generally enhances CO_2 adsorption compared to oxygen doping, underscoring the significance of surface chemistry in low-pressure CO_2 collection. In high-pressure CO_2 capture applications, including natural gas purification and vehicular storage, pore volume and surface area significantly influence the adsorption efficacy of CTFs. Under elevated pressure, multilayer adsorption transpires, and an increased surface area correlates with a greater adsorption capacity for CO_2. MCTP-1, possessing a greater surface area, demonstrated superior CO_2 absorption compared to MCTP-2 at 300 K and 35 bar. The CTF TRIPTA demonstrated an escalating CO_2 adsorption with pressure, attaining 290.8 $cm^3\ g^{-1}$ at 273 K and 5 bar, with no saturation evident at this pressure, indicating potential for greater capacity at elevated pressures. The polymer TRITER-1 exhibited a similar pattern, reaching a peak CO_2 absorption of 300 $cm^3\ g^{-1}$ at 273 K under 5 bar. The results demonstrate the significant reliance of high-pressure CO_2 adsorption on textural characteristics, including surface area and pore volume, rather than solely on chemical functionality.[90–92]

Table 5 Comparison of CTFs for CO_2 capture

CTF	Surface area ($m^2\ g^{-1}$)	Pore volume ($cm^3\ g^{-1}$)	Pore size (nm)	CO_2 capacity ($cm^3\ g^{-1}$@273 K) low pressure	Q_{st} (kJ mol^{-1})	Ref.
CTF-CSU37@post	488	0.39	—	29.0	—	93
TAT-DHBD (1)	750	0.36	2.61, 3.79	30.4	27.2	94
TFM-1 (CH_3SO_3H)	738	—	—	30.8	27.8	95
PCBZL	341	0.36	—	32.6	39.6	96
PAF-1-6-2	979	—	—	42.2	30.3	97
Zn@CTF	598.2	0.35	0.53, 1.26	23.0	32.5	98
CTF-CSU41	333	0.78	—	52.3	44.6	93
PHCTF-4	1270	0.79	—	52.4	24.3	99
PCTF-8	625	0.32	—	56.0	37.0	100

1. CTFs for electrocatalytic CO_2 conversion

For the CO_2 conversion process to lower CO_2 levels,[101,102] CTF catalysts with an abundance of pyridinic-N doped active sites were first explained in 2018. The synthesized catalyst demonstrates an effective reduction of CO_2 to CO, achieving a faradaic efficiency (FE) of approximately 82% at an overpotential of 560 mV. This study facilitates the systematic design of porous CTFs for electrocatalytic CO_2 reduction reactions.[103] The fluorination of CTFs was identified as an effective electrocatalyst, demonstrating remarkable selectivity for the conversion of CO_2 to CH_4, with a FE of 99.3% under aqueous conditions.[104] A boron-doped CTF was investigated in a separate study for the electroreduction of CO_2 to CO. The researchers found that boron doping significantly improved the selectivity of CO up to 91.2%. CTF/CNTs hybrids demonstrate efficacy as electrocatalysts for the CO_2 reduction reaction, producing carbon monoxide with a FE of around 81%.[105] Altering the surface of CNTs with OH^- groups enhances the interaction between the CTF and CNT, thereby promoting electron transfer during the CO_2RR process. The integration of metals such as Cu, Ni, Co, *etc.* into CTF effectively modulates the electrocatalytic CO_2 reduction reaction (CO_2RR).[106,107]

Kai Ao *et al.* (2024) investigate an interesting instance of exceptional Ni–N/CNT@CTF electrocatalyst, exhibiting a high %FE for the reduction of CO_2 to CO. The catalyst was synthesized through the pyrolysis of residual nickel species within carbon nanotubes (CNTs), utilizing a soluble, π-conjugated CTF nanosheet as a nitrogen precursor and interfacial stabilizer. CTF's slender two-dimensional structure enables it to conform closely to carbon nanotubes, preserving their inherent curvature while preventing excessive graphitic overgrowth. High-resolution HRTEM, HAADF-STEM, and EDS mapping revealed the formation of atomically dispersed Ni–N_x sites (Fig. 17a). Electrochemical experiments demonstrated the catalyst's high performance: in H-type cells, it achieved a FE of 96% at −0.77 V *vs.* RHE, while in a flow-cell system, it exhibited a CO partial current density of 201 mA cm^{-2} at −0.9 V with 98% FE. The stability observed exceeded 10 hours in H-cells and 5 hours in flow systems. The Tafel slope analysis, measured at 56 mV dec^{-1}, indicated that the rate-limiting step was the formation of COOH* (Fig. 17b–d). The identification of the Ni_3 configuration as the primary active site through DFT calculations was significant. The curvature of the CNT induced compressive strain, resulting in shorter Ni–N bonds (1.83 Å compared to 1.84 Å in planar graphene), thereby enhancing the binding strength of $*CO_2$ and *COOH. The alteration in structure rendered the reaction energetics more thermoneutral, thereby enhancing turnover efficiency.[108]

Feng *et al.*[99] reported a family of MPTFs (M = Mn, Fe, Co, Ni, Cu), synthesized by iono-thermal trimerization of porphyrin units with incorporated metal centers (Fig. 18a). Among these, NiPTFs-600 exhibited outstanding catalytic performance as shown in (Fig. 18b and c), achieving a remarkable FE for CO production of 97.6% at −0.8 V *vs.* RHE, with a broad potential window (−0.55 to −0.95 V) where FE > 90% was maintained. The high performance was attributed to the abundant, homogeneously distributed Ni–N_x active sites (8.43 at% N content, 696 m^2 g^{-1} surface area) that promote CO_2 activation and protonation steps ($*CO_2$ → *COOH → *CO) (Fig. 18d). NiPTFs-600 also demonstrated a high CO partial current density (10.8 mA cm^{-2} at −0.8 V) and stability over 10 hours with negligible structural degradation (Fig. 18e). Compared to other MPTFs, Ni-based frameworks showed superior kinetics (Tafel slope of 129.8 mV dec^{-1}) and minimal charge

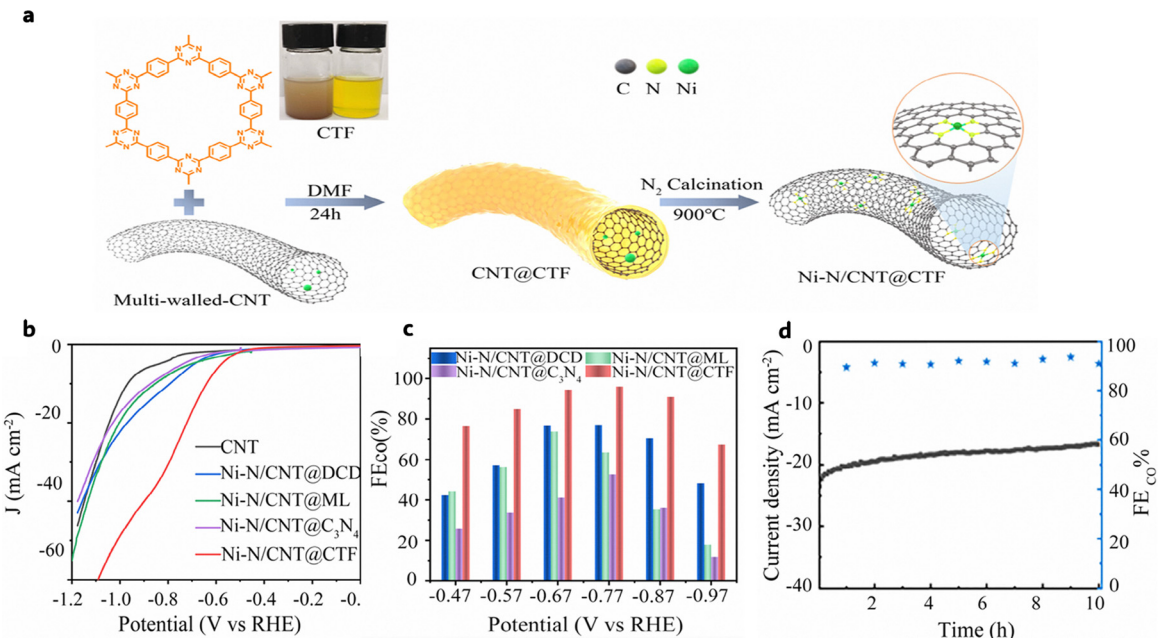

Fig. 17 (a) Schematic illustration for the synthesis, TEM image of Ni–N/CNT@CTF. (b) and (c) Electrocatalytic activity tests (d), stability of CNT, Ni–N/CNT@DCD, Ni–N/CNT@ML, Ni–N/CNT@C_3N_4, and Ni–N/CNT@CTF in a H-type cell. Reprinted (adapted) from *Small Struct.*, **5**, 2300500. Copyright © 2024 The Authors. Small Structures published by Wiley-VCH GmbH under the terms of CC-BY license.

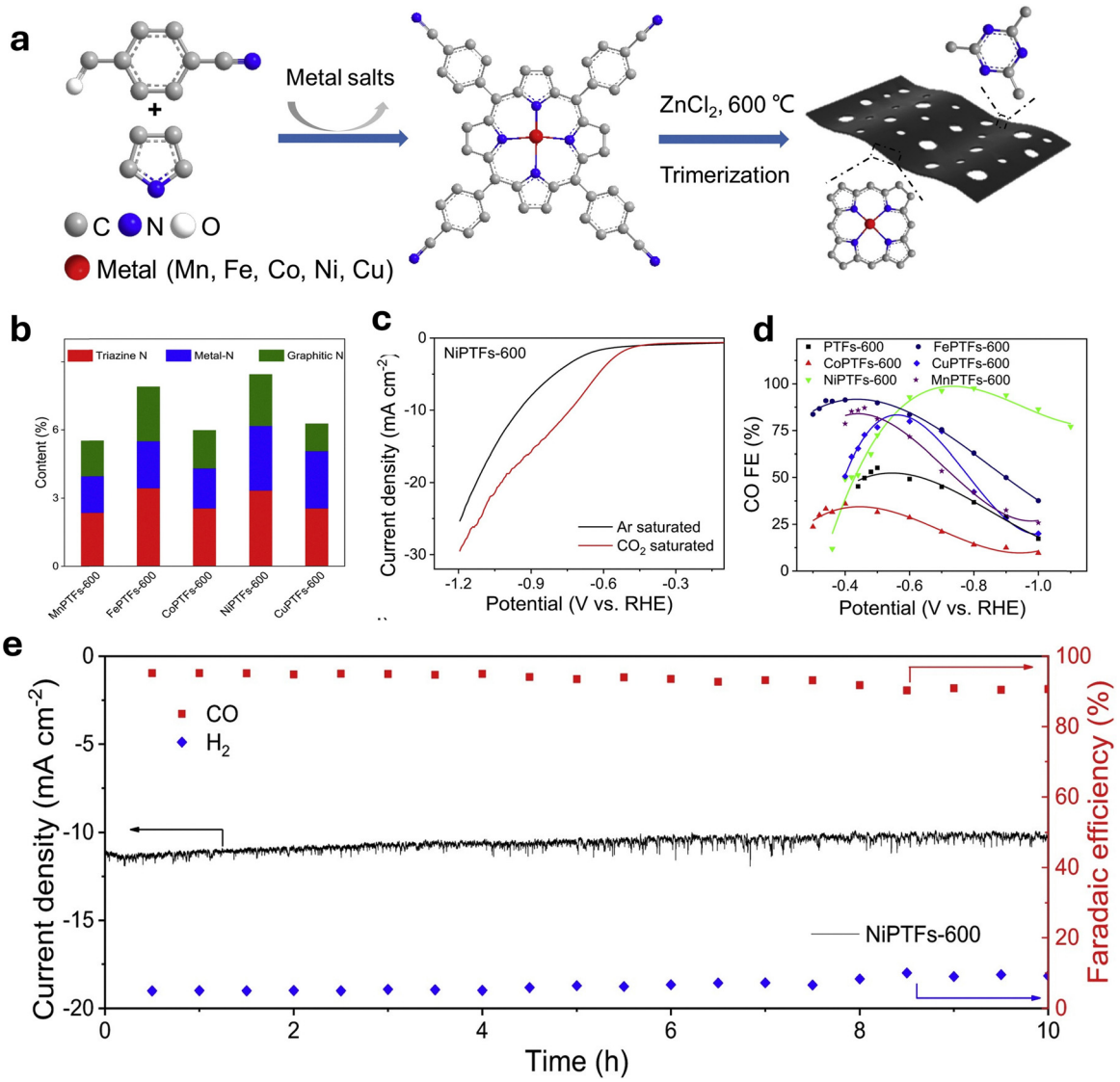

Fig. 18 (a) Schematic illustration of the fabrication process for MPTFs-600. (b) The percentages of fitted N species on MPTFs-600. (c) Polarization curves of NiPTFs-600 in 0.5 M $KHCO_3$ solution under Ar and CO_2 flowing. (d) Corresponding CO Fes for MPTFs-600. (e) Stability tests of NiPTFs-600 at −0.8 V and corresponding FEs of CO and H_2 productions at each half an hour. Reprinted (adapted) from *Appl Catal B*, 2020, **270**, 118908. Copyright © 2020 Elsevier B.V. All rights reserved.

transfer resistance (9.7 Ω), underscoring the key role of Ni–N_x sites in facilitating efficient CO_2RR.[109]

Su *et al.*[88] investigated the incorporation of coordinatively unsaturated 3d transition metals, such as Co and Ni, within CTFs, and how it will enhance the electrocatalytic CO_2RR. M-CTFs were prepared by polymerization reaction of 2,6-dicyanopyridine and incorporating carbon black for conductivity, followed by metalation using MCl_2 (M = Co, Ni, or Cu). The as-prepared M-CTFs are dispersed atomically within the microporous structure of the support. High-resolution XPS, and EXAFS analysis confirmed that these metal atoms were in a highly unsaturated coordination significantly different from the saturated planar geometry found in conventional tetraphenyl porphyrin (TPP) complexes. Notably, Ni-CTF exhibited a first-shell coordination number of approximately 3.4, lower than the tetra-coordinate Ni-TPP standard, indicating that Ni was stabilized within the CTF matrix in a catalytically advantageous unsaturated state (Fig. 19a–c). This structural tuning translated into a dramatic improvement in catalytic performance specifically for Ni-CTF achieve 90% FE for CO at −0.8 V *vs.* RHE which is shown in LSV measurement under CO_2-saturated 0.5 M $KHCO_3$ solution showed a marked increase in cathodic current, indicating active CO_2 conversion (Fig. 19c and d). CO and H_2 as the main products, with the Ni-CTF showing a CO : H_2 ratio far superior to Co-CTF and Cu-CTF, which was confirmed by GC measurements. While for Ni-CTFs, a Tafel slope analysis revealed a value of ∼86 mV dec^{-1} for Ni-CTF, indicating a favorable kinetic profile consistent with COOH* formation as the rate-determining step. In addition to the electrocatalytic activity, the material also possessed high stability and durability across prolonged electrolysis sessions.

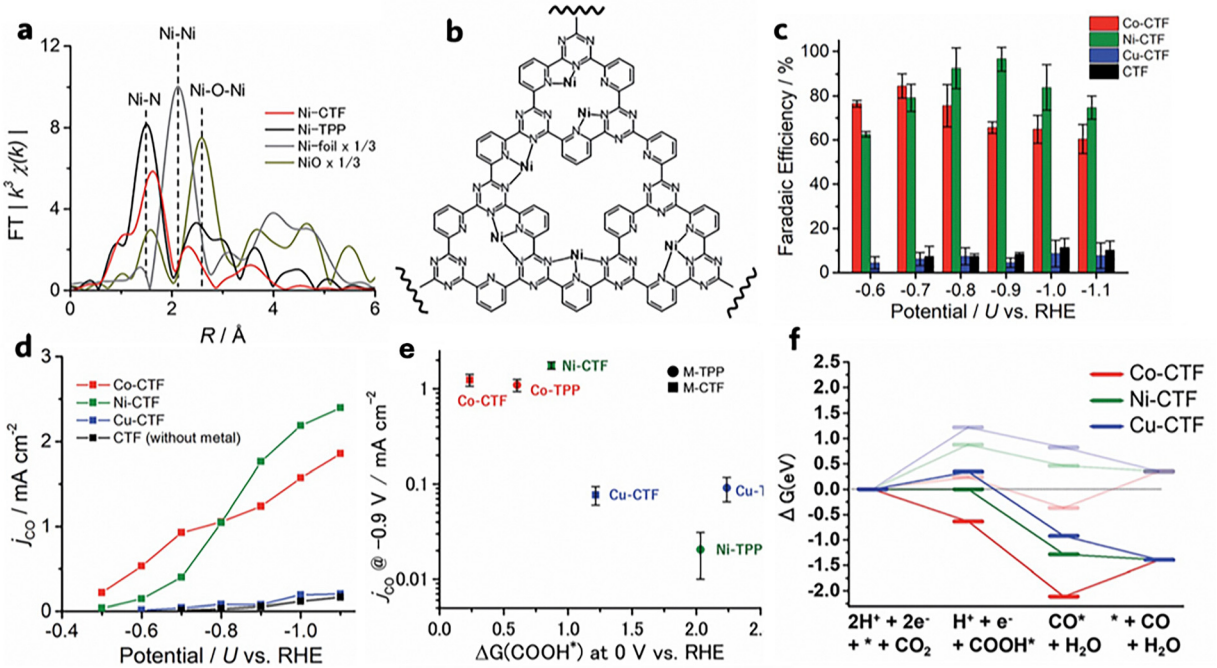

Fig. 19 (a) The k^3-weighted Fourier transform EXAFS spectra at the Ni K-edge. (b) An illustration showing the Ni sites in Ni-CTF. (c) Faradaic efficiency values during the CO_2RR to generate CO. (d) Partial current density values during the CO generation reaction. (e) and (f) Free energy diagrams for CO_2 reduction to CO. Reprinted (adapted) from *Chem. Sci.*, 2018, **9**, 3941. Copyright © 2018 the Royal Society of Chemistry under the terms of CC-BY license.

The experimental outcomes are concise with the DFT calculations. These revealed that the free energy barrier for COOH* formation on Ni-CTF was significantly lower than on Ni-TPP (0.59 eV *vs.* 0.85 eV), due to both the reduced steric hindrance and the stronger electronic coupling between the unsaturated Ni centers and the π-conjugated triazine framework. Moreover, the adsorption energies of *CO and *COOH intermediates followed an optimal volcano-type relationship that aligned Ni-CTF near the top of the activity curve. This synergy between structural engineering and electronic optimization demonstrates how coordination in well-defined porous supports like CTFs can unlock new electrocatalytic pathways, particularly for metals like Ni that are traditionally inactive under standard configurations, as shown in (Fig. 19e and f).[88]

2. CTFs for integrated CO_2 capture and electrocatalytic conversion

CTFs exhibit bifunctionality for CO_2 capture and electrochemical conversion into value-added products. The significant affinity of CTFs for CO_2 uptake is due to the high surface area and microporous structure through physisorption within the pores and CO_2 interaction *via* dipole–quadrupole with triazine and other nitrogen-rich groups.[86] The reduction process is initiated by the formation of active intermediates on the surface from the electron-transfer step, such as $CO_2^{\bullet -}$, which subsequently form the products.[106] Enhancement of CO_2 adsorption on CTFs can occur by rational design of CTFs through the incorporation of functional groups such as –NH_2, –OH, or –F, which alter local polarity, thereby enhancing the adsorption of CO_2 on the surface and facilitating electron transfer during the reduction process. In addition, enhancement of the selectivity of CTFs for CO_2 reduction by incorporation of metal centers such as Ni, Co, and Cu into the nitrogen coordination of CTFs creates isolated catalytic sites that are selective for the reduction of CO_2 into C_{2+} products.[106] By introducing such functional groups or metal centers that make the modifications which reduce the energy barrier for CO_2 reduction and control the product distribution by stabilizing intermediates. Additionally, the modifications on pore dimensions and their interconnections affect gas diffusion and the stability of transition states during CO_2 reduction reactions. Their approach integrates selective CO_2 adsorption with efficient catalytic conversion within a single, chemically stable material.[106,110]

(Fig. 20) quantifies how ICCC integration reprograms CO_2RR thermodynamics through co-adsorption: capture platforms (CTFs/MOFs) pre-concentrate flue-gas CO_2 (ΔG_{ads} = −0.35 eV *via* N-quadrupole), eliminating mass-transport limits at 0.01–0.15 bar P_{CO_2} and slashing the prohibitive $*CO_2 \rightarrow *COOH$ barrier from 1.05 eV (conventional gas-phase, dashed red) to 0.45 eV (ICCC, solid blue), positioning the rate-determining step within the Sabatier volcano optimum (±0.2 eV) while suppressing competing HER (0.45 → 0.75 eV *via* pore-confined pH). This pathway bifurcation explains Ni-CTF's 90% FECO (0.59 eV *COOH barrier, 86 mV dec^{-1} Tafel), NiPor-CTF's 92.3% FECO at 12.8 mA cm^{-2} over 20 h (0.58 eV), and Cu/ICTF-50's C_2H_4 selectivity (35% FE, 4.14 mA cm^{-2} *via* 1.3 mmol g^{-1} adsorption boost), enabling >90% FE across −0.6 to −1.0 V directly from dilute feeds and transforming kinetic bottlenecks into thermoneutral pathways for industrial currents ≥200 mA cm^{-2}.[86,88,91,106,110]

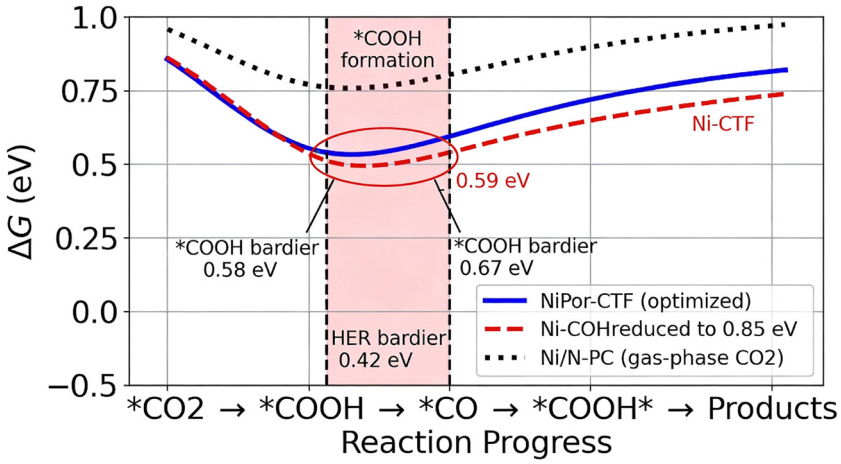

Fig. 20 Gibbs free energy profiles demonstrating capture-enhanced CO_2RR in integrated carbon capture and conversion (ICCC).

In a compelling demonstration of dual-function material design, Lu *et al.*[91] reported a Ni-porphyrin-based covalent triazine framework (NiPor-CTF) that integrates atomically dispersed NiN_4 centers into a nitrogen-rich, microporous polymeric matrix, offering both efficient CO_2 capture and electrocatalytic CO_2 conversion. Synthesized *via* an ionothermal method using $ZnCl_2$ as both solvent and Lewis acid catalyst, NiPor-CTF was formed by trimerizing 5,10,15,20-tetrakis(4-cyanophenyl) porphyrin–nickel at 400 °C for 40 h (Fig. 21a). Structural characterization using XPS and EXAFS confirmed that Ni atoms were uniformly anchored in a square-planar NiN_4 configuration, with no evidence of Ni nanoparticles or clusters (Fig. 21f). The Por-CTF exhibits higher adsorption capacity of CO_2 uptake in comparison with NiPor-CTF as listed in (Table 6). However, the electrocatalytic activity is coming from Ni metal center. The higher adsorption capacity is attributed to BET surface area of 815 $m^2\ g^{-1}$ and thus a CO_2 uptake capacity of 2.4 mmol g^{-1} at 298 K, outperforming Ni/N-PC analogues. The NiPor-CTF showed superior electrochemical activity and selectivity of CO_2 reduction into CO where the measurements in CO_2-saturated 0.5 M $KHCO_3$ electrolyte revealed a low onset potential of approximately 443 mV *vs.* RHE, with faradaic efficiencies exceeding 90% across a wide potential window (−0.6 to −0.9 V), peaking at 92.3% at −0.8 V, and delivering a corresponding current density of 12.8 mA cm^{-2}. Compared with catalysts (Ni-free Por-CTF and Ni/N-PC), NiPor-CTF exhibited superior electrocatalytic performance, attributed to the dense population of NiN_4 active sites and to efficient mass transport enabled by the porous network (Fig. 21b and c). In addition to the activity and selectivity, the catalysts exhibit Long-term durability, which was confirmed through chronoamperometric tests over 20 hours, showing negligible loss in current density or CO selectivity (Fig. 21d and e). The superior performance is also explained by DFT calculations (Fig. 21g and h). (Fig. 20) illustrates how CTF-localized CO_2 adsorption (ΔG_{ads} = −0.4 eV *via* N-quadrupole) lowers the $*CO_2$ → COOH barrier from 0.85 eV (Ni/N-PC, gas-phase CO_2) to 0.58 eV (NiPor-CTF), while raising the competing HER barrier (H → H_2) from 0.42 eV to 0.67 eV—achieving thermoneutral *COOH formation and suppressed H_2 evolution. This pathway bifurcation positions NiPor-CTF at the volcano peak: *COOH ΔG = 0.12 eV (optimal range ±0.2 eV), *versus* Ni-TPP's over-stabilized *CO (ΔG = −0.45 eV, desorption limit). Similarly, Su *et al.* report Ni-CTF's unsaturated Ni_3 coordination reduces *COOH barrier to 0.59 eV (*vs.* 0.85 eV Ni-TPP), with Tafel slope 86 mV dec^{-1} confirming fast *COOH formation. (Fig. 19) contrasts neutral CTF *vs.* Cu/ICTF-50: imidazolium cations enhance CO_2 adsorption (1.3 mmol g^{-1} ↑ at 273 K), stabilizing *CO dimerization (ΔG = −0.22 eV) for C_2H_4 (35% FE, 4.14 mA cm^{-2}) *versus* neutral CTF's *CO desorption pathway. These diagrams quantify how capture-modulated adsorption energies shift RDS from $*CO_2$ activation (gas-phase) to *CO dimerization (integrated), enabling >90% FE across wide potential windows (−0.6 to −1.0 V).

Mao *et al.*[111] recently reported a complex bifunctional electrocatalyst that incorporated copper nanoparticles (Cu/ICTF) and was prepared from imidazolium-functionalized cationic covalent triazine frameworks (ICTFs). The adsorption capacity is enhanced by the cationic nature of the imidazolium moieties, resulting in strong electrostatic interactions. During the reduction reaction the Cu–C bonds are formed as the imidazolium groups undergo additional *in situ* transformation into N-heterocyclic carbene (NHC) species (Fig. 22a). In addition to locally enriching CO_2, this dual mechanism stabilizes the Cu NPs, avoiding agglomeration and guaranteeing sustained catalytic activity in comparison with neutral Cu/CTF, the Cu/ICTF-50 composite (containing 50 weight percent Cu) performed noticeably better. For 10 hours, Cu/ICTF-50 maintained a partial ethylene current density of 4.14 mA cm^{-2} and a C_2H_4 faradaic efficiency of 35% at −1.0 V *vs.* RHE in CO_2-saturated 0.1 M $KHCO_3$ electrolyte, which is noted to be better than Cu/CTF (Fig. 22c–e). From physicochemical characterization such as PXRD and Raman verified the ICTF's structural integrity, while TEM showed uniform Cu NP dispersion that enhances the CO_2 adsorption and electroreduction. The adsorption capacity of CO_2 by ICTF is confirmed from BET measurements, The imidazolium-induced adsorption enhancement was highlighted by CO_2 adsorption isotherms (Micromeritics ASAP 2020), which showed a higher adsorption capacity than neutral CTF by 1.3 mmol g^{-1} at 273 K. Furthermore, Cu/ICTF

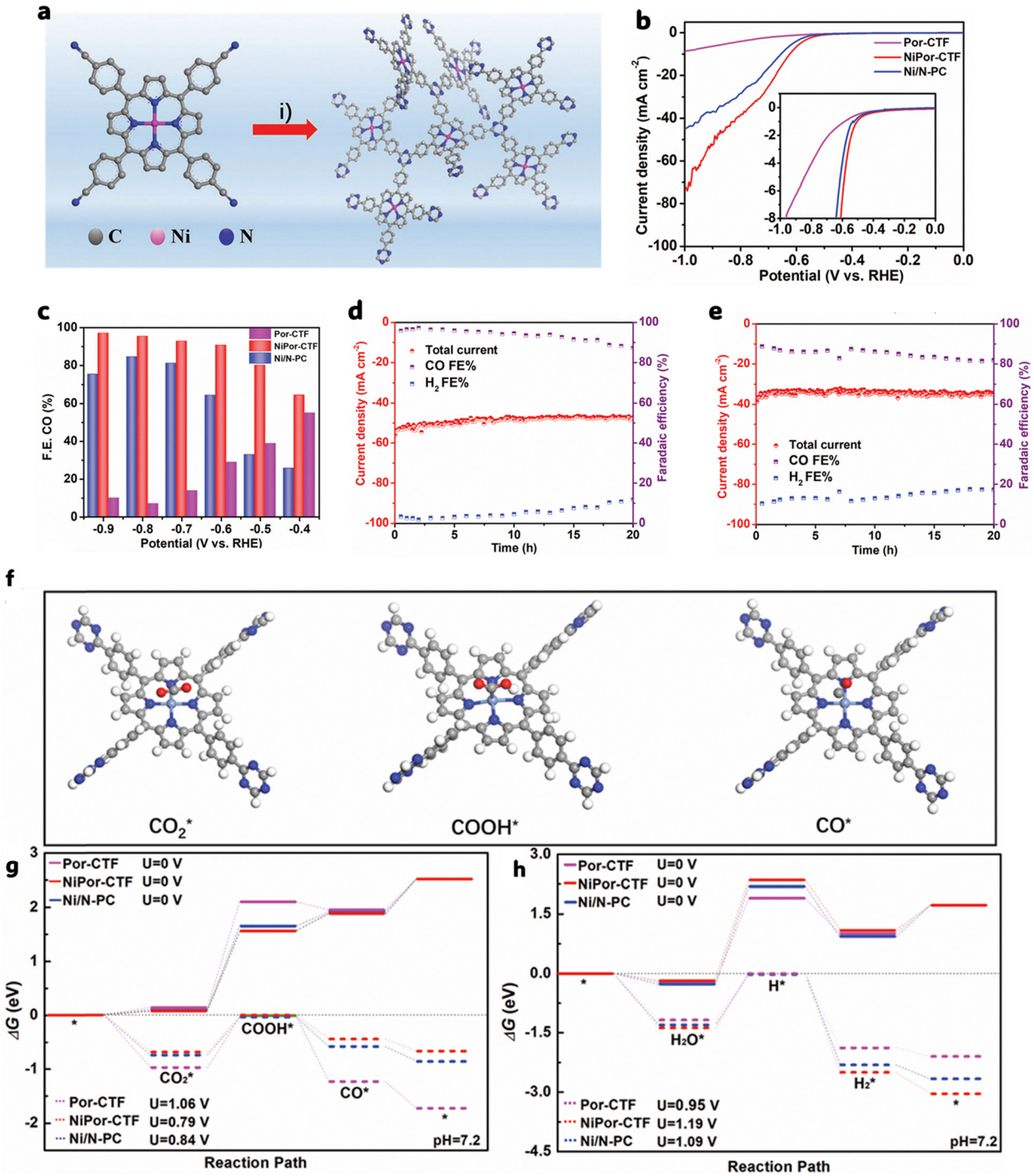

Fig. 21 (a) Schematic representation of NiPor-CTF synthesis by ionothermal strategy. (b) LSV curves and (c), CO faradaic efficiency at various specific potentials of of Por-CTF, NiPor-CTF, and Ni/N-PC in CO_2 saturated 0.5 m $KHCO_3$ solution. (e) and (d) Current–time curve for NiPor-CTF, and Ni/N-PC. (f) The DFT-calculated representative models: NiPor-CTF with CO_2, COOH, and CO adsorbed. (g) Schematic Gibbs free energy profile for the CO_2RR pathway on the three models with a pH of 7.2, and (h), schematic Gibbs free energy profile for the HER pathway on the three models with a pH of 7.2. Reprinted (adapted) from *Adv. Funct. Mater.* 2019, **29**, 1806884. Copyright © 2019 Wiley-VCH Verlag GmbH & Co. KGaA, Weinheim.

exhibited decreased charge-transfer resistance in EIS measurements, indicating better electron transfer kinetics (Fig. 22b). Key reaction intermediates (*CO, *COH, and *CHO) were identified by *operando* FTIR spectroscopy, confirming a multistep mechanistic pathway that leads to the formation of C_2H_4.

Conjugated microporous polymers (CMPs)

A vital class of POP materials with uses in energy and environmental concerns are CMPs, which are amorphous polymers

Table 6 N_2 and CO_2 physisorption results of as-prepared materials

Sample	S_{BET}[a] ($m^2\ g^{-1}$)	S_{micro}[b] ($m^2\ g^{-1}$)	V_{Tot}[c] ($cm^3\ g^{-1}$)	V_{micro}[d] ($cm^3\ g^{-1}$)	D_{av}[e] (nm)	CO_2[f] [mmol g^{-1}] 273 K	298 K
Por-CTF	1099	113	1.77	0.13	6.5	6.7	2.5
NiPor-CTF	815	89	0.75	0.08	3.7	5.0	2.4
Ni/N-PC	959	94	0.95	0.11	4.0	3.9	1.6

[a] Specific surface area measured by BET model. [b] The microporous surface area analyzed by *t*-plot method. [c] The total pore volume measured at $P/P_0 = 0.99$. [d] The microporous volume analyzed by *t*-plot method. [e] Average pore size. [f] CO_2 physisorption data.

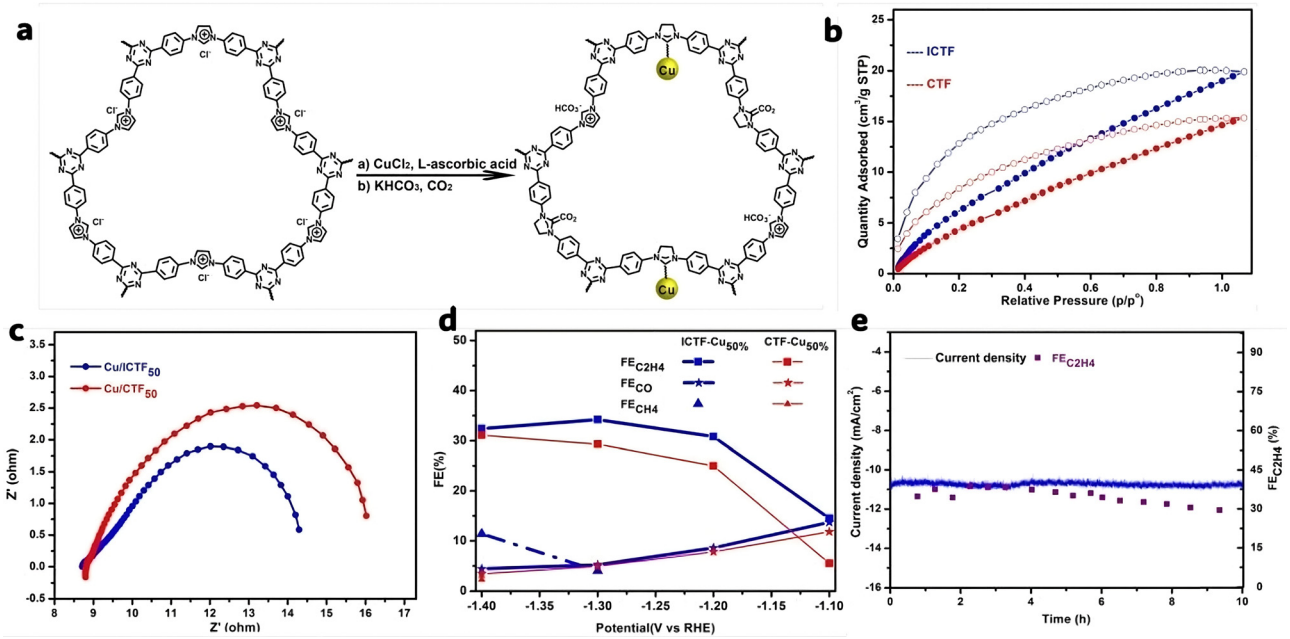

Fig. 22 (a) Schematic representation of the preparation of Cu/IC. (b) CO_2 adsorption–desorption isotherms at 298 K for ICTF and CTF. (c) Nyquist plots of different samples over the frequency range from 100 kHz to 10 mHz. (d) Faradaic efficiency of CO_2 reduction products from Cu/ICTF50 modified electrode (blue) and Cu/CTF50 modified electrode (red) at various potentials. (e) Stability curve. Reprinted (adapted) from *ChemCatChem* 2020, **12**, 3530. Copyright © 2020 Wiley-VCH Verlag GmbH & Co. KGaA, Weinheim.

with a three-dimensional network backbone. Since 2007 synthesis by Jiang *et al.*,[112] CMPs have been developed and found applications in energy storage, light harvesting, supercapacitors, CO_2 reduction and capture, and fuel cells (Fig. 23). Large surface areas, variety, modularity, structural tunability, and exceptional physiochemical stability are all provided by them.

Because of their appealing characteristics, such as enhanced π-conjugation and tunability, CMPs are attracting more attention as adaptable solutions for a variety of energy and environmental problems, including light harvesting, energy storage, adsorbents, heterogeneous catalysts, and luminous materials. One of the main benefits of CMPs is the variety of synthesis methods that are accessible.[113] Several metal-catalyzed couplings to metal-free condensation processes can be used to create CMPs on a much bigger scale. Most processes used in the synthesis of COFs are reversible at high temperatures, which limits the choice of functional building blocks to those that can resist these harsh conditions. The primary difference between CMPs and COFs is their structural makeup; CMPs are more flexible in their design since they are amorphous, whereas COFs are crystalline. It is challenging to create multi-component CMP catalysts using COF materials, but this characteristic allows for the development of multi-step tandem reactions, expanding the design options.[113,114] This modular framework architecture makes it possible to create hierarchical pore systems to improve transport kinetics and, in certain cases, well-accessible pores. Catalytic moieties may be directly integrated into the CMP framework to create heterogeneous CMP catalysts, which is a significant advancement in the utilization of CMPs for heterogeneous catalysis. Based on these fundamental ideas, it is quite possible to develop and synthesize CMPs with one or more active site types that will help collect and catalyze the conversion of CO_2.[115,116]

1. CMPs for CO_2 capture

By incorporating metal centers, CMPs can enhance CO_2 affinity through chemisorption, further improving their capture efficiency. Moreover, CMPs uniquely combine gas storage and catalytic properties, enabling simultaneous CO_2 capture and conversion into valuable products. These features position CMPs as a

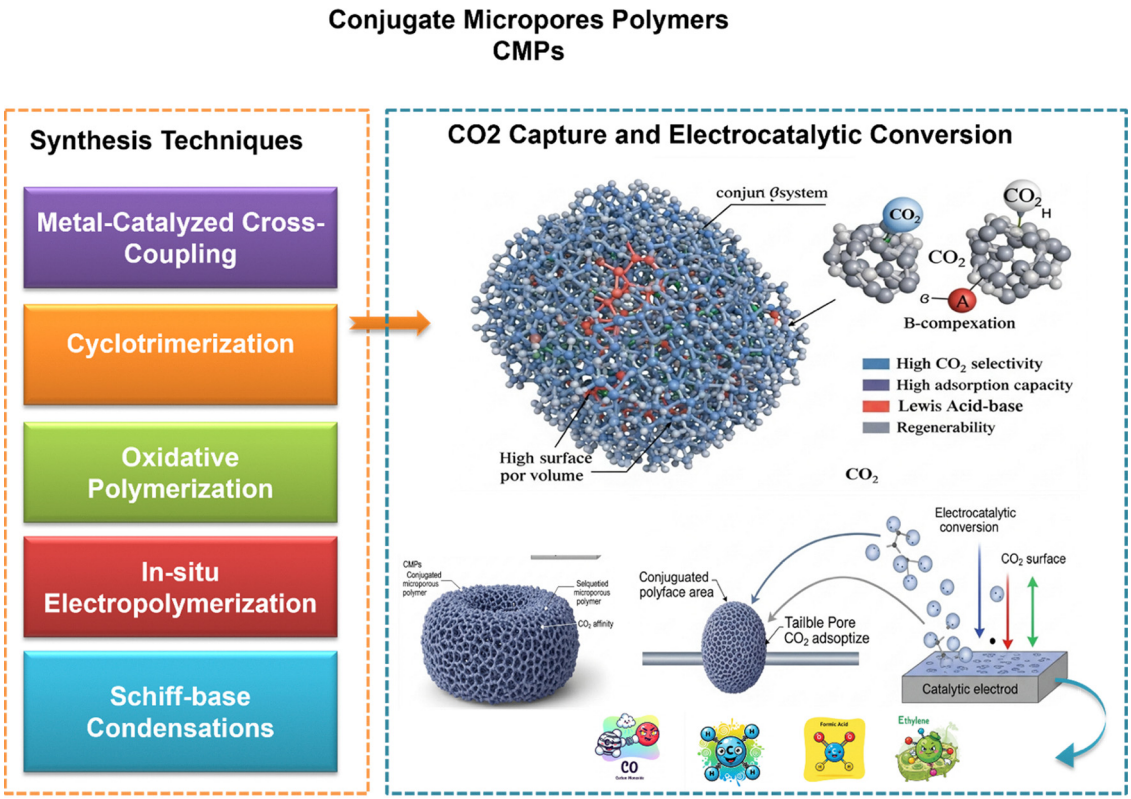

Fig. 23 Schematic illustration of CTFs for CO_2 capture and electrocatalytic reduction.

promising platform for sustainable carbon management technologies. Xie *et al.*[117] developed a Co/Al coordinated CMP that exhibits exceptional capabilities in capturing and converting CO_2 at room temperature and atmospheric pressure. These polymers, characterized by extended p-conjugation in an amorphous organic framework, demonstrate CO_2 storage capacities comparable to metal–organic frameworks while also serving as effective catalysts for CO_2 and propylene oxide reactions. Metal-functionalized CMPs, like the Salen-Co/Al-coordinated CMPs discussed, offer combined gas sorption and catalytic capabilities, making them ideal candidates for CO_2 capture and conversion. The synthetic procedure for preparing Co-CMP involved synthesizing dibromo-functionalized precursor monomers (Salen-Co) and treating them with 1,3,5-triethynylbenzene in the presence of a Pd(0) catalyst to produce Co-CMP. Al-CMP was prepared differently. The Co-CMP structure exhibited a porous three-dimensional network structure with high thermal stability and insolubility in organic solvents (Fig. 24a). Morphological analysis revealed that both polymers consisted of uniform solid sub-micron spheres with nanometer-sized pores on the surface (Fig. 24b and c). Nitrogen and CO_2 analyses indicated both micropores and mesopores in Co-CMP and Al-CMP. Co-CMP had a much higher BET surface area (965 $m^2\ g^{-1}$) than either Al-CMP (798 $m^2\ g^{-1}$) or CMP (772 $m^2\ g^{-1}$) (Fig. 24d). According to Table 7, the total pore volume of Co-CMP was 2.81 $cm^3\ g^{-1}$, which is substantially larger than the volume of several high-pore-volume MOFs, including UMCM-2 (2.31 $cm^3\ g^{-1}$), MOF-177 (1.89 $cm^3\ g^{-1}$) and NOTT-112 (1.62 $cm^3\ g^{-1}$). Co-CMP and Al-CMP exhibited high CO_2 adsorption capacities at atmospheric pressure and room temperature. The CO_2 uptake reached 79.3 mg g^{-1} and 76.5 mg g^{-1} in Co-CMP and Al-CMP, respectively. Under the same conditions, CMP absorbed 71.0 mg g^{-1} CO_2, possibly as a result of the relatively low BET surface area (Fig. 24e), in comparison with the CO_2 adsorption capacities of Co-CMP and Al-CMP with those of the MOFs in the literature. Under identical conditions to those in our study, CO_2 uptakes of 106.7 mg g^{-1}, 71.5 mg g^{-1} and 10.4 mg g^{-1} were reported for MC-BIF-2H, MC-BIF-3H and MC-BIF-5H, respectively. Despite having a relatively low surface area, Co-CMP and Al-CMP exhibited comparatively high CO_2 absorption, indicating that Co-CMP and Al-CMP are good CO_2 capture materials (Fig. 24f).

2. CMPs for CO_2 electrocatalytic reduction

Electrochemical transformation of CO_2 into valuable chemicals and fuels is a crucial endeavor, particularly when powered by renewable energy sources. Given CO_2's inherent inertness and the multi-electron and multi-proton pathways involved in its reduction, electrocatalysts are indispensable for lowering the energy barrier and enhancing selectivity. CMPs offer advantages such as permanent micropores and robust structures, making them promising photo-/electrocatalysts. However, CMPs often face challenges with conductivity for electrocatalysis and precise control over their amorphous structures to effectively expose catalytic sites and facilitate charge transfer. Molecular catalysts like metal phthalocyanines (MePcs) are highly selective for producing single C-containing products, primarily CO. Wang *et al.*[118] presented a compelling case for

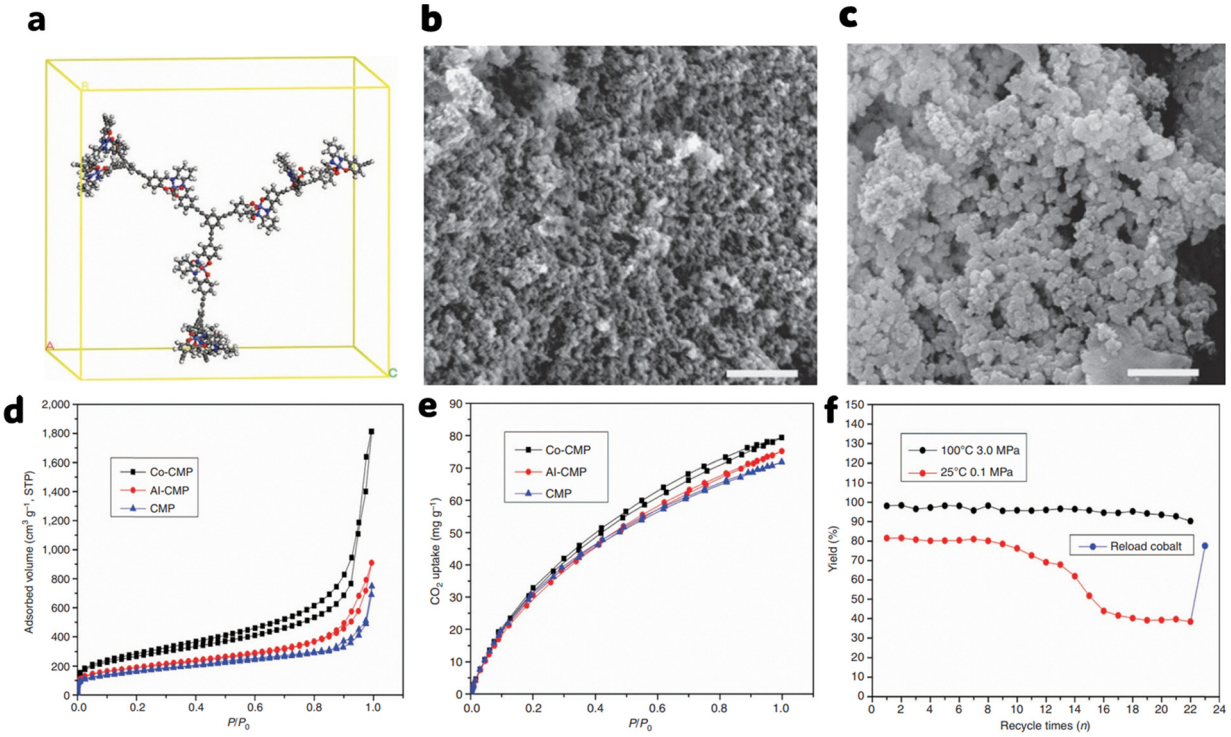

Fig. 24 (a) The amorphous structure of CMP in 3d. SEM images of (b), Co-CMP, (c) Al-CMP, (d) N_2 adsorption isotherms, and (e) CO_2 Uptake isotherm. (f) The recycling stability of Co-CMP under various experimental conditions. Reprinted (adapted) from *Nat. Commun.*, 1960, **4**, 2013. Copyright © 2013, The Authors. Published by Springer Nature under the terms of CC-BY license.

Table 7 Surface area and CO_2 uptake of the CMP, Co-CMP, Al-CMP

CMPs	S_{BET} ($m^2 g^{-1}$)	S_{micro} ($m^2 g^{-1}$)	V_{tot} ($cm^3 g^{-1}$)	V_{micro} ($cm^3 g^{-1}$)	M_{calc} (wt%)	M_{ICP} (wt%)	CO_2 uptake ($mg g^{-1}$)
CMP	772	283	1.21	0.117	0	0	71.0
Co-CMP	965	293	2.81	0.419	8.20	7.19	79.3
Al-CMP	798	315	1.41	0.298	4.01	3.46	76.5

the design of highly efficient electrocatalysts for CO_2 reduction to CO, addressing the limitations of traditional metal phthalocyanine (MePc)-based catalysts, which often suffer from limited molecular modulation and unsatisfactory conductivity. The researchers successfully synthesized an ultrathin CMP sheath around carbon nanotubes (CNTs) through an iono-thermal copolymerization of cobalt phthalocyanine (CoPc) and metal-free phthalocyanine (H_2Pc) *via* a Scholl reaction. This innovative approach ensures the atomic dispersion of CoII metal as single atoms on the polymer sheath, maximizing catalytic sites, while the H_2Pc moieties act synergistically as proton/electron donors, enhancing the nucleophilicity of Co sites for CO_2 binding and stabilizing reactive intermediates through H-bonding interactions (Fig. 25a). The resulting CNT@CMP(CoPc-H_2Pc) composite demonstrated remarkable performance, achieving a high faradaic efficiency (FE) of up to 97% for CO production at −0.9 V (*vs.* RHE) within broad potential windows, and an exceptional turnover frequency (TOF) of 97 592 h^{-1} at −0.65 V, along with a large current density exceeding 200 mA cm^{-2}. Furthermore, the catalyst exhibited superior selectivity and stability compared to other related catalysts, maintaining high CO FE for at least 10 hours of continuous electrolysis, with only a marginal decrease in current density (Fig. 25b and c).

3. CMPs for integrated CO_2 capture and electrochemical conversion

CMPs have shown significant results as a bifunctional electrocatalyst for integrated CO_2 capture and electrocatalytic conversion due to their cross-linked polymeric skeleton, high carrier space, and wide contact surface areas. These properties ensure fast kinetics and high electrochemical performance in energy-driven catalytic applications. The π-conjugated structure enhances physiochemical stability and surface area, while suppressing active material dissolution in organic electrolytes. The utilization of CMPs in ECO_2R introduces a novel field of inquiry; thus, there is a scarcity of published studies that explore the application of CMPs as electrocatalysts. At present, the predominant types of reported CMPs for ECO_2R are metal-based and hybrid systems that incorporate conductive carbon materials, as elaborated upon in the following sections.[119]

In the study of integrated CO_2 capture and electrocatalytic conversion, Qui *et al.*[120] introduces a new class of CPMs, with

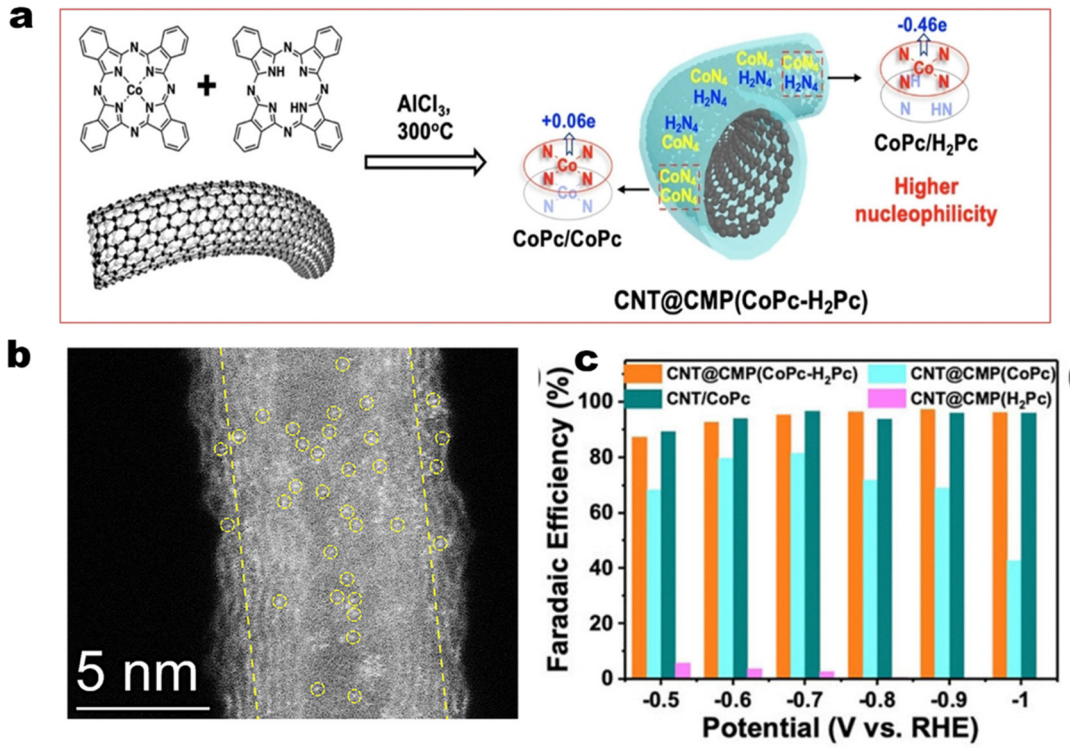

Fig. 25 Represents the (a), the schematic synthesis of CNT@CMP (CoPc-H_2Pc), (b) HAADF-STEM image and (c), CO FEs for the CNT@CMP(CoPc-H_2Pc) in a flow cell. Reprinted (adapted) from *Chem. Int. Ed.* 2022, **61**, e202115503. Copyright © 2021 Wiley-VCH GmbH.

CMPANI-3 that acts as a promising catalytic material due to its exceptional design incorporating pyrazine-functionalized with cobalt porphyrin functions (Fig. 26a). The synergetic effect generated from cobalt embedded in the CPM structure with porphyrin function enhances both CO_2 adsorption and catalytic performance. As detailed in (Table 8), CMPANI-3 exhibits the highest CO_2 uptake capacity with 0.88 mmol g^{-1} at 273 K. This result is explained by the strong Lewis acid–base interactions

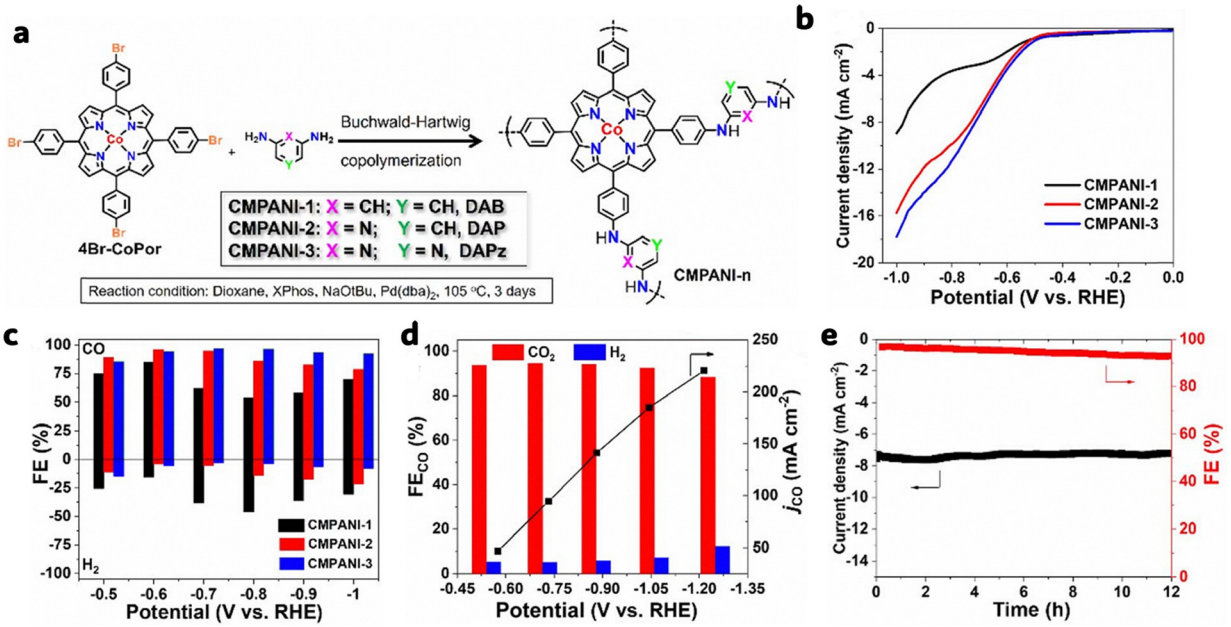

Fig. 26 (a) Synthesis route to CMPANi-*n* with different diamino aromatics. (b) Linear sweep voltammetry curves. (c) CO faradaic efficiency (d), potential-dependent FECO and partial current density; and (e), long-term stability of CMPANI-1 and CMPANI-3 in CO_2-saturated 0.5 M $KHCO_3$ electrolyte. Reprinted (adapted) from *J. Mater. Chem. A*, 2024, **12**, 33572–33580. Copyright © 2024 Royal Society of Chemistry.

Table 8 N_2 and CO_2 physisorption properties of CMPANi-*n*

Sample	S_{BET}[a] ($m^2\ g^{-1}$)	V_{tot}[b] ($cm^3\ g^{-1}$)	D_{av}[c] (nm)	CO_2[d] (mmol g^{-1})@ 273 K	CO_2[d] (mmol g^{-1})@ 298 K
CMPANI-1	12	0.09	2.2	0.46	0.38
CMPANI-2	30	0.12	3.1	0.52	0.35
CMPANI-3	34	0.26	2.7	0.88	0.66

[a] Specific surface area calculated using the BET equation. [b] Total pore volume at P/P_0 = 0.99. [c] Average pore size. [d] Calculated from CO_2 physisorption isotherms.

between the electron-deficient pyridinyl nitrogen atoms and CO_2 molecules. Additionally, the high porous structure of CPM is acquired with a surface area of 34 $m^2\ g^{-1}$ to enhance the gas diffusion and adsorption capacity on the active sites. The electrocatalytic activity and selectivity of CMPANI-3, evaluated in a CO_2-saturated 0.5 M $KHCO_3$ electrolyte, reveals an outstanding FE (CO) of 97% at −0.7 V *vs.* RHE, with a corresponding partial current density more than 200 mA cm^{-2}; moreover, a turnover frequency (TOF) of 2264 h^{-1} for CO, significantly surpassing its counterparts CMPANI-1 and CMPANI-2 (Fig. 26b–d). These improvements stem from the engineered coordination microenvironment around the CoN_4 active site, where the pyrazine-N groups act as internal proton relays, effectively accelerating the proton-coupled electron transfer step critical for *COOH intermediate formation. This mechanism is clearly evidenced by *in situ* ATR-FTIR spectroscopy, which shows stronger and earlier formation of *COOH species in CMPANI-3, and KIE analysis that confirms enhanced proton transfer dynamics. Electrochemical analysis further supports this claim Tafel plots demonstrate the lowest slope (174 mV dec^{-1}) for CMPANI-3, indicating faster kinetics, while Nyquist plots show it has the lowest charge transfer resistance (31.89 Ω), suggesting superior conductivity and reaction interface dynamics. Moreover, when integrated into a gas diffusion electrode and tested in a flow cell, CMPANI-3 maintains FECO above 90% even at 200 mA cm^{-2}, reaching a TOF of 52 390 h^{-1}, and thus rivals or surpasses leading CO_2-to-CO catalysts including CoPc, Au–C, and Ag systems (Fig. 26e).

Smith *et al.*[121] investigated a novel metal–organic conjugated microporous polymer (CMP-(bpy)20-Mn) that has dual functionality for CO_2 capture and electrocatalytic conversion (Fig. 27a and b). The material maintains substantial porosity after Mn incorporation with a surface area of 549 $m^2\ g^{-1}$ and achieves moderate CO_2 uptake of 1.06 mmol g^{-1} at 298 K and 1 bar, though this capture performance remains below benchmark materials like BPL carbon (Fig. 27c). Most notably, the rigid CMP structure prevents the problematic reductive dimerization of the $[Mn(bpy)(CO)_3Br]$ catalyst that typically occurs in solution-based systems, enabling direct formation of the catalytically active $[Mn(bpyCMP)(CO)_3]^-$ species as evidenced by a single reduction peak at −1.35 V (Fig. 27d). The material is affected by two catalytic pathways: a slow pathway (−1.2 to −1.4 V) showing modest current enhancement with CO_2 binding, and a fast substrate-limited pathway (−1.6 to −1.8 V) with scan-rate dependent behavior indicating higher TOF. Bulk electrolysis at

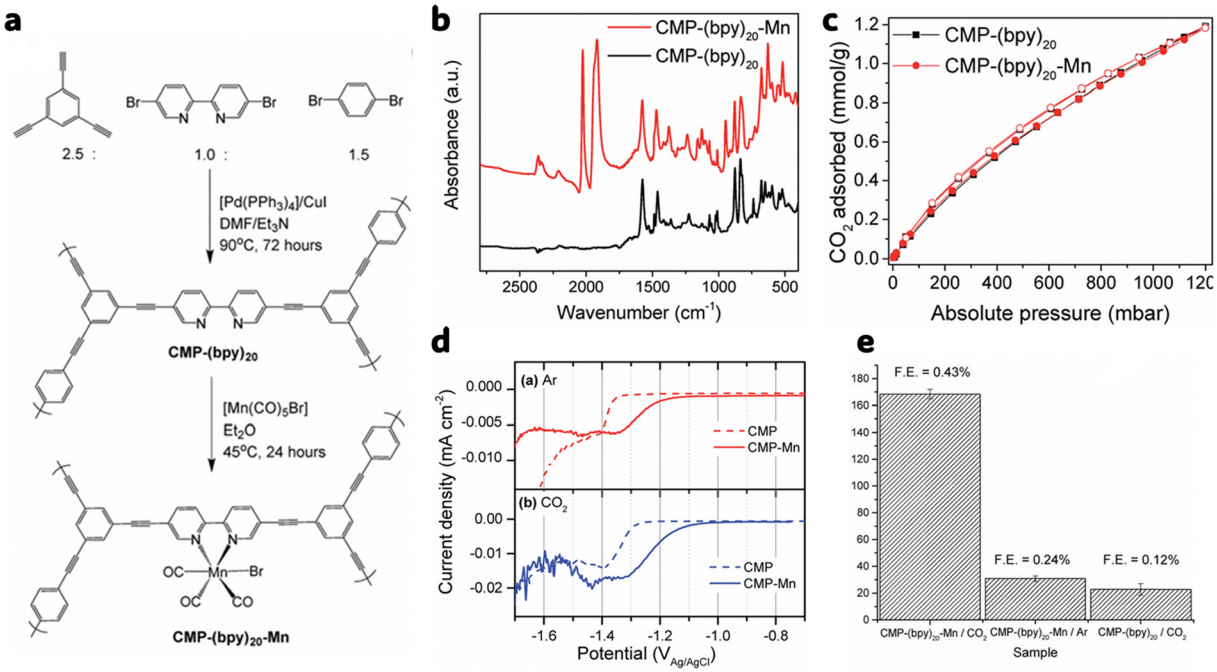

Fig. 27 (a) Synthetic route to CMP-(bpy)20-Mn, (b) FTIR spectra and (c), CO_2 adsorption–desorption isotherms measured at 298 K for CMP-(bpy)20 (black) and CMP-(bpy)20-Mn (red), (d) square wave voltammograms (a) and (b) of CMP-(bpy)20 (dashed) and CMP-(bpy)20-Mn (solid), CMP-(bpy)20-Mn shows an additional reduction (−1.35 V) assignable to $[Mn(bpy)(CO)_3Br]$ moieties (e), CO evolution rate during bulk electrolysis experiments at −1.6 V Ag/AgCl for 3 hours. The faradaic efficiencies are for CO. H_2 was the only other product detected. Reprinted (adapted) from *Sustainable Energy Fuels*, 2019, **3**, 2990–2994. Copyright © 2019 Royal Society of Chemistry.

Table 9 Summary of CMP-based electrocatalysts for ECO_2RR

Polymeric material	BET [m^2 g^{-1}]	Electrolyte	Applied potential [V]	Main product [FE%]	Ref.
PF-5 film	1000	0.1 M Et_4NBF_4/acetonitrile solution	n.r.	CO	122
PyPOP@G	582.7	0.1 M $KHCO_3$	−1.0 (*vs.* RHE)	n.r.	123
CMP-$(bpy)_{20}$-Mn	549	0.06 M Phosphate buffer	−1.6 (*vs.* Ag/Ag^+)	CO (0.43%)	124
CNS-NiSA	458	0.5 M $KHCO_3$	−0.8 (*vs.* RHE)	CO (95%)	118
CNT@CMP (CoPc-H_2Pc)	70	0.5 M $KHCO_3$	−0.9 (*vs.* RHE)	CO (97%)	125
COP-SA	106.33	0.5 M $KHCO_3$	−0.65 (*vs.* RHE)	CO (96.5%)	125
Pt/TPE-CMP	360	0.5 M $KHCO_3$	−1.5 (*vs.* Ag/Ag^+)	(C1–C8) (>95%)	126
CoPPc-TFPPy-CP	464.9	0.1 M KCl	−1 (*vs.* RHE) −1.2 (*vs.* RHE)	C_2H_5OH 43.25% HCOOH 13.91%	127
BNPI-1 (NaF 0.99)	54	0.1 M $KHCO_3$	0.03 (*vs.* RHE) −0.26	HCOOH 91%	128
BNPI-1 (NaI 0.66)	728		−0.26 (*vs.* RHE)	CH_3OH 85%	
BNPI-2	26		−0.26 (*vs.* RHE)	HCOOH 45% CH_3OH 67%	
pPI-1	20	0.1 M $KHCO_3$	−0.76 (*vs.* RHE) −0.26 (*vs.* RHE)	HCOOH 14% CH_3OH 52%	129
pPI-2	342		−0.56 (*vs.* RHE) −0.26 (*vs.* RHE)	HCOOH 20% CH_3OH 95%	

Table 10 A comparative analysis of various POPs for CO_2 capture and electrocatalytic conversion, emphasizing faradaic efficiency (FE%) and key reduction products

Catalyst	Synthesis method	Surface area (m^2 g^{-1})	Faradaic efficiency (FE%)	Reduction products	CO_2 uptake (mmol g^{-1})	Ref.
TTF-1	Triazine linkage polymerization	1234	82% at −0.6 V *vs.* RHE	CO, HCOOH	2.86	63
POP-Py(0)/CoTCPP	Benzyl bromide & pyridine reaction	Not specified	83% at −0.6 V *vs.* RHE	CO	Not specified	63
PyPOP@G	Pyrimidine-based polymer on graphene	Not specified	85% at −0.7 V *vs.* RHE	CO, CH_4	Not specified	63
POP@MWCNT	Polymerization on multi-walled CNTs	Not specified	80% at −0.75 V *vs.* RHE	CO, HCOOH	Not specified	63
Bi-MOF	Solvo-thermal	Not specified	92% at −0.9 V *vs.* RHE	COOH	1.50	63
FePC-POP	Friedel–Crafts alkylation	427	88% at −0.65 V *vs.* RHE	CO	1.50	130
DTTBQ-CMP	Polycondensation	Not specified	92% at −0.8 V *vs.* RHE	CO, C_2H_4O	Not specified	130
BSPOP-Co	Triptycene-based polycondensation	280	87% at −0.7 V *vs.* RHE	CO	1.70	130
$CuPcF_8$-CoNPc-COF	Condensation of phthalocyanine derivatives	452	97% at −0.62 V *vs.* RHE	CO, CH_4	0.80	131
2D-Co-COF500	COF formation on Mg/Al-LDH	123	96.5% at −0.8 V *vs.* RHE	CO	Not specified	131
f 2D cobalt(II)-phthalocyanine based COFs	Triazine-based framework	Not specified	87% at −0.6 V *vs.* RHE	CO	Not specified	131
isox-CTF-500	Triazine-based framework	1683	90% at −0.75 V *vs.* RHE	CO, CH_3OH	4.92	131
acac-CTF-500	Triazine-based framework	1556	85% at −0.6 V *vs.* RHE	CO, HCOOH	3.30	131
cCTFs-400	Triazine-based framework	744	89% at −0.65 V *vs.* RHE	CO, CH_4	2.86	131
cCTFs-450	Triazine-based framework	861	91% at −0.7 V *vs.* RHE	CO, C_2H_4	2.25	131
cCTFs-500	Triazine-based framework	1247	95% at −0.75 V *vs.* RHE	CO, CH_3OH	3.02	131
LKK-CMP-1	1,3-Dialkyne linkage polymerization	467	86% at −0.7 V *vs.* RHE	CO, CH_4	2.24	132
6FA-PEPH-CL	Crosslinked polyimide	653	82% at −0.6 V *vs.* RHE	CO, HCOOH	1.65	63
6FA-PE-CL	Crosslinked polyimide	698	88% at −0.65 V *vs.* RHE	CO, CH_3OH	2.02	63
Tt-POP-2	Triptycene-based polymerization	368	85% at −0.7 V *vs.* RHE	CO, CH_4	0.40	133
Tt-POP-3	Triptycene-based polymerization	974	90% at −0.75 V *vs.* RHE	CO, C_2H_4O	0.62	133

−1.6 V demonstrates selective CO production as the sole carbon-based product with a 7-fold enhancement over the catalyst-free control and an estimated turnover number of ∼1296 over 4 hours, though the faradaic efficiency remains low at 0.43% due to competing hydrogen evolution (Fig. 27e). More examples of CMP-based electrocatalysts for ECO_2RR are summarized in (Table 9) while comparative analysis of various POPs for CO_2 capture and electrocatalytic conversion are detailed in (Table 10).

4. Future outlook of CTFs and CMPs

CTFs and CMPs exhibit superior affinity for capturing CO_2 and electrocatalytic conversion, owing to large surface areas, adjustable pore architectures, and amazing stability in heat and chemicals. The triazine function of CTFs, which can be made in several ways, like high-temperature iono-thermal trimerization with $ZnCl_2$ and superacid-catalyzed approaches, which let you control the porosity and nitrogen content very well, both of which are important for selective and effective CO_2 adsorption.[63,134] Ultramicroporous CTFs (pore width <7 Å) have a lot of nitrogen, which makes dipole-quadrupole interactions with CO_2 stronger. This gives them great selectivity for CO_2 over N_2 and CH_4, and they can hold up to 57.2 cc g^{-1} at 298 K, with some frameworks getting CO_2/N_2 selectivity ratios above 100. The chemical diversity of CTFs is enhanced by the incorporation of charged or functional groups, or by their combination with active metal sites. This increases their capacity for CO_2 adsorption and improves their efficacy as electrocatalysts.[135,136]

The π-conjugation and microporosity of CMPs give them enormous interior surface areas up to 556 m^2 g^{-1} BET and excellent CO_2 adsorption capabilities, usually more than 1 mmol g^{-1} at room temperature. Adding different electron-rich parts, such as triazine, pyrrole, and thiophene, through modular synthesis processes can change the structure of the pores and how well they absorb CO_2.[77,96,136] CMPs, like CTFs, are very thermally stable, with decomposition temperatures often over 300 °C. They can also be chemically modified to add catalytic centers that help CO_2 reduction into products like CO, formate, or methane. While the CTFs and CMPs are good for capturing and CO_2 reduction owing to their excellent properties such as tunable pore size distribution and can be designed at the molecular level to maximize adsorption and catalytic activity. However, it is still hard to control crystalline and active site dispersion precisely. For example, CTFs often have low crystallinity under iono-thermal conditions, and the uneven pore distribution in CMPs can make it harder to predict how easily sorption or catalytic sites can be accessed.[77,96,136] Moreover, research is also needed on scalability and long-term operating stability under electrochemical circumstances. Future goals include making greener, more scalable syntheses, enhancing structural order (to come closer to single-crystalline domains in CTFs), and using hybridization with conductive support or targeted functionalization like site-specific metalation or heteroatom doping. The combination of computational design and systematic structure–property studies is expected to accelerate the development of next-generation POPs with finely tuned performance for capturing CO_2 and converting it efficiently *via* electrocatalysis, which directly help technologies that fight climate change.[77,98,135]

Covalent organic frameworks (COFs)

Covalent organic frameworks (COFs) significantly enhance integrated CO_2 capture and conversion systems, providing a transformational platform due to their outstanding porosity, design flexibility, and strong chemical stability. The crystalline, lightweight materials, composed of multiple parts and interconnected by strong covalent bonds, demonstrate huge surface areas and adjustable pore sizes, making them effective for CO_2 capture and catalytic conversion into valuable chemicals.[137,138] Additionally, the bottom-up reticular synthesis approach enables precise control through molecular building design, allowing the addition of specific functional groups that enhance charge transport and catalytic efficiency, particularly for CO_2 reduction. COFs are crystalline and porous polymers made up of covalently bonded, organic building blocks with different structural configurations, such as benzene rings, triazine units, Imine linkages, and porphyrin.[139] The structural flexibility and durability of COFs make them a promising material for developing integrated systems that effectively combine CO_2 capture and conversion[140–142] as shown in (Fig. 28).

The primary synthetic methods for COFs include solvothermal synthesis, iono-thermal synthesis, mechanochemical synthesis, and microwave-assisted synthesis (Fig. 29).[143–145] COFs can be modified with metal centers or functional groups to enhance CO_2 adsorption, leading to the conversion of CO_2 into valuable products, such as CO, methane, or ethylene.[137,138,146] Also, as the majority of COFs are produced through cross-coupling or condensation reactions involving organic aromatic building blocks and linkers, the entire framework.[144,147–149]

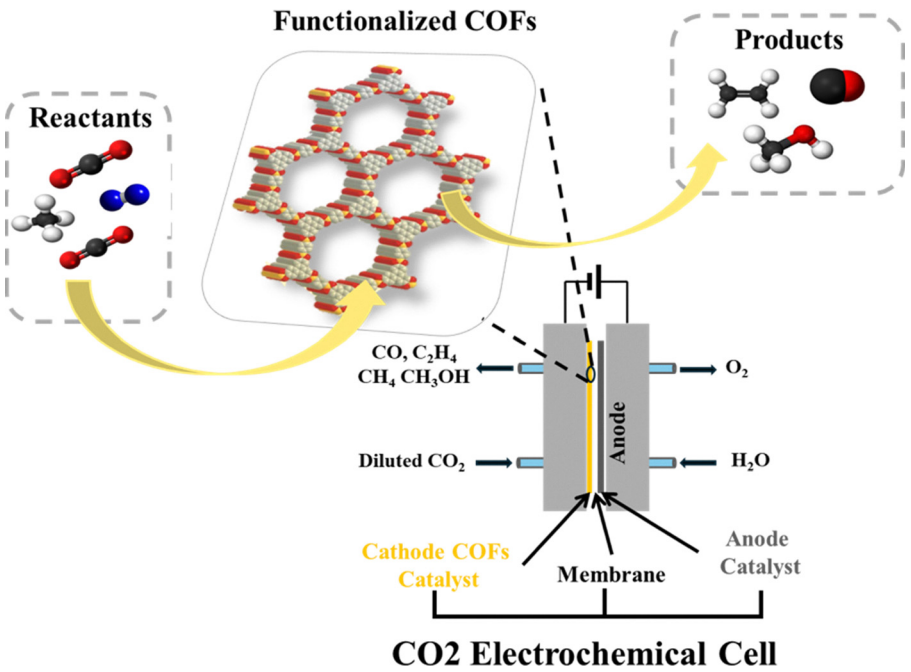

Fig. 28 Graphical abstract of COF for CO_2 capture and electrocatalytic conversion.

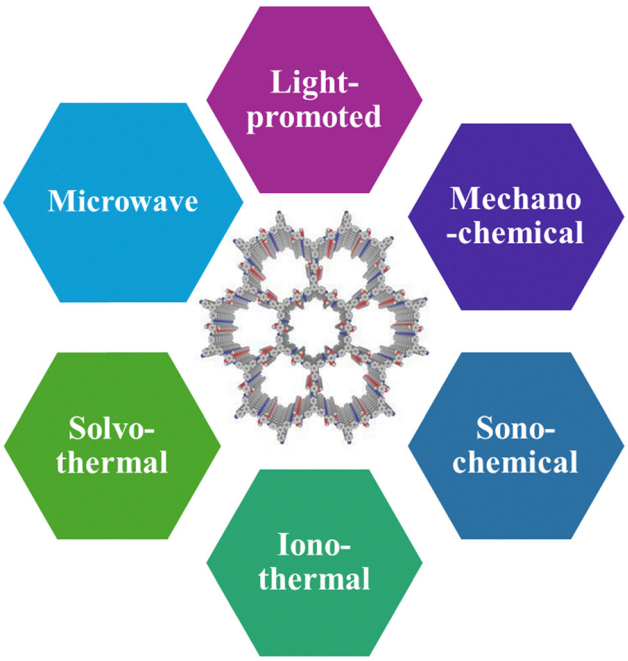

Fig. 29 Schematic illustration of COFs different synthesis techniques.

1. Structure and properties of COFs

COFs exhibit a unique structural flexibility and tunable properties, making them promising candidates for CO_2 capture and conversion. The crystalline, microporous structures constructed from organic building blocks through reticular synthesis offer large, adjustable pore sizes and high surface areas, enabling efficient CO_2 diffusion, adsorption, and enrichment near catalytic sites.[148,150] They are also suitable for long-term electrocatalytic applications due to their unique, porous, and stable properties at high temperatures. The modular nature of COFs facilitates the integration of conductive elements, such as graphene or electron-attracting groups, which enhance electron transport and boost overall catalytic performance.

2. Mechanisms of CO_2 adsorption in COFs

COFs' capture process initiates as CO_2 molecules infiltrate the porous structure and are adsorbed onto active sites, including metal centers (Co, Ni, Cu) or nitrogen-rich linkers. This comprehensive method allows for the rapid activation of CO_2, facilitating the electron transfer of the adsorbed molecules to generate reactive intermediates such as CO_2^- or *COOH.[151] After that, the intermediates go through several steps of proton-electron transfer, which create products such as CO, formic acid, methane, or even multi-carbon hydrocarbons, depending on the catalyst design and reaction conditions.[149] The mechanisms of CO_2 adsorption can be clarified by examining several critical factors, such as the type of adsorption (physisorption or chemisorption), the significance of functional groups, and the impact of pore size and topology.[144]

In the first step, CO_2 is adsorbed through physisorption, characterized by weak van der Waals forces, without a change in the electronic structure of COFs.[144,152] Chemisorption, on the other hand, involves the formation of chemical bonds between CO_2 and the functional groups present in the COFs. This process may result in more stable adsorption; however, it could necessitate increased energy for desorption.[150] Regarding Functional groups, such as amines and imides, they play a crucial role in enhancing CO_2 adsorption. These groups can interact with CO_2 through hydrogen bonding or coordinate covalent bonding, significantly increasing the adsorption capacity. The existence of nitrogen-rich sites is especially advantageous, as they can provide additional binding sites for CO_2, thereby enhancing the overall effectiveness of the COF in CO_2 capture. Han *et al.* demonstrate that the two-dimensional polyimide-linked phthalocyanine COFs (CoPc-PI-COF-1 and CoPc-PI-COF-2) exhibit similar nitrogen-rich sites that facilitate effective CO_2 capture, demonstrating the importance of these functional groups in the adsorption process.[148] The other crucial factor, the pore size and topology of COFs, determines their CO_2 adsorption performance. Larger pore sizes enhance the accessibility of CO_2 molecules, allowing for greater adsorption. Additionally, the specific arrangement of the pores can influence the diffusion of CO_2, affecting the overall efficiency of the adsorption process.[147]

3. COFs for CO_2 capture

Materials scientists have recently developed an interest in COFs due to their highly porous, crystalline structures, which offer the flexibility of adjusting pore sizes and functional groups. COFs were first discovered by Yaghi and colleagues in 2005,[153] marking a significant step forward in reticular chemistry, as they enabled scientists to use pre-made molecular building blocks, such as porphyrin cores, triazine, and benzene, to control the shape of the framework precisely.[154,155]

The outstanding CO_2 adsorption properties of COFs naturally correspond to their structure–property relationships. The π-stacking between layers makes the structure more rigid, allowing guests and hosts to interact more easily due to induced dipole and quadrupolar interactions, particularly in reactions, given CO_2's linear geometry and quadrupole moment. The formation of COFs relies on dynamic covalent chemistry, which enables reversible reactions (such as imine condensation and boronate ester formation) that allow self-correction during synthesis. To successfully design COFs for CO_2 capture, three key elements are required:[137] (1) the selection of building blocks (such as triazine, benzene, or porphyrin cores) that dictate functionality and binding affinity toward CO_2, (2) the geometrical integrity of the framework to ensure periodicity and stable pore architectures, and (3) reversible covalent bond formation, which is important for crystallinity, recyclability, and defect healing. Three primary factors determine how COFs capture CO_2:[143] the kind of linkage between the building units, the porosity type, and the types of COF building blocks. In this section, the main properties of COFs' effectiveness in CO_2 capture and conversion will be discussed: the dimensionality effect, the types of covalent bonds, the textural properties effect, and the functional groups and active sites effect.

The dimensionality of COFs significantly influences their porosity, gas diffusion properties, and adsorption capacity. 1D COFs are primarily non-centrosymmetric linear crystalline polymers formed by the haphazard packing of organic chains caused by entropy.[139] These chains consist of 1D COFs, confined covalent bonds, and non-covalent interactions such as hydrogen bonding and π–π interactions. Singh and Nagaraja[156] developed SO_3H-functionalized 1D-COFs with polar channels to improve adsorption. Two-dimensional COFs are composed of planar building blocks that stack *via* π–π interactions, resulting in layered crystalline structures.[157] These frameworks are effective platforms for CO_2 capture because they typically have large surface areas, accessible channels, and well-organized micropores. For example, Gao *et al.*[158] developed TPE-COF-II, a 2D COF with a frustrated bonding network resulting from an unusual [2+4] condensation pathway. The CO_2 uptake capacity of 23.2 weight percent (118.8 cm^3 g^{-1} at 273 K and 1 atm) is among the highest reported for 2D COFs due to its open pores and unreacted functional groups that enhance host–guest interactions.

In contrast, three-dimensional COFs (3D COFs) have longer, more interconnected networks with more internal voids and structural rigidity, resulting in better CO_2 adsorption capacities than their two-dimensional counterparts.[159,160] For instance, Zhu *et al.*[161] developed a family of crystalline 3D COFs (RICE-3 to RICE-7) made from logically constructed trigonal and rectangular-planar linkers to demonstrate the structural advantages of 3D COFs over 2D counterparts. To illustrate, (Fig. 30a–f), shows how these linkers form interconnected polyhedral cages with hierarchical porosity and long-range order. The remarkable CO_2 uptake performance of ∼50 cm^3 g^{-1} at 273 K and 1 bar made RICE-5 stand out due to its large mesopore aperture (∼4.6 nm), high porosity (∼94.2%), and exceptionally low framework density (∼0.094 g cm^{-3}). RICE-3 and RICE-7 visualizations (Fig. 30g and h), show how pore size distribution affects gas adsorption. RICE-7 is more microporous (1.0 nm), resulting in lower uptake, whereas RICE-3 has larger mesopores and wider inter-channel windows, which promote better diffusion. The 3D COFs featuring hierarchical and interconnected pores, such as RICE-5, exhibit enhanced adsorption capacities due to improved accessibility, effective packing, and diminished diffusion resistance, as evidenced by the CO_2 isotherms (Fig. 30i and j). The findings underscore the significant influence of topology and dimensionality in 3D frameworks on the advancement of COF-based greenhouse gas capture technologies.

Covalent bonds can be classified as follows: ether bonds (–C–O–C–), thioether (–C–S–C–), hydrazone bonds (–C═N–NH_2), azine bonds (–C═N–), boronate ester bonds (–B(OR)–O–), imine bonds (–C═N–), and triazine bonds (–C_3N_3–).[162,163] Noting that, Amine bonds (N-based) and boronate ester bonds (B-based) are widely used in CO_2 capture and conversion processes because of their ability to interact with CO_2 *via* Lewis' acid–base interaction. Also, COFs with reversible imine linkages (–C═N–) can adsorb and release CO_2 molecules under

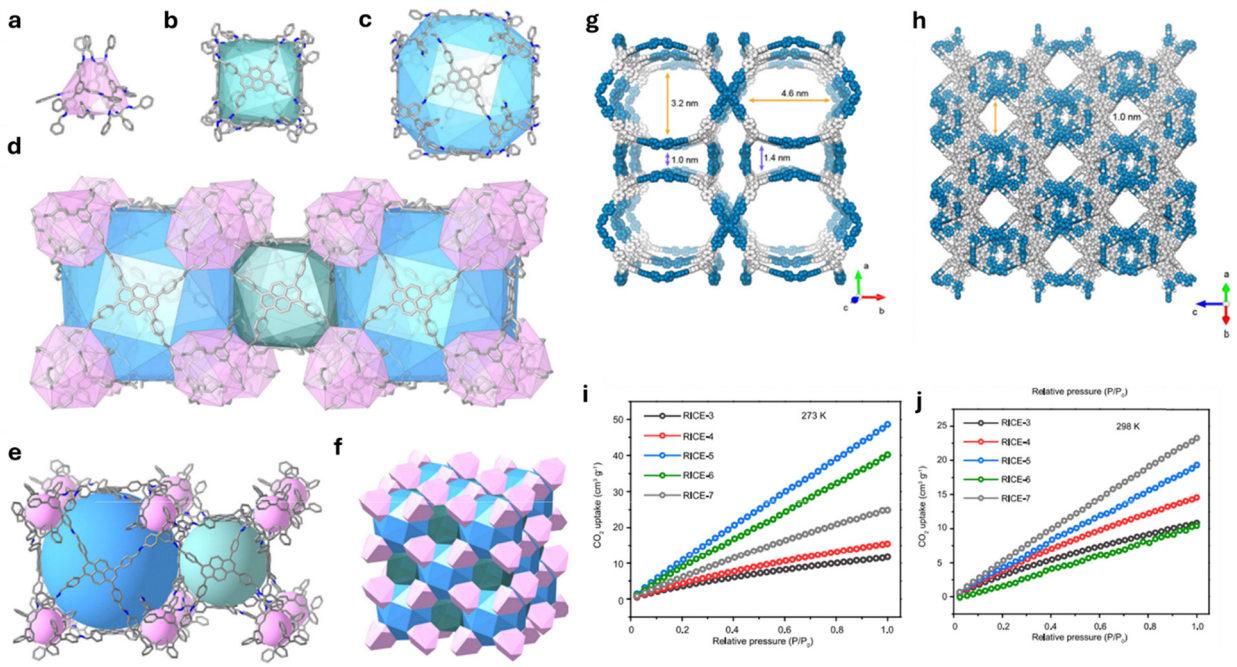

Fig. 30 Structural design, pore geometry, and CO_2 adsorption performance of RICE-COFs. (a)–(c) Polyhedral cages in RICE-7, including a truncated tetrahedron (T^6, pink), a small cube (B^{66}, green), and a large cube (C^{66}, blue). (d)–(f) Crystal structure of RICE-7 showing cage connectivity and the *mhq-z* net topology formed *via* face-sharing packing. (g) and (h) Pore visualizations of RICE-3 and RICE-7, highlighting their mesoporous (∼4.6 nm) and microporous (∼1.0 nm) structures, respectively. (i) and (j) CO_2 adsorption isotherms of RICE-3 to RICE-7 at 273 K and 298 K, confirming the superior uptake of RICE-5 (∼50 cm^3 g^{-1} at 273 K) due to its low framework density and hierarchical porosity. Reprinted (adapted) from *Nat Commun*, 2023, **14**, 2865. Copyrights © 2023 The Authors. Published by Springer Nature under the terms of CC-BY license.

various conditions, including temperature, pressure, and gas composition changes.[164] CO_2 adsorption can cause Imine-linked COFs to expand structurally, leading to increased capacity for storage. Additionally, Imine bonds improve the catalytic potential of COFs for CO_2 conversion by facilitating coordination and promoting reaction pathways. A notable example is the 3D-Ru-COF, which is composed of tetrakis (4-aminophenyl) methane (TAPM) and N-functionalized [2,2′-bipyridine]-5,5′-dicarbaldehyde (BPDCA). Kumar *et al.*[165] demonstrated that THF-assisted solvent treatment increased CO_2 uptake by 21% by causing flexible "pedal motion" in imine linkages (from 3.94 to 4.76 mmol g^{-1} at 273 K). Imine-linked 3D COFs exhibit dynamic and reusable properties in gas capture and catalytic applications, as evidenced by their structural modulation stability over seven consecutive adsorption–desorption cycles.

Increased CO_2 uptake is correlated with higher surface areas (*e.g.*, >3000 m^2 g^{-1}), which are determined by textural properties such as surface area, pore volume, and pore size distribution.[166] Yaghi *et al.*[153] developed 3D covalent organic frameworks (COFs) like COF-102 and COF-103 using a rational topological approach that combines tetrahedral (*e.g.*, TBPM, TBPS) and trigonal (*e.g.*, HHTP) building blocks *via* boroxine or boronate ester linkages (Fig. 31).

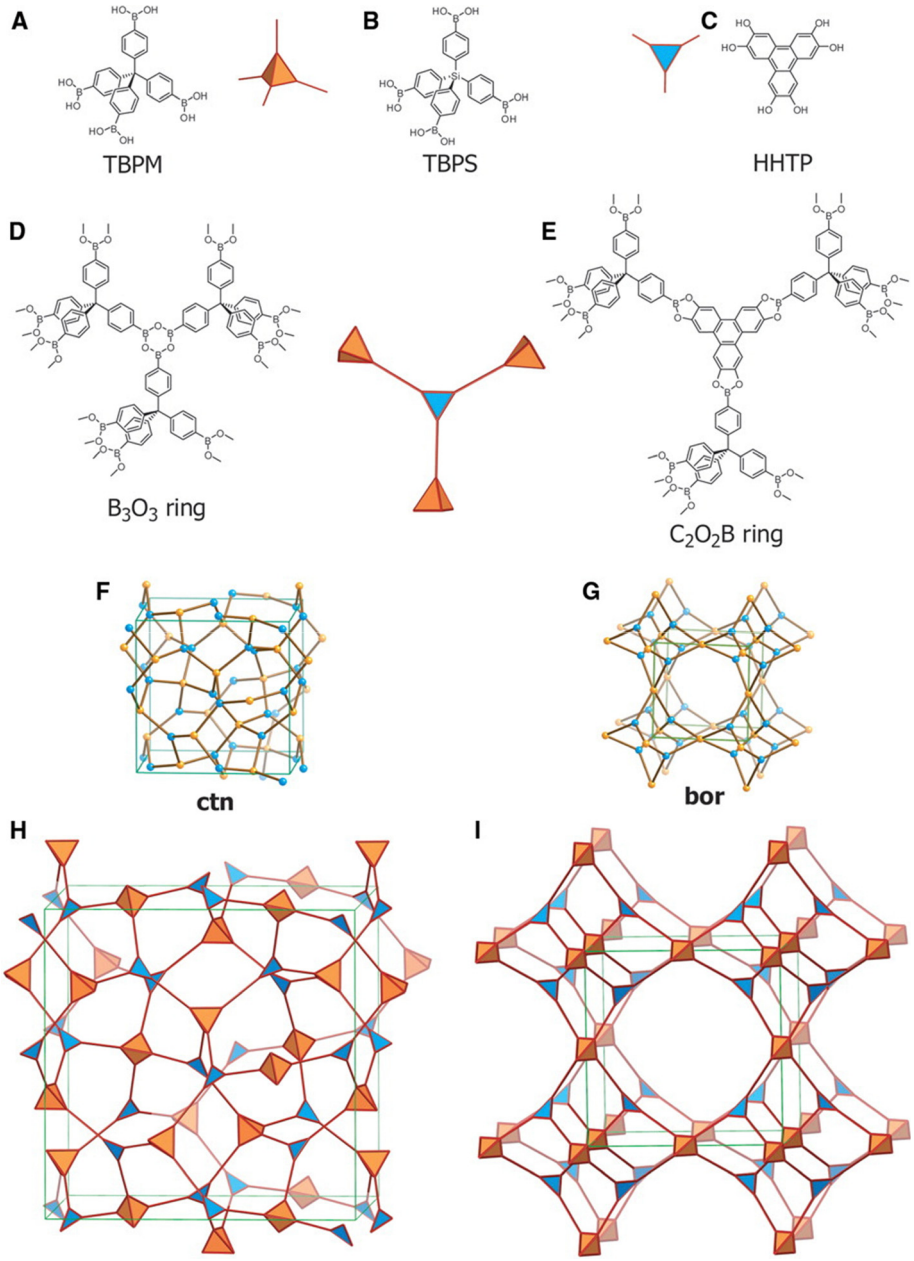

Fig. 31 Representative building units and topologies for 3D COFs. (A) and (B) Tetrahedral. (C) Trigonal. (D) Linkers form boroxine. (E) Boronate ester. (F) and (H) Rings, assembling into *ctn*. (G) and (I) *Bor* networks, as observed in COF-102 and COF-103. Reprinted (adapted) from *Science* (5822), 268–272. Copyright © 2007, The American Association for the Advancement of Science.

These configurations yield highly crystalline and porous frameworks with ctn and bor net topologies. The precise reticular design creates ultrahigh surface areas of 3472 $m^2 g^{-1}$ for COF-102 and 4210 $m^2 g^{-1}$ for COF-103, resulting in exceptional CO_2 uptake capacities of up to 27 mmol g^{-1} at 298 K and 1 bar, respectively. Also, Alahakoon *et al.*[167] developed an azine-linked COF (HEX-COF-1) with a BET surface area of 1214 $m^2 g^{-1}$ and a narrow pore size distribution of ~1 nm. With an enthalpy of adsorption of 42 kJ mol^{-1} and a relatively moderate surface area, HEX-COF-1 showed a high uptake of CO_2 of over 20 weight percent at 273 K, indicating strong quadrupolar interactions between CO_2 and the polar framework.

The inclusion of functional groups and active sites, such as $-SO_3H$, $-NH_2$, triazine, or metal centers, improves CO_2-framework interactions through polar binding or catalytic activation.[168] Functionalization strategies, whether post-synthetic or through direct monomer design, allow for modification of the chemical environment, adsorption strength, and selectivity.[169] Wei *et al.*[168] conducted a thorough study on several 3D COF-300 derivatives featuring $-SO_3H$, $-NO_2$, –OH, and $-NH_2$ groups to investigate their ability to capture CO_2. While selectively changing the chemical environment inside the pores, these COFs were derived from a common parent framework (COF-300-THF) and retained the same underlying topology (Fig. 32a), the addition of polar functional groups considerably altered the behavior of CO_2 uptake. As illustrated in (Fig. 32b), COF-300-SO_3H nearly five times outperformed the unmodified COF-300-THF in terms of adsorption capacity, reaching a maximum of 6.23 mmol g^{-1} at 298 K and 100 kPa. The strong hydrogen-bonding and electrostatic interactions facilitated by the sulfonic acid groups, which serve as high-affinity binding sites, are responsible for this improvement. The nitro-functionalized framework (COF-300-NO_2) also showed high uptake (~4.8 mmol g^{-1}), whereas substitutions with –OH and $-NH_2$ produced moderate improvements over the parent material. Significant gains in CO_2/N_2 selectivity resulted from the N_2 adsorption isotherms (Fig. 32c), which showed little uptake across all COFs, especially in the more polar variants. This effect is shown in (Fig. 32d), selectivity of (~393) for COF-300-SO_3H was significantly higher than that of COF-300-NO_2 (~31), COF-300-OH (~11), and COF-300-NH_2 (~10), demonstrating the crucial role that electronegativity and functional group polarity play in gas separation performance. Radial distribution function (RDF) analyses and CO_2 density distribution maps provided additional mechanistic insights. CO_2 molecules were found to preferentially localize close to the functional groups at both low (10 kPa) and high (100 kPa) pressures, particularly in COF-300-SO_3H and COF-300-NO_2. This pattern is supported by the RDF plots, which show that the NO_2 group also exhibited favorable interaction behavior. In contrast, the SO_3H–CO_2 interaction displays the shortest and most intense peak (~2.5 Å), indicating strong binding affinity. The distributions of NH_2 and OH groups, on the other hand, were wider and less intense. This is consistent with their lower selectivity and weaker binding.

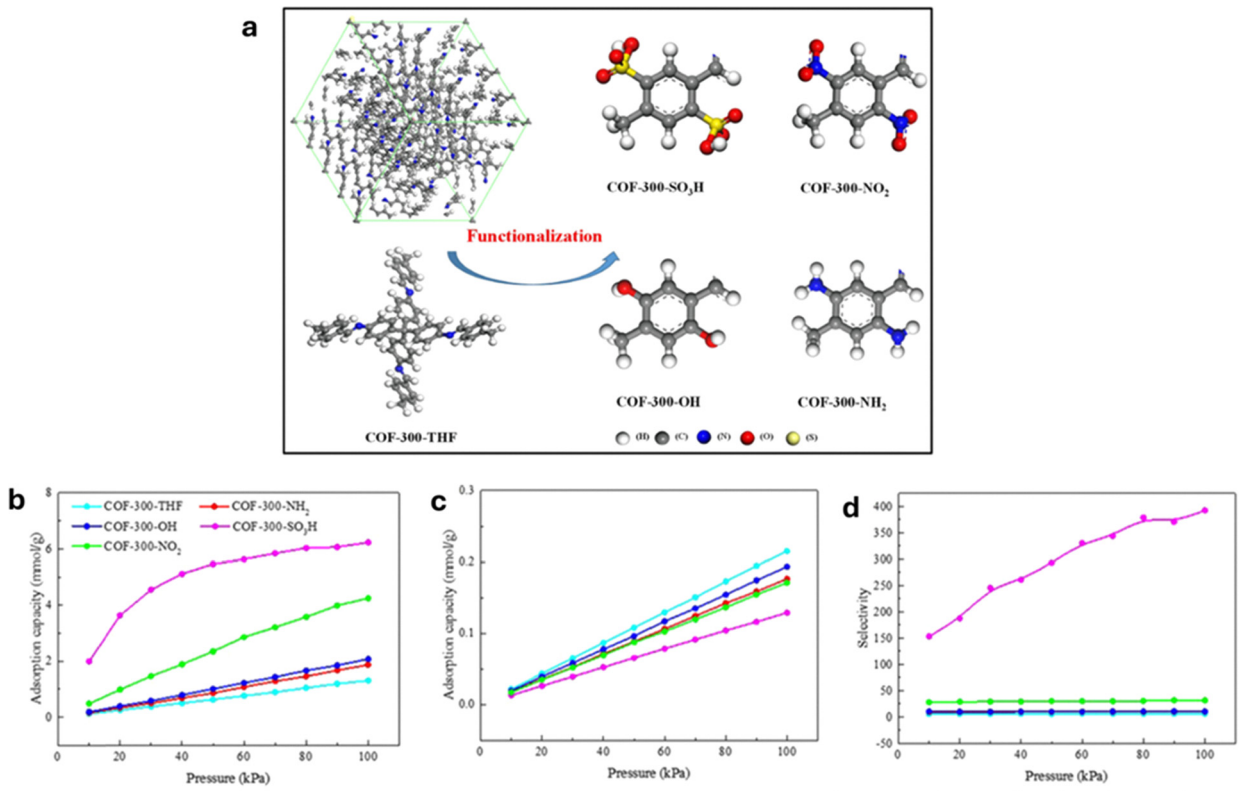

Fig. 32 (a) COF-300s with different functional groups. (b) CO_2 adsorption isotherms, (c) N_2 adsorption isotherms, and (d) selectivity of CO_2 over N_2 in COF-300s at 298 K. Reprinted (adapted) from *Adv. Theory Simul.* 2022, **5**, 2200588. © 2022 Wiley-VCH GmbH.

4. COFs for CO_2 electrochemical conversion

Electrocatalytic technology, which facilitates faster electron transfer between electrodes, reduces CO_2. It has several advantages, including mild operating conditions, reactors that can be successfully integrated, controlled reaction rates and selectivity, and the ability to utilize renewable energy sources. The electrocatalytic process consists of three fundamental steps: (1) adsorption of reactant species on the surface of active sites; (2) formation of intermediate states; and (3) desorption of the products.[143,170] COFs can provide a useful platform for enhancing CO_2 conversion efficiency through the CO_2RR process due to their unique structural components and chemical properties. COFs converted a large surface area into numerous active sites by incorporating organic components into their structure, which produced spaces that reacted well. Additionally, transition metal species (*e.g.*, Fe, Ni, Co) present in COFs are used as active centers for the conversion of CO_2 in electrochemical reactions due to their active d-electrons and vacant orbitals.[171] Atomic size and electronegativity are two fundamental properties of metal active sites in COFs that significantly impact their inherent selectivity and activity. This approach has been demonstrated in the investigation of Lin *et al.*;[172] wherein isolated cobalt porphyrin units were incorporated into ultrathin 2D COF nanosheets. The atomic dispersion of cobalt provided a consistent coordination environment, minimizing electronic fluctuations across sites and resulting in improved CO selectivity and enhanced catalytic stability.

The successful outcome of CO_2 reduction can be significantly enhanced by incorporating transition metals, alkaline-earth metals, and single-atom sites into organic or carbon-based frameworks, as numerous studies have demonstrated. For instance, Wu *et al.*[173] reported that single-atom Mg and Ca attached to nitrogen-doped carbon exhibited outstanding selectivity for formate production at near-zero overpotentials by favoring *OCHO intermediate formation. Dagnaw *et al.*[174] demonstrated a unique molecularly cationic covalent organic frameworks that incorporate transition metals (Cu and Pd) as active sites for the extremely selective electrochemical reduction of CO_2 into CO. They synthesized two COFs, CuCOF and CuCOF$^+$, by coordinating Cu(I)-bisphenanthroline complexes with terpyridine-based organic linkers. CuCOF$^+$ was further modified with ethyl groups to improve its positive surface charge and hydrophilicity, which ultimately promoted CO_2 accessibility and inhibited the HER side reaction. The COFs displayed a distinctive, three-dimensional woven framework (Fig. 33). The resulting CuCOF-Pd and CuCOF$^+$-Pd catalysts showed significant increases in faradaic efficiency after loading Pd nanoparticles (NPs) into the pores of CuCOF and CuCOF$^+$. For CuCOF$^+$-Pd, the selectivity of CO reached up to 95.45% at −0.8 V *vs.* RHE.

Additionally, catalytic activity and electron transport efficiency in CO_2 reduction systems can be improved simultaneously by combining metal active centers and conductive structural units in a single framework. For instance, Zhu *et al.*[175] designed a series of metalloporphyrin–tetrathiafulvalene-based covalent organic frameworks (M-TTCOFs) that provide a convincing example of how combining metal active centers and conductive structural units within a single framework can simultaneously enhance catalytic activity and electron transport efficiency in CO_2 reduction systems. The M-TTCOFs were produced by Schiff-base condensation between 4-formyl-TTF and M-TAPP (where M = Co or Ni), as shown in (Fig. 34a). This resulted in 2D layered structures with a unique porous structure and π-conjugated frameworks. The embedded metalloporphyrin moieties (such as Co or Ni) act as catalytically active sites in this system. While tetrathiafulvalene (TTF) acts as a highly conjugated electron donor, creating direct charge-transport pathways. This building improves the accessibility of redox-active centers and facilitates effective charge migration throughout the framework. As shown in the LSV curves (Fig. 34b) and FECO profile (Fig. 34c), the Co-TTCOF exhibited the highest catalytic activity, maintaining over 90% selectivity within a wide potential range (−0.6 to −0.9 V) and achieving a faradaic efficiency for CO (FE_{CO}) of 91.3% at −0.7 V *vs.* RHE. After exfoliation into nanosheets (~5 nm thick), the FE_{CO} further increased to a maximum of 99.7% at −0.8 V, among the highest reported for COF-based electrocatalysts.

5. COFs for integrated CO_2 capture and electrochemical conversion

Recent progress in COFs has demonstrated that they can integrate CO_2 capture and electrochemical conversion into a single material. This addresses the significant issue of separating CO_2 from flue gas, which requires an energy-intensive process. For instance, Liu *et al.*,[176] demonstrated a dual-functional covalent organic framework (PA-Co-COF) that combines CO_2 capture and

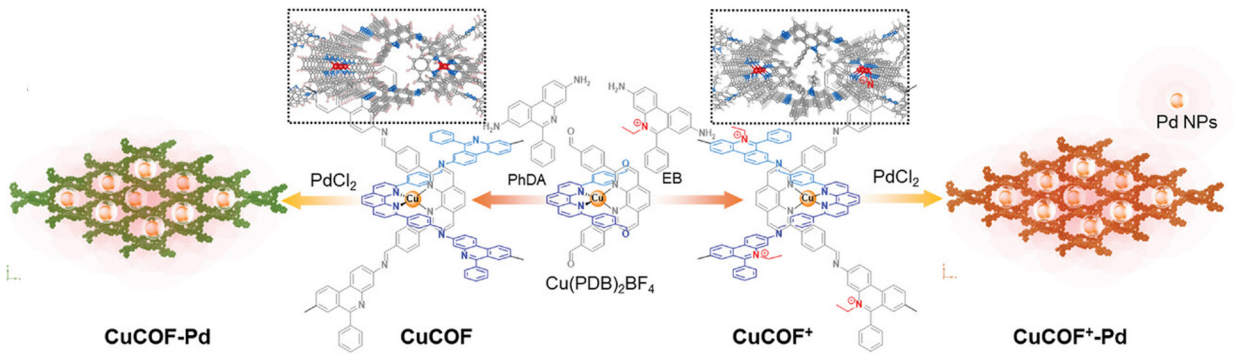

Fig. 33 Synthesis of CuCOF, CuCOF$^+$, CuCOF-Pd, CuCOF$^+$-Pd. Reprinted (adapted) from *Adv. Sci.* 2024, **11**, 2408152. Copyrights © 2024 The Author(s). Published by Wiley-VCH GmbH under the terms of CC-BY license.

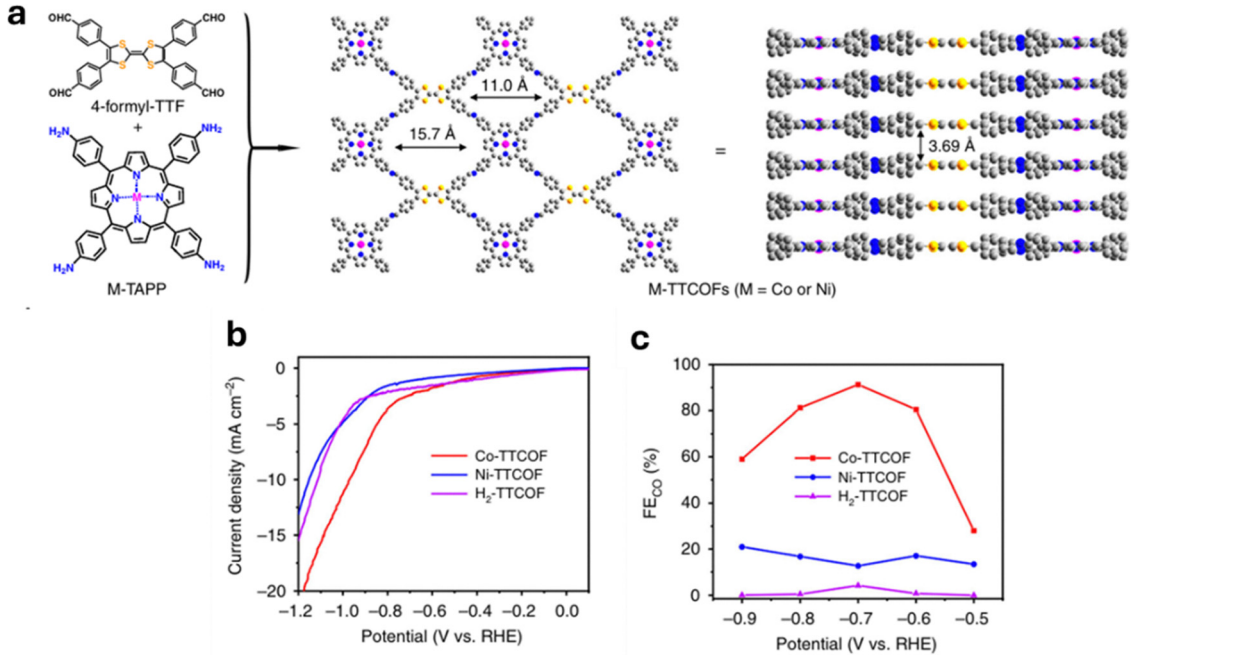

Fig. 34 Structural design and electrocatalytic performance of M-TTCOFs (M = Co or Ni) for CO_2 reductio. (a) Synthesis of 2D M-TTCOFs *via* condensation of 4-formyl-TTF and M-TAPP, forming ordered frameworks with defined pores. (b) LSV curves showing enhanced activity of Co-TTCOF over Ni- and H_2-TTCOFs. (c) Faradaic efficiency for CO production across −0.5 to −0.9 V, with Co-TTCOF showing superior selectivity. Reprinted (adapted) from *Nat Commun*, 2020, **11**, 497. Copyright © 2020, The Author(s). Published by Springer Nature under the terms of CC-BY license.

electrochemical conversion within a single material. This material is effective in environments with low CO_2 concentrations, such as flue gas (approximately 15% CO_2). (Fig. 35) illustrates that the framework consists of phytic acid (PA), which binds to CO_2, and cobalt-porphyrin (CoPor), serving as the catalytic center. (Fig. 35a) shows the conventional Co-COF with unmodified channels, while (Fig. 35b) demonstrates how the inclusion of PA creates CO_2-trapping channels that guide CO_2 molecules toward the catalytic sites. The synthetic pathway in (Fig. 35c) highlights the *in situ* formation of the PA-Co-COF from PYTA, DHTA, CoPor, and PA. Structural analysis in (Fig. 35d) confirms that incorporation of PA and CoPor preserves the crystalline order of the COF framework. The proposed mechanism in (Fig. 35e) shows the elementary steps of CO_2 reduction to CO, proceeding *via* the *COOH intermediate. Electrochemical data presented in (Fig. 35f and g) demonstrate that PA-Co-COF achieves a CO faradaic efficiency of 86.97% at −0.7 V and a maximum turnover frequency (TOF) of 1208.8 h^{-1} at −1.0 V, far above the performance of the unmodified Co-COF. Density functional theory (DFT) calculations in (Fig. 35h and i) expose that PA lowers the energy barrier for *COOH formation (from 0.495 eV to 0.323 eV) and increases the barrier for the competing hydrogen evolution reaction (HER) (from 0.666 eV to 0.887 eV), thereby enhancing both selectivity and activity. Also, some selected COF-based catalysts are summarized in (Table 11) for CO_2 capture and electrochemical reduction.

6. Future outlook of COFs

COFs are emerging as a versatile platform for integrated CO_2 capture and electrochemical conversion. By combining strong CO_2-binding functionalities, such as amine groups, with conductive, π-conjugated networks, COFs can simultaneously adsorb CO_2 and catalyze its reduction, potentially within a single device. Recent reviews highlight the feasibility of bifunctional porous electrodes composed of COFs that act as both capture media and electrocatalysts. Importantly, techno-economic analyses indicate that coupling capture with electrochemical conversion can significantly reduce overall energy consumption, particularly by eliminating energy-intensive CO_2 desorption steps. Future development will focus on enhancing chemical and electrochemical robustness, for instance *via* stable linkers and hydrophobic coatings, and improving charge transport through conductive dopants or metal sites. Scaling up from laboratory microwave synthesis to continuous-flow reactors will also be critical for real-world deployment. Altogether, these integrated COF systems offer a compelling pathway toward compact, energy-efficient CO_2 conversion devices, merging capture and catalysis into streamlined, resilient technologies.

Zeolites

Zeolite is a crystalline, microporous material made up of alumina-silicate structures. It is used in many industrial processes, such as gas separation, ion exchange, and catalysis.[183,184] Its unique properties allow it to effectively adsorb and trap molecules, making it essential in various chemical processes and environmental remediation efforts, as shown in (Fig. 36). Different ways are used, such as an adsorbent, an ion exchanger, and a catalyst.[183,185] Zeolite performs well as a catalyst for conventional uses in refineries and petrochemical businesses.[186]

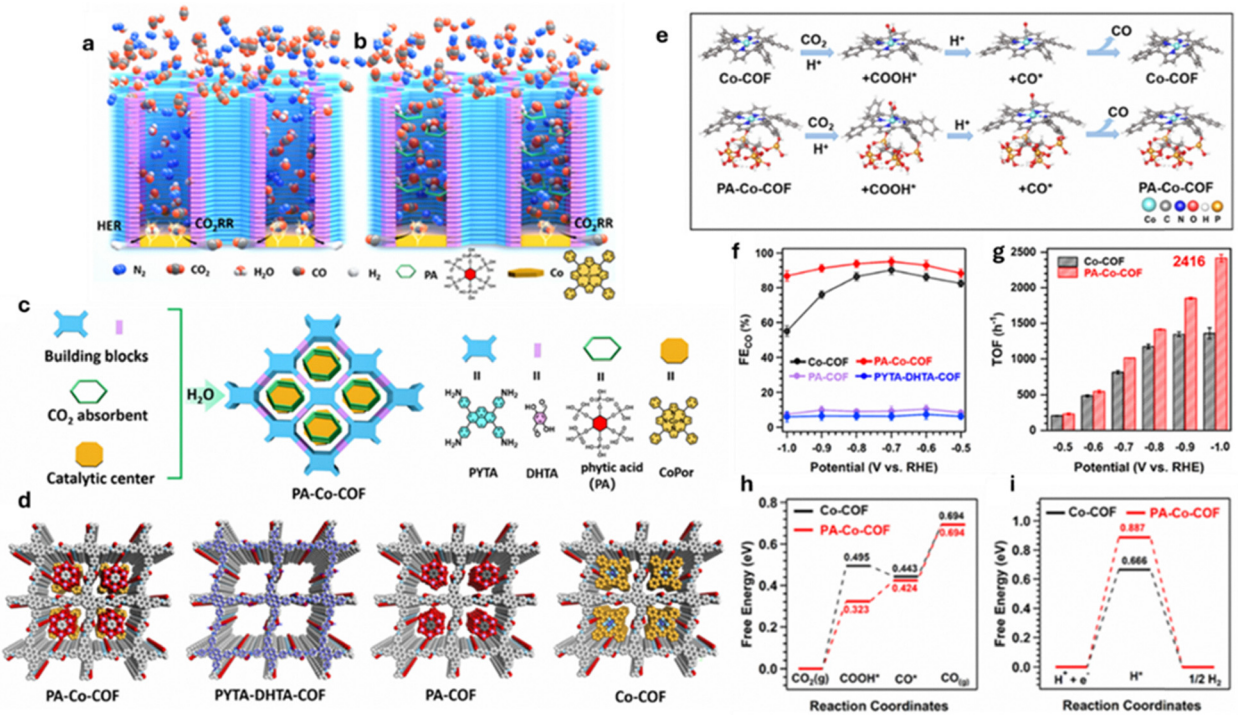

Fig. 35 Integrated schematic and performance data of PA-Co-COF for CO_2 electroreduction under simulated flue gas. (a) Schematic illustration of Co-COF. (b) PA-Co-COF showing transport and catalytic channels for CO_2 reduction reaction (CO_2RR). (c) *In situ* synthesis of PA-Co-COF from PYTA, DHTA, and Co-porphyrin, with phytic acid (PA) acting as both template and pore-filling CO_2 absorbent. (d) Crystal structures of PA-Co-COF, PYTA-DHTA-COF, PA-COF, and Co-COF highlighting retention of crystalline order. (e) Proposed reaction pathway for CO_2-to-CO conversion on CoPor active sites. (f) CO faradaic efficiency (FE_{CO}) of different COF structures from −0.5 to −1.0 V *vs.* RHE. (g) Calculated turnover frequency (TOF) for CO, showing enhanced reaction kinetics for PA-Co-COF. (h) DFT-calculated Gibbs free energy profile for the CO_2 reduction reaction, indicating a lower energy barrier for PA-Co-COF. (i) DFT-calculated Gibbs free energy profile for the competing hydrogen evolution reaction (HER), showing that H_2 formation is suppressed on PA-Co-COF. Reprinted (adapted) from *ACS Catal.* 2024, **14**, 14, 11076–11086. Copyright © 2024 American Chemical Society.

Zeolite is characterized by microporous structure (less than 2 nm) that is organized by TO_4 tetrahedra, where (T stands for tetrahedrally coordinated Si or Al).[187–189] Molecular shape selectivity, a large surface area, and great thermal stability are some of the wonderful properties of zeolite that make it a great host matrix for metal clusters or nanoparticles.[190,191] This makes multipurpose composite materials with great properties owing to these characteristics, it offers a catalytic site for the conversion of the intermediate produced by CO_2 activation in the active metal site to generate hydrocarbons from CO_2.[192,193] Therefore, it would be possible to manipulate the zeolite catalyst's structural or textural characteristics to arrange the hydrocarbon goal yield.[190,194]

During the process of CO_2-integrated collection and conversion, zeolites can perform the functions of both adsorbents and catalysts.[195] The microporous structure of these materials allows them to selectively adsorb carbon monoxide (CO). Because they are catalytic, CO can be changed into compounds with added value, like methanol, hydrocarbons, or syngas.[193] Metal-loaded zeolites, such as those containing nickel, copper, or iron, enhance catalytic performance by enabling the electrochemical reduction or hydrogenation of carbon dioxide. When it comes to structural qualities, product selectivity was found to have a significant relationship between the arrangement of the perfect acid density and the strength of the zeolite catalyst.[196]

Zeolites can be sub-grouped into natural and synthetic. On the one hand, natural zeolites such as ZAPS can be used as dryers and deodorants for air separation and ion exchange for water treatment and soil improvement (Fig. 37). On the other hand, synthetics such as FAU have advantages over natural ones, such as achieving high control over the material's porosity and crystallinity, but they are more expensive compared to affordable natural zeolites. Despite the lower cost of natural zeolites, they have reduced purity, varying composition, and inferior sorption properties.[197,198]

1. Zeolites for CO_2 capture

Boer *et al.* divided the zeolite into two groups. The first is medium and large-pore zeolites, with pore sizes in the range of 4.5–6.0 Å and 6.0–8.0 Å, respectively. The second group is small-pore zeolites, which have pores in the range of 3.0–4.5 Å (Fig. 38).[199] CO_2 is preferentially adsorbed on zeolite surfaces due to its considerably higher quadrupole moment and polarizability relative to other gases in flue gas (Table 12). This understanding is crucial because the 8-membered rings are the only structures in small-pore zeolites that encourage CO_2 diffusion, while the pore sizes of smaller rings (*e.g.*, 6-membered rings) are excessively closed. The capture mechanism for the selective adsorption and separation of CO_2 from gas mixtures utilizing zeolites as adsorbents primarily encompasses equilibrium separation, kinetic separation, and molecular sieving separation.[199–201]

Table 11 Summary of selected COF-based catalysts reported for CO_2 capture and electrochemical reduction

Catalysts	Pore size (Å)	Dimensional	Linkage type	BET surface area ($m^2\ g^{-1}$)	Capacity CO_2 ($mg\ g^{-1}$)	Electrochemical application	Electrochemical TOF or selectivity	Ref.
TFPc-PBBA-COF	22	3D	Boronate Ester	111.8	16.7	CO_2RR	Selectivity for CO 95% TOF = 1695 h^{-1}	177
CoPc-PI-COF-1	16	2D	Imine (polyimide)	181	38.52	CO_2RR	Selectivity for CO 97% TOF = 2.2 s^{-1} TON = 277 000	148
CoPc-PI-COF-2	18	2D	Imine (polyimide)	291	37.78	CO_2RR	Selectivity for CO 96% TOF = 1.9 s^{-1} TON = 71 000	148
CoPor-DPP-COF	20.08	2D	Imine	1021	3.72	CO_2RR	Selectivity for CO 82%	178
Cu-Tph-COF-Dct	12–18	2D	Imine (Porphyrin-based)	335	120.4	CO_2RR	Selectivity for CH_4 80%	179
COF-102	12	3D	Boronated Ester	3620	1200	CO_2 storage	N/A	166
COF-103	12	3D	Boronate Ester	3530	1190	CO_2 storage	N/A	166
(3D-HNU5)	10	3D	Azine	864	123.1	Cyclic carbonate synthesis	TON = 990, Yield > 99%	180
Tz-COF	21	2D	Imine	1439	154	Gas separation	Higher CO_2 selectivity than N_2 (20/12)	181
Cz-COF	20	2D	Imine	871	110	Gas storage & separation	Good recyclability and selectivity	181
Zn-Salen-COF-SDU113	35	2D	Imine	1143	19.8	Cycloaddition with epoxides to carbonates	Yield = 98.2%, TON = 3068.9	182
Cu-COF+	28	2D	Imine (Cationic, ethyl-modified)	27.6	13.7	CO_2RR	Selectivity for CO 57.81%	174
Cu-COF+-Pd	28	2D	Imine (Cationic + Pd)	4.1	8.4	CO_2RR	Selectivity for CO 95.45%	174
PA-Co-COF	16.9	2D	Imine	689	102.9	CO_2RR from the flow gas	Selectivity for CO 86.97% TOF = 1208.8 h^{-1}	176
Co-TTCOF	25.4	2D	Imine (porphyrin + TTF)	486	39.3	CO_2RR	Selectivity for CO 99.7% TOF = 1.28 s^{-1}	175
COF-367-Co (1%)	12–23	2D	Imine	1470	N/A	CO_2RR	Selectivity for CO 40% TOF = 764 h^{-1} TON > 24 000 (TONEA ≈ 296 000)	172
COF-367-Co	12–23	2D	Imine	1470	N/A	CO_2RR	Selectivity for CO 91% TOF = 165 h^{-1} TON = 3901 (TONEA ≈ 48 000)	172

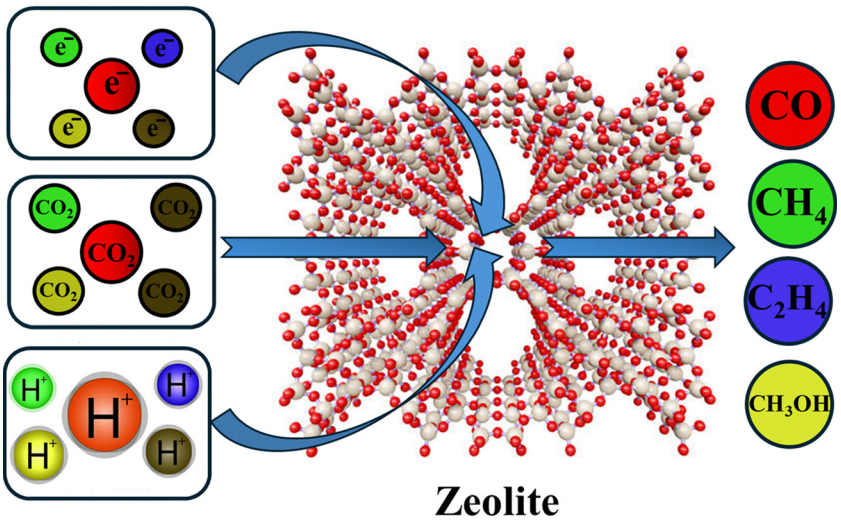

Fig. 36 Schematic illustration of zeolite for CO_2 capture and electrocatalytic conversion.

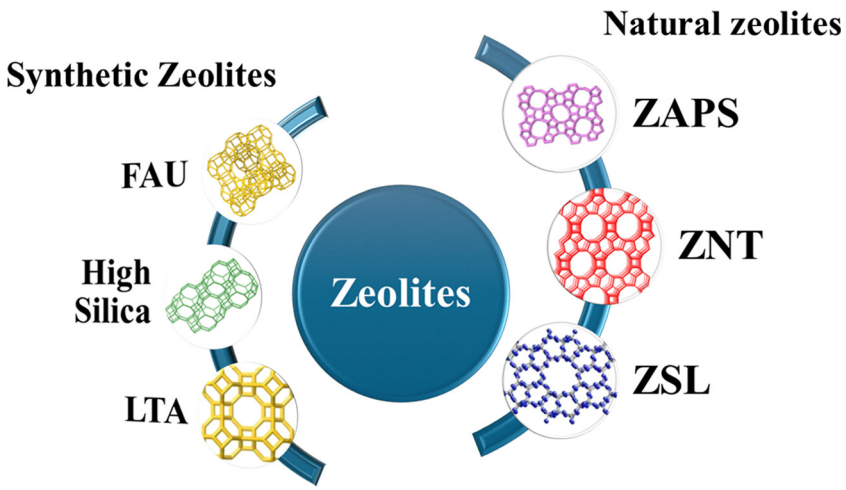

Fig. 37 Classification of zeolites.

Equilibrium separation depends on how the guest molecules and the zeolite micropores interact with each other.[204] These interactions could be physisorption (which involves van der Waals forces and electrostatic interactions) and chemisorption (which involves π-complexation).[205,206] What affects the electric charge exchange between gas molecules and zeolite surfaces are the polarity, polarizability, Si/Al ratios, and the types of metal cations. Kinetic separation relies on the different speeds at which guest molecules move through the tiny holes in zeolite.[207] Kinetic separation is limited by molecular sieving, which needs zeolite micropores that are big enough to let CO_2 through, but not any other exhaust gases.[199,208]

A compelling example of a zeolite-based material for CO_2 capture is the hierarchical ZIF-L nanostructure reported by Ding *et al.* In this study, the authors synthesized a cross-shaped hierarchical ZIF-L using a simple hydrothermal method involving zinc nitrate and 2-methylimidazole at 125 °C. This hierarchical structure, composed of symmetrically connected ZIF-L leaf-like plates, exhibited a significantly enhanced Brunauer–Emmett–Teller (BET) surface area of 304 $m^2\ g^{-1}$ compared to 161 $m^2\ g^{-1}$ for conventional two-dimensional ZIF-L. As a result, the CO_2 adsorption capacity reached 1.56 mmol g^{-1} at 298 K and 1 bar, outperforming both the 2D ZIF-L (0.94 mmol g^{-1}) and even ZIF-8 (0.68 mmol g^{-1}), despite ZIF-8 having a much higher surface area. This superior performance is attributed to the unique cushion-shaped cavities of ZIF-L and the hierarchical architecture, which provides enhanced accessibility to active sites and reduces particle aggregation.

2. Factors affecting CO_2 adsorption over zeolite

Zeolites are commonly used as absorbents for the absorption of CO_2 from flue gas, namely in CO_2/N_2 separation processes.[205] In their study, Zhang *et al.* look at the zeolite extra-framework cation, secondary-pore system, particle size, and Si/Al ratio as important factors that have a big effect on the adsorption mechanism, capacity, and selectivity (Fig. 39).[200]

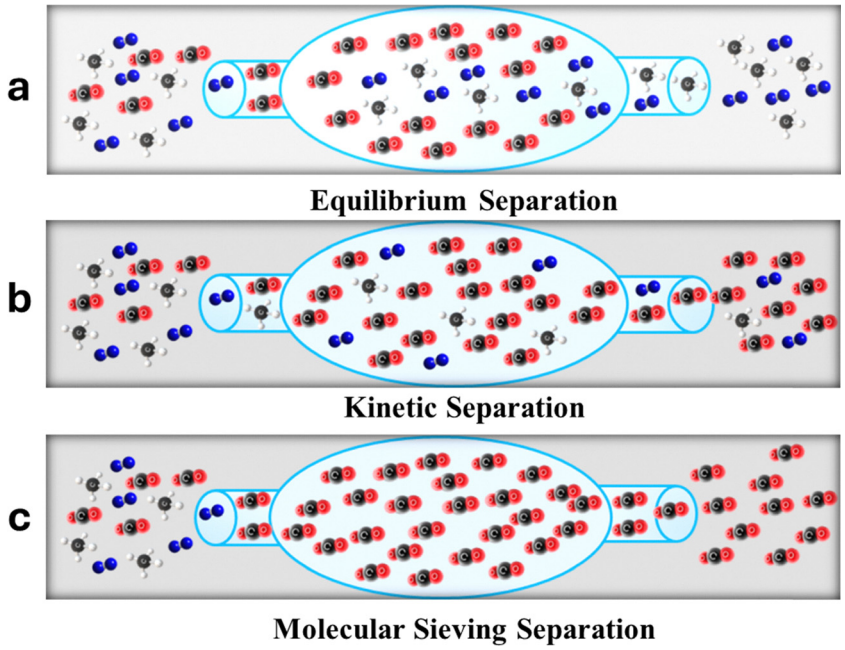

Fig. 38 Different types of CO_2 separation over zeolites. (a) Equilibrium separation, in which CO_2 preferentially adsorbs on the surface of the adsorbent. (b) Kinetic separation, in which CO_2 diffuses faster through the pores. (c) Molecular sieving separation, in which only CO_2 can enter the pores.

Table 12 Properties of gases relevant to CO_2 separation from flue-gas[202,203]

Gases	Kinetic diameter (Å)	Quadrupole (C m^{-2})	Polarizability (cm^3)
CO_2	3.30	13.4×10^{-40}	2.65×10^{-24}
N_2	3.64	4.6×10^{-40}	1.76×10^{-24}
O_2	3.50	—	1.58×10^{-24}
CH_4	3.80	0	2.60×10^{-24}

(A) Type of framework. Different types of zeolites are distinguished by the size and shape of the channels and cages present within their framework, with about 258 fully ordered zeolite frameworks and a few partially disordered frameworks. All zeolite frameworks talked about in the previous chapter can be found in (Table 13).[209] Several essential characteristics can be defined by the zeolite framework type, such as the number of Si/Al atoms in the rings and the related pore size (Å). As the CO_2 molecule only diffuses through at least 3.3 Å of the pore aperture, the ring should be an 8MR or larger. Additionally, zeolites with the same structure and similar crystal size should, in principle, have a similar surface area in their H-form. Additionally, the topography of zeolitic pores is classified into three main types. Cage structures (C), such as LTA, CHA, and FAU, where spherical cavities are interconnected *via* small windows, allowing size-selective diffusion. MFI and BEA serve as exemplars of Intersecting channel systems (IC), which provide a three-dimensional interconnected network enabling multidirectional transport and high accessibility. FER and MOR frameworks represent one-dimensional channels connected to cages (1D+C) which include linear diffusion pathways to isotropic central regions called cages that are usually, but not always severely restricted in mobility due to steric or electrostatic forces.[199,210,211]

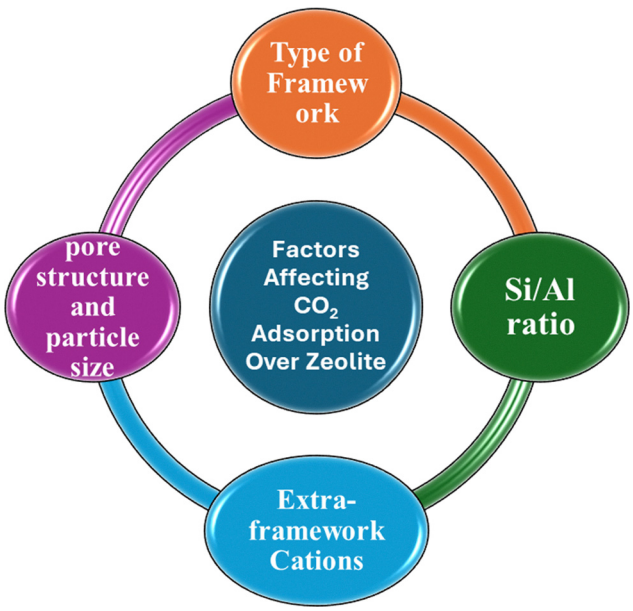

Fig. 39 Factors affecting CO_2 adsorption over zeolites.

Also, the diffusion of adsorbates is affected by the pore topology, the pore size, and the shape of a zeolite, which define its performance as adsorbent as well. Although zeolite frameworks have a certain degree of flexibility, they are often assumed to be rigid and can be induced by temperature, the extra-framework cations, or the presence of adsorbates.[212,213] Also, the studied zeolites of MER and RHO showed an unusual adsorption isotherm with an inflection point attributed to the increase in the pore size, called breathing, and/or the window size.[205,214]

Table 13 Some representative zeolite materials widely used in CO_2 capture and conversion[209]

Framework type	Secondary building units	Max free sphere (Å) (a, b, c)	Ore topology	Composite building units	Framework image
Small-pore zeolites the rings that are large enough to allow CO_2 to diffuse through them					
LTA	8 or 4-4 or 6-2 or 6 or 1-4-1 or 4	4.21 × 4.21 × 4.21 Å	C	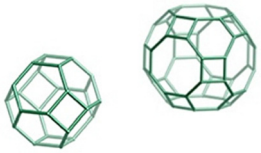	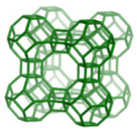
CHA	6-6 or 6 or 4-2 or 4	3.72 × 3.72 × 3.72 Å	C	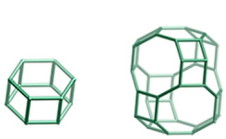	
MER	8-8 or 8 or 4	3.12 × 3.12 × 4.2 Å	1D+C	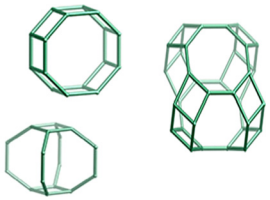	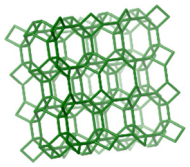
Medium- and large-pore zeolites the rings that are large enough to allow CO_2 to diffuse through them					
MFI	5-1	4.7 × 4.46 × 4.46 Å	IC	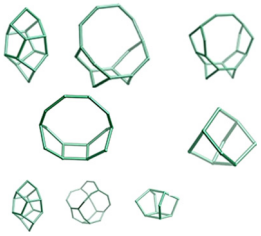	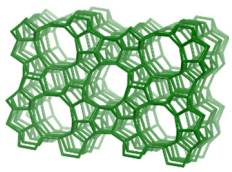
FAU	6-6 or 6-2 or 6 or 4-2 or 1-4-1 or 4	7.35 × 7.35 × 7.35 Å	C	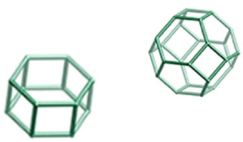	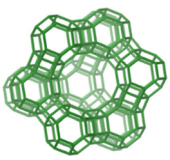
MOR	5-1	1.57 × 2.95 × 6.45 Å	1D+C	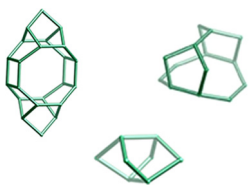	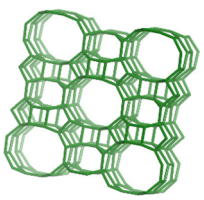
FER	5-1	1.56 × 3.4 × 4.69 Å	1D+C	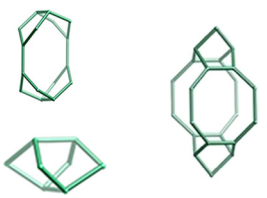	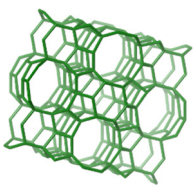

(B) Si/Al ratio. The Si/Al ratio profoundly influences zeolite CO_2 adsorption by controlling framework charge density, cation site density, and pore accessibility. Low Si/Al ratios increase Al content, creating more charge-balancing cations (*e.g.*, Ca^{2+}, Na^{+}) and Lewis basic O atoms adjacent to Al, which strengthen electrostatic interactions with acidic CO_2.[215,216] The zeolite may absorb more CO as the Si/Al ratio decreases, due to an increased number of adsorption sites per unit mass of material.[217] Moreover, silicoaluminate zeolites possess Lewis base sites derived from the oxygen atoms next to aluminum, as a result, the number of these essential sites per unit mass of zeolite escalates with an increase in aluminum content.[218,219] A lower Si/Al ratio suggests more aluminum atom presence inside the framework, thereby producing more negatively charged

sites needing charge-balancing cations like Ca^+. Stronger electrostatic interactions with an acidic CO_2 molecule help these cations to bind additional CO_2 more easily.[196,199,200] For instance, palomino *et al.* illustrated that zeolite LTA with a Si/Al ratio of 1 has a decreased adsorption capacity compared to zeolite LTA with Si/Al ratios of 2 or more, which has been linked to the decreased visible pore volume in the zeolite with Si/Al = 1.[220] Following these assumptions, many studies show that the ability of zeolites to absorb CO_2 usually goes up when the Si/Al ratio goes down.[221] The cation count decreases commensurate with a change in the Si/Al ratio. Strong cations can produce steric hindrance inside the pores, therefore limiting CO_2 transport, for instance, the studies by Hong *et al.* unequivocally show this kind of nature. Na-GIS zeolites with low Si/Al ratios (1.5 and 2.2) showed limited CO_2 absorption ($\leq$0.7 mmol g^{-1}) because of steric hindrance generated by the predominance of Na^+ cations blocking pore access. Reduced cation density allowing more effective CO_2 transfer clearly boosted adsorption (up to 3.7 mmol g^{-1}) seen by increasing Si/Al ratios (2.5–4.7). This work shows how much the Si/Al ratio affects adsorption performance.[222]

(C) Extra-framework cations. Modulating extra-framework cations tunes zeolite pore size, volume, framework basicity, and electrostatic interactions, profoundly affecting CO_2 adsorption capacity and selectivity as shown in (Table 14). Ion exchange of Na^+ with mono- or multivalent cations creates acidic cation sites and basic Al–O sites, where lower cation electronegativity boosts oxygen negative charge and basicity (Cs > Rb > K > Na > Li). Stronger basicity enhances acidic CO_2 interactions, but larger ionic radii weaken polarizing power (Li > Na > K > Rb > Cs), creating an optimal charge-to-radius balance.[223,224] Cation radius also tunes zeolite pore size and volume, altering diffusion kinetics and molecular sieving. Shang *et al.* showed with LTA-type zeolites that the cation charge-to-size ratio is a key descriptor for CO_2 uptake in direct air capture. Higher-charge, smaller cations (Ca^{2+}, Ni^{2+}, Cu^{2+}) strengthen electrostatic interactions and sometimes π-back-bonding with CO_2, giving higher capacities, whereas low-charge or large cations (K^+, Y^{3+}, La^{3+}) perform worse.[225]

Table 14 Shows how cation properties affect metal-exchange LTA zeolite CO_2 absorption capability

CO_2 uptake (mmol g^{-1})	Charge/size ratio (z/r)	Ionic radius (Å)	Charge (z)	Cation
Low	0.98	1.02	+1	Na^+
Low	0.72	1.38	+1	K^+
Moderate	2.78	0.72	+2	Mg^2
High	2.00	1.00	+2	Ca^2
Moderate	2.41	0.83	+2	Mn^2
Moderate	2.53	0.79	+2	Co^2
High	2.90	0.69	+2	Ni^2
High	2.74	0.73	+2	Cu^2
Moderate	2.70	0.74	+2	Zn^2
Low	3.33	0.90	+3	Y^3
Low	2.91	1.03	+3	La^3
Low	2.97	1.01	+3	Ce^3
Low	3.16	0.95	+3	Eu^3
Low	3.26	0.92	+3	Tb^{3+}
Low	3.49	0.86	+3	Yb^{3+}

(D) Impact of secondary pore structure and particle size. Secondary pore systems and particle size strongly impact zeolite CO_2 adsorption performance by improving mass transport and accessibility. Smaller particles reduce diffusion path lengths, enabling faster equilibrium, as seen in CHA-type zeolites where nano-sized crystallites exhibit sharper, more dynamic CO_2 breakthrough curves compared to larger ones. Hierarchical meso-micro networks further enhance capacity and kinetics: Dabbawala *et al.* reported Y (FAU) zeolites rising from 4.5 to 5.4 mmol g^{-1}, while Singh *et al.* found mesoporous LTA zeolites with 29 s faster adsorption, 92 s faster desorption, 20% lower water uptake, and 13 °C lower regeneration temperature *versus* microporous LTA.[226] Concurrently, Dabbawala *et al.* reported an increase in adsorption capacity for hierarchical Y zeolites, from 4.5 mmol g^{-1} for conventional Y (FAU-type) zeolites of CO_2. Increasing the hierarchical Y zeolites to 5.4 mmol g^{-1} under the same conditions is ascribed to the presence of the interconnected micro-meso channel network.[227] Moreover, these mesoporous features also showed a 20% drop in water adsorption capacity, a 14% reduction in the heat of CO_2 adsorption, and a 13 °C lower temperature required for desorption compared to traditional LTA zeolites, signifying energy efficiency.[60] Similarly, two-dimensional 1.38 nm thick LTA zeolites with a lamellar structure demonstrated superior CO_2 capture and separation efficacy than the conventional 3D LTA zeolites.[200,228]

These theoretical insights into the effects of framework topology are well illustrated in the recent work by Al Atrach *et al.* (Fig. 40).[229] The study offers a compelling demonstration of how key structural and compositional factors influence CO_2 adsorption over zeolites, using LEV-type zeolite as a case study. By comparing two LEV samples with different morphologies and compositions: a nanosized sample (Si/Al ≈ 6.6) and a micron-sized sample (Si/Al ≈ 3.5). The LEV framework, characterized by

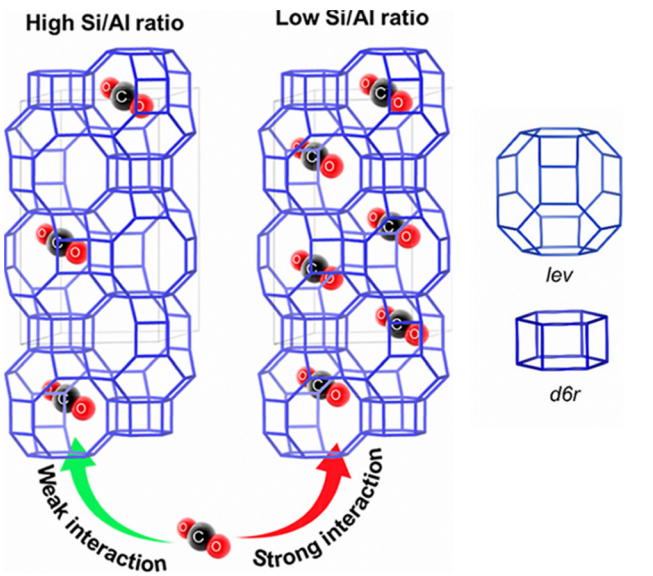

Fig. 40 LEV-type zeolite framework and its composite building units. Reprinted (adapted) from *ACS Appl. Mater. Interfaces* 2025, **17**, 4, 7119–7130. Copyright © 2025 American Chemical Society.

its small-pore topology and pore dimensions of 3.6 × 4.8 Å, offers a favorable steric and electrostatic environment for CO_2 capture due to its compatibility with the kinetic diameter and quadrupole moment of CO_2. As a result, the micron-sized sample exhibits a 22% higher CO_2 uptake (5.81 mmol g^{-1} at 0 °C) and superior selectivity (CO_2/N_2 = 84 at 25 °C) compared to the nanosized sample. Although the nanosized LEV has a higher surface area and mesoporosity, contributing to faster adsorption–desorption kinetics and better reversibility, its lower Na^+ content results in weaker CO_2 binding and reduced capacity.

3. Zeolite in CO_2 conversion

Integrating capture and conversion in zeolites boosts efficiency by eliminating compression and transport steps, as in reactive CO_2 capture (RCC). Electrocatalytic CO_2 reduction (CO_2RR) stands out for its ambient conditions, controllable kinetics, and recyclability *versus* energy-intensive thermal routes.[230,231]

The conversion of carbon dioxide (CO_2) into valuable chemicals is a primary step in carbon capture and utilization (CCU) technology, but CO_2 is a very stable molecule, which makes it difficult for its conversion into alternative compounds difficult, with a high dissociation energy of 750 kJ mol^{-1} as CO_2 possesses strong C═O bonds, which indicates that breaking these bonds requires a significant quantity of energy. Consequently, to split CO_2 molecules, high pressure, high temperatures, or catalysts are needed.[196] In this context, the thermal catalytic conversion of CO_2 into hydrocarbons has primarily followed two main pathways. Also, the selective hydrogenation of CO_2 to CO *via* the reverse water–gas shift (RWGS) reaction is highlighted, which serves as a precursor step to further hydrocarbon in thermochemical systems.[232] Notably, this intermediate step-CO-formation can also be achieved *via* electrochemical CO_2 reduction (CO_2RR), offering an energy-efficient and scalable route under ambient conditions, as will be discussed in subsequent sections. The RWGS can be completed by either of two approaches:

(A) Fischer–Tropsch synthesis. Hydrogenation of CO_2 to CO, after which comes hydrogenation to hydrocarbons employing the Fischer–Tropsch process.

$$CO_2 + H_2 \rightarrow CO + H_2O.\ \{\Delta H = 41.3\ \text{kJ mol}^{-1}\}\ \text{endothermic}$$

(B) Methanol synthesis pathway. CO_2 was initially transformed into methanol and then converted into hydrocarbons.

$$CO_2 + 4H_2 \rightarrow CH_4 + 2H_2O.\ \{\Delta H = -164.7\ \text{kJ mol}^{-1}\}\ \text{exothermic}$$

However, at atmospheric pressure, methanol yield is typically negligible, making this route less favorable. Moreover, methanation is thermodynamically dominant at low temperatures, often suppressing RWGS selectivity. Thus, designing catalysts that favor CO production over CH_4 remains a key challenge.[196,200]

Zhang *et al.*,[233] illustrate the intricate design and mechanistic pathways alongside the electrochemical performance of the CdO@Zn@Zeolite-Y system in a single diagram (Fig. 41a). The schematic captures the entire process of catalyst fabrication. The first step entails the ion exchange of Zn^{2+} into Zeolite-Y to yield ZnY. Subsequent incorporation of Cd^{2+} ions give rise to $Cd(NO_3)_2$@ZnY, and under thermal treatment, it converts to the final perovskite structure of CdO nanoclusters encapsulated within the microporous framework of Zn-doped Zeolite-Y. This form of nanoconfinement not only stabilizes the active sites but also preserves the structural integrity of the zeolite support. Electrochemical activity as defined in (Fig. 41b) is assessed

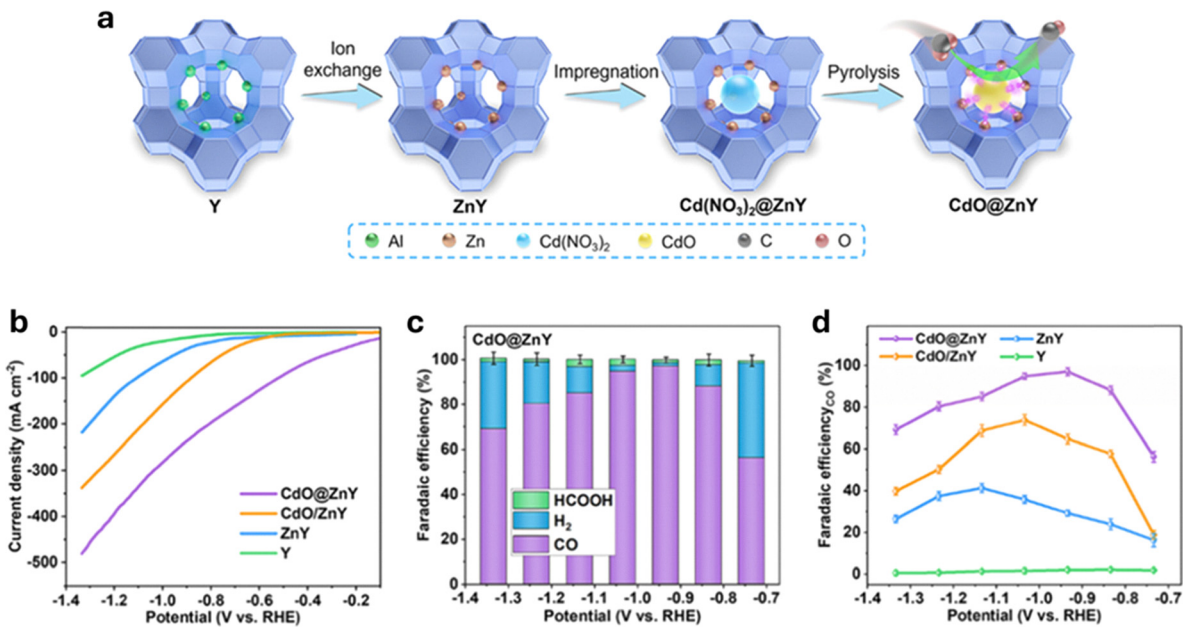

Fig. 41 Overview of structural design, mechanistic insight, and electrochemical performance of CdO@Zn@Zeolite-Y; (a) illustrates the schematic synthesis process; (b) displays total current density in Linear Sweep Voltammetry; (c) assessing faradaic efficiency for CO, H_2, and HCOOH at varying potentials; (d) comparison of CO selectivity between samples. Reprinted (adapted) from *J. Am. Chem. Soc.* 2024, **146**(9), 6397–6407. Copyright © 2024 American Chemical Society.

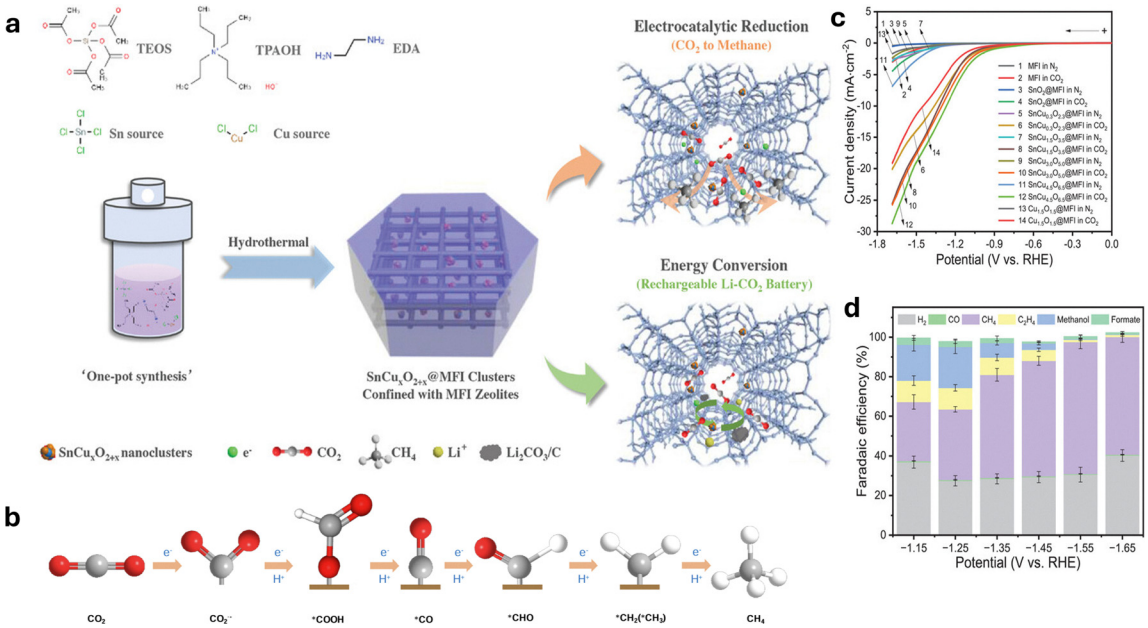

Fig. 42 (a) Schematic of one-pot synthesis of $SnCu_xO_{2+x}$ (x = 0, 0.3, 1.5, 3.0, 4.5) nanoclusters confined within purely siliceous MFI zeolites. (b) Mechanistic View of CH_4 Formation *via* *COOH and *CHO Intermediates. (c) LSV curves in CO_2-saturated 0.5 M KOH. (d) Faradaic efficiencies for CH_4/C_2H. Reprinted (adapted) from *Adv. Energy Mater.*, **13**, 2204143. Copyright © 2023 Wiley-VCH GmbH.

through Linear Sweep Voltammetry (LSV) profiles, and as expected, CdO@ZnY doesn't disappoint. This hybrid catalyst achieves the highest total current density among all tested catalysts, suggesting unparalleled activity in CO_2RR. In (Fig. 41c), product distribution analysis confirmed that CO was the dominant product, with a faradaic efficiency exceeding 90% at −0.8 V *vs.* RHE, while H_2 and HCOOH contributions were almost negligible. In (Fig. 41d), it further compared the CO selectivity of all samples, which, alongside galvanostatic experiments, resulted in reinforcing the performance of CdO@ZnY in all tested voltages. Overall, (Fig. 41) serves as a strong multidisciplinary argument on how catalyst design, specifically based on zeolite nanoconfinement and bimetallic synergies integrated, can enhance CO_2 conversion technologies.

Following the work of Zhang *et al.*, Zhu *et al.*[234] proposed a confined $SnCu_xO_{2+x}$@MFI catalyst that goes beyond CO_2 capture to activation and electrochemical conversion into C_1 and C_2 products, including methane and ethylene. This shift highlights the increasing multifunctionality of zeolite support, from enabling *CO evolution to incorporating multi-step, multi-carbon sculpting processes. They designed a zeolite-constrained bimetallic oxide system, $SnCu_xO_{2+x}$@MFI, to promote high-efficiency CO_2 electroreduction to methane production. As depicted in (Fig. 42a), the synthesis strategy involved the nanoconfinement of Sn–Cu oxide nanoclusters within the micropores and mesoporous framework of MFI zeolite. This spatial confinement stabilized the active metal–oxide interface, prevented nanoparticle aggregation, and significantly enhanced ion/electron transport due to the resulting mesoporosity (~3.2 nm). (Fig. 42b) illustrates the comprehensive mechanistic and electrochemical activity of the $SnCu_xO_{2+x}$@MFI catalyst in the electrochemical reduction of CO_2. A detailed top diagram describes the multi-step conversion of CO_2 into CH_4. Initiation commences with the CO_2 adsorption and activation step, which is *COOH-intermediate forming, an essential species confirmed *via* the *in situ* SEIRAS analysis. Subsequent decoupling steps yield *CO, *CHO, and finally, *CH_x intermediates, which lead to methane. Electrolysis of CO_2 is demonstrated in (Fig. 41c), illustrating the electrochemical performance and LSV curves, where $SnCu_{1.5}O_{3.5}$@MFI was found to have the greatest CO_2 current density within the CO_2 saturated conditions, indicative of improved performance compared with reference catalysts. As shown in (Fig. 42d), faradaic efficiency attributed to C_2H_4 as a secondary function of *CH_4 and C1 products reveals that a high-grade level is attained below −1.2 V, further supporting the previously mentioned hypotheses, while the production of H_2 and HCOOH remains at the decuple level.

4. Future outlook of zeolite

Zeolites remain strong contenders for CO_2 capture due to their high selectivity, thermal stability, and well-defined micropores. To improve real-world performance, ongoing research aims to engineer hydrophobic or hierarchical pore structures, introducing mesopores or cation-exchanged frameworks, to enhance moisture resistance and mass transfer. Future efforts will likely focus on creating zeolite–metal hybrid systems or membrane-reactor designs that can conduct CO_2 capture and conversion in a single unit, leveraging the high CO_2/N_2 selectivity and thermal resilience of zeolite membranes.

To realize this vision, key innovations include:

- Water-resistant coatings and pore tuning to maintain capture efficiency in humid streams.
- Mesostructuring to accelerate the diffusion of reactants and products.
- Hybrid material design, embedding zeolites in electrodes with catalytically active metals or conductive supports.

• Membrane reactor integration, enabling one-step CO_2 separation and conversion in a compact, energy-efficient system.

Metal–organic frameworks (MOFs)

Metal–organic frameworks (MOFs) constitute a relatively recent category of crystalline porous materials made up of multimetallic clusters, referred to as secondary building units (SBUs), which are linked by organic connectors known as linkers (Fig. 43).

Through the careful design and modification of these SBUs, linkers, and pore environments, MOFs provide an extraordinary level of structural and chemical adaptability to tackle global energy and environmental challenges.[235] Because of their varied, customizable structural properties, which include but not limited to highly porous surface area, powerful organic and inorganic catalytic sites and tunable postsynthetic structure, MOFs are intriguing materials.[236–238] These relatively new materials indicate themselves for general use in catalysis (photo-, electrocatalysis), energy storage, gas storage, hazardous adsorption, and so forth.[236,239–242] MOFs have proven to be particularly effective as adsorbents and catalysts because of several significant benefits: (i) predictable and functionalizable structures. The design flexibility of MOFs allows for precise control of their architecture, facilitating the integration of accessible adsorption and catalytically active sites. (ii) Hybrid compatibility – MOFs can be combined with other materials to create composites or act as precursors/templates for MOF-derived structures that exhibit improved physical and chemical attributes. (iii) Superior catalytic performance. MOFs serve as a link between homogeneous and heterogeneous catalysis, delivering high catalytic efficiency while ensuring stability, easy separation, and reusability. (iv) Tailorable structure–property relationships. The well-defined, customizable nature of MOFs yields important insights into how alterations in structure impact catalytic performance, aiding in the rational design of catalysts. These distinctive features make MOFs extremely promising candidates for CO_2 capture and utilization, fueling ongoing research aimed at optimizing them for sustainable energy and environmental uses as illustrated in (Fig. 44).

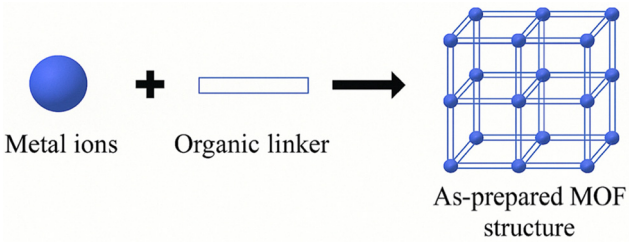

Fig. 43 Metal ions act as nodes bonding with organic linker to form MOF structure.

1. MOFs for CO_2 capture

MOFs are considered highly promising materials for CO_2 capture due to their exceptional porosity, tunable structures, and high surface areas. MOFs are crystalline materials that consist of metal ions or clusters linked by organic ligands with high design fixability that enables high degree of optimization of their pore size, functionality, and chemical environment to boost CO_2 adsorption.[235,243,244] MOFs are one of the most studied class of materials for gas storage and separation applications, with special focus on CO_2 capture from flue gases and direct air capture.[235,245]

MOFs with their physiochemical adsorption strategy have shown high CO_2 absorption capacities under both low- and high-pressure conditions, which is one of their primary advantages over conventional adsorbents like zeolites and activated carbon that depend solely on physical adsorption. For example, the well-defined pore structures and the presence of open metal sites in MOF-808 and its derivatives have demonstrated a better

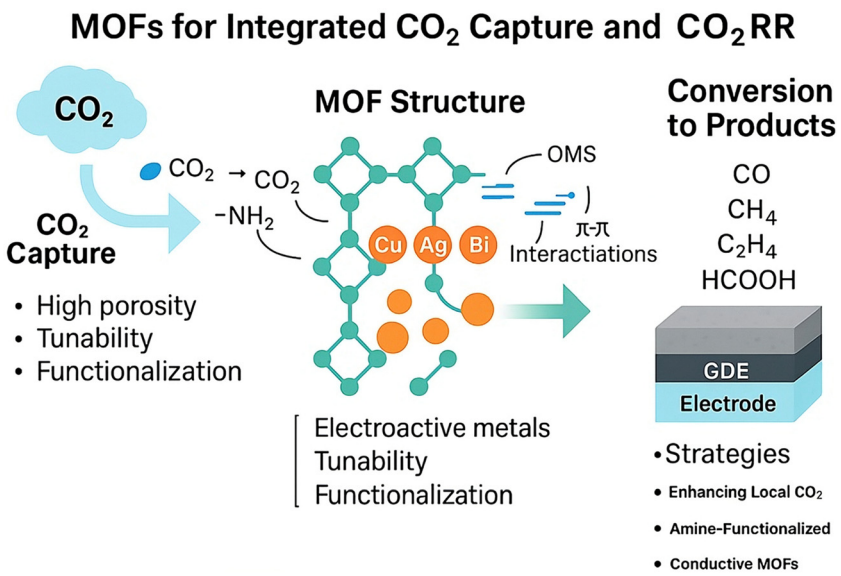

Fig. 44 Graphical abstract of MOFs for integrated CO_2 capture and electrocatalytic conversion.

ability to absorb CO_2.[246] Another group investigated the CO_2 absorption of HKUST-1 (MOF with OMSs) at 42 par and room temperature,[247] recording roughly 10 mmol g^{-1}. The CO_2 adsorption isotherm of HKUST-1 at ambient temperature resulted in a typical Type I isotherm, reflecting that most of the gas is adsorbed at low pressures, indicating the MOF's high affinity for CO_2 at low partial pressures. Given that the material will have a substantial CO_2 capture working capacity, these conditions are intriguing for practical CO_2 adsorption from gas streams. Because of its exceptional CO_2 uptake capacities at low pressures, the M-MOF-74 (M = Mg^{2+}, Ni^{2+}, Co^{2+}, Zn^{2+}) isoreticular series, which consists of a sequence of one-dimensional hexagonal channels with OMSs at the SBUs, has emerged as one of the most extensively researched sets of MOFs for CO_2 capture. The accessibility of coordinatively unsaturated metal sites in the pores, the integration of heteroatoms within the pores and their covalently linked functionality to the backbone, the specific interactions of MOF building units, the hydrophobicity of the pores, and a combination of these structural features are the main strata involved in the CO_2 capture by MOF, as shown in (Fig. 45) represent the main strategies involved in the CO_2 capture by MOF including presence of accessible coordinatively unsaturated metal sites in the pores; integration of heteroatoms within, as well as covalently linked functionality to, the backbone; specific interactions of MOF building units; hydrophobicity of the pores; and a hybrid of these structural features. While MOFs are well-recognized for their CO_2 uptake capacities, their modular structure also makes them highly tunable for catalytic activity.

2. MOFs for CO_2RR

One interesting path to energy conversion and/or high-value chemical manufacture is the electroreduction of CO_2.[248,249] Electrochemical CO_2 reduction (CO_2RR) offers a sustainable approach to converting CO_2 into valuable chemicals and fuels, leveraging renewable electricity to operate the system under mild conditions. An appealing platform to lower the negative impacts of carbon dioxide, as well as a supply of fine chemicals, is this electrochemical approach for converting CO_2 into fuels using plenty of renewable energy resources.[249–251] However, the slow reaction kinetics, which consist of numerous steps of electron and proton transfers, along with competing hydrogen evolution reaction (HER), produce low productivity and efficiency. These are the main challenges to the practical application of an electrocatalyst to lower CO_2 emissions.[252,253]

MOFs were originally applied as electrocatalysts for CO_2RR in 2012;[254,255] the copper rubeanate MOF (CR-MOF) had shown enhanced CO_2RR performance. Since the CO_2RR occurs at a complicated three-phase interface between liquid electrolyte gaseous CO_2 solid catalyst. The primary crucial steps of the electrocatalytic processes are CO_2 activation, surface reaction, and product desorption processes comprising (1) electron transfer, (2) mass diffusion, and (3) electrochemical reaction on the surface *via* three-phase interface. These three elements define the whole basis of the resulting catalytic activity; they are summed under the name ''proficiency of active sites''. MOFs offer a wide range of possibilities in creating varied catalytic materials with many benefits, especially after electrochemical/thermal breakdown/pyrolysis, including (i) high mass transfer and availability of active sites, (ii) controls the electronic

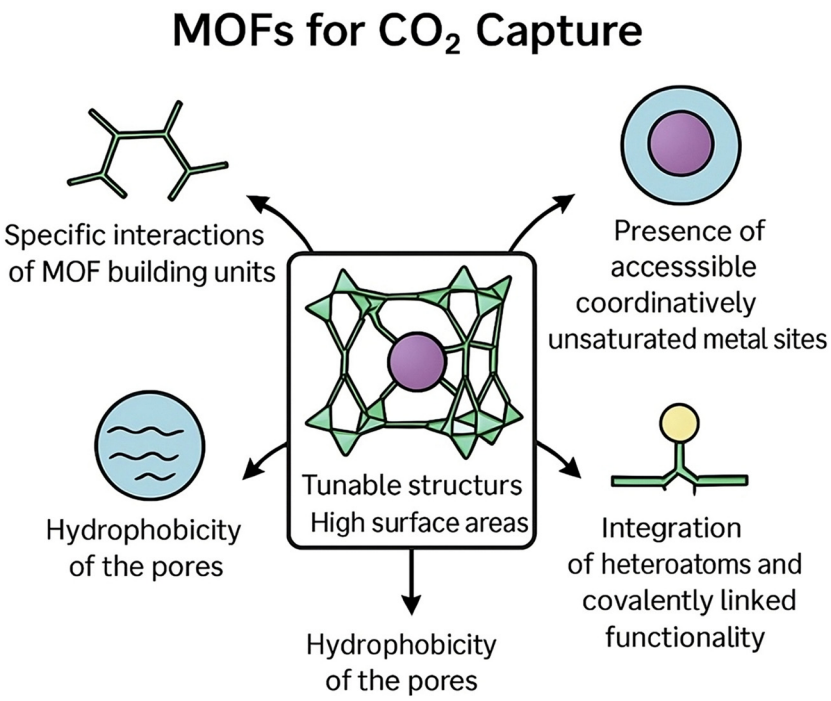

Fig. 45 Main strategies involved in the CO_2 capture by MOF.

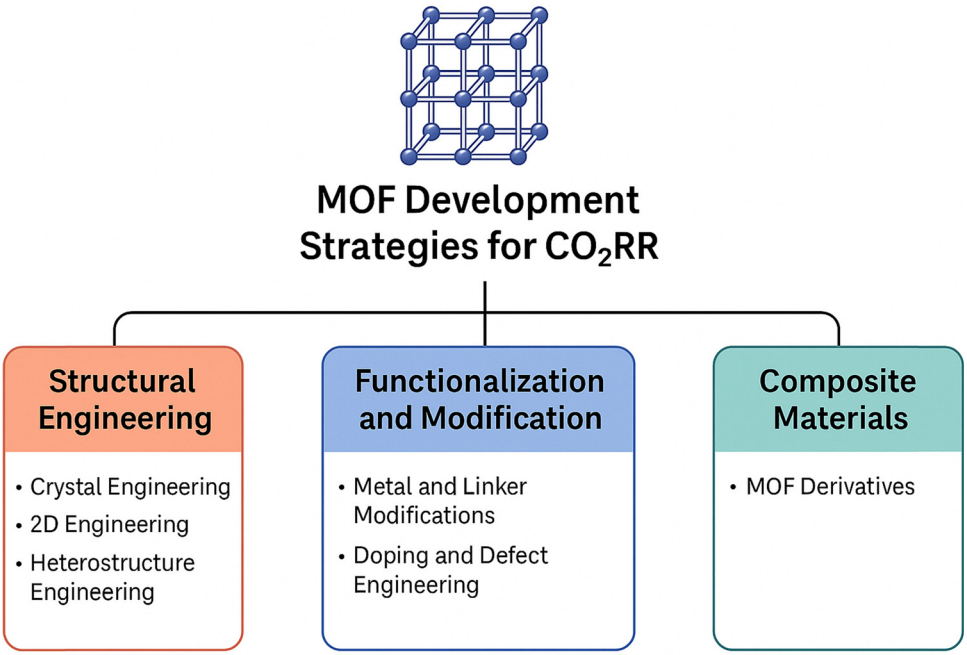

Fig. 46 A summary of MOF's development strategies for CO_2RR.

structure by simple heteroatom doping, and (iii) inherits the features of the pristine-MOFs. Consequently, MOF-based porous materials with the above-described properties are quite interesting candidates for CO_2 electrocatalysis. Due to their highly adjustable architectures, vast surface areas, and variety of chemical functions, MOFs have become very adaptable platforms for the electrochemical reduction of carbon dioxide (CO_2RR). Nevertheless, inherent difficulties including low electrical conductivity and restricted active site accessibility have prompted the creation of a number of engineering techniques to improve their catalytic effectiveness. The efficiency of CO_2 conversion has been increased by structural engineering techniques, summarized in (Fig. 46), including crystal engineering to maximize electron transport, two-dimensional (2D) engineering to enhance surface exposure, and heterostructure formation to integrate MOFs with conductive or catalytically active materials.[256] The modification of MOF's metal centers and organic linkers substitution significantly enhances the CO_2RR selectivity and stability.[257,258] Defect engineering and heteroatom doping can also improve overall reaction kinetics by introducing additional catalytically active sites and adjusting the electronic characteristics.[259] Their use in CO_2RR applications is further supported by the improved durability and charge transfer provided by MOF-based composites and derivatives, such as MOF-derived porous carbons or hybrids with conductive supports.[260] There are comprehensive reviews discussing the utilization of MOFs and their derivatives in CO_2RR, which is not the focus of this review.[261–263]

3. MOF for integrated CO_2 capture and conversion

Most of the CO_2 electroreduction systems operate using concentrated CO_2, which requires numerous energy to separate from N_2 (CO_2 purification cost per ton is \$70–100).[264] Utilizing MOFs in integrating CO_2 capture and electrochemical conversion can eliminate the need for having capture and conversion in separated unites, which offers a highly efficient and scalable approach to carbon utilization.[265] The precise engineering of MOF's porous structure and the organic linker with specific functional groups facilitates CO_2 adsorption. MOFs can possess Lewis acidic metal sites, basic nitrogen-rich functionalities, and π-electron-rich surfaces, which enhance CO_2 affinity, allowing CO_2 capture from mixed gases even under low partial pressures.[266–270] The fixability of MOFs construction allows for the incorporation of electroactive metal centers (Cu, Fe, Co, or Ni) for CO_2RR.[271] Once CO_2 is captured, multi-electron reduction take place and valuable carbon product can be produced over the MOF's electrocatalytically active sites. It is worth noting that dispersing these electroactive metal centers within MOF matrix offers higher utilization efficiency and can insure agglomeration prevention.[243] Although MOFs are electrochemically inactive and considered insulating materials, several strategies can be employed to make them conductive. For instance, using conductive linkers, redox-active centers incorporation, or synthesizing them with conductive materials (*e.g.*, carbon nanotubes, graphene, or metal nanoparticles) considerably boost electron transport.[271] Pyrolyzing MOFs is another approach that can result in conductive metal–nitrogen–carbon structure and maintaining the original framework properties such as the high surface area and the hierarchical porosity. Furthermore, MOF's high porosity can overcome CO_2 and electrolyte diffusion limitations and enhance the kinetics of the reaction. The morphology control of MOFs in the form of nanosheets or core–shell structures enables charge transfer and electrolyte accessibility optimisation. Another important key

determining factor for product selectivity is the ability of MOFs to stabilize reaction intermediates by modifying the electronic environments. By modifying the ligand environment or introducing co-catalysts, researchers can further steer reaction pathways to favor specific reduction products.[243] Here we will discuss how MOFs were utilized in CO_2 capture and conversion process.

Liu *et al.* 2023[272] engineered gas diffusion electrodes (GDEs) consisting of a series of silver cluster-based MOFs intended for the concurrent capture and reduction of CO_2 to carbon monoxide (CO) from simulated flue gas containing 15% CO_2 in nitrogen. The MOFs employed in this research possess amine groups, acknowledged for their capacity to absorb and concentrate CO_2 from simulated flue gases in humid environments (Fig. 47a). These frameworks demonstrate significant porosity, allowing for efficient CO_2 capture, while the silver clusters inside the MOFs promote the electrochemical reduction of the captured CO_2 to CO. The CO_2/N_2 adsorption selectivity of Ag-MOF, Ag-MOF-CH_3, and Ag-MOF-NH_2 were 67, 42, and 280 at 298 K, respectively (Fig. 47b). When using NH2-MOF with pure CO_2, the catalyst achieved a CO partial current density of 380 mA cm^{-2} and dropped slightly to 355 mA cm^{-2} despite an 85% decrease in CO_2 concentration (Fig. 47c). In contrast, limited retention of 44% and 37% was observed on Ag-MOF and Ag-MOF-CH_3, respectively. The findings indicated that the faradaic efficiency (FE) for CO production and the CO partial current density were markedly affected by the presence of amine groups when utilizing flue gas as the feedstock. When the CO_2 concentration reduced from 15% to 5%, the eCO_2RR performance decreased significantly, and the minimum CO_2 concentration that didn't influence the performance of the 1-NH_2 significantly was 10%. The performance metrics obtained with flue gas were analogous to those recorded under pure CO_2 circumstances, highlighting the essential function of amine groups in improving CO_2 capture efficiency. It is worth noting that the continuous operating time of 1-NH_2 is much longer than that of the materials reported to date (<100 hours).

Embedding MOFs into mixed matrix membranes (MMMs) is a promising approach for enhancing their stability and been intensively utilized in CO_2 capturing. Al-Attas *et al.*, 2023 reported a permselective MOF-GDL (PGDE):[273] an innovative method for CO_2 conversion from quasi-flue gas utilizing a permselective gas diffusion electrode (PGDE). This novel design combines a metal–organic framework (MOF)-based mixed matrix membrane (MMM) with a silver electrocatalyst, facilitating selective CO_2 penetration and its conversion into carbon monoxide (CO) with high efficiency (Fig. 47d). The MMM integrates CALF-20, a metal–organic framework recognized for its capacity for CO_2 physisorption in humid gas streams. This concept seeks to improve CO_2 selectivity while preserving mechanical stability in industrial environments. The PGDE is designed with the MMM on the gas diffusion side of a porous PTFE electrode, which selectively permits CO_2 to permeate while restricting the passage of other gases such as N_2 and O_2. CO_2 diffuses through the membrane by concentration gradient. CALF-20 exhibited more than 4.5 times higher uptake for CO_2 (3.97 mmol g^{-1}) as compared to N_2 and O_2 at 298 K and 1 bar based on the CO_2 physisorption isotherm and low adsorption affinity toward the CO_2R (CO) target product of this study. When a mixed gas of 10% CO_2 balanced with N_2 permeated through the PGDE, it showed 1.1 × 10^6 gas permeation units (GPUs) with selectivity of 2.1 for CO_2/N_2. That is confirmed by the remarkable drop of N_2 partial pressure across

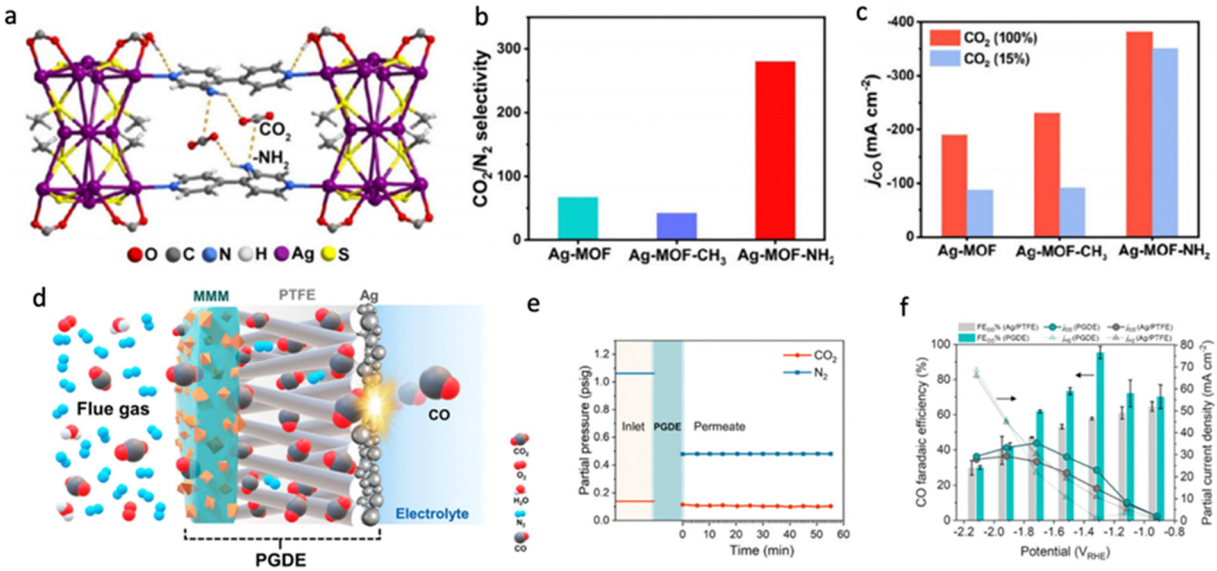

Fig. 47 (a) Schematic illustration of the interaction between the Ag-MOF-NH_2 catalyst and the CO_2 molecule. (b) CO_2/N_2 selectivity from CO_2/N_2 adsorption for different catalysts. (c) Comparison of the CO partial current density for different catalysts in pure CO_2 and 15% CO_2. Reprinted (adapted) from *Angew. Chem., Int. Ed.* 2023, **62**, e202311265. Copyrights © 2023 Wiley-VCH GmbH. (d) Schematic diagram of CO_2 capture and conversion through MOF permselective gas diffusion electrode (PGDE). (e) CO_2 permeation through PGDE (7 mg cm^{-2} CALF-20 in the MMM layer), and (f) faradaic efficiency of CO and partial current density for CO and H_2 obtained at different applied potentials on the Ag/PTFE and PGDE (7 mg cm^{-2} CALF-20 in the MMM layer). Reprinted (adapted) from *ACS Energy Lett.* 2023, **8**(1) 107–115. Copyright © 2022 American Chemical Society.

the PGDE from 1.06 to ~0.48 psig while CO_2 partial pressure only decreased ~0.03 psig (Fig. 47e). The PGDE attained an impressive CO FE of 95% in the conversion of N_2-diluted CO_2 streams compared to 58% for the Ag/PTFE at −1.32 (Fig. 47f). The ideal loading of CALF-20 in the MMM was determined to be 7 mg cm^{-2}, which optimized efficiency and inhibited pore obstruction. The PGDE exhibited resilience to the introduction of O_2, sustaining 84% of its performance and displaying minimal impact from the wetness of the gas stream. However, the MMM's propensity for water absorption may result in the degradation of CO_2-selective binding sites, a crucial factor for sustained operation, which was revealed while testing the stability. Also, the high overpotential applied means more energy is needed per mole of CO produced, hindering their scalability.

Zhang *et al.*, 2018[274] introduced $Cu_3(BTC)_2$ (Cu-MOF) into a carbon paper-based gas diffusion electrode (GDE) as a CO_2 capturer, mixed with copper nanoparticles serving as the active catalyst. The CO_2 adsorption capacity of Cu-MOF was quantified at 1.8 mmol g^{-1}, signifying moderate efficacy in augmenting local CO_2 concentration at the catalyst interface. The GDE was altered by 10 weight percent. Cu-MOF exhibited enhanced catalytic activity for CO_2 reduction, achieving faradaic efficiencies for methane production that were 2–3 times greater than those of GDEs lacking Cu-MOF. The incorporation of Cu-MOF markedly inhibited the competitive hydrogen evolution process (HER), diminishing its faradaic efficiency to 30%. The study elucidates two opposing effects of Cu-MOF in the CO_2 reduction reaction: an insulating effect that may impede electron transfer to Cu active sites and an augmentation of CO_2 concentration at the electrode–electrolyte interface, which promotes the reaction. The interaction between these factors ultimately determines the reaction rate and product selectivity. Although CH_4 FE was enhanced by introducing Cu-MOF compared to the blank, the maximum FE was moderate (17%), with the optimum Cu-MOF content relative to the theoretical maximum, and a significant portion of the current was directed to HER (30%), especially at higher overpotentials. Moreover, the Cu-MOF structure showed stability issues when used for 24 h due to hydrolysis or phase transformation in aqueous solution.

Selectivity is one of the main challenges in CO_2RR, especially towards C_{2+} products, given their high benefit-to-cost ratio.[275] The electrochemical reduction of CO_2 (CO_2RR) to ethylene (C_2H_4) is a viable approach for sustainable chemical synthesis. Nonetheless, attaining industrially significant productivity (>200 mA cm^{-2}) and energy efficiency (>50%) poses challenges due to the solubility constraints of CO_2 in aqueous electrolytes and the occurrence of competing side reactions. Nam *et al.*, 2022[276] developed MOF-augmented gas diffusion electrodes (MOF-GDEs) to increase local CO_2 availability in proximity to catalytically active copper sites, therefore improving CO_2RR selectivity and rate. The hierarchical electrode structure comprises a hydrophobic polytetrafluoroethylene (PTFE) substrate, a metal–organic framework (MOF) interlayer, and a sputtered copper catalyst (Fig. 48a). Two metal–organic frameworks, HKUST-1 and SIFSIX-3-Cu, with differing

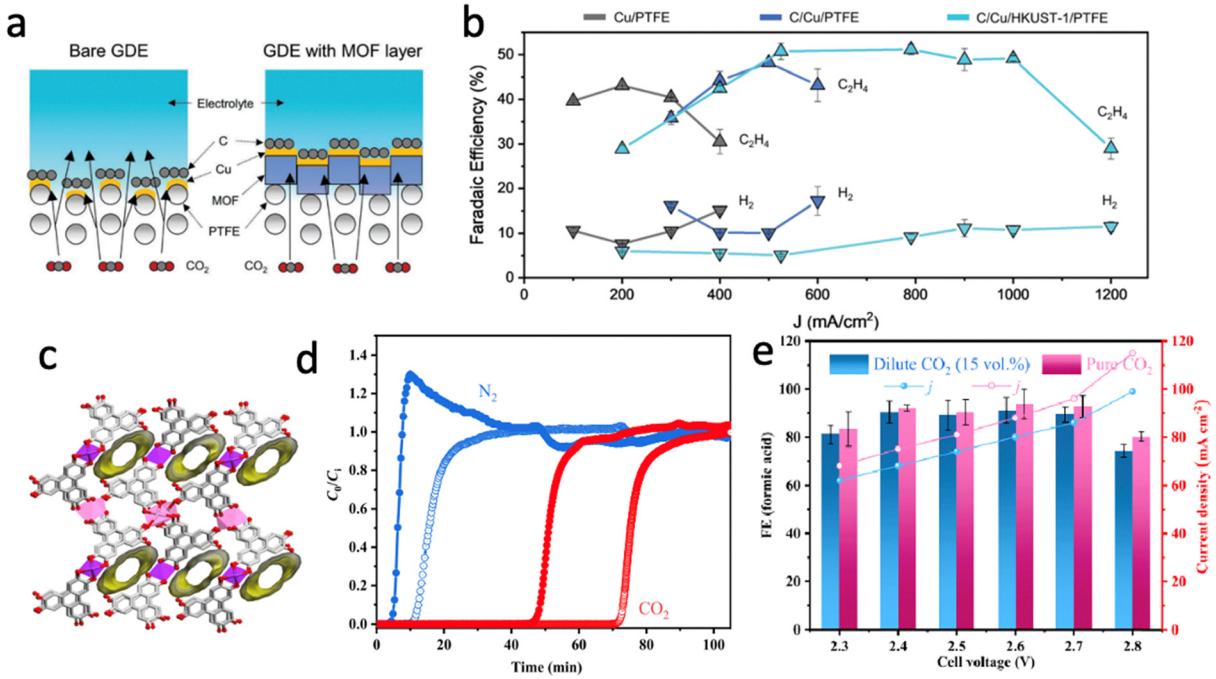

Fig. 48 (a) Cross-sectional schematic diagram of bare GDE (Cu/PTFE) and MOF-augmented GDE (Cu/MOF/PTFE) during CO_2RR in the flow cell. (b) Electrochemical CO_2RR of MOF-augmented GDE in the flow cell. Reprinted (adapted) from *Adv. Mater.* 2022, **34**, 2207088. Copyrights © 2022 Wiley-VCH GmbH. (c) 3D π−π stacking structure of Bi-HHTP with 1D pores along the *b*-axis direction. (d) Breakthrough curves for a 15 : 85 CO_2/N_2 (v/v) mixture with 0% (open) and 40% relative humidity (solid) at 298 K and 1 bar. Ci and C0 are the concentrations of each gas at the inlet and outlet, respectively. (e) (FEs) formic acid and current densities under different cell voltages in high-purity CO_2 and dilute CO_2 (15 vol%, CO_2/N_2 = 15 : 85, v/v) atmospheres, respectively. Reprinted (adapted) from *J. Am. Chem. Soc.* 2024, **146**(20), 14349–14356. Copyright © 2024 American Chemical Society.

CO_2 adsorption capabilities, were evaluated for their efficacy in enhancing CO_2 concentration at the catalyst interface. The MOF-enhanced GDEs exhibited significant enhancements in ethylene production. In flow cell systems, MOF-modified electrodes attained a faradaic efficiency (FE) of 49% for ethylene at a current density of 1 A cm^{-2}, surpassing traditional Cu/PTFE electrodes (Fig. 48b). The elevated local CO_2 concentration enhanced CO_2 adsorption and inhibited the hydrogen evolution reaction (HER), hence augmenting C_{2+} selectivity. The notion was further corroborated in zero-gap MEA electrolyzers, where MOF films situated on Cu electrodes markedly improved ethylene output. A peak ethylene partial current density (J C_2H_4) of 220 mA cm^{-2} was attained, representing a 2.7-fold enhancement compared to unmodified GDEs. Furthermore, for the carbon monoxide reduction reaction (CORR), the MOF-enhanced GDEs exhibited a 15-fold increase in ethylene production rate compared with bare Cu/PTFE electrodes, underscoring the significant impact of CO_2 enrichment in high-current-density operations. The X-ray absorption spectroscopy (XAS) indicated that the MOF layers experienced structural alterations under electrochemical circumstances, resulting in the creation of organic-metal interfaces that enhanced CO_2 adsorption and reaction kinetics. The electrodes' stability was evidenced after 65 hours of uninterrupted operation, sustaining ethylene selectivity above 50%. The results underscore the necessity of enhancing MOF characteristics, such as porosity, CO_2 adsorption capacity, and hydrophobicity, to optimize electrocatalytic efficacy. The MOF-augmented GDEs maintain $>50\%$ FE for ethylene over 65 hours at industrially relevant current densities, with total C_{2+} product FE above 70% for 59 hours. Although the system achieves high current densities and good selectivity, the cell voltages required (up to -4.2 V in MEA mode) are relatively high, implying significant energy input per mole of product.[277]

Zhao *et al.*, 2024[278] reported a groundbreaking approach for the integrated capture and eCO_2RR of dilute CO_2 (15 vol%, mimicking flue gas) into 100% pure aqueous formic acid with 90% FE, addressing two challenges in CO_2 utilization; (i) the need for high-purity CO_2 as a feedstock and (ii) the separation of liquid products after the reaction. A conductive bismuth-based-MOF, Bi-HHTP (where HHTP = 2,3,6,7,10,11-hexahydroxytriphenylene), was utilized and served as a CO_2 adsorbent and as an electrocatalyst. The Bi-HHTP possesses a microstructure π-conjugated framework with one-dimensional (1D) zigzag chains of distorted tetrahedral and pentahedral BiO_4 nodes, interconnected through π–π stacking to form a 3D architecture (Fig. 48c), which enable a high CO_2 selectivity and uptake (23.6 cm^3 g^{-1} = 1.05 mmol g^{-1} at 298 K, CO_2/N_2 selectivity ~91), under humid conditions (40% RH) (Fig. 48d), which is critical for industrial applications. The adsorption mechanism involves electrostatic interaction, hydrogen bonding and metal coordination, resulting in strong binding between CO_2 and Bi-HHTP. It was found that H_2O binds well to Bi-HHTP, forming hydrogen bonds, competing slightly with CO_2, yet adsorbed H_2O provides protons supporting the eCO_2RR. Formic acid FE was slightly lower in dilute CO_2 (CO_2/N_2 = 15 : 85, v/v) than in a high-purity CO_2 atmosphere, with maximum values of 91% and 93% at 2.6 V, respectively (Fig. 48e). The formation of *OCHO intermediate* was confirmed by *Operando* ATR-FTIR spectroscopy, which is a key intermediate for formic acid formation. The DFT showed Bi-HHTP requires less energy (ΔG = 0.31 eV) to carry out the rate-determining step in the process compared to other bismuth-based catalysts like metallic Bi or Bi_2CO_5. The OCHO binds to Bi-HHTP just strongly enough (ΔE = −0.22 eV) to react efficiently, without poisoning the surface or releasing too early. The Technoeconomic analysis estimates a production cost ($0.74 per kg), highlighting commercial feasibility. Further examples of MOF-based materials for integrated CO_2 capture and conversion are summarized in (Table 15).

Generally, when designing an adsorbent layer on a GDE, it is crucial to create robust adsorbents with elevated CO_2 adsorption capacity and selectivity, while also considering factors such as kinetic rate, active porosity, surface area for adsorption, and resistance to moisture and contaminants.

The electrochemical stability of metal–organic frameworks (MOFs) is a critical factor determining their applicability in electrocatalytic systems. During electrochemical operation, the applied potential drives the migration of ionic species from the electrolyte toward the MOF surface, leading to the formation of an electrical double layer.[279] The accumulation of charge at this interface generates pronounced local ion concentration gradients, particularly involving protons or hydroxide ions, which can cause substantial deviations of the interfacial pH from that of the bulk electrolyte. Such localized pH fluctuations impose chemical stress on both the metal nodes and organic linkers, often resulting in partial or complete structural degradation of the framework.[280,281] This instability is especially problematic under neutral and strongly alkaline conditions, where many MOFs are inherently susceptible to hydrolysis or ligand displacement. As a result, achieving durable performance in these media remains a key challenge for MOF-based catalysts in the CO_2 electroreduction reaction (CO_2RR). Moreover, repeated potential cycling further accelerates degradation by continuously reshaping cationic and anionic distributions at the electrochemical interface. These dynamic chemical gradients can promote metal leaching and coordination bond cleavage, ultimately driving the *in situ* conversion of MOFs into metal oxides, hydroxides, or oxyhydroxides during prolonged electrocatalytic operation.[279,282]

Achieving concurrent chemical, structural, and electrochemical robustness in metal–organic frameworks (MOFs) under operating electrocatalytic conditions remains intrinsically challenging, as strategies that enhance stability (*e.g.*, stronger metal–ligand bonds, increased hydrophobicity) often compromise properties such as electronic conductivity, porosity, or active-site accessibility. Over roughly the past decade, sustained progress in linker design, node selection, and composite engineering has nevertheless enabled significant improvements in MOF durability under electrochemical CO_2 reduction (CO_2RR) conditions, particularly in aqueous and humid environments. Despite these advances, a central question persists regarding the true nature of the catalytically active phase: in many reported systems, it remains ambiguous whether the pristine

Table 15 MOF-based materials for integrated CO_2 capture and conversion

Material	Composition and structure	CO_2 adsorption capacity	Faradaic efficiency (FE)	Key findings	Ref.
Cu-MOF-GDE	Cu_3(BTC) 2 (Cu-MOF) incorporated into carbon paper-based gas diffusion electrode with copper nanoparticles	1.8 mmol g^{-1}	CH_4 FE increased 2–3× with Cu-MOF (~20%); HER FE reduced to 30%	Cu-MOF enhances local CO_2 concentration at the catalyst interface	274
Permselective MOF-GDL (PGDE)	CALF-20 MOF-based mixed matrix membrane (MMM) combined with silver electrocatalyst	CALF-20 exhibited 4.5 times higher uptake for CO_2 (3.97 mmol g^{-1}) as compared to N_2 and O_2 at 298 K and 1 bar. The PGDE showed 1.1 × 10^6 gas permeation units (GPUs) with a CO_2/N_2 selectivity of 2.1 for a mixed gas stream of ~ 10% CO_2 and N_2 balance	CO FE up to 95%	The MMM selectively allows CO_2 permeation while restricting other gases. The weak binding of CO_2 coupled with the specific pore structure minimizes CO_2 chemisorption	273
MOF-functionalized GDE	HKUST-1 and SIFSIX-3-Cu MOFs as interlayers on hydrophobic PTFE substrate with sputtered copper catalyst	SIFSIX-3-Cu showed higher CO_2 affinity (2.4 mmol g^{-1} *vs.* 0.3 mmol g^{-1} for HKUST-1) and better stability at lower mass loading	C_2H_4 FE up to 49% at 1 A cm^{-2} in flow cell (2.7-fold compared to bare Cu/PTFE electrodes), 52% for C_2H_4 in MEA, in CORR, the modified GDE demonstrated a 15-fold increase in ethylene production	MOF layers increase local CO_2 concentration, enhancing ethylene production and suppressing hydrogen evolution	276
Ag_{12} cluster-MOF-GDE	Silver cluster-based MOFs with amine function groups	1-NH_2 MOF exhibited a CO_2 uptake of 0.90 mmol cm^{-3} (≈ 9 mmol g^{-1})	CO FE ~96.4% under simulated flue gas (CO_2/N_2 = 15 : 85) at 120 mAcm2 ~96.3–97.3% under pure CO_2	Amine-functionalized MOFs enhance CO_2 capture from flue gas, with silver clusters promoting electrochemical reduction to CO. Performance under flue gas conditions is comparable to pure CO_2	272
Bi-HHTP-MOF	Bismuth-based-MOF, Bi-HHTP (HHTP = 2,3,6,7,10,11-hexahydroxytriphenylene)	1.05 mmol g^{-1} at 298 K	100% pure aqueous formic acid with 90% FE	Conductive Bi-HHTP acts both as a CO_2 adsorbent and an electrocatalyst	278

MOF operates as the genuine electrocatalyst, or whether the framework instead serves as a sacrificial or pre-catalyst that reconstructs into metal oxides, hydroxides, oxyhydroxides, or other derived phases under applied bias. Resolving this ambiguity requires rigorous *operando* or *in situ* characterization, such as X-ray absorption spectroscopy, X-ray diffraction, vibrational spectroscopy, and electron microscopy, combined with systematic post-reaction structural and compositional analyses to verify chemical integrity, crystallinity, and metal speciation after prolonged electrolysis. Such mechanistic insight is essential for the rational design of MOF-based architectures that can sustain CO_2RR over technologically relevant timescales.[282,283]

During electrochemical operation, MOFs are subjected to a complex and dynamic reaction environment that includes liquid water, electrolyte cations and anions, dissolved reactants and products, interfacial electric fields, and continuous electron and ion fluxes. Among these factors, water frequently plays a primary role in triggering degradation, as it can coordinate to metal nodes and promote competitive ligand exchange or hydrolysis of coordination bonds, ultimately yielding hydrated or hydroxylated metal species in alkaline media and protonated or partially detached organic linkers in acidic media.[282,283] These processes often lead to partial or complete leaching of metal centers and ligands into the electrolyte, progressively eroding the long-range order of the framework. In parallel, specific electrolyte anions can substantially accelerate degradation pathways: strongly coordinating species such as phosphate, carbonate, or sulfate may outcompete the MOF linker for binding to high-valence metal centers, thereby destabilizing the metal–ligand coordination network. Zirconium-based carboxylate frameworks, which are otherwise chemically robust, have been reported to undergo rapid degradationin phosphate-containing electrolytes, where strong Zr–phosphate interactions drive fast deterioration of the Zr_6-oxo clusters and loss of crystallinity on experimentally relevant timescales.[284,285]

Framework instability under electrochemical conditions is not confined to carboxylate-based MOFs. Zeolitic imidazolate frameworks (ZIFs), despite their topological analogy to zeolites and relatively strong metal–imidazolate bonds, can also undergo structural transformation or collapse under CO_2RR- or ORR-relevant potentials, particularly in electrolytes containing additional metal cations. Ion-exchange processes at the node, followed by nucleation and growth of metal (oxy)hydroxide phases, have been widely observed, frequently leading to the formation of mixed-metal hydroxide or oxide nanostructures at the expense of the original framework.[286] Beyond purely chemical degradation, reaction-derived products impose additional mechanical and chemical stress on MOFs: gas-evolving reactions often generate nanoscale bubbles at or within the porous structure, imposing localized pressure and shear that can induce cracking, delamination, or fragmentation of MOF crystallites. Furthermore, soluble products or intermediates from CO_2RR (*e.g.*, formate, carbonate, or multicarbon species) may coordinate to metal nodes or interact strongly with linkers, promoting further reorganization or dissolution of the framework over extended operation.[287,288]

The intrinsic susceptibility of many MOFs to humidity and aqueous environments commonly manifests as rapid performance degradation, especially in neutral and alkaline media, where moisture-mediated attack on metal centers and linkers leads to decomposition or phase transformation. In this context, metal–ligand bond strength has emerged as a key design parameter governing MOF stability under electrochemical conditions. Stronger coordination interactions generally correlate with enhanced resistance to hydrolysis, ligand displacement, and nucleophilic attack. Guided by this principle, stability is often improved by employing high-valent, hard metal centers and appropriately matched ligands. Frameworks constructed from hard, high-charge-density metal ions—such as Zr^{4+}, Cr^{3+}, Al^{3+}, and Fe^{3+} paired with oxygen-donor carboxylate ligands typically display superior chemical robustness, in line with Hard–Soft Acid–Base (HSAB) considerations. These strong metal–oxygen bonds not only increase resistance to hydrolysis and ligand loss in aqueous and humid environments but can also impart persistence under moderately acidic conditions, particularly when the carboxylate linkers possess low pK_a values and form highly stable coordination clusters (*e.g.*, $Zr_6O_4(OH)_4$ nodes in UiO-type frameworks).[289–292] Collectively, these design concepts underpin ongoing efforts to develop MOF-based electrocatalysts that combine structural integrity, chemical resilience, and sustained activity for CO_2 electroreduction.

4. Future outlook of MOF

Despite these advances in utilizing MOFs in integrated CO_2 capture and conversion, several encounters still need to overcome to address their practical application. Some of these challenges are long-term stability under electrochemical conditions, the large-scale production of MOF, and developing conductive MOFs at a reduced cost. Recent advances in synthesis techniques, including microwave-assisted and mechanochemical methods, are addressing these issues by enabling faster, more cost-effective production of robust MOFs.[293] Another determining factor is the faradaic efficiency and current densities that requires further improvement to meet industrial-scale necessities. Nonetheless, continued advancements in MOF design, hybridization strategies, and *in situ* characterization techniques hold great promise for optimizing MOFs as next generation electrocatalysts for sustainable CO_2 capture and conversion.

Metal oxides

A series of amine-functionalized SnO_x nanoparticles were developed by[294] demonstrating an interesting strategy for CO_2 capturing from simulated flue gas (15% CO_2, 8% O_2, 77% N_2) and selective conversion to formate spontaneously; a general concept has been illustrated in (Fig. 49).

DEA–SnO_x/C was synthesized by a one-pot hydrothermal reaction of carbon black, $SnCl_2$, and DEA in ethanol, as shown in (Fig. 50a). The dual-function catalyst developed *via* grafting alkanolamines such as diethanolamine (DEA) onto SnO_x surfaces (DEA–SnO_x/C) that augments local CO_2 concentration *via* Lewis base interactions while also tailoring reaction selectivity toward formate. DEA–SnO_x/C exhibited significantly higher CO_2 adsorption capacity than the non-functionalized SnO_x (SnO_x/C) (Fig. 50b), indicating the strong interaction between DEA and CO_2. This combined with the enhanced hydrophobicity and suppression of side reactions resulted in a standout performance of 84.2%

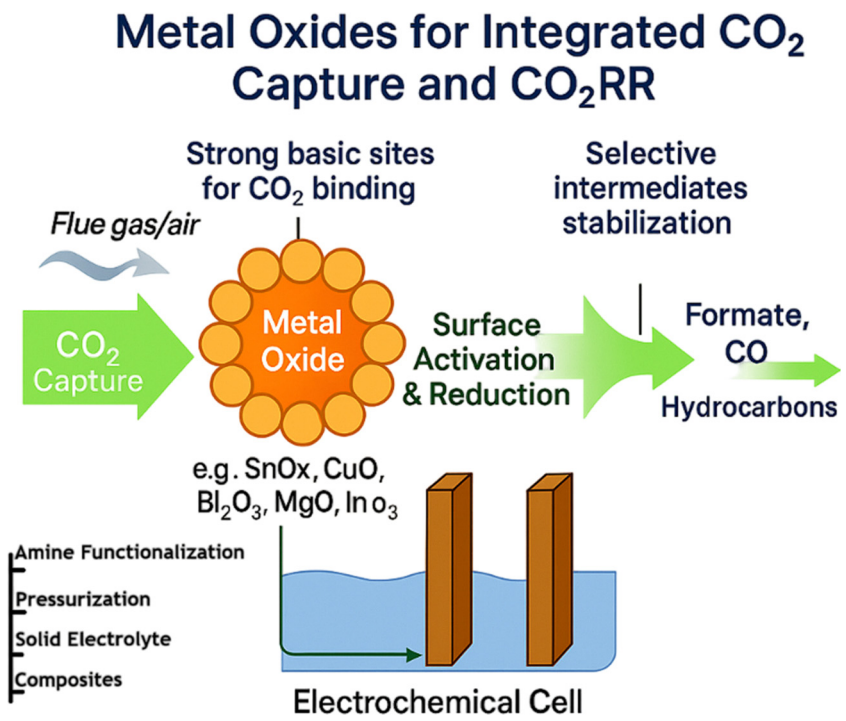

Fig. 49 Graphical abstract of metal oxides for integrated CO_2 capture and electrocatalytic conversion.

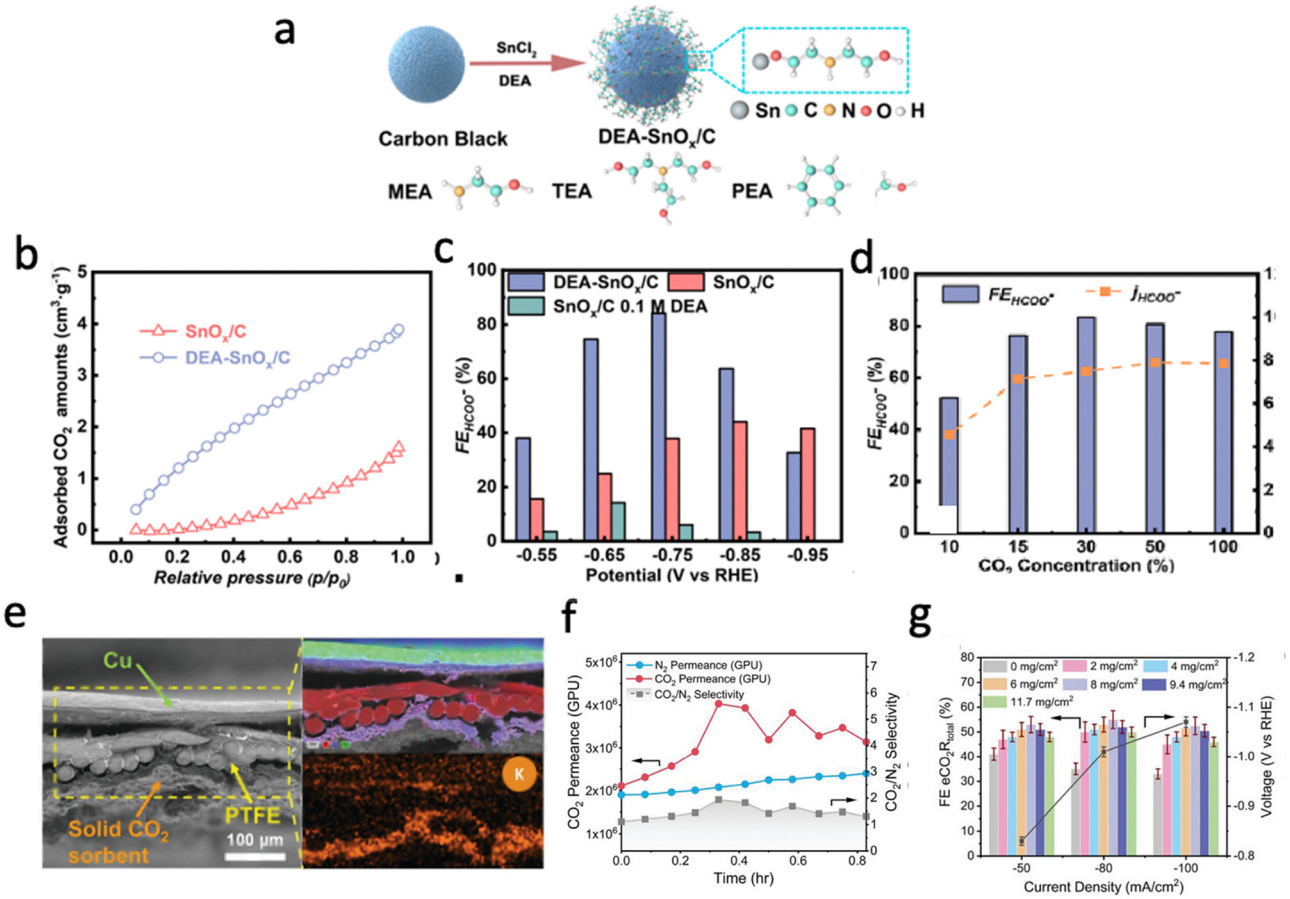

Fig. 50 (a) Fabrication of DEA–SnO_x/C and structures of alkanolamines. (b) CO_2 adsorption isotherms of SnO_x/C and DEA–SnO_x/C (b). $FEHCOO^-$. (c) $jHCOO^-$ of the above samples in 0.5 M $KHCO_3$ electrolyte under SFG (glassy carbon, 0.071 cm^2). (d) $FEHCOO^-$ and jHCOO at −0.75 V *vs.* RHE of DEA–SnO_x/C using different concentrations of CO_2 (0.5 M $KHCO_3$, glassy carbon, −0.071 cm^2). Reprinted (adapted) from *ACS Energy Lett.* 2021, **6**(9), 3352–3358. Copyright © 2021, American Chemical Society. (e) SEM image showing the cross section of the integrated BGDE with both HPC and polycrystalline copper while energy dispersive X-ray spectroscopy (EDX) mapping reveals the presence of C, F, Cu, and K (from synthesis). The copper layer may appear to be thicker than 300 nm owing to handmade sectioning by the razor blade. (f) Mixed gas CO_2 permeance and CO_2/N_2 selectivity for *in situ* configuration (BGDE with Cu/HPC). (g) Operating conditions: CO_2 flow = 10 cm^3 (STP) min^{-1}, N_2 flow = 90 cm^3 (STP) min^{-1}, feed pressure = 1.0 psig (1.07 atm), HPC loading = 8 mg cm^{-2}. Optimization of sorbent loading for maximum eCO_2R product formation at P_{CO_2} = 0.1 atm. (c) eCO_2R product distribution at P_{CO_2} = 0.1 atm and sorbent loading of 8 mg cm^{-2}. Reprinted (adapted) from *Adv. Mater.* 2023, **35**(24), 2300389. Copyrights © 2023 The Authors. Published by Wiley-VCH GmbH under the terms of CC-BY license.

faradaic efficiency for formate at −0.75 V *vs.* RHE (Fig. 50c). The DEA–SnO_x/C can operate at low CO_2 concentration (10%) and FE_{hcoo^-} reaching over 80% (CO_2 = 30%) whereas the jHCOO peaked when the concentration was 50% reaching 7.9 mA cm^{-2} (Fig. 50d). Despite this notable selectivity performance, the formate jHCOO of 6.7 mA cm^{-2} is below industrially relevant benchmarks (≥100 mA cm^{-2}). Furthermore, the degradation of amine groups limited the catalyst's stability over a prolonged period, and the catalyst was evaluated in a static setup (single-compartment design) with a small electrode area (0.071 cm^2), not in continuous flow or gas diffusion configurations, limiting scalability.

A recent study by Nabil *et al.*[295] reported an integrated approach for the simultaneous capture and electrochemical conversion of CO_2 from dilute gas streams using a bifunctional gas diffusion electrode (BGDE). A high-density polyethylene-derived porous carbon (HPC) was employed as a physisorbent combined with polycrystalline copper as the electrocatalyst (Fig. 50e). The BGDE structure utilized a concentration gradient-driven desorption mechanism, which allows efficient CO_2 capture and release at low CO_2 concentration (~10 vol%), eliminating the need for energy-intensive regeneration steps commonly applied with traditional capture technologies. HPC permeance of CO_2 was as high as 4.0×10^6 GPU and a CO_2/N_2 selectivity of ≈1.3. When testing the CO_2RR without sorbent (HPC) the total selectivity for eCO_2R products with partial pressure P_{CO_2} = 0.1 atm (10% $CO_2$90% N_2) ranged from 33% to 41% depending on the voltage and current density, while with the sorbent (HPC = 8 mg cm^{-2}) it increased by about 20% (Fig. 50f). However, lower selectivity resulted with higher HPC loading due to the blocking PTFE pores during airbrushing and thus deterring CO_2 diffusion (Fig. 50g). Notably, the BGDE maintained its performance under humid environments, due to the hydrophobic and CO_2-selective characteristic of carbonaceous HPC. Based on molecular dynamics

simulations and gas permeance studies, the high CO_2/N_2 selectivity ($\approx$1.3) is emphasized, caused by the molecular sieving properties incorporated within the micropores of HPC, significantly boosting the CO_2 transport to the catalyst interface. The techno-economic study showed that this *in situ* system could dramatically diminish the minimum selling price of ethylene up to ~79% when compared to the decoupled capture and conversion method.

Yan *et al.* (2024)[296] developed a redox-mediated electrochemical platform for integrated CO_2 capture and utilization (eCCU) utilizing anthraquinone (AQ)-grafted polymer electrodes. The polymeric film, constructed from a polyacrylamide backbone, chemically binds CO_2 *via* reversible carbamate production when the AQ groups are in their oxidized (quinone) state. During electrochemical reduction, the AQ units emit CO_2 *in situ*, which subsequently diffuses to an adjacent Ag catalyst layer for electrochemical conversion. This electrochemical regeneration circumvents thermal desorption, functions at ambient settings, and facilitates fine redox-tunable control over capture and release. *In situ* ATR-FTIR and DFT analyses (Fig. 51a–d) validate the generation of CO_2-AQ adducts and their reversible conversion during potential cycling. The system exhibits stable multi-cycle functionality, preserving capture–release efficiency and CO_2 consumption without necessitating gas-phase CO_2 input or supplementary purification. The system achieves a faradaic efficiency of up to 82% for CO generation on the Ag catalyst under optimal electrochemical conditions. The platform provides a solvent-free, modular design that integrates capture and conversion inside a singular reactor architecture. The capture capacity is constrained by the loading and accessibility of AQ functional groups, and increasing the film thickness or redox density presents trade-offs with ion transport and conductivity. The reaction is presently limited to CO_2-to-CO conversion, constraining subsequent chemical flexibility. Future work may concentrate on broadening the platform to encompass multi-carbon product catalysts, augmenting the stability of AQ functions, and designing more conductive or porous film morphologies to enhance throughput and scalability. This redox-active electrode method represents a notable step towards low-energy, continuous electrochemical carbon capture and utilization systems, providing a framework for integrating CO_2 binding and conversion into a single electrochemical unit.

Xu *et al.* (2020)[297] attempted to use pressurization (10–15 bar) to enhance CO_2 mass transfer as a strategy to produce C_{2+} from simulated flue gas. This strategy enabled efficient C_{2+} production (91% FE, at 15 bar without O_2). The study showed that while pressurization enhances CO_2 availability and suppresses the hydrogen evolution reaction (HER), it also increases the oxygen reduction reaction (ORR), distracting most of the current towards ORR because of the lower thermodynamic and kinetic requirements for ORR compared to CO_2RR (Fig. 52a). To counteract this, the authors first tried mixed Nafion-bound carbon nanoparticles layer to stabilize CO_2RR which failed in O_2-containing CO_2 streams. They introduced a hydrophilic ionomer-TiO_2 catalyst layer on a Cu-based gas diffusion electrode that significantly slowed O_2 transport and maintained CO_2 accessibility (Fig. 52b). This design leverages the lower volatility of CO_2 compared to O_2, allowing selective gas transport through hydrated nanopores. The ionomer-TiO_2 structure stabilizes the Cu catalyst and reduces O_2

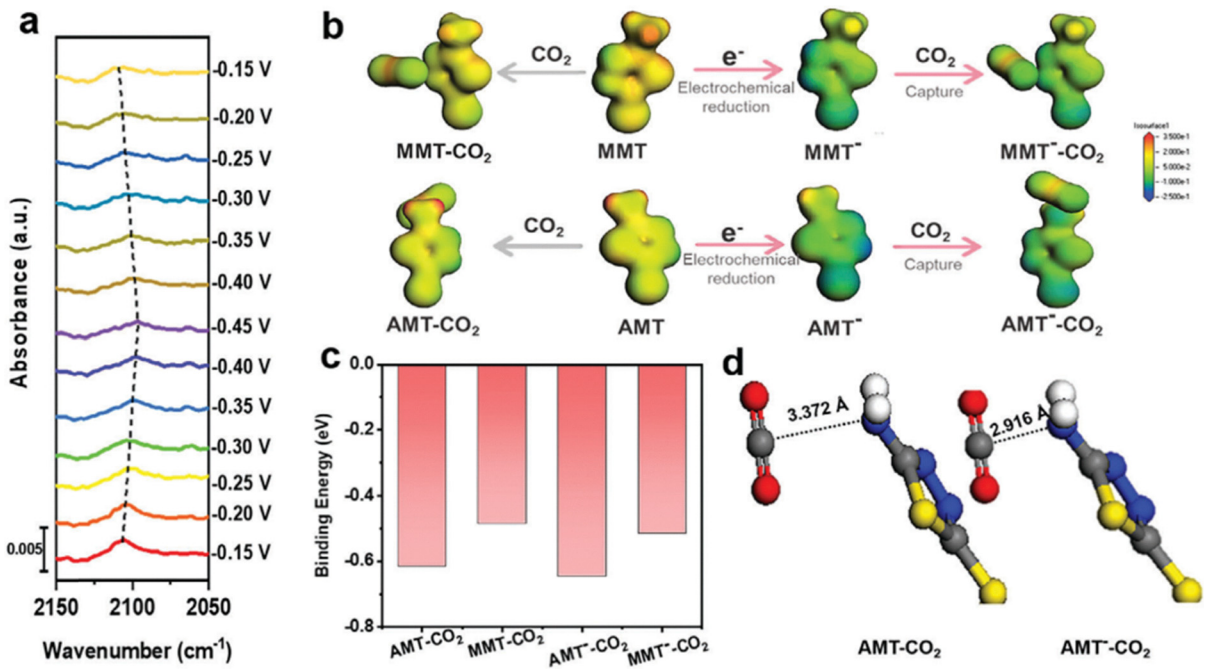

Fig. 51 (a) *In situ* IR spectra of AMT–Au at the different potential in 0.5 M $KHCO_3/H_2O$ electrolyte under SFG. (b) Electrostatic distribution mapping on the electron density surfaces. Blue indicates high electronegativity areas, and red indicates high positive charge areas. (c) The binding energy of capture CO_2. (d) The interaction distance of CO_2 with AMT and AMT^-. Reprinted (adapted) from *Adv. Funct. Mater.* 2024, **34**, 2311733. Copyrights © 2024 Wiley-VCH GmbH.

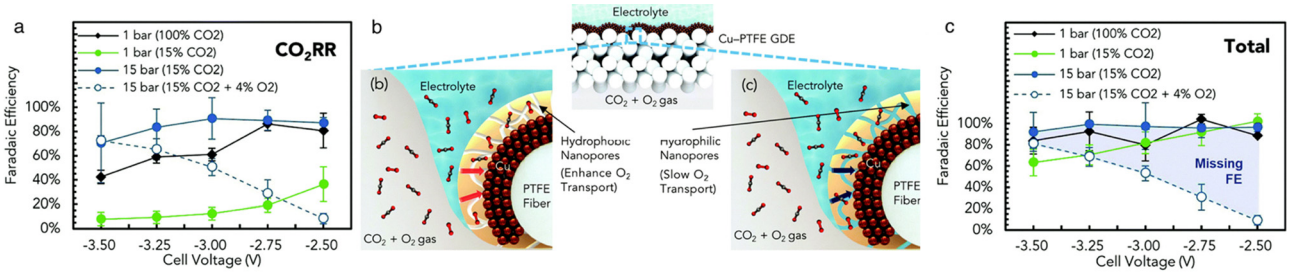

Fig. 52 (a) Effect of pressure and the presence of O_2 on product selectivity for CO_2RR with flue gas CO_2 concentrations on a Cu catalyst. (b) Schematic illustration of the Cu-PTFE GDE. (c) The FE toward C2 products for different ionomers. Reprinted (adapted) from *Energy Environ. Sci.*, 2020, **13**, 554. Copyrights © 2020 Royal Society of Chemistry.

mass flux by an order of magnitude compared to hydrophobic ionomers (*e.g.*, Nafion). Fig. 52b shows 68% FE for C_2 products (ethylene and ethanol) was achieved at 10 bar, and 26% full-cell energetic efficiency over 10 hours, even with O_2, which is comparable to pure CO_2-fed systems (Fig. 52c). However, additional studies using real flue gas with other impurities (*e.g.*, SO_x, NO_x) and investigating long-term catalyst stability and scalability are still needed.

Zhu *et al.*, 2023[298] illustrated a pioneering, continuous, integrated system for CO_2 capture and release utilizing a modular electrochemical solid–electrolyte reactor (Fig. 53a–d). This concept integrates absorption and release within a single unit, operates at ambient conditions, and uses only water as input, in contrast to amine scrubbing or disconnected electrochemical/chemical systems. At the cathode, oxygen reduction (ORR) produces OH^-, establishing a localized alkaline environment that interacts with CO_2 to yield carbonate ions. The ions traverse an anion-exchange membrane into the solid–electrolyte layer, whereas protons generated by water oxidation (OER) at the anode pass through a cation-exchange membrane. The ions recombine, releasing high-purity (>99%) CO_2 gas continuously. The system achieves high capture rates (about 440 mA cm^{-2}, 86.7 kg CO_2 day^{-1} m^{-2}), exceeds 90% faradaic efficiency, and approaches 98% carbon-removal efficiency in simulated flue gas (Fig. 52e–h). Notwithstanding these benefits, the methodology is constrained by limitations such as mass-transport bottlenecks at low CO_2 concentrations (resulting in decreases in faradaic efficiency, CO poisoning of Pt/C catalysts, and energy losses due to ohmic drops in the solid–electrolyte layer. The authors investigated the utilization of cobalt single-atom catalysts (Co-SAC) that are resistant to CO poisoning while preserving high efficiency, even at diminished CO_2 concentrations. They additionally suggest enhancements such as minimizing solid–electrolyte thickness, employing different redox couples (*e.g.*, $2e^-$ ORR for H_2O_2 production to increase electron efficiency to approximately 0.7 CO_2 per electron), and sophisticated catalyst and membrane engineering. These tactics could decrease capture costs from approximately $83 to around $33 per ton, establishing this electrochemical platform as a viable method for sustainable, decentralized CO_2 capture in conjunction with renewable energy and subsequent conversion operations.

Li *et al.* (2024)[299] enhanced this design by amalgamating direct air capture and electrochemical conversion into a unified solid-state platform, functioning effectively at ambient settings, utilizing ambient air and water as feedstocks. Utilizing CO-tolerant, non-precious Cu catalysts alongside a polymer-based electrolyte, they tackle challenges related to catalyst expense, CO poisoning, and energy inefficiency, while directly generating ethylene without the need for intermediate CO_2 purification, providing a more efficient and sustainable approach for decentralized carbon utilization. This study introduces a solid-state electrochemical reactor that efficiently captures CO_2 and H_2O from ambient air and converts them into ethylene and oxygen at approximately 25 °C, achieving FE of around 34%, remarkable energy efficiency of around 80%, and operating at a low voltage of about 0.6 V with a current of 1 A. Simple and scalable cathode fabrication method is shown in (Fig. 54a). The anode structure is presented in (Fig. 54b). The solid polyelectrolyte facilitates the migration of OH^- ions from the conductive cathode to the nickel anode under an electric field, while also enabling the transfer of produced water from the nickel anode to the conductive cathode (Fig. 54c). The system employs a stratified architecture: a cathode composed of conductive carbon foam integrated with copper nanoparticle-coated SWCNTs for CO_2 reduction catalysis, a PEO/KOH-infused polypropylene membrane serving as a solid electrolyte for OH^- transport, and a nickel foam anode facilitating oxygen evolution. CO_2 is sequestered by PEI/zeolite 13X composites, while H_2O is absorbed by $CaCl_2$-based hygroscopic salts, facilitating the *in situ* synthesis of formate and CO, which are then reduced on the Cu catalyst surface to provide ethylene by CO–CO coupling (Fig. 54d). This method facilitates compact, scalable, and continuous direct air capture (DAC) and conversion of low-concentration CO_2 without the need for compression or gas purification. The system effectively generates around 70 mg of ethylene per hour, demonstrating the reactor's capability to generate hydrocarbons from air-sourced carbon under ambient settings without the need for gas purification or compression.

The incorporation of metal oxides for concurrent carbon dioxide (CO_2) collection and electrochemical reduction (CO_2RR) signifies a viable approach for enhancing carbon-neutral energy and chemical output. Due to their distinctive physiochemical characteristics, such as high CO_2 affinity, surface tunability, and catalytic activity, metal oxides, including SnO_x, CuO, Bi_2O_3, and In_2O_3, have become attractive options for dual-function systems. These materials not only promote CO_2 adsorption *via* acid–base

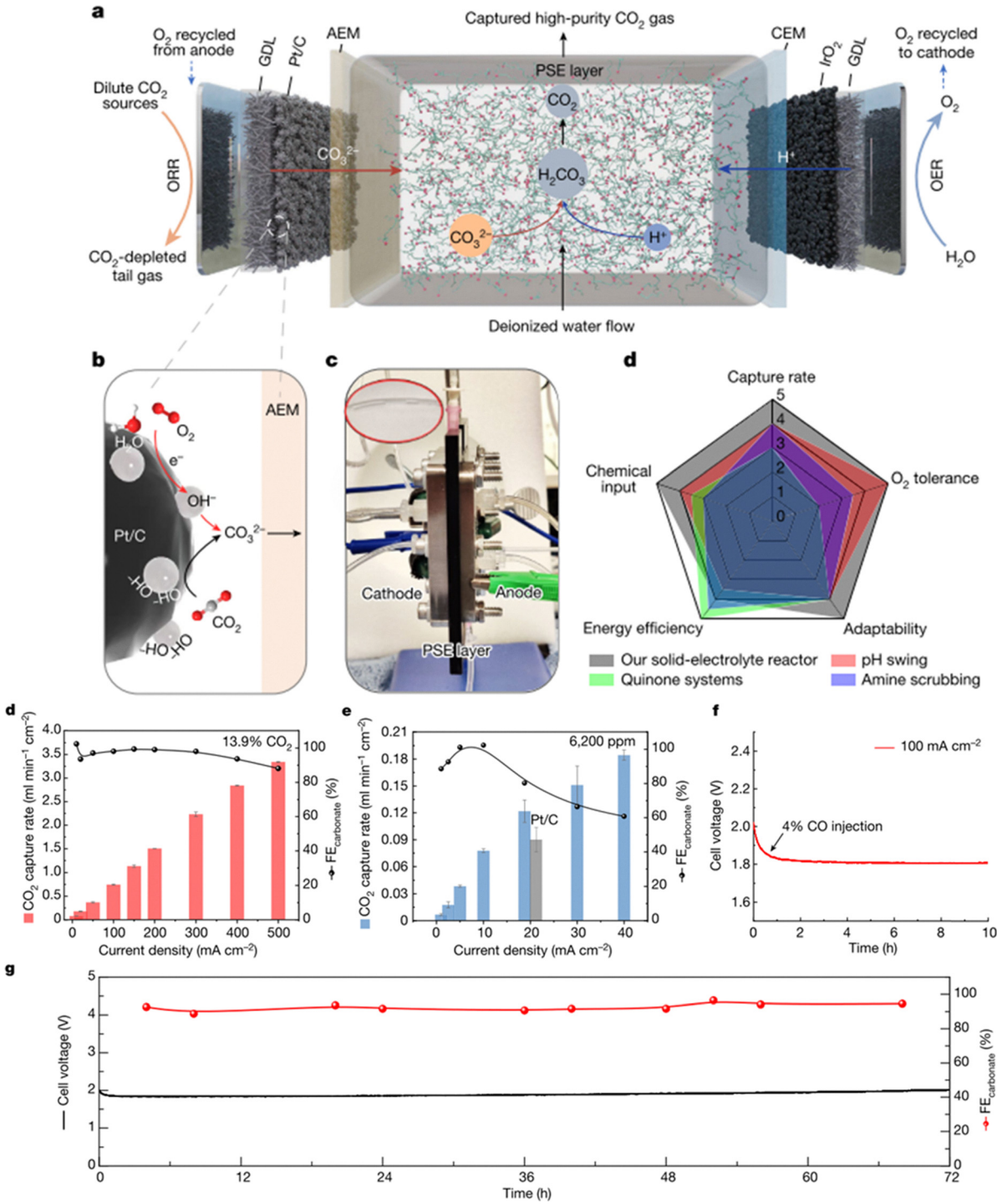

Fig. 53 Solid–electrolyte reactor design for carbon capture from different CO_2 sources. (a) Schematic of the solid–electrolyte reactor for carbon capture. (b) Schematic of the reaction mechanism at the catalyst–membrane interface. (c) Photograph of the solid–electrolyte reactor and captured CO_2 gas (inset) flowing out of the solid–electrolyte layer. (d) A radar plot comparison of different carbon-capture technologies. (e) and (f) The carbon-capture performance of Co-SAC under 13.9% and 6200 ppm CO_2 concentration, which showed a large improvement compared with Pt/C under low-CO_2-concentration regions. (g) The high resistance of Co-SAC catalysts to CO poisoning, while the cell voltage remained stable after the injection of CO gas. (h) Stability test of Co-SAC catalyst under a fixed current of 100 mA cm^{-2}, over 72 hours. Reprinted (adapted) from *Nature* 2023, **618**, 959–966. Copyrights © 2023, The Author(s), under exclusive license to Springer Nature Limited.

interactions and surface changes (*e.g.*, amine functionalization) but also work as active electrocatalysts that convert CO_2 into valuable products such as formate, carbon monoxide, ethylene, and ethanol. Notwithstanding substantial advancements, some essential knowledge deficiencies persist that must be resolved to enhance the practical implementation of metal oxide-based

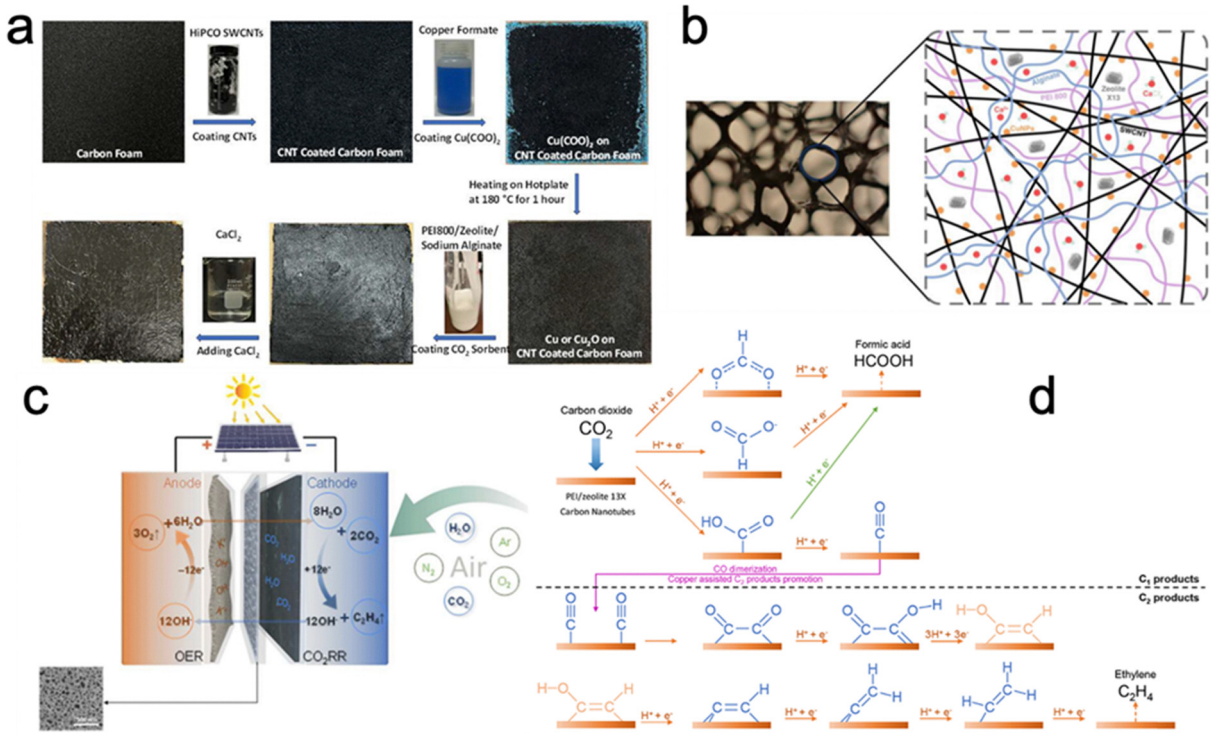

Fig. 54 (a) Procedures of cathode fabricating. (b) Photographic picture of carbon foam (left) and cartoon illustration of zeolite 13X/PEI800 and SWCNTs with copper nanoparticles embedded in the ionotropic gelation of sodium alginate and calcium chloride (right). (c) Cartoon illustration of direct air capture of CO_2 and H_2O, electroreduction of CO_2 into ethylene in the cathode and the oxygen evolving reaction in the anode, and the transportation of OH^- and H_2O in the solid electrolyte reactor. (d) Catalytic electrochemical reduction mechanism of direct air captured CO_2 and H_2O into ethylene and O_2. Reprinted (adapted) from *Energy Fuels* 2024, **38**(11), 10390–10393. Copyrights © 2024 American Chemical Society.

integrated CO_2 capture and conversion systems. Present constraints encompass sub-industrial current densities for product generation, inadequate comprehension of the long-term stability of oxide-based catalysts (particularly under variable gas compositions and humid environments), and a lack of mechanistic understanding regarding surface transformations and intermediate stabilization during operational conditions. Further details are listed below:

- Rational interface and catalyst design: engineering hybrid systems that integrate metal oxides with conductive substrates (*e.g.*, carbon nanomaterials, metal–organic frameworks, or polymers) may enhance charge transport, catalytic stability, and overall efficiency.
- *Operando* and *in situ* characterization: utilizing sophisticated spectroscopic and microscopic methods (*e.g.*, XAS, FTIR, Raman, and TEM) under operational conditions is crucial for clarifying active sites, reaction intermediates, and degradation routes.
- Surface functionalization and defect engineering: modifying the surface characteristics of metal oxides through doping, the introduction of oxygen vacancies, or the grafting of alkanolamines can markedly improve CO_2 affinity and adjust product selectivity.
- System-level integration and optimization: the integration of metal oxides into modular platforms, including gas diffusion electrodes, pressurized flow reactors, and solid-state electrochemical cells, is essential for enhancing technology readiness. Employ strategies such as pressure manipulation and permselective membranes to improve gas transport and reaction kinetics.

Solvent-based CO_2 capture and conversion

The following section concentrates on the description of some of the liquid-phase techniques for CO_2 capturing, focusing on new solvents such as amines, ionic liquids, and Eutectic Solvents, and their uses in the integrated systems of electrochemical CO_2 capture and conversion. These advanced liquid media will be explained in detail and then compared with traditional electrolytes in terms of prior research articles to highlight their advantages, disadvantages, and possibilities for rapid implementation in carbon-neutral technologies.

Amines

Among the available capture technologies, Amine-based absorbents are widely used for CO_2 capture in industrial settings due to their rapid reactivity, ease of use, and adaptability in different applications, as Fig. 55 shows, which are applied in both pre- and post-combustion systems.[300–302]

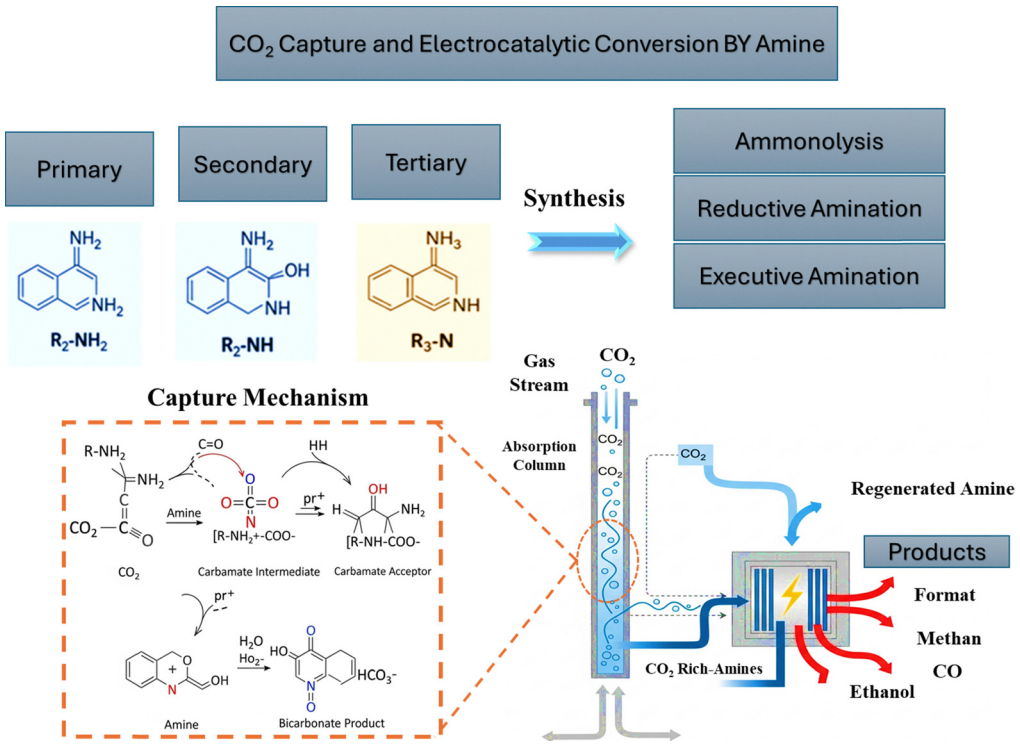

Fig. 55 Comprehensive schematic of integrated CO_2 capture and electrocatalytic conversion through reductive aminolysis using multifunctional amine solvents.

1. Amine chemistry and mechanisms of CO_2 capture

The fundamental chemistry behind amines capturing the CO_2 involves different mechanisms depending on the amine type, whether it is primary (like MEA), secondary (like DEA), or tertiary (like methyl diethanolamine (MDEA).

(A) Primary and secondary amines. Primary and secondary amines efficiently capture CO_2 by forming carbamates in a two-step process, often termed the *zwitterion mechanism*: "A zwitterion is a molecule that carries both positive and negative charges on different parts of its structure, but it remains electrically neutral overall. This charge separation arises from factors such as solvation effects, resonance, and the molecule's geometry, which localize charges to distinct functional groups. The term comes from German, meaning "hybrid" or "hermaphrodite."

(a) Step 1: formation of the zwitterionic intermediate. In the instance of CO_2 absorption, the zwitterion intermediate forms when the lone pair of the amine nitrogen bonds to the electrophilic carbon of CO_2, creating a positively charged nitrogen and a negatively charged oxygen.[303–305]

$$RNH_2 + CO_2 \rightleftharpoons RNH_2^+–COO^- \quad (1)$$

Due to bond angles and spatial arrangements, limited overlap means those charges are localized and cannot undergo internal proton transfer (a proton moved from one site to another) or delocalization that would neutralize them, so the intermediate zwitterion is very reactive and short-lived.

(b) Proton transfer and carbamate stabilization. A second amine molecule acts as a base, abstracting a proton from the zwitterion. This forms a stable carbamate ion and a protonated amine:

$$[RNH_2^+–COO^-] + RNH_2 \rightarrow RNHCOO^- + RNH_3^+ \quad (2)$$

The zwitterion is stabilized by solvent effects and structural features of the molecule, but without a second amine to abstract the proton, it cannot convert efficiently to a carbamate. This explains both the rapid reaction rates and the need for at least two amine molecules per absorbed CO_2 molecule. From eqn (1) and (2), the overall reaction of primary and secondary amines capturing CO_2 will be as follows:

$$CO_2 + 2RNH_2 \leftrightarrow RNHCOO^- + RNH_3^+ \quad (3)$$

Since these reactions don't require special conditions, they are carried out at moderate temperatures ($\sim$40 °C), making them highly effective in industrial capture systems.[305]

(B) Tertiary amines or sterically hindered. Tertiary amines do not form carbamates because they lack a hydrogen atom on the nitrogen. Rather, they absorb CO_2 in the presence of water and form bicarbonate ions:

$$CO_2 + R_3N + H_2O \leftrightarrow R_3NH^+ + HCO_3^- \quad (4)$$

Although tertiary amines react more slowly, they generally require less energy for regeneration and exhibit better thermal stability. For this reason, blends like MEA-MDEA or DIPA-MDEA are often used to balance absorption kinetics, solvent stability, and energy consumption in industrial applications.[306,307]

(C) Aqueous ammonia and other systems. Other chemical solvents, such as carbonate systems (*e.g.*, K_2CO_3) and aqueous ammonia, have been studied. However, due to slow reaction

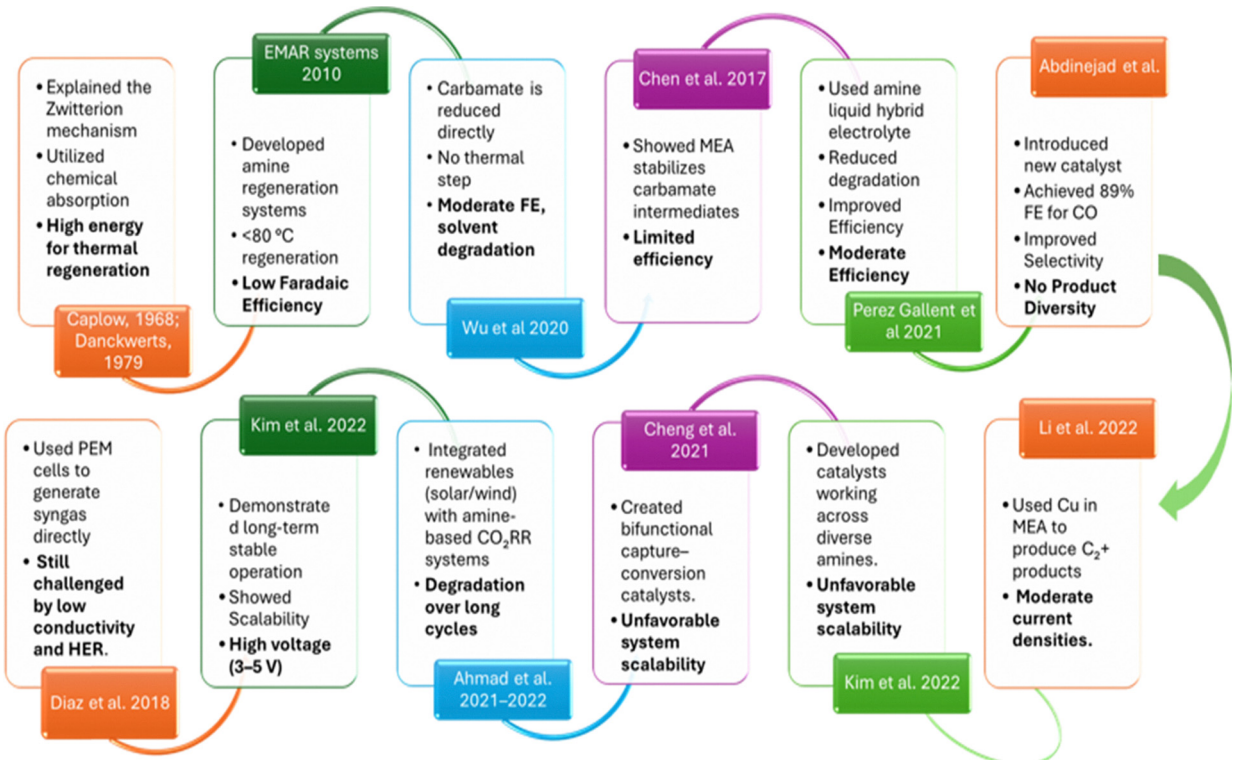

Fig. 56 A graphical timeline of the major developments in amine-based CO_2 capture and electrochemical conversion systems.

kinetics, carbonates are not very efficient, and ammonia slip, along with volatile losses, are problematic. Because of these issues, amine-based systems remain favored in industry for their efficiency and flexibility across a range of capture conditions.[308] Comparison between different amine types is shown in (Fig. 56).[309]

2. Recent studies for the use of amine in electrochemical capturing and conversion

Amines are pivotal in integrated electrochemical CO_2 capture and conversion by efficiently chemisorbing CO_2 to form carbamate and bicarbonate species, which increase local CO_2 concentration near catalysts and enable simultaneous capture and electrochemical reduction, thus bypassing traditional energy-intensive thermal regeneration.[310] Industrially, MEA has been a benchmark for rapid carbamate formation since the mid-20th century. Early electrochemically mediated amine regeneration (EMAR) used bipolar membranes and redox-active quinones to lower regeneration temperatures (<80 °C) but suffered from low faradaic efficiencies ($<50\%$), solvent degradation, and scalability issues. The direct electrochemical reduction of carbamate species, leverages alkali cation effects to compress the electrochemical double layer and enhance CO_2-to-CO conversion efficiency to 72%, while it was demonstrated that amine protonation aids formation of CO_2 radical anions for selective CO and formate production ($\sim 60\%$ FE). Hybrid amine–ionic liquid electrolytes further mitigate degradation and sustain formate production, while Amines also suppress hydrogen evolution and stabilize CO dimer intermediates, promoting multi-carbon product formation. Furthermore, catalyst innovations with iron-porphyrin and Cu-based systems have improved selectivity and product diversity. Also, advanced bifunctional catalysts, such as single-atom Ni and alkanolamine-functionalized SnO_2, enhance efficiency and stability. Integration with renewable energy enables efficient, scalable CO_2 conversion with cost savings, supported by continuous-flow reactors that sustain high current densities and employ radical scavengers or sterically hindered amines (*e.g.*, AMP) to curb degradation. Early polymer electrolyte membrane (PEM) systems demonstrated electrochemical syngas production from amine-captured CO_2, emphasizing the role of electrolyte conductivity and pH control, aided by inorganic salts to reduce ohmic losses.

A recent study by Pérez-Gallent *et al.* demonstrated the dual functionality of amines for an integrated CO_2 capture and electrochemical conversion owing to their, chemical and physical absorption functions.[311] From physical properties prospectives of amines which transforms the inherent ohmic heating into raising the reactor temperature from 15 °C to 75 °C that enhance the CO_2 desorption step nearly 8-fold and increase the format reaction rate by a factor of 10, reaching 0.56–0.7 mmol m^{-2} s^{-1} (Fig. 57a). In addition to the high capture capacity of CO_2, the product selectivity was also notable, with faradaic efficiencies up to 50% for formate and 45% for CO, alongside the detection of glycolate and oxalate as additional reduction products. Electrolyte composition and concentration proved critical: replacing propylene carbonate (PC) with water caused a 70% decline in formate yield due to competing hydrogen evolution, while optimizing AMP concentration at 2 M maximized efficiency and reaction rates, whereas higher concentrations introduced viscosity-related mass transfer

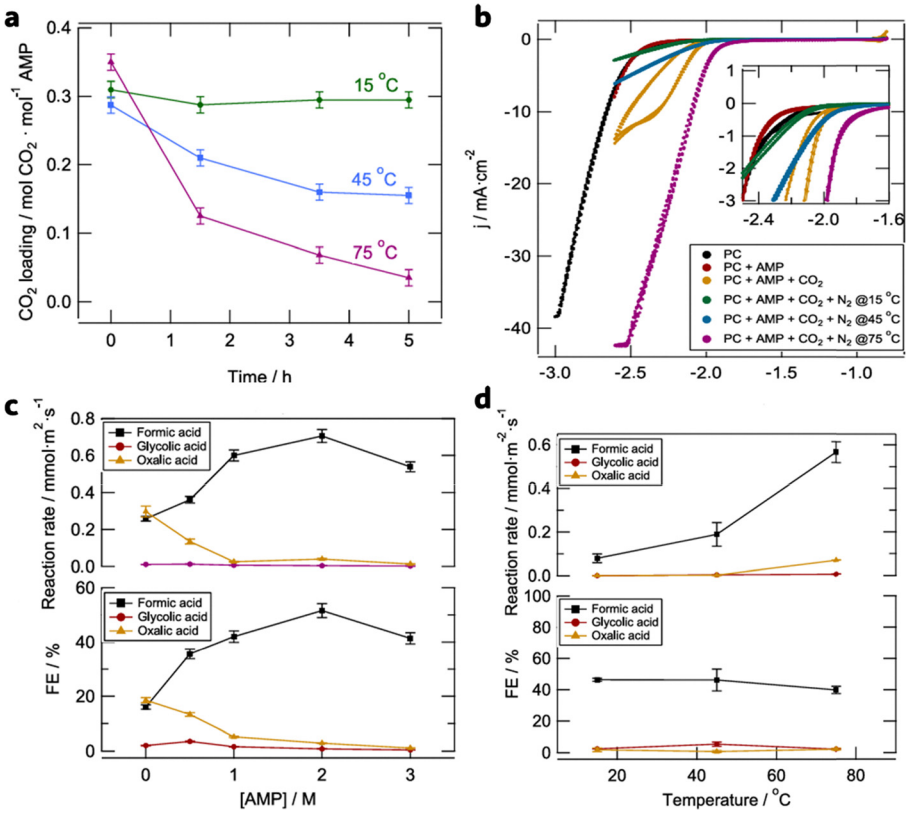

Fig. 57 (a) CO_2 loading as a function of electrolysis time at −2.5 V *vs.* Ag/AgCl on a Pb electrode in 0.7 M TEACl in PC containing 1 M AMP preloaded with CO_2 at different temperatures. (b) Cyclic voltammograms of a Pb electrode in 0.7 M TEACl in PC: without AMP (black), with 1 M AMP (red), with CO_2-saturated 1 M AMP at 1 bar and 15 °C (yellow), with CO_2CO_2-loaded 1 M AMP after N_2 stripping at 15 °C (green), 45 °C (blue), and 75 °C (purple). (c) Reaction rate and faradaic efficiency (FE) of formate, glycolate, and oxalate as a function of temperature. (d) Reaction rate and FE of formate, glycolate, and oxalate during electrolysis at −2.5 V *vs.* Ag/AgCl. Reprinted (adapted) from *Ind. Eng. Chem. Res.* 2021, **60**(11), 4269–4278. Copyrights © 2021 American Chemical Society.

limitations. However, in the absence of AMP, oxalate dominated with initial faradaic efficiencies of 80%, though this decreased over time (Fig. 57b and c). The reaction rate of CO_2 electroreduction increased strongly with electrolyte temperature, with formate production rising from 15 to 75 °C (0.56 mmol m^{-2} s^{-1}) while maintaining a relatively constant faradaic efficiency, reaching 40% at 75 °C. Compared to Alvarez-Guerra *et al.*, who reported lower rates (0.075 mmol m^{-2} s^{-1}) despite higher efficiencies (80%) on Pb in aqueous bicarbonate, the PC-based system offers a better balance of rate and selectivity. The organic solvent plays a critical role, as a high current density (40 mA cm^{-2}) was observed at 75 °C, compared to aqueous AMP, where the FE towards formate dropped to 3% after five h due to increased HER. CO_2 loading studies further revealed that higher temperatures accelerate CO_2 desorption, with only 10% retained after five h at 75 °C, compared with 93.5% at 15 °C (Fig. 57d).

A side-by-side comparison of main catalyst-electrolyte systems and their performance metrics is presented in Table 16, emphasising the variation in faradaic efficiencies, operating potentials, and current densities achieved in different configurations.

The (Table 16) indicates amine-based media are promising for electrochemical conversion of CO_2 with moderate to high selectivity towards CO and formate, especially when co-catalysts, salts, or surfactants are added. Besides electrode design, mass transport, and electrolyte conductivity improvements, additional progress is needed toward industrially meaningful current densities.

3. Remaining challenges and outlook

Despite these developments, some of the most significant challenges remain:

- Low ionic conductivity and high Ohmic losses: technologies based on amines are less ionic in their conductivity than alkaline electrolytes, resulting in greater cell voltages and energy consumption. Alkali cation electrolyte engineering increases electron transport but does not fully eliminate this challenge.[318]
- Competing hydrogen evolution reaction (HER): HER decreases CO_2 reduction selectivity, especially at high overpotentials and current densities. Catalyst and electrolyte modification decreases HER to some extent, but cannot eliminate it.
- Amine degradation: oxidative and thermal degradation of amines during electrolysis creates byproducts that decrease solvent lifetime and increase operating expenses. Use of sterically hindered amines, radical scavengers, and optimal operating conditions reduces but cannot prevent degradation.
- Scalability and moderate current densities: while continuous-flow systems can sustain current densities of as

Table 16 Studies on the use of amine solutions in electrochemical capturing and conversion

Catalyst/electrode	Potential (V *vs.* RHE)	Product	FE (%)	Current density (mA cm^{-2})	Solvent/conditions	Ref.
Ag/carbon-black on 300 nm Ag film	−0.8	CO	72	50	30 wt% MEA + 2 M KCl, 60 °C	312
Ag/carbon-black on 300 nm Ag film	−0.8	CO	100	30	30 wt% MEA + 2 M KCl, 60 °C	
Ag/carbon-black on 300 nm Ag film	−0.66	CO	30	—	2 M MEA + 2 M CsCl, 25 °C	
Ag/carbon-black on 300 nm Ag film	−0.66	CO	<5	—	2 M MEA, no salt	
Cu + MEA	−0.78	CO	22	14.8	0.1 M $NaClO_4$ aq. + CO_2-loaded MEA	313
Cu + EDA	−0.78	CO	58	18.4	0.1 M $NaClO_4$ aq. + CO_2-loaded EDA	
Cu + DCA	−0.78	CO	19	9.7	0.1 M $NaClO_4$ aq. + CO_2-loaded DCA	
Ag (porous + CTAB)	−0.8	CO	38.2	39.1	30% MEA w/w aq., CO_2-saturated + 0.1% CTAB	314
In (porous + CTAB)	−0.8	$HCOO^-$	54.5	~13.4	CO_2-saturated 30% MEA, 0.1% CTAB	
In (porous + CTAB)	−0.8	CO	22.8	~2.0	CO_2-saturated 30% MEA, 0.1% CTAB	
Pb (porous + CTAB)	−0.8	$HCOO^-$	60.8	~2.2	CO_2-saturated 30% MEA, 0.1% CTAB	
Bi (porous + CTAB)	−0.8	$HCOO^-$	36	~18.3	CO_2-saturated 30% MEA, 0.1% CTAB	
Sn (porous + CTAB)	−0.8	CO	16.6	~8.9	CO_2-saturated 30% MEA, 0.1% CTAB	
Sn (porous + CTAB)	−0.8	$HCOO^-$	11.6	~4.1	CO_2-saturated 30% MEA, 0.1% CTAB	
HCl-modified Ag	−0.91	CO	91 ± 7	~3.0	1 M AMP + 0.3 mM CTAB, CO_2-sat. aq., RT, H-cell	315
HCl-modified Ag	−1.01	CO	91	(higher than at −0.91 V)	1 M AMP + 0.3 mM CTAB, CO_2-sat. aq., RT, H-cell	
HCl-modified Ag	−0.91	CO	54	—	1 M MEA aq., no CTAB (*vs.* AMP system)	
HCl-treated Cu	−0.61	$HCOO^-$	~68	—	1 M AMP + 0.3 mM CTAB, CO_2-sat. aq., H-cell	
HCl-treated Zn	−0.91	CO	~40–50	—	1 M AMP + 0.3 mM CTAB, CO_2-sat. aq., H-cell	
Ni–N/C (single atom)	−0.9 to −1.1	CO	78.3	−2.6	5 M MEA, H-cell	316
Ni–N/C (MEA cell)	—	CO	64.9	−50.0	5 M MEA, zero-gap membrane electrode assembly	
Ag nanoparticles	−0.9 to −1.1	CO	38.3	−0.79	5 M MEA, H-cell	
Ag nanoparticles (MEA cell)	—	CO	25.5	−50.0	5 M MEA, membrane electrode assembly	
Cu Nanodendrites	−0.77	$HCOO^-$	54.78	~21.0	CO_2-sat. aq. ethanolamine (0.05 mol frac.)	317
Ag Nanodendrites	−0.77	$HCOO^-$	35.84	~7.9	CO_2-sat. aq. ethanolamine (0.05 mol frac.)	
Au Nanodendrites	−0.77	$HCOO^-$	60.3	~46.6	CO_2-sat. aq. ethanolamine (0.05 mol frac.)	

much as 200 mA cm^{-2}, batch systems realize lower current densities, which limit throughput and industrial scalability.

• Inefficient capture medium regeneration: electrochemical conversion does not always fully regenerate amine solvents, which requires extra processing steps.

Integrated capture and conversion electrochemistry can reduce the energy requirement for carbon capture hardware by up to 44% compared with conventional thermal regeneration, primarily by excluding the high-temperature stripping step 1. However, inefficiencies in currently available systems, such as high cell voltages (3–5 V at 100 mA cm^{-2}), solvent degradation, and modest current densities, limit economic competitiveness. Integration of renewable power will help offset electricity costs and improve sustainability, but intermittency and system longevity remain concerns. Since amine-based electrolytes are hindered by low ionic conductivity, competition with hydrogen evolution (HER), solvent degradation, and moderate current densities, new capture media such as ionic liquids (ILs) and deep eutectic solvents (DESs) are gaining increasing research interest. These solvents have greater CO_2 solubility, enhanced electrochemical stability, and adjustable physicochemical properties, which can surpass the intrinsic shortcomings of amines and allow for more efficient, stable, and scalable integrated CO_2 capture and conversion systems.[319]

Ionic liquid

Amines capture CO_2 primarily by forming a chemical bond through the direct reaction of the nitrogen lone pair with CO_2. However, many of these amine-derived salts are solid at room temperature, which limits molecular mobility and thus restricts mass transport. This results in reduced efficiency during CO_2 absorption and subsequent desorption.[320] To overcome these limitations, amine-based materials have been engineered into ionic liquids (ILs): salts that are liquid at or near room temperature. The concept of ILs originated from early studies on ammonium salts, such as ethylammonium nitrate ($[EtNH_3][NO_3]$), first reported by Paul Walden in 1914. This salt, formed from ethylamine (an amine) and nitric acid, remains liquid at room temperature (melting point 12 °C) and is considered the archetype of ionic liquids. These early ILs were essentially ammonia- or amine-derived salts (ammonium cations paired with various anions) that could absorb gases like CO_2 or NH_3, similar to how aqueous amine solutions are used in industrial gas scrubbing, as shown in (Fig. 58).[321]

The success of ammonium-based ionic liquids demonstrated the feasibility of creating room-temperature molten salts by pairing organic (alkylammonium) cations with appropriate anions. Building on these principles, researchers have designed a wider array of ILs, moving beyond simple ammonium salts by pairing various organic cations (such as imidazolium, pyridinium, or phosphonium) with inorganic or organic anions (*e.g.*, BF_4^-, PF_6^-, NTf_2^-). Importantly, these new ILs do not require specific functional groups for gas binding; their effectiveness largely stems from the use of bulky, asymmetric cations (often inspired by amines or ammonium ions) and weakly coordinating anions, which ensure the resulting salt remains liquid at room temperature and provides high ionic mobility.

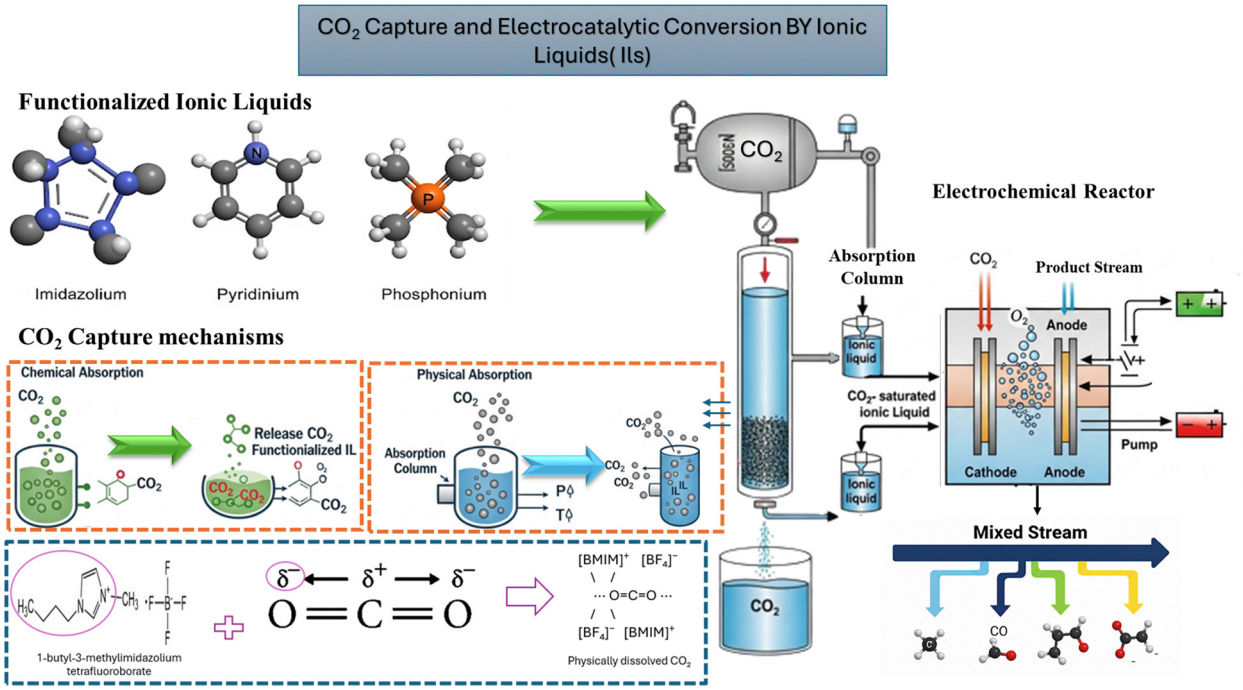

Fig. 58 Detailed process schematic of integrated CO_2 capture and electrocatalytic conversion using functionalized ionic liquids (ILs) in a continuous ICCC system.

ILs retain the reactive functionalities of amines while offering versatile and tunable physical properties. They serve as liquid electrolytes, demonstrate strong thermal and electrochemical stability, and can be precisely tailored for specific applications. These features make ILs ideally suited for integration with electrochemical systems, allowing the seamless co-integration of CO_2 capture and conversion processes, such as electrochemical reduction, thereby advancing sustainable carbon management solutions.

1. Ils mechanism

Ionic liquids (ILs) and aqueous amines capture CO_2 with two different approaches, as demonstrated in (Fig. 59). In amine-based systems (top group), reagents such as ethanolamine chemically react with CO_2 and form stable carbamate species through a zwitterionic intermediate. This process occurs *via* covalent bonding and proceeds at a 1 : 2 CO_2 : amine ratio, making it highly effective for capture but energetically costly for regeneration, as the bond must be broken to liberate CO_2. In contrast, ILs are salts that are entirely composed of cations and anions and are liquid at or near 100 °C, that interact with CO_2 primarily *via* physical absorption (bottom panel).[322] ILs such as 1-butyl-3-methylimidazolium tetrafluoroborate ([Bmim][BF_4]) physically dissolve CO_2 *via* weak, non-covalent interactions, including van der Waals forces, Coulombic attractions, and Lewis acid–base interactions (in this case with the anion).[323]

The structure of IL plays a crucial role in the CO_2 solubility. Fluorinated anions ([PF_6]$^-$, [Tf_2N]$^-$) and long alkyl chains on the cation can enhance free volume and hydrophobicity, favouring CO_2 uptake. For example, phosphonium-based ILs like [P_{66614}].[324] For instance, [P_{66614}][2-CNpyr] has a capacity of 76.5 mg CO_2 per g solvent at 22.1 °C and 57.4 mg CO_2 per g solvent at 40.1 °C and 1 bar of CO_2.[324,325]

Numerous studies have examined the influence of IL structural properties on CO_2 solubility and absorption. These reports reiterate that in conventional ILs, the physical forces dominate and solubility is principally governed by anion features, free volume, and the strength of weak intermolecular forces.[326] The following (Table 17) presents a summary of notable contributions in this sense, including some insight into the creation of ILs for CO_2 capture.

Conventional ionic liquids (ILs) have a great deal of potential for CO_2 capture due to their tunable structures, low volatility, and ability to absorb CO_2 through weak non-covalent interactions (*i.e.*, van der Waals forces, coulombic interactions, or Lewis acid–base interactions); however, they are limited to CO_2 uptake as ILs contain no chemically reactive sites. With the potential drawbacks of traditional ILs, researchers have synthesized, modified, or functionalized ILs with reactive functional groups (most commonly amino, hydroxyl, carboxyl, or heterocyclic donors) that can form covalent, or at least reversible bonds with CO_2, thereby enhancing uptake capacity and selectivity.[333] Incorporating chemical functionality into ILs changes the role of ILs from purely being physical solvents with non-covalent interactions and has a diverse range of possible applications because they can now be classified in two broad categories; the first category is Amino-functionalized ILs (AFILs), which are usually designed to mimic traditional alkanolamines carbamate-forming behavior relative to CO_2, these typically incorporate (–NH_2) amine groups into the alkyl side chains of cations (*e.g.* imidazolium, pyrrolidinium), or add it to the anion (which would simultaneously bond chemically to the CO_2 to form a carbamate or bicarbonate

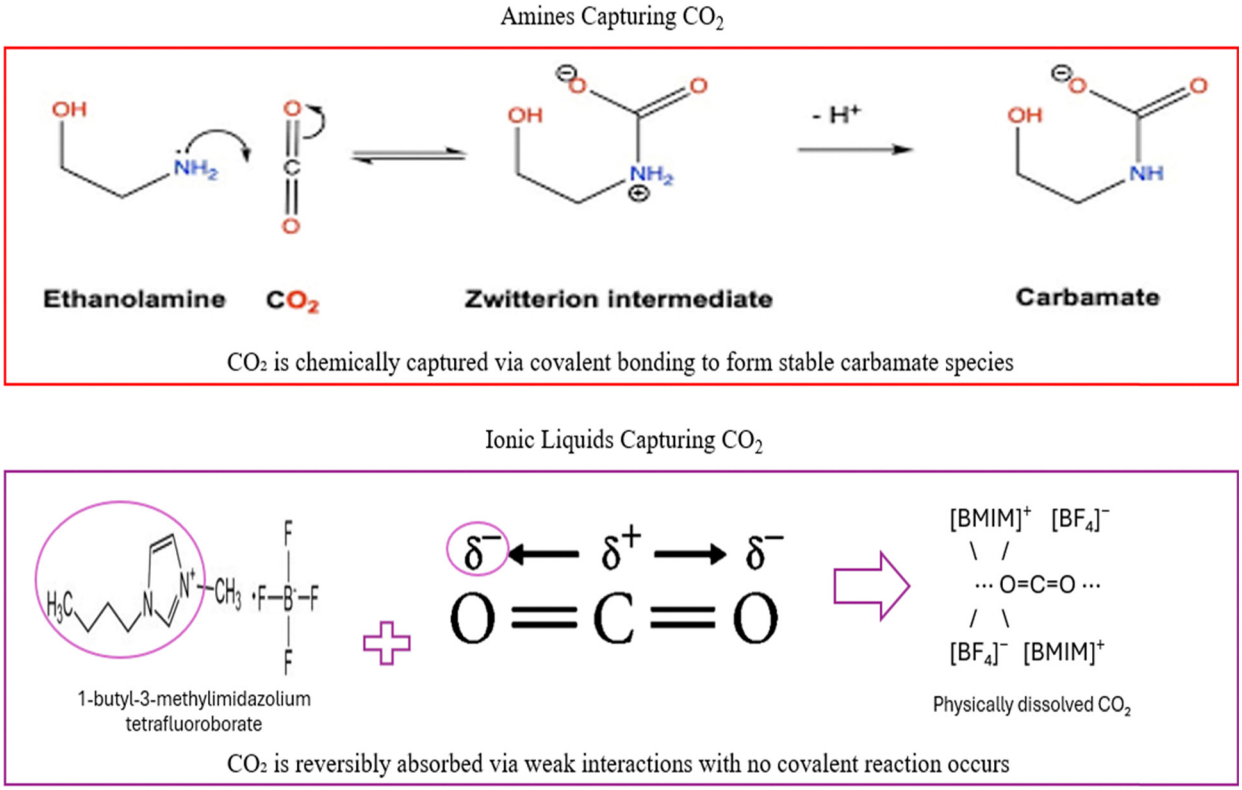

Fig. 59 ILs capturing mechanism in comparison with amines.

Table 17 Summary on the use of ILs in CO_2 capture

ILs studied	Key findings	Ref.
[Bmim][PF_6]	High CO_2 solubility observed in [Bmim][PF_6]; at 40 °C and 93 bar, the IL phase contained a CO_2 mole fraction of 0.72	327
General imidazolium-based ILs	CO_2 solubility increases with longer alkyl chains on the cation; solubilization is mainly physical	328
[Bmim][PF_6], [Bmim][BF_4]	weak Lewis acid–base interactions between CO_2 and IL anions, which enhance dissolution	329
Various imidazolium-based ILs	Combined experiments and simulations; concluded CO_2–anion interactions dominate solubility behavior	330
Various imidazolium-based ILs	Physical solubility in ILs depends on anion–CO_2 interactions	331
Conventional imidazolium-based ILs	Emphasized van der Waals forces and hydrogen bonding; solubility is governed by weak physical interactions, not covalent bonds	332

species). In fact, according to the position of the reactive functional group, AFILs can also be classified based on:

• Cation-functionalized ILs, containing NH_2 or –OH groups that can react with CO_2 through nucleophilic attack (producing zwitterionic carbamates in a 1 : 2 CO_2 : IL ratio).[333,334]

• Anion-functionalized ILs, holding reactive functional groups (carboxylates, amino acids) that capture CO_2 through a stoichiometric path (1 : 1 equivalence) to create carbamic acids.[335,336]

• Dual-functionalized Ils combine both cationic and anionic functionalities to create multiple binding sites, thereby enhancing CO_2 absorption capacity (exceeding 2 mol CO_2 per mol IL), improving absorption kinetics, and offering greater operational flexibility.[337,338]

The nature of the functional groups, whether they are amino, carboxyl, phenolate, or nitrile, plays a role in defining the mechanism and overall efficiency of CO_2 capture. The functionalized group type can be tailored (Fig. 60).

Table 18 provides a comparison of several representative amino-functionalized ILs, as well as a summary of functional groups used, CO_2 capacities relative to non-functionalized analogues, and associated operation advantages and disadvantages.

As shown in (Table 18) and (Fig. 61), the introduction of pyrrolide, phenolate, and hydroxypyridine heterocyclics into the anion structure showcases selective tailoring of non-amino functionalized ILs (non-AFILs). These groups not only enhance CO_2 reactivity toward AFILs, but they also mitigate the viscosity issues that often arise from amino functionalization. Hydrophilic –NH_2 groups in AFILs tend to form hydrogen-bonded networks with anions, which dramatically increases viscosity and immobilizes mass transfer. Non-AFILs bypass this hydrodynamic issue with three basic design characteristics.

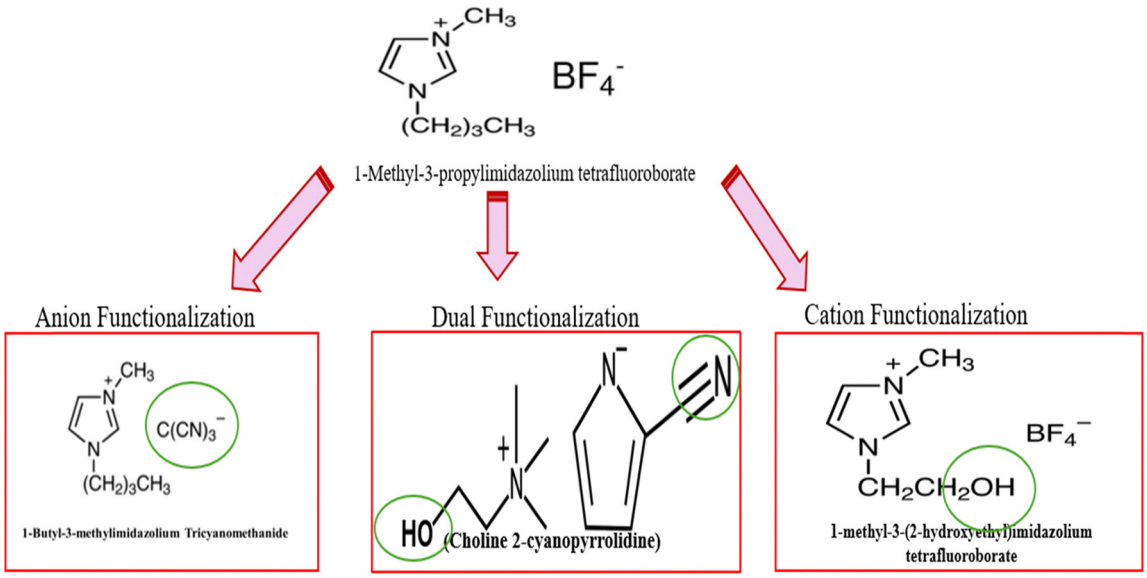

Fig. 60 ILs types (a) anion functionalized (b) dual functionalization C. Cation functionalization.

Firstly, the lack of amino groups means that no protonation or hydrogen bonding leads to viscosity surges. Secondly, cation/anion pairs like imidazolium/$[BF_4]^-$ and phosphonium/$[PF_6]^-$ have low electrostatic interaction.[343,344] Lastly, the presence of heterocyclic anions, which are poor hydrogen bond donors, enhances fluidity, completing.[345] These principles have empirically been shown to decrease viscosity relative to AFILs, enabling faster CO_2 mass transfer and improving performance in electrochemical applications.[346]

For instance, $[P_{66614}][2\text{-CNPyrr}]$ falls into the category of ILs that have somewhat moderate CO_2 capacities with limited change in viscosity. $[P_{66614}][PhO]$, on the other hand, is a phenolate based IL that has been shown to offer balance as a IL with moderate capacity (0.85 mol CO_2 per mol IL) and low viscosity (246.7 cP), while hydroxypyridine-based ILs such as $[P_{66614}][2\text{-Op}]$ achieve high capacities ($\sim$1.7 mol CO_2 per mol IL) but suffer from significant viscosity increases post-capture.[333]

Mechanistic and experimental evidence reveal that certain heterocyclic anions, for example, $[BF_4]^-$, act as hydrogen bond acceptors which are thought to stabilize both the ionic liquid network and the CO_2 adducts.[347] The use of some non-amino functionalized ionic liquids like phenolate-based $[P_{6614}][PhO]$ has been classified as having moderate layered CO_2 absorption ability (0.85 mol CO_2 per mol IL) and a reasonable viscosity (246.7 cP), which makes CO_2 capture more manageable when considering the fluid dynamics associated with high viscosity solvents. Regarding $[P_{6614}][PhO]$ a note of caution, it is unstable in some cases after it reacts with CO_2 which typically increases viscosity and the irreversibility of the adducts limits its practical usage, especially in humid conditions.[348,349] Lastly, it should be noted that the non-amino functionalized ILs with tunable chemistry are attractive features for the carbon capture opening frontier. As an example, $[P_{6614}]$-$[2\text{-CNPyrr}]$ has a CO_2 affinity that is concerned with the improvement of flow, CO_2 capture avoids a 1 : 1 irreversible rate of reaction with CO_2, and the viscosity did not change significantly after capture.[350–352]

2. Recent studies utilizing Ils in CO_2 electrochemical capturing and conversion

In integrated electrochemical carbon dioxide, Ionic Liquids can be used as electrolytes, electrolyte additives, or electrode modifiers, as shown in (Fig. 62).

(A) Ionic liquids as electrolytes. Ionic liquids (ILs) and particularly imidazolium-based ionic liquids have shown great potential as electrolytes for electrochemical carbon dioxide reduction (CO_2ER), ultimately by lowering activation barriers, increasing reaction kinetics, and improving product selectivity. These ILs lower overpotentials due to selective interactions between their cations ($[Emim]^+$, $[Bmim]^+$) and CO_2 while allowing for tunable outcomes that can include the generation of formate, CO, and carbonates simply through the modification of the IL's ionic components.

(Table 19) listed various ILs that have been reported in the literature, in addition to many examples in which faradaic efficiencies greater than 80% and energy consumption have been significantly lowered. For example, $[Emim][BF_4]$ has been used several times in conjunction with silver or copper electrodes, where it performed admirably due to its ability to stabilize *COOH intermediates and lower the overpotential needed for formate production.[353,354]

(B) Ionic liquids as additives to electrolytes. Based on work done with pure ionic liquid (IL) electrolytes, recent research approached ILs as a new additive to commonplace electrolytes to overcome the challenges of viscosity and diffusivity and cost (while retaining the added benefits of their inherent characteristics, particularly on improving CO_2 activation, stabilizing intermediates, and selectivity towards products). IL additives, used at low concentrations (normally 0.01 to 0.5 M) in aqueous

Table 18 A summary of the key characteristics of representative amino-functionalized ionic liquids

IL example	Functionalization	Key functional group(s)	CO_2 absorption (*vs.* non-funct. IL)	Comparison IL	Advantages	Disadvantages	Other notes	Ref.
$[P_{66614}][AA]$	Anion	$-NH_2$/–COOH (amino acid)	1.6–2.0 mol mol^{-1} (2.5–3.3× higher)	$[P_{66614}][DCA]$ (0.6 mol mol^{-1})	Low viscosity	Water-sensitive; humidity effects	Carbamic acid stability is humidity-dependent	339
1-(3-Aminopropyl)-3-butylimidazolium BF_4	Cation	Primary amine ($-NH_2$)	~0.5 mol CO_2/mol (much higher)	[hmim][PF_6]	High, reversible absorption; recyclable	High viscosity	Stable carbamate over cycles (IR/NMR confirmed)	340
[apbin][BF_4], *etc.*; dual-functionalized	Cation, Anion, Dual	Amino, Alkoxide, Carboxylate	Up to 2.6 mol CO_2 per mol (1–2× higher)	[Bmim][BF_4], [Bmim][PF_6]	High capacity; tunable properties	High viscosity; synthesis complexity	Forms carbamates, carbonates, or zwitterions	333
$[P_{66614}][2\text{-CNPyrr}]$	Anion	Nitrile (–C≡N, AHA anion)	~1.0 mol mol^{-1} (2× *vs.* [Pro])	$[P_{66614}][Pro]$	Low viscosity, stable, fast kinetics	Slightly lower capacity than azolates	Zwitterionic product; minimal viscosity increase	324
$[N_2111][2\text{-CNpyr}]$, *etc.*	Cation + Anion	2-Cyanopyrrolidine (AHA)	Much higher *via* ylide chemisorption	General RTIL/alkanolamine refs	High stability, strong chemisorption	High viscosity, cost, and complexity	Zwitterion framework, IR/thermodynamics supported	326
$[Bmim][B(CN)_4]$, *etc.*	Anion	Multiple nitrile (–CN)	Increases with more –CN	[Bmim][SCN]	Tunable high solubility, diffusivity	May increase viscosity	CO_2 solubility dictated by cation–anion binding	326
Amine-ILs (*e.g.*, [Apbim][BF_4])	Cation	Amine ($-NH_2$/–NH–)	Up to 4× non-funct.	[Bmim][BF_4], [Bmim][Tf_2N]	High-low-P CO_2 capacity	Higher viscosity, regen. energy	Carbamate mechanism; good for low P_{CO_2}	333
Ether-ILs ([CH_3OCH_2-mim]X)	Cation	Ether (–O–)	Improved (up to 0.9 mol mol^{-1})	[emim][BF_4]/[PF_6]	Tunable, low volatility	Mainly physical, not chemical	Solubility boosted by the acetate anion	341
Nitrile-imidazolium ([NC-C3mim][Tf_2N])	Cation	Nitrile (–CN)	Enhanced *vs.* alkyl ILs	Alkyl-imidazolium ILs	Good selectivity (separation)	Viscosity/stability may vary	Useful for post-combustion CO_2	341 and 342

or organic solvents, generate cooperative reactions that may enhance reaction kinetics and efficiency, with no obligation to scale. Some principal means for the improved aspect are:

- greater the solubility and mobility of CO_2 (*e.g.*, [Emim][BF_4] is a 3× increase *versus* water)
- reaction of ''electroactive'' monolayers of cations at the interface $[Emim]^+$ (334×10^{-3} M), reducing activation energy
- transfer of protons will be influenced by anions like $[TFO]^-$ chosen to suppress H_2 evolution
- selectivity will be influenced by the functionalization of ions necessary to get products such as CO or formate.

There are some critical merits to using this strategy rather than pure IL systems (as seen in Table 20): very low viscosity ($\leq$5 cP as compared to 50–500 cP), good economic performance ($\leq$20% IL weight %), optimized H^+ conductivity, and suitability for industrial applications. Both Neubauer *et al.* and Yuan *et al.* demonstrated a peak in efficiency depending upon concentration (0.01–0.5 M), with both systems favoring formate and MeCN improved CO selectivity. Functionalized cations such as $[Emim]^+$ completely dominate because OH–CO_2 (binding energy of −0.36 eV), and flow reactors were used for 10+ hours at (83%+ efficiency). This method has been proven to resolve viscosity/cost problems, but the key challenges still exist (*i.e.* all of the other effects with regard to deliquescent interactions of co-additives/solvents; long-term stability; and the optimal triads of screening). Therefore, future work should focus on obtaining *operando* interface measurements using machine learning with suitable IL. Consequently, hybrid systems still hold the greatest industrial promise for electrocatalytic carbon capture.[366–368]

(C) Ionic liquid as electrode modifier. Transitioning from bulk electrolytes and additives, ionic liquids (ILs) deployed as electrode surface modifiers offer a transformative strategy that overcomes viscosity, conductivity, and cost constraints while enabling precise interfacial engineering. By immobilizing ILs directly onto electrode surfaces (*e.g.*, *via* covalent tethering or self-assembled monolayers), this approach creates a tailored microenvironment that enhances CO_2 adsorption, stabilizes critical intermediates (*CO, *COOH, *OCCO), and suppresses competing hydrogen evolution, all without requiring high-volume IL usage. Key mechanisms include:

- Microenvironment tuning: ILs generate structured interfacial layers, aligning and optimizing local charge distribution and reaction pathways, increasing selectivity[369]
- Intermediate stabilization: noncovalent interactions (*e.g.* binding of CO_2 to imidazolium) decrease the energy barriers for *COOH formation by 0.3–0.5 eV.[330]
- Chain length optimization: moderate length (*e.g.*, $[Bmim^+]C_4$) *N*-alkyl chains maximize the surface interaction by balancing increasing thickness with accessibility; longer chains ($>C_8$) significantly decreased efficiency and accessibility to the site[330]
- Pathway steering: functionalized ILs direct products toward specific outputs (*e.g.* C_2H_4 or methanol) by influencing electron/proton transfer[370]

As summarized in (Table 21), this strategy offers several notable performance improvements:

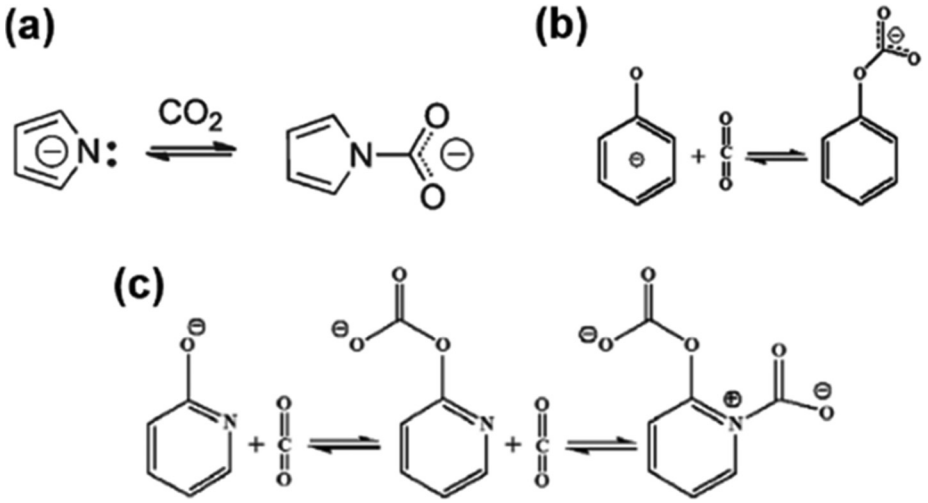

Fig. 61 Illustration of chemical absorption mechanisms of carbon dioxide by different organic anions: pyrrolide, phenolate, and hydroxypyridine.

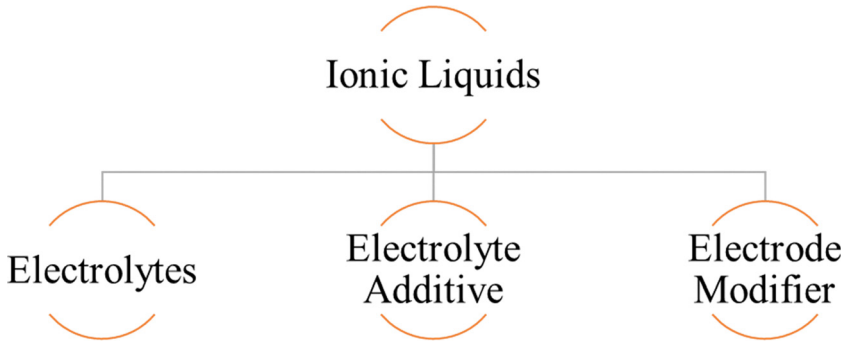

Fig. 62 The three primary roles of Ionic Liquids in integrated carbon capture and electrochemical conversion: electrolytes, electrolyte additives, or electrode modifiers.

• CO selectivity: hydrophobic imidazolium ILs toward Ag foam surface increased the production rate of CO from CO_2RR

• C_2 efficiency: [Bmim][NO_3] on Cu lowers the energy barrier for *CO dimerization, giving greater C_2H_4 yield

• Low energy conversion: phosphonium-ILs toward Au support formate/methanol at record low overpotentials

• Hydrogen evolution reaction (HER) suppression: polymerized ILs on graphene gave $>$ 40% suppression of H_2 evolution while increasing efficiency for formate production

From the above table, although IL-modifiers address the volumetric barriers associated with ILs, they still have:

• Stability: capacity to retain IL longevity under high-current operation.

• Synthesis: covalent grafting is still a multi-step functionalization process.

• Structure–activity trade-offs: alkyl chain length must be balanced based on accessibility *vs.* strength of interaction factors.

Ionic liquid (IL) surface modifiers have multiple distinct advantages relative to the bulk and additive options. In terms of relative IL consumption, bulk IL electrolytes require significant IL amounts (100% consumption) while IL additives require moderate amounts (typically in the range of 5–20%), whereas surface modifiers only need to use modest quantities due to the monolayer-level deployment. In terms of viscosity, bulk ILs increase the viscosity significantly (by 50, 500 cP), with the viscosity increase of IL additives being moderate (viscosity increase of 2–10 cP), and negligible from surface modifiers.[377]

Dongare *et al.* have recently investigated the bifunctional ionic liquid (IL) 1-ethyl-3-methylimidazolium 2-cyanopyrrolide ([Emim][2-CNpyr]) dissolved in acetonitrile as a multifunctional electrolyte for integrated CO_2 capture and conversion (Fig. 63a).[378] This IL has a dual role by its capability for CO_2 adsorption and electrochemical activity, which lets it selectively reduce CO on silver electrodes. The system exhibited elevated CO selectivity ($>$94%) with consistent performance over 12 hours. The addition of 0.1 M [Emim][2-CNpyr] resulted in a positive shift of the CO_2 reduction onset potential by 240 mV, indicating a substantial reduction in energy input relative to benchmark electrolytes (Fig. 63b and c). The CO_2 capture mechanism is shown through the synergetic effect of imidazolium cation ($[Emim]^+$) and the 2-cyanopyrrolide anion ($[2\text{-CNpyr}]^-$). The anion binds CO_2 by attacking it with a nucleophile, which makes carbamate-like adducts. The protonated anion can produce a carbene

Table 19 A summary of ILs as electrolytes in the integrated carbon capture and electrochemical conversion

Electrode/ catalyst	Ionic liquid electrolyte	Functionalized?	Product	Faradaic efficiency	Enhancement	Comparison/other electrolytes	Disadvantages	Ref.
Ag electrode	[Emim][BF_4]	No	Formate	>96%	Overpotential <0.2 V; activation energy reduction	Aqueous electrolytes	Not specified	355
Carbon nanofibers	[Bmim][BF_4]	No	Formate	Not specified	Overpotential reduced to 0.17 V; CO_2 complexation	Not specified	Not specified	356
Not specified	[Bmim][NTf_2]	No	Formate/ carbonate	Not specified	Optimal cation-dependent onset potential	Other ILs	Excess IL disrupts proton flux	357
Not specified	[Emim][BF_4]	No	Formate	Not specified	CO_2 pre-activation (binding: −0.36 eV)	Water (binding: −0.11 eV)	Not specified	358
Not specified	[Bmim][BF_4]	No	Formate	Not specified	[Bmim-COOH] intermediate stabilization	Not specified	Not specified	359
Not specified	[Emim][BF_4]	No	Formate	Not specified	[Emim-COOH] pathway *via* DFT; monolayer formation	Not specified	Not specified	360
Large electrode (495 cm^2)	IL-based ([BF_4]$^-$)	No	Formate	83.90%	Stable selectivity for 10+ hours	Not specified	Not specified	361
Not specified	[Emim][TFO]	Cation-functionalized	CO	~80%	Monolayer formation; minimal IL usage	Acid electrolytes	High viscosity at scale	362
Porous dendritic Cu	[Emim][BF_4]	Cation-functionalized	Formate	~75%	CO_2 activation; H-atom redirection	Aqueous electrolytes	Concentration sensitivity	363
Not specified	[Bmim][PF_6], [DBU-H][PF_6]	Dual-functionalized	CO/formate	CO ~70%, formate ~60%	Anion-dependent selectivity: [PF_6]$^-$ promotes CO/formate	MeCN solvent	Cost-intensive synthesis	364
Not specified	[Emim][BF_4]	Cation-functionalized	Not specified	Not specified	*COOH stabilization *via* non-covalent interactions	Molecular dynamics simulations	High IL concentrations reduce activity	365
Large-scale flow cell	Various ILs	Various	CO	83.90%	Optimized flow rate; stable long-term operation	Water-based	Scalability challenges	361

Table 20 A summary of ILs as additives to electrolytes in the integrated carbon capture and electrochemical conversion

IL used	Cation	Anion	Electrolyte system	Main product	FE	Solvent	IL type	Key findings	Ref.
[Emim][TFO]	Ethyl-methylimidazolium	Trifluoromethane-sulfonate	Water-based	CO	~80%	Water	Cation-functionalized	Optimal IL concentration (0.334 M) forms monolayers, boosting efficiency with minimal IL usage	362
[Emim][BF_4]	Ethyl-methylimidazolium	Tetrafluoroborate	Water-based	Formate	~75%	Water	Cation-functionalized	Activates CO_2 and redirects H atoms, enhancing formate on porous Cu electrodes	363
[Bmim][PF_6]	Butyl-methylimidazolium	Hexafluorophosphate	MeCN-based	CO	~70%	Acetonitrile	Non-amine	Promotes CO; [DBU-H][PF_6] favors formate, demonstrating IL-driven selectivity	364
[Emim][BF_4]	Ethyl-methylimidazolium	Tetrafluoroborate	Simulations	—	—	—	Cation-functionalized	Stabilizes *COOH intermediates *via* non-covalent interactions, reducing energy barriers	365
[Emim][BF_4]	Ethyl-methylimidazolium	Tetrafluoroborate	Molecular dynamics	—	—	—	Cation-functionalized	High IL concentrations disrupt proton transfer, degrading catalytic activity	365
Various ILs	Various	Various	Water-based flow cell	CO	83.90%	Water	Various	Optimized flow rate + IL additives achieve 83.9% CO efficiency with long-term stability	361

Table 21 A summary of ILs as additives to electrolytes in the integrated carbon capture and electrochemical conversion

IL Used	Electrode material	Main product	Key findings	Ref.
Hydrophobic imidazolium ILs	Ag foam	CO	Enhanced CO selectivity/production; alkyl chain length dictates surface accessibility	371
[Bmim][NO_3]	Cu	C_2H_4	Reduced *CO → *OCCO barrier; boosted C_2H_4 efficiency	372
Phosphonium-IL + imidazole	Au	Formate/methanol	Formate/methanol synthesis at low potentials; intermediate stabilization	373
Imidazolium SAMs	Au	Ethylene glycol	High activity at low overpotentials; enabled ethylene glycol production	374
Polymerized IL (PIL)	Graphene	HCOOH	Suppressed HER by >40%; enhanced formate formation	375
Imidazole-based ILs	Au(111)	Not specified	Vertical CO_2 adsorption mode; improved activation energy	376

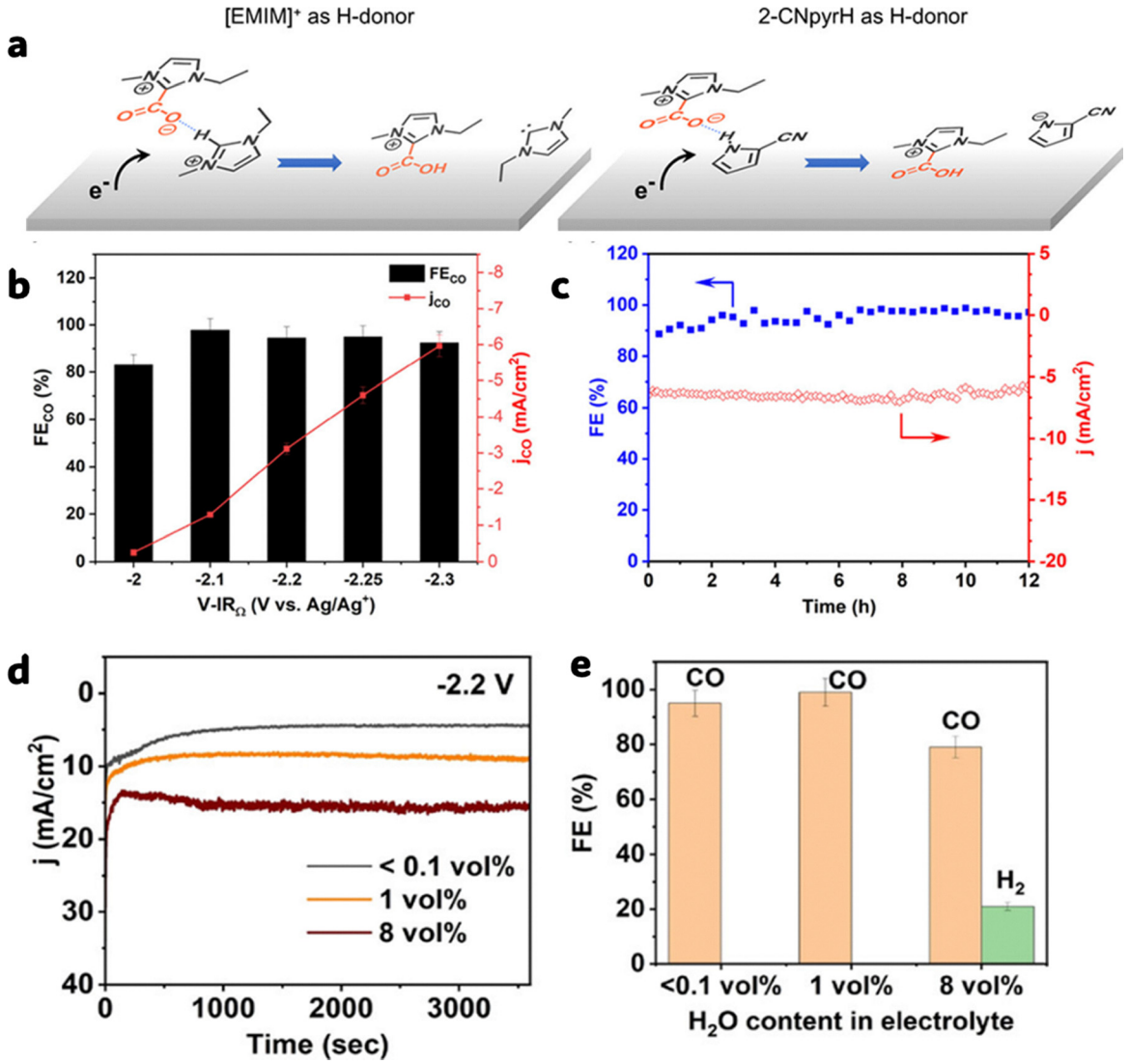

Fig. 63 (a) Illustration of the possible interactions on the electrode surface. (b) Faradaic efficiency (FECO) and partial current density of CO (j_{CO}) at different potentials during CO_2RR over Ag with 0.1 M [Emim][2-CNpyr] in the supporting electrolyte. (c) FE (filled blue squares) for CO production and total current density (red hollow diamonds) during 12 h of continuous CO_2RR with 0.1 M [Emim][2-CNpyr] in the supporting electrolyte on the Ag electrode at −2.2 V *vs.* Ag/Ag^+. (d) Faradaic efficiencies measured from chronoamperometry shown in. and (e), Gaseous product composition was determined by GC. Reprinted (adapted) from *ACS Catal.* 2023, **13**(12), 7812–7821. Copyright © 2023, The Authors. Published by American Chemical Society under the terms of CC-BY-NC-ND 4.0 license.

intermediate that interacts with CO_2 in an additional step. At the same time, the cation accumulates at the electrode interface, which helps stabilize CO_2 adsorbed there and accelerates electron transfer. *Operando* Spectro-electrochemical methods (SERS and EPR) validated the generation of IL–CO_2 adducts, surface-bound CO intermediates, and radical species, hence corroborating the

suggested cooperative mechanism. One of the most interesting factors that affects the selectivity is the water content. By adding up to 1 vol% water, the FE of CO increases up to 98%, while adding too much water makes hydrogen evolution more likely. This tunability underscores the importance of the solvent environment in guiding reaction paths (Fig. 63d and e).

3. Future work

Ionic liquids (ILs) are advantageous for CO_2 capture and CO_2ER due to their high CO_2 solubility, tunable structures, and electrochemical stability. Future directions of research should focus on improving the capacity of ILs to absorb CO_2, decreasing viscosity through optimizing IL-CO_2 interactions, and using supported ILs or hybrid materials such as SIL-coated membranes for enhanced performance. For CO_2ER, it will be critical to minimize IL dosage while maintaining catalytic efficacy with particular focus on understanding IL-CO_2 complexation, electric double layer structures, and co-catalytic effects. Future work should focus on *in situ* IL-regeneration methods for IO and on investigating machine-learning-optimized IL and electrode combinations. Hybrid architectures (*e.g.*, PIL-coat gas-diffusion electrodes) present an exciting avenue to scale C_2^+ production.

Supported ionic liquids (SILs) contribute an additional layer of functionality to IL-modifiers and have the potential to be a scalable and practical approach to eliminating economic and mass-transfer limitations associated with bulk ILs for CO_2 capture. SILs also consist of ionic liquids immobilized within porous solids, which is a particularly advantageous sub-approach, where high-surface-area solids such as MCM-41 or Al_2O_3 as wise support materials, ILs are capable of significantly higher gas–liquid contact while being able to also significantly decrease the volume of ILs needed to achieve the same level of mass-transport, often by +50% volume depending on the complex! This approach is compelling; SILs delivered a 2–3 times improvement in CO_2 with absorption rates compared to neat ILs with extended cyclic stability and retained tunable selectivity with target gases. These characteristics make SILs a desirable platform for the industrial-scale carbon capture and integrated conversion approaches.

The improved performance of SILs is due to multiple synergistic processes. The porous supports physically control IL distribution, specifically anchoring the anions (primarily on Al_2O_3 surfaces), which enhances CO_2 adsorption by reducing desorption losses. Materials such as MCM-41 greatly expedite mass transfer by exposing a larger interfacial area where both the gas and liquid can interact, more than doubling the CO_2 diffusion rate compared with unsupported ILs. At the optimum IL loadings, around 5 wt%, the supports allow the efficient uptake of CO_2 by avoiding pore blockage without filling the pores completely and still allowing a favorable economic and operational conditions. Moreover, advances in poly(ionic liquid) (PIL) networks, such as P[[VBTMA][PF_6]], have demonstrated even greater performance improvements, as high as 77% CO_2 uptake by weight and CO_2/N_2 selectivity of 70 : 1, and consistency with no degradation over 100 absorption–desorption cycles.[379,380]

As summarized in (Table 22), recent studies have explored a range of IL-support configurations and functionalizations, revealing important design considerations for future development.

4. Challenges and economic analysis

Although ionic liquids (ILs) have notable properties for CO_2 capture and conversion (*e.g.*, high ionic conductivity, thermal stability, and tunable structures), their challenges remain significant limiting factors for industrial application and large-scale deployment. ILs are often synthesized through energy-intensive processes that use costly raw materials (*e.g.*, fluorinated anions) and environmentally toxic reagents, creating barriers to scale. It is also essential to consider that concerns over toxicity (such as imidazolium persistence) are compounded by severe transport limitations inherent to the solvent matrix. Unlike aqueous electrolytes, ionic liquids are characterized by high viscosity, typically ranging from 50 to 400 cP at room temperature (*e.g.*, ~300 cP for [Bmim][PF_6]), which is two orders of magnitude higher than that of water (~0.89 cP).[321] This high viscosity suppresses mass transfer, restricting the diffusion coefficient of CO_2 (D_{CO_2}) to approximately 1–8 × 10^{-6} cm^2 s^{-1}, compared to ~2 × 10^{-5} cm^2 s^{-1} in aqueous media.[330] Furthermore, despite being composed entirely of ions, the ionic conductivity of common ILs is relatively low (~1–10 mS cm^{-1}) compared to standard alkaline electrolytes (*e.g.*, >200 mS cm^{-1}), leading to significant ohmic losses during electrolysis.[324] Consequently, without the use of elevated temperatures or gas-diffusion electrodes, IL-based systems are often limited to partial current densities below 10–20 mA cm^{-2}, significantly lower than industrial benchmarks (Table 23).

These limitations necessitate a transition towards simpler structures or hybrid systems for electrochemical capture and conversion. Despite these physical hurdles, ionic liquids (ILs) still offer potential economic advantages as electrolytes for CO_2 electrochemical reduction (CO_2R), especially for producing carbon monoxide, which remains the only economically viable carbon C1 product pathway when appropriately optimized. TEAs indicate that CO-production, at a rate of 100 tons/day, reaches a net present value (NPV) of $13.5 million, and the production of formic acid (HCOOH) reaches $39.4 million. The cost of electricity can highly influence the profitability of these products, with a variation of $0.01 per kWh changing the NPV

Table 22 A summary of recent studies on various ionic liquid (IL)-support configurations and functionalizations for future material development

Research focus	Key findings	Ref.
Amino-ILs on MCM-41/Al_2O_3	Al_2O_3 enhances CO_2 adsorption *via* anion anchoring; charge-dependent IL distribution	381
[P_{66614}][2-Op] on MCM-41	CO_2 absorption rate 2× higher than pure Ils	325
Organic solvents on MCM-41	Weaker solvent-support interactions increase CO_2 absorption synergistically	382
Poly(IL) P[[VBTMA][PF6]]	77% CO_2 uptake (wt); 70 : 1 CO_2/N_2 selectivity; 100-cycle stability	383

Table 23 Key physical properties of ionic liquids (ILs) compared to aqueous electrolytes relevant for CO_2 electrochemical conversion

Property	Ionic liquids (ILs)	Aqueous electrolytes
Viscosity (cP)	50–400 (*e.g.*, ~300 for [Bmim][PF_6])	~0.89
CO_2 diffusion coefficient (D_{CO_2}, $cm^2\ s^{-1}$)	~1–8 × 10^{-6}	~2 × 10^{-5}
Ionic conductivity ($mS\ cm^{-1}$)	~1–10	>200
Partial current density ($mA\ cm^{-2}$)	10–20[a]	>100

[a] Measured under standard conditions without elevated temperature or gas-diffusion electrodes; aqueous electrolytes achieve higher current densities due to lower viscosity, faster CO_2 diffusion, and higher ionic conductivity.

by ~$40 million for higher value products like *n*-propanol. CO could be economically viable, even at low faradaic efficiencies (<50%), as long as the overpotential does not exceed ~0.4 V. In comparison, for methanol it would require efficiencies greater than 60% and for ethanol, something greater than 90%. For products identified as C1 other (*e.g.*, CH_4, syngas), TPC currently exceeds the market prices (*e.g.*, 4.09 € per kg for CH_4, market price is 0.18–0.35 € per kg). Scalability in the future must reduce IL synthesis costs, minimize energy-intensive processes, particularly the energy required for the synthesis of fluorinated anions, and improve lifetime stability to reduce high capital expenses.[368,383–388]

Deep eutectic solvents (DESs)

Deep eutectic solvents (DESs) are a new class of tunable solvating media consisting of a hydrogen-bonding solvent, formed by a hydrogen bond donor (HBD) and a hydrogen bond acceptor (HBA), which forms a eutectic mixture that exhibits a melting point well below that of either individual component. The term "eutectic" is derived from the Greek term that means "easily melted," which designates the unique temperature at which both components crystallize together from the molten liquid; and usually consist of innocuous, bio-based components, such as choline chloride (HBA) and urea, glycerol, or organic acids (HBDs). DESs have been formed by mixing components at mild thermal conditions, typically without cumbersome purification and hazardous reagents[389] as shown in (Fig. 64).

The easy preparation of DESs is in stark contrast to the often energy-intensive, expensive synthesis of ionic liquids (ILs), making them a more eco-efficient and technologically and commercially valuable solvent. DESs represent the next-generation solution to the limitations of ILs, as shown in (Fig. 65):

- Simplified synthesis: combining low-cost hydrogen bond acceptors (HBAs; *e.g.*, choline chloride) and donors (HBDs; *e.g.*, urea) at mild temperatures, avoiding complex purification.[390]
- Eco-efficiency: bio-sourced components (*e.g.*, organic acids) enable biodegradable, non-toxic formulations with minimal environmental impact.
- Cost reduction: raw materials are 10–50× cheaper than ILs, with 80% lower synthesis energy demands.

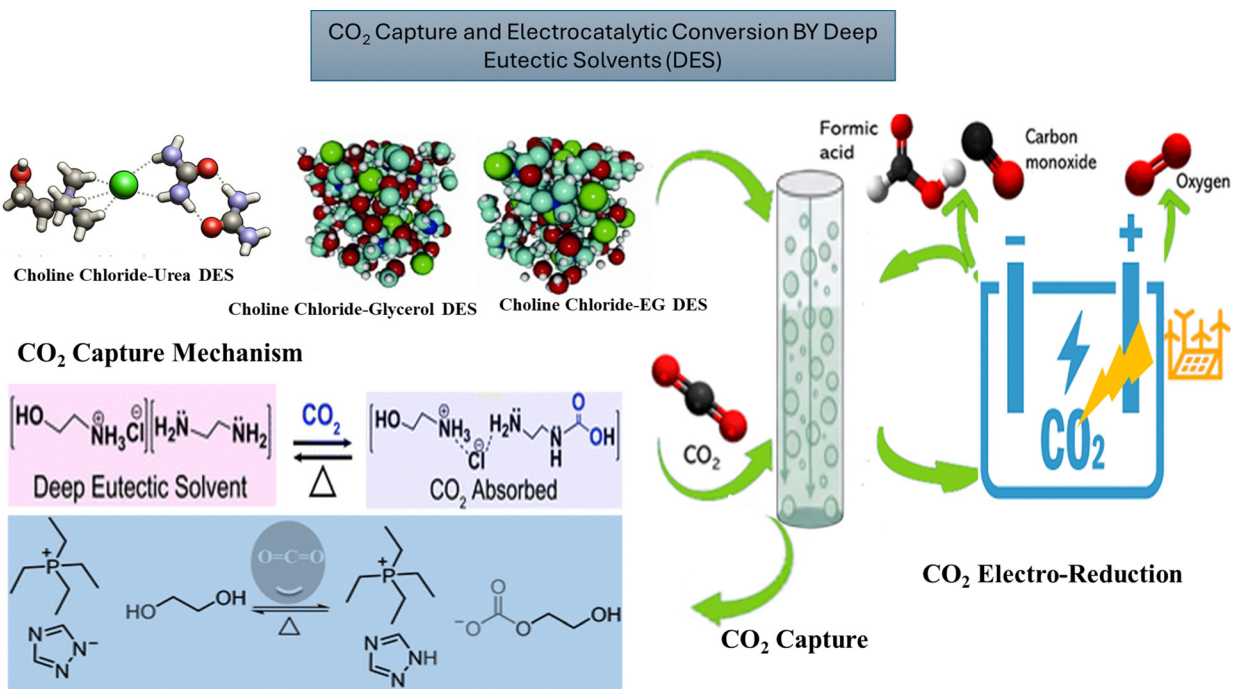

Fig. 64 Detailed schematic of integrated CO_2 capture and electrocatalytic conversion using choline chloride – deep eutectic solvents (DESs) in a synergistic ICCC process.

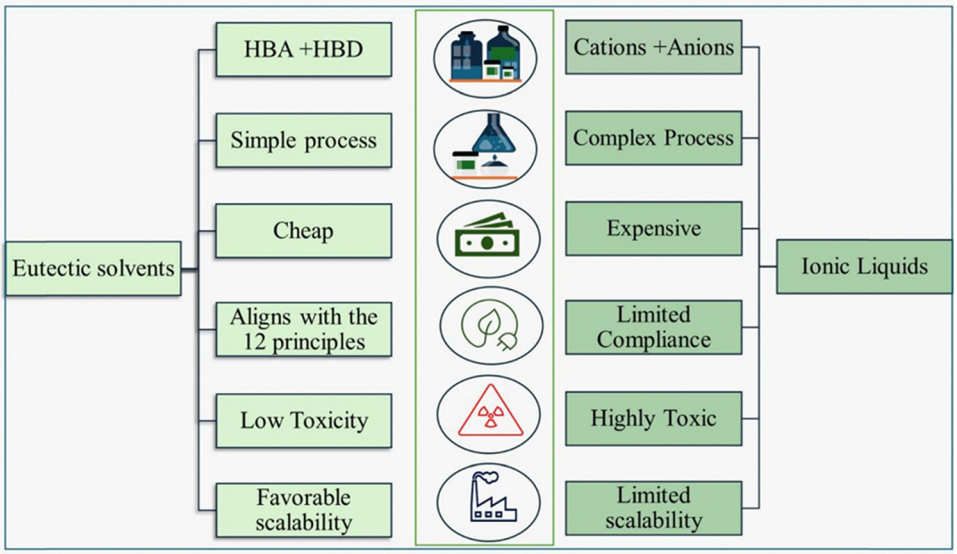

Fig. 65 A comparative analysis of eutectic solvents and ionic liquids.

• Performance parity: DESs match ILs in CO_2 solubility (*e.g.*, choline chloride/urea: 0.6 mol CO_2 per kg) while enhancing mass transfer *via* lower viscosity (200–500 cP *vs.* 500–1000 cP for ILs).[391,392]

1. Deep eutectic solvents: DESs mechanism

The first-generation Eutectic Solvents were produced from Hydrogen Bond donors with a quaternary ammonium. DESs are an adaptable class of green solvents synthesized from the complexation of a hydrogen bond acceptor (HBA), which is most often a quaternary ammonium salt like choline chloride, with a hydrogen bond donor (HBD), which could be urea, ethylene glycol, glycerol, or many organic acids, most often in a defined molar ratio. This interaction establishes an extensive hydrogen-bonding network and a significant lowering of the melting temperature of the resulting mixture when compared to the original components.

Typically, DESs follow a general formula Cat^+X^-zY, where Cat^+ is a cation (commonly ammonium, phosphonium, or sulfonium), X^- is of course a Lewis base (most commonly a halide), and Y is a Lewis or Brønsted acid (associated with a donor). Depending on the exact donor and acceptor within each DES, they can be subdivided into four categories, each providing different physicochemical properties and applications. The versatility of DESs is due to the fact that there can be a substantial number of HBA's and HBD's that can be combined in a DES, and the ability to carefully control attributes of the DES, including its viscosity, polarity, ionic conductivity, and basicity,[393,394] and the following (Table 24) shows four different DES systems used in the literature.[395–397]

(Table 25) presents key quantitative and qualitative properties of representative DES systems, with a focus on Type III (the most common), and notes on electrochemical activity types.

Mechanistically, DESs interact with CO_2 through both physical and chemical interactions. The key role in the overall reaction mechanism is explained by the structuring of the functional groups found in the constituent components of the DES. So, while physical absorption is happening through physical interactions (dipole-quadrupole interactions or van der Waals interactions) that occur with CO_2 molecules and the DES matrix, the availability of other properties that can influence the DES (viscosity, polarity, and density) will affect the extent to which CO_2 can be absorbed. While the primary focus is the use of DES as electrolyte for capturing and conversion, some other research used the DES in electrodeposition Bohlen *et al.*[404] performed the electrodeposition of indium from 1 : 2 M choline based DES (ChCl : EG–1 : 2), employed them as an electrocatalyst for the electrochemical reduction of CO_2 to formate.[405]

(Table 26) demonstrates the way several deep eutectic solvents (DESs) utilize both chemical and physical mechanisms in relation to CO_2 capture, with their effectiveness determined by a complex balance of inherent molecular properties and environmental influences. Factors such as viscosity can be critical

Table 24 A summary of the four different DES systems

Components	Type	Example components	Notes
Quaternary ammonium salt + metal chloride	Type I	Choline chloride + $ZnCl_2$	Early studied DESs, often used in electrochemistry
Quaternary ammonium salt + metal chloride hydrate	Type II	Choline chloride + $CrCl_3{\cdot}6H_2O$	Like Type I but with hydrated metal salts
Quaternary ammonium salt + hydrogen bond donor	Type III	Choline chloride + urea, glycerol, acids	Most common; includes classic DESs and many NADES
Metal chloride hydrate + hydrogen bond donor	Type IV	$ZnCl_2{\cdot}6H_2O$ + urea	Metal-based, used for specific applications

Table 25 A quantitative and qualitative analysis of the different DES systems

Formation/ components	Type	HBA/HBD	Meltin point (°C)	Viscosity (mPa s, 25 °C)	Conductivity (mS cm^{-1}, 25 °C)	CO_2 interaction mechanism	Electrochemical suitability/ activity type
Choline chloride + $ZnCl_2$	I	ChCl/$ZnCl_2$	~20[398]	~750[399]	1.0–2.0[400]	Limited, depends on metal salt[401]	(Electroplating, batteries)[401]
Choline chloride + $CrCl_3 \cdot 6H_2O$	II	ChCl/$CrCl_3 \cdot 6H_2O$	~25[398]	~800[399]	0.8–1.5[400]	Limited, hydration effect[401]	(Electroplating, batteries)[401]
Choline chloride + urea (1 : 2)	III	ChCl/Urea	12[398]	750[399]	1.2–1.6[399]	Strong H-bonding; van der Waals; interaction energy with CO_2: −10.65 kcal mol^{-1},[401]	(Wide electrochemical window, electrocatalysis, batteries)[401]
Choline chloride + glycerol (1 : 2)	III	ChCl/Glycerol	−40 to −30[402]	324[399]	1.1–1.5[399]	H-bonding, moderate CO_2 affinity[403]	(Flow batteries, electrocatalysis)[401]
Choline chloride + ethylene glycol (1 : 2)	III	ChCl/EG	−66[401]	35[399]	2.0–3.0[399]	H-bonding, moderate CO_2 affinity[403]	(Electrocatalysis, sensors)[401]
$ZnCl_2 \cdot 6H_2O$ + urea	IV	$ZnCl_2 \cdot 6H_2O$/ urea	~30[398]	~900[399]	0.9–1.3[400]	Partial, less studied[401]	(Metal recovery, catalysis)[401]

since lower viscosity allows for greater gas diffusion and CO_2 solubility, while high viscosity can prevent mass transfer.[406–408] Adjustment of the molar ratio of hydrogen bond donors (HBD) and hydrogen bond acceptors (HBA) may mitigate this source of viscosity limitation.[409,410] Generally, increasing HBD content reduces viscosity and increases CO_2 uptake. Addition of co-solvents, including water or alcohols, for example, expands the range of operational conditions, while reducing viscosity and assisting with gas transport, but they also add to the risks of compromising the chemical reactivity of the DES solvent.[411,412] The presence of specific functional groups in the molecular structure of component one and two strongly influence the capture mechanism; amines will chemically bond CO_2 *via* the formation of carbamate, hydroxy groups can enhance bicarbonate creation, and basic anionic groups like acetate facilitate acid–base interactions.[370,407,413,414]

The polarity of DES solvents also contributes to solubility and overall absorption strength; higher polarity generally favors physical absorption, while stronger basicity promotes stronger chemical binding. The hydrogen bonding network present in the DES solvents also facilitates stabilization of CO_2-derived interaction intermediates, improving both capacity and selectivity.[415,416] Environmental conditions such as moderate temperatures optimize the balance between absorption and desorption, while increased pressure typically enhances CO_2 solubility, particularly in DESs that rely more on physical absorption.[417,418] Finally, hydrophobicity and density impact both the solvent's regeneration efficiency and its thermal stability. Together, these factors underscore the tunability of DESs and their promising potential for efficient and selective CO_2 capture.[419,420]

2. DES in carbon capture and electrochemical conversion

DES have become a recognized class of sustainable solvents for integrated CO_2 capture and electrochemical conversion, with unique properties that enable high CO_2 solubility and tunable physicochemical properties, as well as broad electrochemical stability. DESs are formed by a complexation of a hydrogen bond acceptor (HBA; *e.g.*, choline chloride) with a hydrogen bond donor (HBD; *e.g.*, urea, ethylene glycol, or proline), which generates an extensive hydrogen-bonding matrix. With complexation, melting points decrease substantially (for example, ChCl:urea has a melting point of over 300 °C, and when complexed, its melting temperature drops to ~12 °C). The fluidity and chemical reactivity exhibited by the DES enhances gas (CO_2) diffusion, with increased interaction from CO_2 molecules both through physical absorption and chemical binding (*i.e.*, carbamate or bicarbonate formation), directly dependent on the state of the DES (*i.e.*, higher interacting environment when functionalized with amines, hydroxyls, and carboxylic acids). Furthermore, the extensive hydrogen-bonding framework affords stabilization of important reaction intermediates, which yield a better selectivity and lower energy barrier of the electrochemical CO_2 reduction (ECO_2R) pathways. DESs also have a wide electrochemical window, often exhibiting >3 V, which support multi-electron CO_2 conversion reactions at cathodic potentials (*e.g.*, −1.9 V *vs.* SHE) without solvent degradation. The modular nature of DESs permits fine-tuning of viscosity, conductivity, and polarity, thus optimizing mass transfer and charge transfer during electrolysis. The low-cost, biodegradable ingredients used to produce DESs, for example, choline chloride produced from vitamin B4, make DESs cost-effective and environmentally friendly options compared to ionic liquids and traditional electrolytes. DESs offer the functionality of both a CO_2 absorbent and electrochemical medium with regard to certain formulations of DESs, including metal salt-based DESs, such as $ZnCl_2$:ethylene glycol. Metal salt-based DESs contain Lewis acid sites that catalysis CO_2 through redox chemistry directly at the electrode interface. This has been shown in studies resulting in faradaic efficiencies of 78% for CO (ChCl:urea) and 71% for formate (ChCl:proline), and the addition of the versatility of the product selectivity depending on the electrode material (Ag, Sn, Cu, Bi, Zn) utilized during the electrochemical process. While there are challenges associated with electrode stability over relatively long periods of time, as well as the difficulty associated with C_2^+ product formation, continuous advances such as the development of task-specific DESs and formatting targeted functional groups will likely expand applicability.[402,429–434]

A recent study by Halilu *et al.* investigated bifunctional ionic deep eutectic solvents (DESs) made of diethyl ammonium chloride (DEACI) and diethanolamine (DEA).[435] The study found that these solvents could be used as dual-function

Table 26 A summary of various deep eutectic solvents (DESs) that capture CO_2 through a combination of physical and chemical mechanisms

DES components (HBA:HBD)	DES type*	CO_2 capture mechanism	CO_2 capacity	Additional factors affecting adsorption	Ref.
TPAB : formic acid (1 : 2)	Type III (choline chloride analog)	Physical and chemical *via* hydrogen bonding from –OH of formic acid	Higher absorption with 1 : 2 ratio; viscosity at 25 °C: 53.98 mPa s	Viscosity decrease with higher HBD ratio enhances CO_2 solubility; temperature-dependent viscosity	410
DBN : ethylene glycol (varied ratios)	Type III	Chemical absorption *via* carbamate and carbonate formation (amine + hydroxyl synergy)	Max 0.17 g CO_2 per g DES at optimal ratio	Molar ratio of HBD critical; FTIR and NMR confirm carbamate and carbonate species	421
Methyltriphenylphosphonium bromide : ethylene glycol (1 : 4)	Type III	Physical absorption (physisorption)	0.074 mol CO_2 per mol DES at 303 K, 12 bar	Temperature and pressure influence solubility	391
Methyltriphenylphosphonium bromide : glycerol (1 : 3)	Type III	Physical absorption	0.075 mol CO_2 per mol DES at 303 K, 12 bar	Similar to above; solvent polarity and viscosity matter	391
Tetraalkylammonium chloride : 3-amino-1-propanol (1 : 4)	Type V (amine-based)	Chemical absorption *via* carbamate formation confirmed by FTIR	Best uptake among studied DESs (exact capacity not specified)	Molar ratio of HBD influences chemisorption efficiency	422
Choline chloride: proline: ethylene glycol (ternary)	Type V	Chemical absorption *via* carbamate formation with proline anion	Not quantified explicitly	Synergistic effect of amine and hydroxyl groups; thermal stability and viscosity important	413
Vanillin : 4-oxoisophorone (1 : 3)	Type III (hydrophobic)	Physical absorption	Comparable to selexol solvent (exact capacity not given)	Hydrophobicity, density >1.0 g mL^{-1}, thermal stability below 420 K	423
Various IL/DES combinations	Mixed types	Both physical and chemical absorption	Top 10 ILs/DESs ranked by CO_2 capture efficiency (specific values vary)	Polarity, viscosity, basicity, and COSMO-RS predicted properties influence performance	406
MTPB : diethylene glycol (1 : 4)	Type III	Physical absorption	0.1 mol CO_2 per mol DES@303 K, 12 bar	Low viscosity, increased pressure enhances solubility	424
MTPB : glycerol (1 : 3)	Type III	Physical absorption	0.075 mol CO_2 per mol DES	Hydrogen bonding density affects performance	424
TPAC : ethanolamine (1 : 4)	Type III	Chemical absorption (enhanced with EA)	1.4 mol CO_2 per kg DES	Functionalization with EA increases solubility to 3.2 mol kg^{-1}	425
[DBNH][Oxa] : EG (1 : 0.5)	Type III	Chemical absorption (carbamate + carbonate)	0.17 g CO_2 per g DES	Strong synergy of imino and hydroxyl groups	426
TBAB : 3-amino-1-propanol (1 : 4)	Type III	Chemical absorption	Not specified	Molar ratio significantly affects solubility	422
[MEAHCl][MDEA]	Type III	Carbamate + carbonate formation	Not specified	Best performance among amine-based DESs tested	427
[CHO][Arg]	Type III	Chemical absorption	0.6046 mol mol^{-1}@288.15 K, 4 bar	Amino acid-based IL, multiple amine sites increase uptake	428
TEAC : acetic acid (1 : 1) + GLY/EA	Type III	Physical absorption	Decreased compared to unfunctionalized	Addition of third component can reduce capacity	425
ChCl:MEA	Type III	Chemical absorption	Highest among tested (*vs.* DEA & MDEA)	High viscosity limits performance despite strong chemisorption	416
[MEA.Cl]:EDA	Type III	Chemical absorption	25.2 wt% CO_2 @ 0% water	Uptake drops as water content increases (competition for sites)	414

electrolytes for CO_2 capture and electroreduction, with the DEACI-DEA (1 : 3) composition showing the best results (Fig. 66a). This DES had a deep eutectic point of −69.78 °C, good thermal stability, and a long cathodic limit of −1.7 V *versus* Ag/AgCl. This made it possible to reduce CO_2 at −1.5 V with a faradaic efficiency (FE) of 94% and a capture capacity of 52.71 mol L^{-1} after 350 s of sparging (Fig. 66b and c). Conventional aqueous electrolytes, on the other hand, usually have CO_2 solubilities < 0.03 mol L^{-1} at room temperature and only sometimes reach 40–60% FE because the hydrogen evolution process (HER) is more common at negative potentials. Ionic liquids can also have high FE (70–90%), but they usually have low CO_2 solubility ($\sim$0.2–0.4 mol L^{-1}) and high viscosity, which makes it hard to move mass and scale up (Fig. 66d and e). DEACI–DEA, on the other hand, has a strong CO_2 uptake and an efficient conversion while keeping HER low. Electrochemical impedance spectroscopy demonstrated CO_2 chemisorption by a decrease in double-layer capacitance from 8.76×10^{-9} F to 3.15×10^{-9} F. Simultaneously, COSMO-RS analysis indicated bifunctional interactions of both HBA and HBD sites with CO_2 through n-orbital overlap in the non-polar region (Fig. 66f). Chronoamperometric studies revealed an initial diffusion-limited regime succeeded by a steady state in which capture, and conversion reached equilibrium, thereby establishing a direct correlation between absorption capacity and electroreduction kinetics. These results collectively demonstrate that, in contrast to aqueous or ionic liquid systems, DEACI-DEA provides a distinctive equilibrium of solubility, stability, and selectivity, thereby establishing bifunctional deep eutectic solvents (DESs) with enhanced cathodic windows as a logical design framework for next-generation CO_2 capture and electro conversion technologies.

Based on (Table 27), Deep eutectic solvents (DESs) possess numerous electrochemical advantages over traditional aqueous electrolytes for CO_2 reduction applications. As mentioned above, there are some cases when DESs have marginally lower ionic conductivities than aqueous media, the larger electrochemical

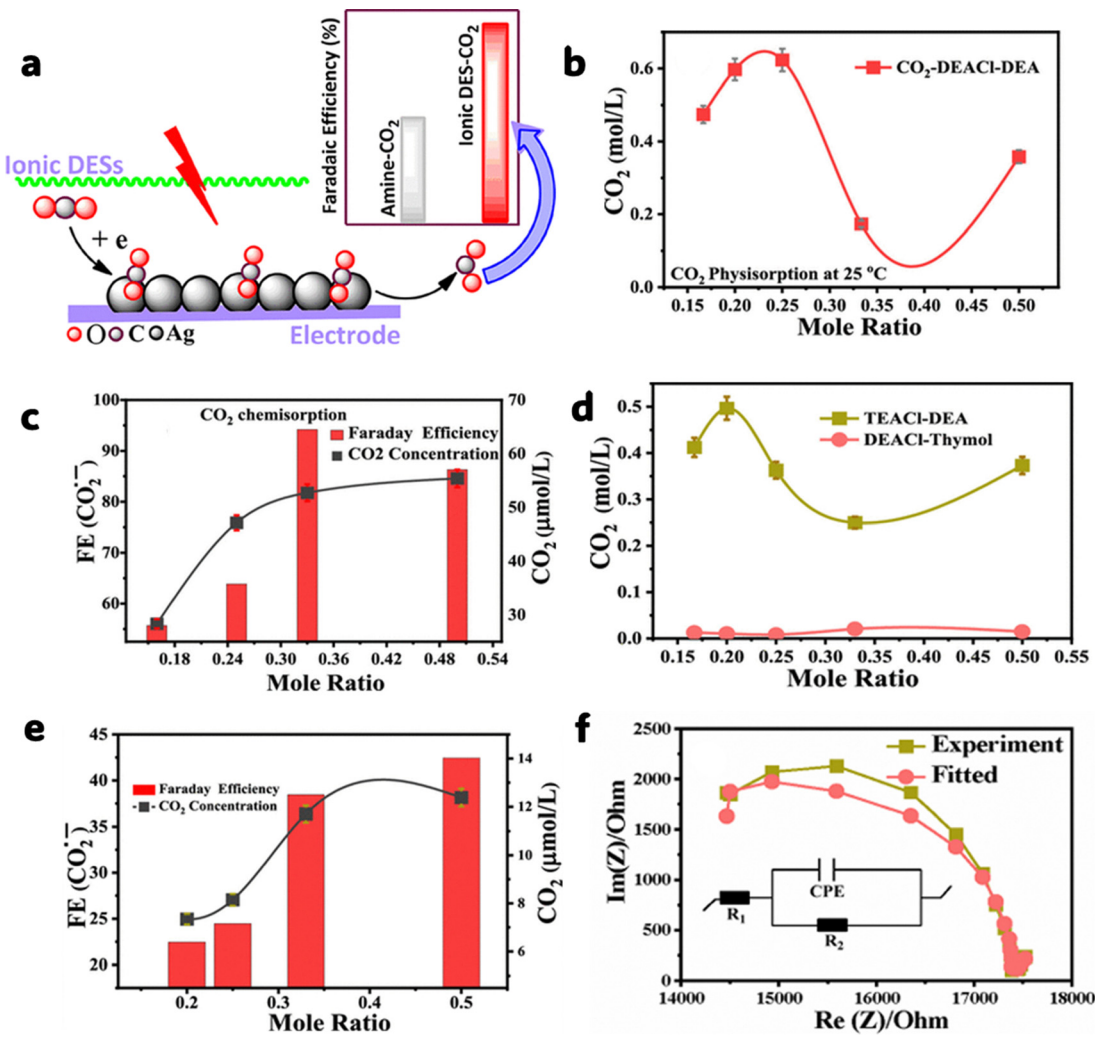

Fig. 66 (a) The graphical representation of CO_2 adsorption and electroreduction by DEACl–DEA. (b) Physisorption of CO_2 by DEACl–DEA. (c) FE of CO_2 electroreduction to CO_2. (d) Physisorption of CO_2 by DEACl-thymol and TEACl–DEA. (e) FE of CO_2 electroreduction to CO_2 in TEACl–DEA where the secondary axis shows the amount of CO_2 chemisorbed. (f) Nyquist plot for CO_2 saturated DEACl–DEA. Reprinted (adapted) from *ACS Omega* 2022, **7**(42), 37764–37773. Copyright © 2022, The Authors. Published by American Chemical Society under the terms of CC-BY-NC-ND 4.0 license.

Table 27 The performance of various Deep Eutectic Solvents (DESs) used in carbon capture and electrochemical conversion

DES used (HBA : HBD, ratio)	Electrode	Main product	FE (%) (DES *vs.* aq.)	Current density (mA cm^{-2})	Conductivity (DES/aq.)	Conventional electrolyte (comparison)	Electrochemical advantage	Ref.
Choline chloride : ethylene glycol (1 : 2)	Au sheet	CO	81.8% (DES, not compared to aq.)	1.1 (at −1.6 V)	6.8 mS cm^{-1} (DES)	0.1 M $TBAPF_6$/DMF	Lower overpotential, higher CO_2 solubility, selective CO production	436
Choline chloride : urea (1 : 2)	Ag foil	CO	96% (DES, not compared to aq.)	∼4.8 (at −0.884 V)	34.5–131.4 mS cm^{-1} (with KCl)	0.5 M $KHCO_3$	High selectivity for CO, HER suppression	429
Choline chloride : ethylene glycol (1 : 2)	Ag foil	CO	78–98.8% (in acetonitrile)	0.4–20 (in acetonitrile)	Not specified	Water, Acetonitrile, Propylene Carbonate	High CO selectivity in aprotic media, tunable viscosity/ selectivity	437
Choline chloride : urea (1 : 2)	Ag NPs/GDE	CO	94.1% (DES, not compared to aq.)	11.6 (at −0.83 V)	34.5–131.4 mS cm^{-1} (with KCl)	0.5 M H_2SO_4	High selectivity, improved current density with salt	436
Choline chloride : ethylene glycol (1 : 2), choline chloride : urea (1 : 2)	Au, Ag, Cu, Zn	CO, HCOOH	15.8–98.8% (varies)	0.1–20 (varies)	1.5–1244 cP (viscosity)	Aqueous, acetonitrile, propylene carbonate	Wide potential window, tunable selectivity, high CO_2 solubility	430
Choline chloride : urea (1 : 2)	Roughened Ag foil	CO	96%	∼4.8 at −0.884 V *vs.* RHE	0.1 M $KHCO_3$	HER suppression, surface restructuring	HER suppression, surface restructuring	438
Choline chloride : urea (1 : 2)	Ag	CO	90%	Not specified	0.5 M $KHCO_3$	High selectivity, low overpotential	High selectivity, low overpotential	430
Choline chloride : urea (1 : 2)	Ag	CO	92%	Not specified	0.5 M $KHCO_3$	High selectivity, improved current density	High selectivity, improved current density	
Choline chloride : urea (1 : 2), with KCl	Ag-based GDE	CO	Not directly reported; higher j_{CO} with DES/KCl	Not specified (improved with KCl in DES)	Not specified	Aqueous KOH, KCl, Emim Cl	Enhanced CO_2 absorption, improved current density	437
Choline chloride : ethylene glycol (1 : 2), imidazolium chloride:EG	Ag	CO	High FE for CO (exact % not specified)	Not specified	Not specified	RTILs, aqueous	Non-toxic, cost-effective, improved solubility/selectivity	439
$ZnCl_2$: EA (1 : 4), $CoCl_2$: EA (1 : 4); DEACl : DEA (1 : 3)	Single-atom Ag, Ag	CO_2	Up to 94% (DEACl:DEA 1 : 3)	Not specified	Up to 36 200 μS cm^{-1} ($ZnCl_2$/EA)	Not specified	High CO_2 absorption, unique interfacial phenomena, bifunctional sorption, wide cathodic window	
MEAHCl:MDEA	Ag	CO	71%	Not reported	Not reported	Not reported	Amine-functionalized DES promoted CO_2-to-CO conversion	429
ChCl : ethylene glycol (1 : 2)	In	Formate	Up to 95%	Not reported	Not reported	Not reported	Selective formate production in DES medium	
[Ch][Cl] : urea (1 : 2), 50 wt% in H_2O	Roughened Ag foil	CO	96% *vs.* lower in aq. $KHCO_3$	∼4.8	34.5 mS cm^{-1} (DES), 131.4 mS cm^{-1} (DES + KCl)	0.5 M $KHCO_3$	Restructures Ag surface, suppresses HER	
[MEAH][Cl] : MDEA (1 : 4), 0.4 M in H_2O	Ag foil	CO	71% *vs.* lower in water	10.5	Not explicitly given	Aqueous only	Amine-DES enhances COOH* intermediate stabilization	
[Ch][Cl] : EG (1 : 2), 0.1 M in H_2O	Ag foil	CO	Up to 94.1%	11.6 (w/KCl: 22.1)	34.5 → 131.4 mS cm^{-1} (w/KCl)	Aqueous H_2SO_4	Addition of KCl doubled current density with same FE	
[Ch][Cl] : urea (1 : 2), 2 M in H_2O	Ag NPs/GDE	CO	94.10%	11.6	Not directly reported	Aqueous	KCl enhances conductivity and performance	
[Ch][Cl] : EG (1 : 2), 1 M in acetonitrile	Not specified	CO	98.80%	20	Not specified	—	High FE in aprotic solvent system	
[Ch][Cl] : EG (1 : 2), neat	Au metal sheet	CO	81.80%	1.1	Not reported	—	High selectivity even without co-solvent	
[Ch][Cl] : EG (1 : 2), in propylene carbonate	$Cu_{0.3}Zn_{9.7}$ on Cu foam	CO	94.90%	∼16	Not specified	0.1 M H_2SO_4	Enhanced CO selectivity on Cu-based alloy	

window (often more than 3 V) when using DESs permits the application of higher overpotentials for CO_2 reduction without stress from solvent degradation.[430,436]

DESs have consistently produced higher faradaic efficiencies for target products such as CO, formate, and ethylene, due in part to their higher solubility of CO_2, as well as providing a more stable medium for intermediates formed throughout the reaction, which benefit from the networks of hydrogen bonding exhibited in these solvents. The DESs have also improved product selectivity and stability when subjected to reaction conditions compared to their aqueous counterparts, leading to less decay of phase separation and electrode damage over cyclic runs while DESs can be prepared readily in a single step from low-cost precursor materials, and do not require a purification step.[429,440]

3. Challenges, future outlook, and economic analysis

While the results are promising, several challenges are present. First, there is still limited information about the intermediate species formed during the reduction process. Second, the stability of some DES electrodes appears poor over the long term. Third, multi-carbon product selectivity is difficult to obtain. However, one promising direction in research involving deep-eutectic-solvents (DES) is investigating hybrid or polymer-modified DES systems to improve CO_2 capture and electrochemical conversion efficiencies further. The incorporation of polymers in DES matrices presents a valuable avenue to modify physicochemical properties such as viscosity, conductance, and stability, which may even address some of the challenges present in traditional DES. Improvements on mass transfer may be possible, enabling the potential for lower viscosity and the formation of microenvironments that facilitate CO_2 diffusion, transport, and interactions with active sites. In addition to manipulating the viscosity of DES, the addition of polymers may also introduce additional functional groups that can interact with the DES to create chemical absorption interactions, improve the stabilization of reactive intermediates during electrochemical reduction, and, due to their modification of the viscosity, also improve the electrochemical stability of DES.

Polymer-enhanced deep eutectic solvents

Polymer-based eutectic systems, particularly polymerizable deep eutectic solvents (DES), offer distinct advantages over traditional DES by integrating polymerization capabilities directly into the eutectic framework. These systems act as multi-functional platforms serving simultaneously as solvent, monomer, and templating agent, which streamlines synthesis while enhancing material properties. For instance, DES-polymer hybrids achieve superior mechanical strength (*e.g.*, hydrogels with high cross-linking density, reducing swelling) and improved thermal stability compared to non-polymerized DES. They also enable faster polymerization kinetics under milder conditions (*e.g.*, visible-light RAFT polymerization in open air) and facilitate eco-friendly synthesis by eliminating volatile organic solvents. Additionally, polymerizable eutectics expand application versatility, enabling advanced electrochemical performance in batteries (*e.g.*, high ionic conductivity and cycling stability) and precision in nanostructured sensing films. These advantages position polymer-enhanced eutectics as transformative for sustainable material design.[441] In CO_2 capturing, based on the search results, only one publication explicitly details the use of polymer-enhanced deep eutectic solvents (DES) for CO_2 capture. The study by Nunes (2021) developed Polymeric Deep Eutectic Solvents (PRIDES) hybridized with the bi opolymer chitosan for CO_2 capture[442] as illustrated in (Table 28).

The ternary deep eutectic solvent (DES) composed of choline chloride, glycerol, and citric acid, when combined with 1% w/w chitosan, achieved a remarkable CO_2 capture capacity of 768.74 mmol kg^{-1} at 10 bar, significantly outperforming the same DES without chitosan, which captured only 110.11 mmol kg^{-1} at atmospheric pressure. This enhancement is attributed to chitosan's amino groups, which facilitate additional chemical adsorption of CO_2 under elevated pressure. In comparison, a standalone DES of tetrabutylammonium bromide and polyethylene glycol (PEG 200) captured 120.44 mmol kg^{-1} at ambient conditions. Notably, among available studies, only Nunes (2021) explores a DES-polymer composite system, highlighting the unique role of chitosan in improving CO_2 capture performance, whereas most other research focuses on additives such as amines or support materials such as silica, rather than incorporating polymeric matrices.

To boost the kinetics of CO_2 electrochemical conversion, we need to optimize the reactor configuration and the operating conditions. Gas diffusion electrodes (GDEs) typically used in flow cells allow direct CO_2 to contact the catalyst interface, drastically boosting mass transport while reducing the ubiquitous diffusion limitations found in other liquid-phase reactors, as shown in (Fig. 67).[443] By pressurizing the electrochemical cell, the solubility of CO_2 is significantly increased in the reaction medium due to Henry's law, which maximizes the availability of CO_2 at the interface and/or reduces the kinetics as detailed in (Table 29).[444] With regards to gas solubility and kinetics, lowering the temperature also has advantages, but greater gains may need to be weighed against lower reaction rates at lower thermal energies.[445] Additionally,

Table 28 A summary of the DES composition, polymer used, and key performance metrics

DES composition	Polymer used	Polymer concentration	CO_2 capture performance	Conditions
Choline chloride-glycerol-citric acid	Chitosan	1% w/w	768.74 mmol CO_2 per kg DES	10 bar pressure
Choline chloride-glycerol-citric acid	—	0% w/w	110.11 mmol CO_2 per kg DES	Atmospheric pressure, CO_2 flow
Tetrabutylammonium bromide-PEG 200	None	N/A	120.44 mmol CO_2 per kg DES	Atmospheric pressure, 25 °C

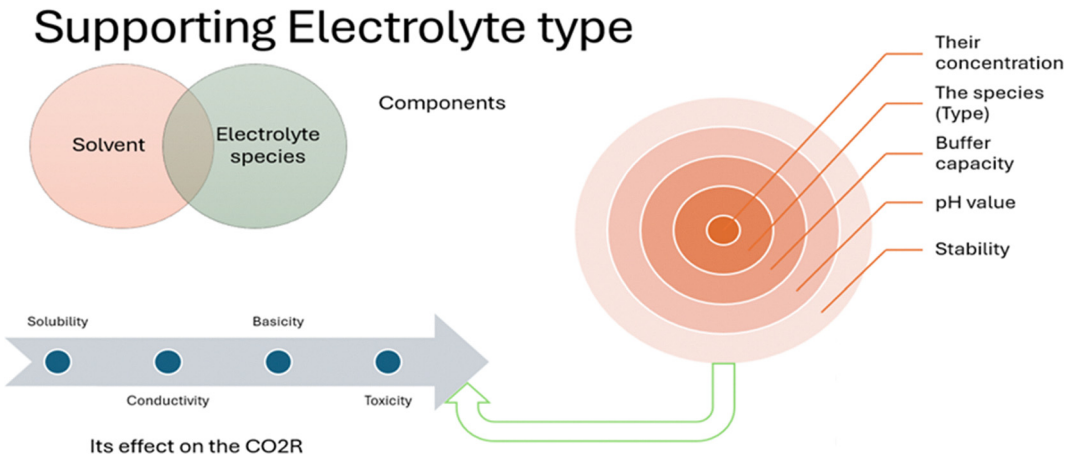

Fig. 67 A schematic overview of a supporting electrolyte, detailing its core components and the key physicochemical properties.

Table 29 Key operational parameters and the kinetic impact on the electrochemical reduction of CO_2

Parameter	Kinetic impact
Gas diffusion electrodes (GDEs)	↑ Mass transport; ↑ Stability (~450 mA cm^{-2} for 200+ hours)
Pressure optimization	↑ CO_2 surface coverage; ↑ Formate selectivity (up to 50 bar)
Flow rate tuning	↑ CO_2 supply; ↓ Blockage (optimal: 10–20 sccm)
Catalyst nanostructuring	↑ C_2^+ selectivity; ↑ Current density (*e.g.*, Cu nanowires: 77.7% FE at 233.2 mA cm^{-2})
Reactor configuration	↓ Ohmic resistance; ↑ Efficiency (*e.g.*, zero-gap cells at 10 bar)
Temperature management	Balances CO_2 solubility/reaction kinetics (20–40 °C)

some studies have reported that tuning ionic strength or salinity of the electrolyte will impact the CO_2 capture and transport across the two-phase interface, but at times, the results are conflicting or complex.[446] Flow rate, while not specifically noted in the literature, is critical for maintaining the available CO_2 supply and removing the gaseous product, in turn affecting kinetics and selectivity. Higher flows will optimize the mass transfer but will decrease the residence times, so greater effort may need to be directed to optimizing flow rate depending on scale and design.[443]

Molten salts

The Molten salt CO_2 electrolysis is an innovative method that integrates CO_2 capture and conversion. The method's development commenced in the 1960s and has rapidly proliferated since the 2000s. This technology facilitates the capture of CO_2 from elevated-temperature flue gas, enabling the direct conversion of the collected CO_2 in the molten salt electrolyte at high temperatures into useful products, including carbon, carbon monoxide, and O_2.[447] Due to its higher energy consumption and reduced current efficiency, CO is not an optimal product. Researchers are increasingly focused on the production of high-quality carbon materials and the manipulation of their nanostructures.

Molten salt electrolysis, utilizing an anhydrous electrolyte that focuses on carbon creation, can yield a singular solid carbon product with elevated current efficiency, thereby circumventing intricate byproducts that necessitate challenging or many separations. Moreover, the *in situ* conversion of CO_2 into value-added products obviates supplementary expenses following carbon capture, such as CO_2 transportation fees, disputed and uncertain storage, and maintenance expenditures, *etc.*[448,449] A molten salt CO_2 electrolysis facility is anticipated to generate a net profit of $50 000 per ton of captured CO_2 for a power station when the final electrolysis product is carbon nanotubes (CNTs).[450] A common technique for synthesizing carbon nanotubes (CNTs) is chemical vapor deposition (CVD), requiring at least 1440 MJ and producing 28.55 kg of CO_2 for the generation of one gram of CNTs.[451,452] Thus, this profit and these advantages can promote the expansion of the molten technique for prospective plants and improve the execution of carbon capture in conventional power plants, surpassing the financial drawbacks linked to the aforementioned technologies, as shown in (Fig. 68).

The method of capturing CO_2 using molten salt and electrochemical conversion is efficient and advantageous, as it facilitates the immobilization of CO_2 and its transformation into valuable goods. The molten salt electrochemical unit features a straightforward design comprising an insulated electrolyzer, electrolyte, heating unit, cathode, and anode. The absence of additional equipment facilitates ease of usage and management.[453,454] Secondly, the molten salt possesses an extensive electrochemical window, and no side reactions occur during operation.[455,456] Third, electrons serve as the reducing agent for CO_2 reduction *via* molten salt. The effective current density during electrolysis can be adjusted to regulate the conversion rate of CO_2 into solid carbon compounds.[457,458] The molten salt electrolyte primarily consists of carbonate, which is inexpensive to produce and can be reused, hence minimizing operational costs.[457,459] Ultimately,

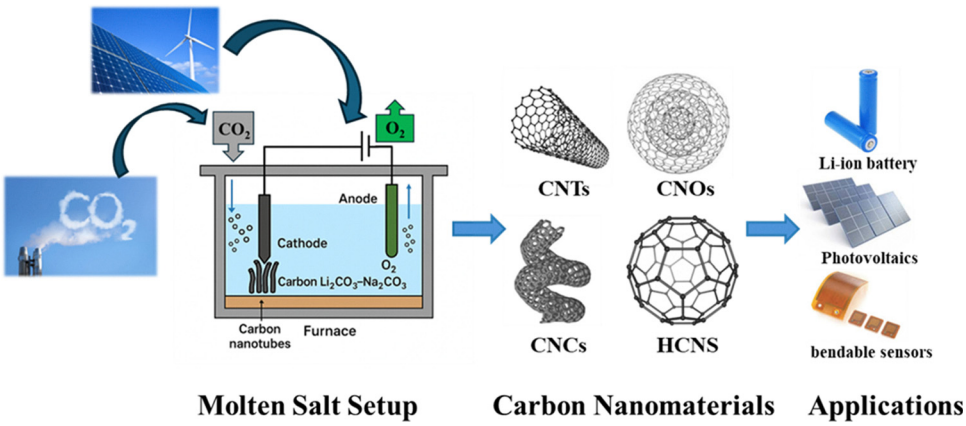

Fig. 68 Process schematic of molten salt electrolysis for integrated CO_2 capture, electrocatalytic conversion, and carbon nanomaterial production with rate-matched kinetics.

carbonate electrolyte exhibits high solubility in CO_2 and is highly effective in capturing CO_2.[460]

1. Process of CO_2 capture and conversion in molten salt systems

The process of CO_2 capture and conversion in molten salt systems is governed by a combination of chemical absorption and electrochemical transformation steps.

(A) CO_2 capture in molten salts. When CO_2 gas is introduced into the molten salt (commonly carbonates or chlorides), it reacts with oxide ions (O^{2-}) or directly dissolves to form carbonate ions (CO_3^{2-}):[461,462]

$$CO_{2g} + O^{2-} \rightarrow CO_3^{2-} \quad (1)$$

The efficiency of this absorption is highly dependent on the composition of the molten salt, with ternary carbonates (*e.g.*, Li–Na–K) and binary chlorides (*e.g.*, Li–K) showing high solubility for CO_2 and favorable absorption kinetics:[462]

(B) Electrochemical conversion at electrodes

(a) Cathode reactions. The widely accepted cathodic reactions are the 4-electron reaction and the 2-electron reaction processes, which are closely related to the electrolyte reaction temperature.

- The 4-electron reaction (low to moderate temperatures):

$$CO_3^{2-} + 4e^- \rightarrow C_s + 3O^{2-} \quad (2)$$

This reaction leads to the deposition of solid carbon (which can be amorphous carbon, carbon nanotubes, or other nanostructures) on the cathode.[463]

- The 2-electron reaction (higher temperatures):

$$CO_3^{2-} + 2e^- \rightarrow CO_g + 2O^{2-} \quad (3)$$

At elevated temperatures, the formation of CO becomes thermodynamically favored over solid carbon, shifting the selectivity toward CO production.[464]

(b) Anode reactions. The oxygen ions generated at the cathode migrate to the anode, where they are oxidized to release oxygen gas:[465]

$$2O^{2-} \rightarrow O_{2g} + 4e^- \quad (4)$$

In some systems, the anode may also participate in the oxidation of other species, depending on the electrode material and cell design.

(C) Electrolytes. Researchers have predominantly examined carbonates, chlorides, and oxides containing Li^+, Ca^{2+}, Na^+, and K^+ due to their extensive electrochemical windows and high CO_2 solubility.[466] Carbonates and chlorides are prevalent in salts, typically containing oxides in concentrations between 1 wt% and 30 wt%. Various types of salts possess distinct advantages and disadvantages, prompting researchers to amalgamate them to get optimal results, such as reduced melting points. However, it is essential to understand the characteristics of the salts prior to their amalgamation.

(a) Carbonates or chlorides. Molten chlorides such as LiCl–KCl exhibit inadequate CO_2 absorption. Consequently, chlorides must collaborate with oxides or carbonates to enhance carbon absorption and conversion, as shown in (Fig. 69a). In comparison to carbonate electrolytes with oxide additives, chloride electrolytes with oxide additives exhibit accelerated CO_2 absorption, achieving equilibrium within 2 hours, hence indicating superior CO_2 absorption performance. The reaction of Li_2O and CO_2 resulting in Li_2CO_3 is responsible for the high absorption capacity. The conversion efficiency of Li_2O to Li_2CO_3 nearly doubled in molten chloride electrolyte (about 94%) compared to molten carbonate electrolyte (around 45%), demonstrating that the molten salt composition influences both the thermodynamics and kinetics of Li_2O conversion.[467] Moreover, combined salts often have lower melting points than their pure components.[468] Kanai *et al.* are among the limited research groups examining mass transport in molten carbonates, as illustrated in (Fig. 69b). Increased temperature improved CO_2 solubility in both binary (Li–K) and ternary (Li–K–Na) molten carbonates, with solubility values for the two carbonate types being similar.[469]

(b) Cation selections. (Table 30) indicates that carbon deposition occurs more readily in Li, Ca, and Ba carbonates compared to Na or K carbonates.[470] At respective melting points, Li_2CO_3 has a conductivity of 6 S cm^{-1}, which is double that of Na_2CO_3

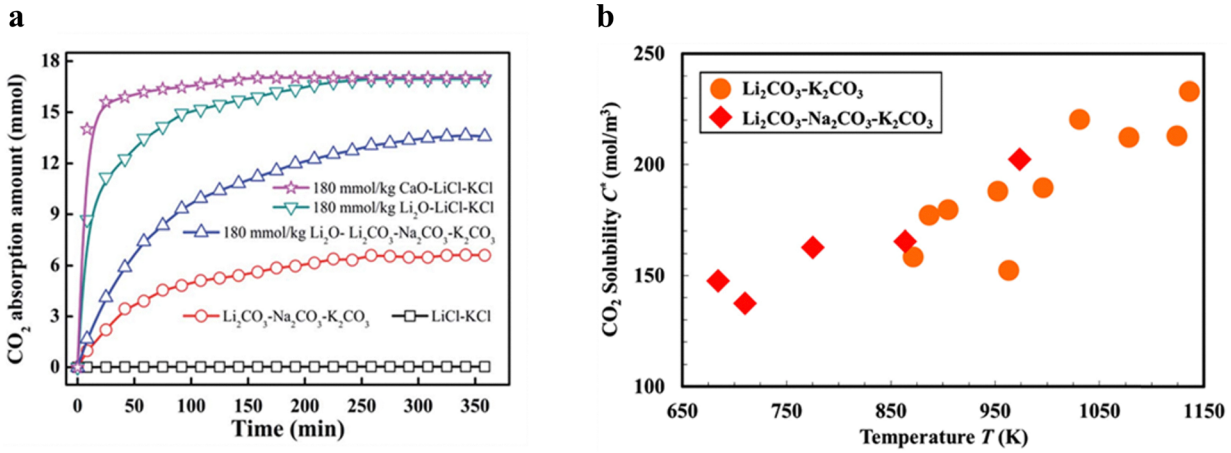

Fig. 69 (a) CO_2 absorption curves in different molten salts at 450 °C with the CO_2 partial pressure of 50 kPa. (b) CO_2 solubility in molten carbonates at different temperatures at 1.01 × 10^5 Pa. Reprinted (adapted) from *Ind. Chem. Mater.*, 2023, **1**, 595. Copyright © 2023, The Authors. Published by Royal Society of Chemistry under the terms of CC-BY license.

Table 30 Deposition potentials (*vs.* CO_3^{2-}/CO_2–O_2) of alkali and alkaline earth metals, and carbon in their molten carbonate salts at 600 °C

Molten salt	Alkali metal (V)	Carbon (V)
$CaCO_3$	−3.033	−1.349
Li_2CO_3	−2.964	−1.719
$BaCO_3$	−3.069	−1.992
Na_2CO_3	−2.546	−2.551
K_2CO_3	−2.612	−3.083

and triple that of K_2CO_3. Increased conductivity reduces ohmic loss, facilitating the movement of electrons or reactants.[471] Furthermore, Li or Ca carbonates exhibit greater stability and utility compared to Na or K carbonates when considering factors such as deposition potentials, thermal decomposition, and the quality of the resultant carbon.

Various cations in carbonates produce distinct carbon nanostructures. Li^+ and Ba^{2+} are believed to facilitate the formation of carbon nanotubes, but K^+ inhibits the growth of carbon nanostructures.[472] Recent studies indicate that electrolytes containing over 50 wt% Na or more than 30 wt% K carbonates inhibit the growth of carbon nanotubes (CNTs) while accelerating the formation of carbon nano-scaffolds (CNS).[473]

(c) Additives. A prominent research area centers on molten salt carbon dioxide capture and electrolysis for the production of carbon nanotubes and other specialized nanostructures. Foreign metal oxides act as essential nucleation sites for the formation of specific carbon nanostructures, particularly carbon nanotubes. Diverse metal oxides have been evaluated and analyzed for carbon nanostructures. Additives of Zn or ZnO were advantageous for the production of carbon nanofibers.[474] Fe_2O_3 is a widely utilized additive, too. In certain instances, the electrodes comprise transition metals that may be reduced to metallic elements during electrolysis.[475] These transition metals enabled the formation of the apex and the end of a carbon nanotube (CNT). The incorporation of metal oxides enhances CO_2 absorption and triggers subsequent carbon deposition, while concurrently introducing significant defects into the resultant carbon products (*e.g.*, CNT).[476,477]

(D) Electrodes. The anode and cathode constitute the primary components of the molten salt CO_2 electrolysis systems. During the capture and conversion process, each component has a distinct role. The primary function of the anode is to facilitate oxygen evolution, whereas the cathode's principal role is to retain carbon, enabling the formation of various carbon nanostructure.[478] For optimal performance, the anode must facilitate oxygen production, while the cathode should possess active sites that promote the nucleation and growth of specific carbon materials, such as carbon nanotubes or nanofibers.[479] Both electrodes must exhibit substantial corrosion resistance, despite their distinct functions. This is due to their operation in extremely hostile conditions, such as molten carbonate salts.[480]

(a) Cathode. The cathode plays a critical role in molten salt CO_2 reduction reactions (CO_2RR) as it controls the efficiency and selectivity of CO_2 reduction as well as the morphology, purity, and functionality of the carbon products that are generated. Recent years have seen significant advancements in cathode material design, process optimization, and mechanistic understanding. Because of their beneficial catalytic properties, metals like Ni, Fe, Mo, Ti, and their alloys have been the subject of most research. Transition metals, particularly Ni and Fe, are known to catalyze the nucleation and growth of carbon nanostructures.[474] Furthermore, alloys including NiCr, CuNi, and FeNi are specifically engineered to balance catalytic performance with corrosion resistance.[481] For example, NiCr alloys have demonstrated improved durability in molten carbonate environments compared to pure Ni, thus extending electrode lifespan and maintaining process efficiency.[482] In addition to solid metals and alloys, low-melting-point metals such as Sn and Bi have also been studied as liquid cathodes. These materials can dynamically catalyze carbon growth and help form core–shell structures such as Sn@C, in addition to suppressing the Boudouard reaction and increasing current efficiency.[483] Furthermore, metal oxides like

TiO_2, NiO, and MoO_3 provide exceptional corrosion resistance and can act as stable scaffolds for catalytic metal nanoparticles. Interestingly, some oxides have the ability to engage in redox cycling, which opens up new channels for the reduction of CO_2.[484–486]

(b) Anode. The anode material must exhibit exceptional resistance to corrosion and degradation from prolonged usage in an oxidative environment. Prevalent anode materials include metals, alloys, metal oxides, and carbon-based compounds. Researchers frequently select alloys composed of tin dioxide (SnO_2), nickel oxide (NiO), platinum (Pt), and nickel (Ni) due to their exceptional durability and superior electrochemical characteristics. This renders them ideal for application in molten salt CO_2 electrolysis systems requiring prolonged operation.[475,487–489] Furthermore, carbon-based anodes such as graphite, glassy carbon, and amorphous carbon are highly useful due to their chemical stability.[490,491]

The anode serves a pivotal function in molten salt electrolysis by catalyzing oxygen evolution and ensuring that O^{2-} ions do not accumulate within the electrolyte.[492] Since free O^{2-} ions are not stable in molten salts, they rapidly react with dissolved CO_2 or metal ions, forming carbonate ions (CO_3^{2-}) and metal oxides.[493,494] To maintain efficient carbon deposition at the cathode, it is essential that O^{2-} ions are removed promptly, which in turn sustains the necessary electrical current for the process as illustrated in (Table 31).

2. Morphology and structure of the carbon products

Licht, S. *et al.* successfully synthesized CNTs with a productivity of 80–100% in molten Li_2CO_3–Li_2O (4 M Li_2O in Li_2CO_3) using a Ni anode and a steel cathode at 750 °C.[505] In this electrolysis system, nickel at the anode is oxidized to form Ni^{2+} ions, which then move to the cathode. There, these ions are reduced back to metallic nickel, providing nucleation sites for carbon nanotube (CNT) growth. Additionally, the presence of Li_2O in the molten mixture converts straight CNTs into tangled ones by introducing extra defects into their structure (Fig. 70a–c).

Peng *et al.* illustrated how the ZnO ratio affects morphology and the percentage of carbon nanotubes (CNTs) in cathodic carbon products.[506] They found that using Li_2CO_3 electrolyte with 1% ZnO supports CNT formation. This is likely because ZnO reduces the energy barrier for both nucleation and carbon deposition. The results show that the ZnO content significantly affects CNT growth; with only less than 50% of CNTs observed in Li_2CO_3 electrolyte containing 0.5% and 2% ZnO, compared to over 90% in the 1% ZnO setup, as shown in (Fig. 70d–f). Additionally, in a Li_2CO_3–Na_2CO_3 (1 : 1 weight ratio) system, adding 1% ZnO results in carbon products with more than 80% CNTs. This evidence indicates that it is possible to use more cost-effective electrolytes for CNT production.

Yu, R. *et al.* developed a novel Ge@CNT composite material to address the limitation of carbon-based anodes in lithium-ion batteries (LIBs) regarding charge capacity.[486] The incorporation of germanium and carbon nanotubes significantly enhances the battery's overall performance. The synthesis occurs in a heated mixture of NaCl, $CaCl_2$, and CaO, which additionally contains GeO_2. The reaction initiates when GeO_2 interacts with ionized Ca^{2+} in the molten salt. This produces a liquid CaGe alloy. This alloy phase facilitates the development of carbon nanotubes by accelerating the process. (Fig. 71a and b) illustrates the completed assembly, featuring several germanium nanoparticles embedded directly into the carbon nanotube matrix. This unique configuration integrates germanium's capacity to retain substantial lithium with the stable, conductive framework of carbon nanotubes. This addresses the common issues associated with carbon. In addition, various M@CNTs, such as Sn@CNTs, Zn@CNTs, and Fe@CNTs, were synthesized, and CO_2 was reduced in molten salts.[483] The mechanisms by which these three M@CNTs evolve are fundamentally different from the nucleation process of liquid metals. (Fig. 71c) illustrates the

Table 31 Effect of molten salt and cathode components on the morphology of carbon products

Electrolyte	T (°C)	Cathode	Anode	Current density	Products	Ref.
Li_2CO_3	770	Galvanized steel; Ni–Cr	Ni–Cr; galvanized steel	1 A	Multi-walled carbon nanotubes (MWCNTs)	482
Ta_2O_5–$CaCl_2$–CaO	650	Ni	Graphite	0.2–1 A cm^{-2}	Carbon particles	490
Li_2CO_3–Li_2O	770	Cu	Ir–Pt	0.2 A cm^{-2}	Carbon nano-onions; CNTs	495
Li_2CO_3–Li_2O–CaO–H_3BO_3	770	Muntz brass sheet	Nichrome sheet	0.2 A cm^{-2}	Carbon nanotubes (CNTs)	496
Li_2CO_3–Na_2CO_3–K_2CO_3–H_3BO_3	670	Muntz brass sheet	Inconel		CNTs	473
Li_2CO_3–Na_2CO_3–K_2CO_3	450–650	Ni	SnO_2	0.2–4 A g^{-1}	Activated carbons	487
Li_2CO_3–Li_2O	770	Muntz brass as	Inconel 718; Nichrome; Incoloy	0.5 A	Fe_3C; CNTs	463
LiCl–Li_2CO_3–$LiBO_2$	550	Ni	Graphite	25–100 mA cm^{-2}	CO	497
LiCl–Li_2CO_3–$LiBO_2$	550	Ni	Graphite		Carbon nanofibers (CNFs); CO	498
Li_2CO_3	730	Galvanized steel	Pt		Graphene; CNTs	488
Li_2CO_3–K_2CO_3–Na_2CO_3	650	NiO–Co_3O_4	$Ni_{10}Cu_{11}Fe$	10 mA cm^{-2}	NiCo@g-c powder	485
Li_2CO_3–K_2CO_3–Na_2CO_3	650–750	Ni	Pt	5–100 mA cm^{-2}	Graphite	499
Li_2CO_3–Na_2CO_3	750	Brass	Inconel 718	200 mA cm^{-2}	CNTs	500
Li_2CO_3	750	Ni	SS	7.5 A	Carbon sphere	501
NaCl-$CaCl_2$-CaO	750	GeO_2	Graphite	2000 mA g^{-1}	Ge@CNTs	486
Li_2CO_3–Na_2CO_3–K_2CO_3	450	nickel foam	Glassy carbon	500 mA g^{-1}	Porous carbon	491
Li_2CO_3	780	nickel foam	Glassy carbon	600 mA g^{-1}	Crystalline nano-graphite	502
Li_2CO_3-K2CO3-Na2CO3	500	Galvanized Fe wire	Ni wire	—	Honeycomb carbon nanostructure	503
Na_2CO_3-K_2CO_3		FeNi foam	$Ni_{10}Cu_{11}Fe$ alloy	100 mA cm^{-2}	CO	504

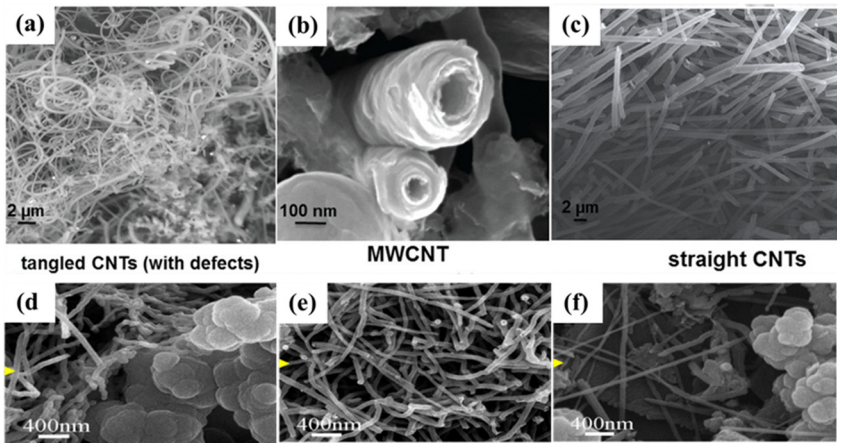

Fig. 70 (a)–(c) SEM images showing the different CNT morphologies formed based on either the addition of Li_2O. Reprinted (adapted) from *ACS Cent. Sci.* 2016, **2**(3), 162–168. Copyright © 2016, American Chemical Society under the terms of CC-BY license. (d)–(f) SEM images of the carbon products prepared in Li_2CO_3 with (d) 0.5% ZnO, (e) 1% ZnO, (f) 2% ZnO. Reprinted (adapted) from *J. Electrochem. Soc.* **168** 083501. Copyright © 2021, IOP Publishing, Ltd.

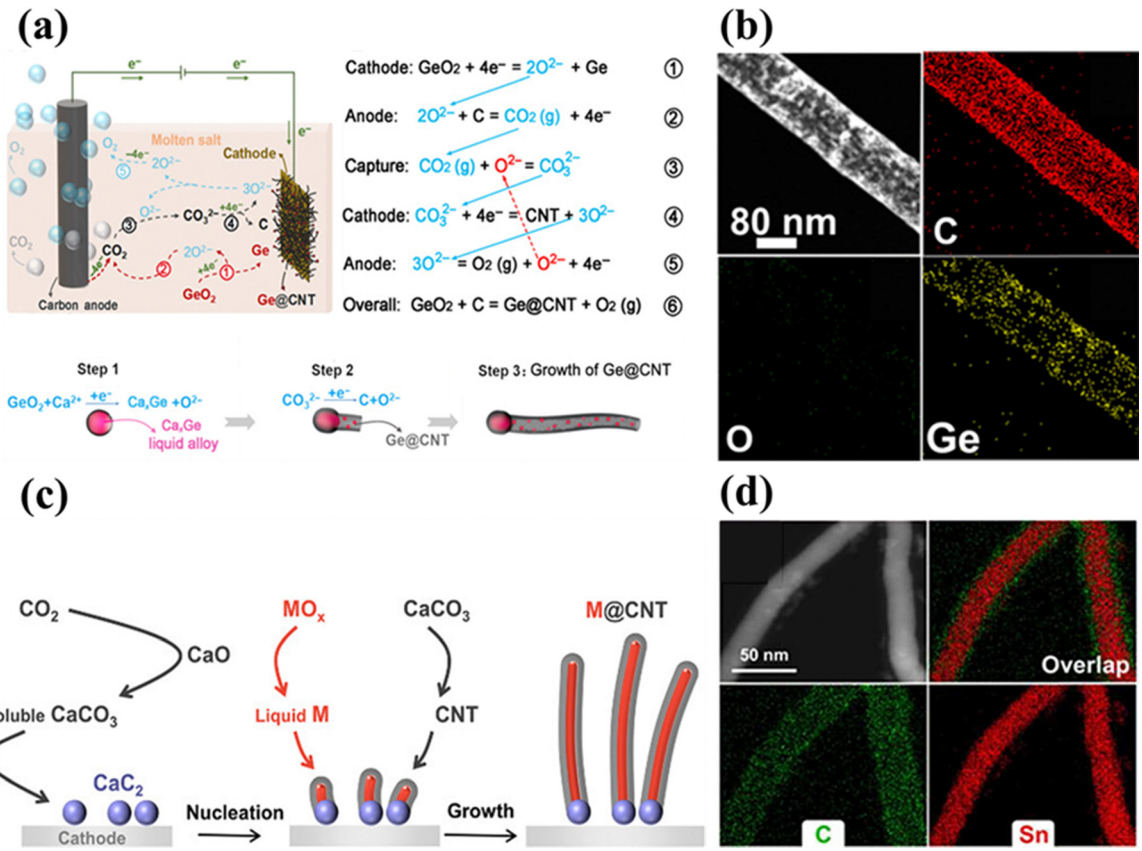

Fig. 71 (a) Schematic illustration of the coelectrolysis of soluble GeO_2 and *in situ*–generated CO_2 at carbon anode to cathodic Ge@CNTs. (b) HAADF-STEM image, and the corresponding elemental mappings of C, O, and Ge. Reprinted (adapted) from *Sci. Adv.* 2020, **6**, eaay9278. Copyright © 2020, The American Association for the Advancement of Science under the terms of CC BY-NC license. (c) Illustration of the preparation of metal-confining CNT (M@CNT) *via* a CaC_2-mediated mechanism. (d) HAADF-STEM image and the corresponding elemental mappings of Sn@CNT. Reprinted (adapted) from *Chem. Int. Ed.* 2023, **62**, e202306877. Copyright © 2023, Wiley-VCH GmbH.

electrochemical reduction of CO_2 in an inexpensive, calcium-containing molten salt. This method effectively generates CNTs and M@CNTs *via* a CaC_2-mediated process. In the synthesis of metal-free carbon nanotubes, calcium carbonate in the melt is first converted into calcium carbide. Calcium carbide (CaC_2) acts as a precursor for the fabrication of carbon nanotubes (CNTs) by the decomposition of calcium carbonate ($CaCO_3$). The CaO and CO_2 cycle subsequently replenishes the consumed $CaCO_3$. In the

production of M@CNTs (Sn@CNTs, Zn@CNTs, and Fe@CNTs), MOx (metal oxides SnO_2, ZnO, and FeO) and $CaCO_3$ are reduced to liquid metals and CNTs, respectively. The liquid metals are subsequently introduced into the internal cavities of the CNTs (Fig. 71d). Sn@CNT shows a significant capacity of 510 mAh g^{-1} at a current density of 1000 mA g^{-1} due to the synergistic interaction between the Sn core and the CNT shell. These techniques illustrate the strategic application of molten salt for the sequestration and transformation of CO_2. They also promote the advancement of novel CNT composites and highlight the adaptability of this technology for production.

Carbon nano-onions are a special type of carbon nanostructure that is made up of many layers of fullerenes. In the past, these structures were made by putting nanodiamonds through pyrolysis at very high temperatures, often reaching 1700 °C, which made the process use a huge amount of energy. Liu *et al.* demonstrated an alternative approach to capture and electrochemically reduce CO_2 in a pure Li_2CO_3 electrolyte with six molal Li_2O. Their tests showed that using galvanized copper as the cathode and platinum flakes as the anode produced about 97% yield of carbon nano-onions. When a nickel sheet was used as the anode, it facilitated carbon nanotubes forming instead of nano-onions. The results show that the type of carbon nanostructure that is made depends on both the electrode material and the ratio of molten salt. Using electrodes and electrolytes that don't contain nickel and are high in Li_2O generally makes more sp^3 defects happen in the solid carbon that forms at the cathode. Adding more sp^3 character makes the carbon layers bend more, which enhances the production of carbon nano-onions, as shown in (Fig. 72a and b).[495] Rui *et al.* discovered that the alkalinity of the electrolyte, electrode substrate, and current density play a crucial role in the growth of carbon nanocoils (CNCs) on graphite electrode in Li_2CO_3–Na_2CO_3–K_2CO_3–0.001 wt% Li_2O as a molten salt, and the alkalinity of the molten salt electrolyte induced specific structural defects in carbon, leading to the formation of coiled structures in a controlled manner[507] as shown in (Fig. 72c and d). Interestingly, through scanning electron microscopy, the *in situ* mechanical properties were measured, and it was found

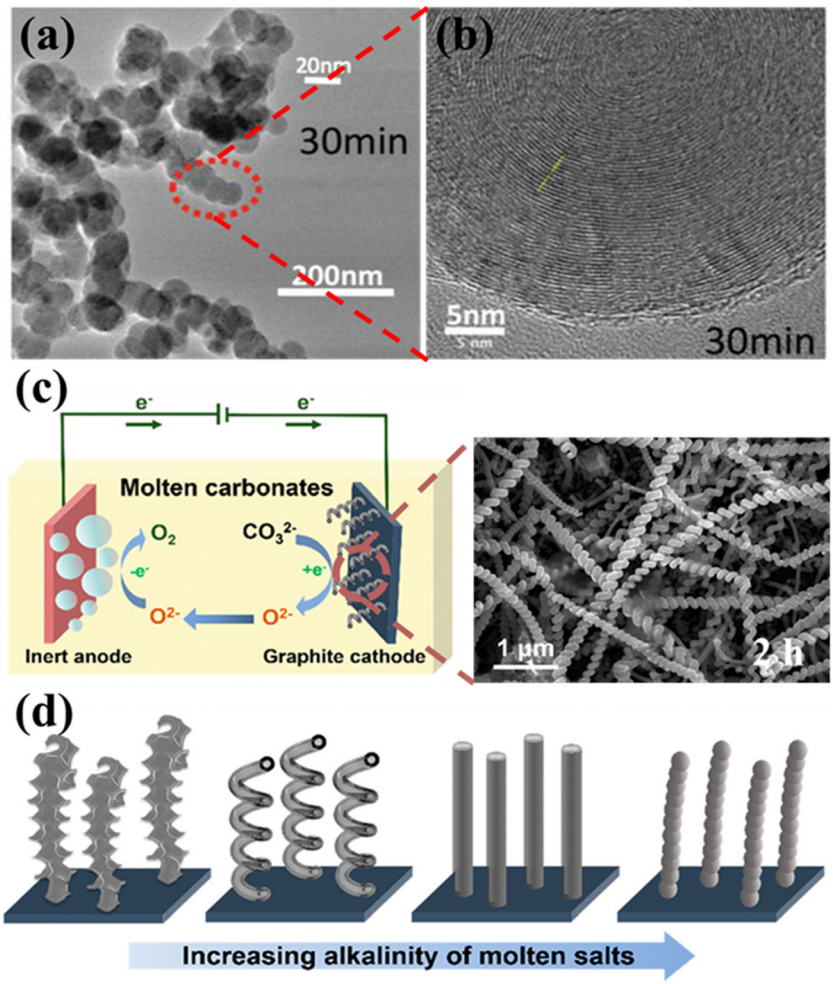

Fig. 72 (a) and (b) TEM of carbon nano-onion synthesis product at 770 °C, without added Ni. Reprinted (adapted) from *Adv. Sustainable Syst.* 2019, **3**, 1900056. Copyright © 2019 Wiley-VCH Verlag GmbH & Co. KGaA, Weinheim. (c) Schematic illustration of the synthesis of carbon nanocoils (CNCs) and SEM images of carbon nanocoils. (d) Schematic illustration of the different carbon structures obtained with the increasing alkalinity of molten carbonate. Reprinted (adapted) from *Nano Lett.* 2022, **22**(1), 97–104. Copyright © 2022, American Chemical Society.

Table 32 Techno-economics of carbon nanotubes produced by different methods.[508–510]

Parameter	Molten salt electrolysis	CVD	Arc discharge	Laser ablation
Production cost	0.05–0.20 per g SWCNs	$0.366–$1.7 per g SWCNs	$100–$150 per g SWCNs	$100–$1000 per g SWCNs
Scalability	High (compatible with industrial-scale reactors)	High (dominant commercial method)	Low (batch process)	Very low (research-scale)
Energy consumption	High (750–900 °C, -intensive)	High (900–1000 °C, hydrocarbon cracking)	Very high (arc plasma)	Extremely high (laser systems)
Raw material cost	Low (uses CO_2 or graphite)	Moderate (hydrocarbons, catalysts)	Moderate (graphite electrodes)	High (graphite targets)
Environmental impact	CO_2-negative potential	High GHG emissions (methane/ethane use)	Moderate (CO_2 from energy)	High (energy-intensive)
Market viability	Emerging (profitable at scale)	Mature (dominant market share)	Limited (niche applications)	Rare (specialized uses)

that the shear modulus and the spring stiffness of the electrolytic CNCs are far larger than those of CVD-derived CNCs and close to the theoretical values. Noting that (Table 32) presents the techno-economics of carbon nanotubes produced by different methods.

Future outlook of molten salts

The CO_2 absorption over molten salts process, cathodic reduction reactions, and the corrosive behavior of inert anodes, as well as the morphologies of electro-deposited carbon. MSCC-ET demonstrates the potential for great applications; on the other hand, there are a lot of unknowns remaining for fundamental investigation and considerable engineering expertise to develop. For example, although different carbon materials were prepared and reported, the detailed reduction mechanism of CO_2 and the assembling pathway of the reduced carbon atoms and their controlling principle are not fully covered. In addition, the optimization of molten salt composition and understanding of the molten salt structure and the gas behavior in molten salt and the electrode/electrolyte interface should further be addressed.

Comprehensive analysis of dual-functional materials (DFMs)

This comprehensive analysis section synthesizes performance, stability, and mechanistic insights to assess the practical viability of DFMs for integrated CO_2 capture and electrocatalytic conversion (ICCC). Tables 33–38 collectively benchmark DFM platforms across comparative performance metrics, operating windows, flue-gas tolerance, and technology readiness levels, while explicitly delineating material-specific advantages and limitations. Thermal and oxidative stability under ICCC-relevant conditions is evaluated, with particular attention to porous polymer network platforms, alongside a unifying mechanistic framework that contrasts established reaction pathways with emerging dual-site hypotheses. Finally, kinetic benchmarking links CO_2 adsorption–desorption dynamics to catalytic turnover frequencies, enabling a system-level assessment of rate compatibility and identifying kinetic mismatches that currently constrain scalable ICCC deployment.

Table 33 highlights that only a few systems such as Ni–N/CNT@CTF, high-performance CMP/CNT composites, MOF-based gas-diffusion electrodes, and molten carbonates, currently combine high selectivity with industrially relevant current densities, whereas most POP/CTF, COF, amine, ionic-liquid, and DES platforms are limited by conductivity, viscosity, stability, or mass-transport constraints. Robust inorganic frameworks like zeolites, oxides, and molten salts offer excellent thermal and chemical durability but often require conductive scaffolds or high-temperature, corrosion-resistant hardware, while molecular media primarily function as tunable electrolytes rather than stand-alone DFMs. As a result, future ICCC development will likely rely on hybrid architectures that merge stable inorganic backbones with engineered porous polymers and optimized liquid environments to achieve high current densities, long lifetimes, and high selectivity under humid, impurity-rich flue-gas conditions at acceptable cost.

Dual-functional materials (DFMs) must operate within constrained flue-gas conditions (373 K, 0.1 bar, 10–15% CO_2, humid/SO_x/NO_x) while delivering catalytic currents $\geq$200 mA cm^{-2} for industrial viability. Table 34 benchmarks operating windows across platforms: molten carbonates excel at 550–900 °C (>90% FE at 1 A cm^{-2}) with complete flue-gas tolerance but high energy costs, zeolites span 25–500 °C with excellent stability yet require nanoconfinement for CO_2RR, and room-temperature DES/ILs offer green scalability (94% FE_{CO}) but remain current-limited (<20 mA cm^{-2}). MOF GDEs achieve breakthrough performance (380 mA cm^{-2} at 15% CO_2) despite hydrolysis risks, while POPs/CTFs need hydrophobic engineering for humidity tolerance yet deliver balanced kinetics (12.8 mA cm^{-2} Ni-CTF). Amines provide high capacity but suffer impurity degradation, positioning zeolites/molten salts as most robust and MOF/DES GDEs as highest-rate room-T solutions. Table 35 quantifies DFM performance under these practical constraints, moving beyond descriptive surveys to assess operating-window-ranked ICCC viability.

Table 35 systematically addresses a unified mechanistic taxonomy across ICCC platforms: physisorptive DFMs (POPs/CTFs/CMPs −24 to −45 kJ mol^{-1}; COFs −42 kJ mol^{-1}; MOFs −30 to −80 kJ mol^{-1}; zeolites −30 to −70 kJ mol^{-1}) generate *CO_2/*COOH at N-sites/OMS *via* weak van der Waals/cation–π interactions, while chemisorptive systems (oxides/DFMs −50 to −90 kJ mol^{-1}; amines −80 to −120 kJ mol^{-1}; DESs −44 to −209 kJ mol^{-1}; molten salts −150 kJ mol^{-1}) form covalent carbamate/CO_3^{2-} species at nucleophilic centers. Capture mode dictates RDS coupling, physisorption sustains high *CO_2 → *COOH barriers (ΔG_{RDS} 0.4–0.8 eV) requiring EDL/co-catalysts, chemisorption eliminates adsorption RDS but bottlenecks at carbamate hydrolysis (amines), R_{ct}-limited *COOH (DESs), or 4e$^-$

Table 33 Comparative performance metrics of dual-functional materials (DFMs) for integrated CO_2 capture and electrocatalytic conversion (ICCC), highlighting advantages, limitations, and technology readiness levels (TRL)

Material class	Capture capacity (273–298 K, ∼1 bar)	Textural/binding metrics	CO_2RR selectivity (FE)	Current density & kinetics	Stability/TRL insight	Ref.
POPs/CTFs	– PHCTF-1a/-4 : 30–52 $cm^3\ g^{-1}$ CO_2 at 273 K – N-rich CTFs (PCBZL, CTF-CSU41): 30–52 $cm^3\ g^{-1}$ at 273 K.	– S_{BET} ≈ 1200–1300 $m^2\ g^{-1}$ – V_{micro} = 58–79% – Q_{st} ≈ 24–45 kJ mol^{-1} (favourable for 10–15% CO_2)	– Metal-free CTF: FE_{CO} ≈ 82% F-CTF: FE_{CH_4} ≈ 99.3% – Ni-CTF: FE_{CO} ≈ 90%; NiPor-CTF: FE_{CO} ≈ 92.3% – Ni–N/CNT@CTF: FE_{CO} ≈ 98%	– NiPor-CTF: j_{CO} ≈ 12.8 mA cm^{-2} – Ni–N/CNT@CTF: j_{CO} ≈ 201 mA cm^{-2} – ΔG_{*COOH} ≈ 0.58–0.59 eV – Tafel ≈ 56–86 mV dec^{-1} (*vs.* ≥0.85 eV and ∼130 mV dec^{-1} for Ni-TPP)	– Good capture at flue-gas P_{CO_2} – Ni–N/CNT@CTF approaches industrial *j* but humidity and long-term oxidative stability remain limiting; TRL ≈ 3–4	65, 66, 82, 84–86, 88, 90–92, 103 and 105
POPs/CMPs	– Co-CMP: 79.3 mg g^{-1} – Al-CMP: 76.5 mg g^{-1} – Parent CMP: 71.0 mg g^{-1} at 298 K, 1 bar (similar to MOF-177, NOTT-112)	– Co-CMP: S_{BET} ≈ 965 $m^2\ g^{-1}$, V_{tot} ≈ 2.81 $cm^3\ g^{-1}$ – Al-CMP: 798 $m^2\ g^{-1}$, 1.41 $cm^3\ g^{-1}$; capacity tracks V_{tot} and metal–CO_2 interactions more than S_{BET}	– CNT@CMP(CoPc–H_2Pc): FE_{CO} ≈ 97% – CMPANI-3: FE_{CO} ≈ 97%; CMP-$(bpy)_{20}$–Mn: FE_{CO} ≈ 0.4% (HER-dominated).	– CNT@CMP(CoPc–H_2Pc) & CMPANI-3: j_{CO} > 200 mA cm^{-2} – TOF up to 9.8 × 10^4 h^{-1}; CMP-$(bpy)_{20}$–Mn: requires −1.6 V for negligible CO.	CMPs can reach industrial *j* and high FE when combined with CNT backbones and proton-relay ligands; stability and flue-gas tolerance still underexplored; TRL ≈ 3	113, 114, 117, 128 and 130
COFs	– TPE-COF-II: 118.8 $cm^3\ g^{-1}$ (23.2 wt%) at 273 K – RICE-5 : 50 $cm^3\ g^{-1}$ at 273 K – COF-102/103: up to 27 mmol g^{-1} at 298 K	– RICE-5: porosity 94%, density 0.094 g cm^{-3} – HEX-COF-1: S_{BET} 1214 $m^2\ g^{-1}$, Q_{st} ≈ 42 kJ mol^{-1} – COF-300-SO_3H: 6.23 mmol g^{-1} CO_2 and CO_2/N_2 selectivity 393 *vs.* 10–31 for other functional groups	– CoPc-PI-COF: FE_{CO} ≈ 96–97% – Co-TTCOF: FE_{CO} ≈ 99.7%; PA-Co-COF: FE_{CO} ≈ 86.97% from 15% CO_2 – Cu-COF^+-Pd: ≈95.5% $FE_{CO+CO_2^-}$	– CoPc-PI-COF: TOF up to 2.2 s^{-1}, TON ≈ 2.8 × 10^5 – Co-TTCOF: TOF ≈ 1.3 s^{-1}; PA-Co-COF: TOF 1208.8 h^{-1} – Most examples operate at $j \lesssim$ 50–100 mA cm^{-2}	COFs offer high FE and tunable binding, but hydrolytic stability, crystallization yield, and limited *j* at low P_{CO_2} restrict ICCC deployment; GDE integration and robust linkers are required; TRL ≈ 2–3	153, 158, 174, 176 and 181
Zeolites	– LEV: 5.81 mmol g^{-1} at 0 °C – LTA: up to 3.7 mmol g^{-1} at 25 °C after Si/Al optimization – CO_2/N_2 selectivity up to ≈80–84	– Low Si/Al and high Na^+/Ni^{2+} densities enhance uptake – Hierarchical LTA reduces adsorption/desorption time by 29–92 s and regeneration *T* by 13 °C	– CdO@Zn@Y: FE_{CO} > 90% at −0.8 V; $SnCu_xO_{2+x}$@MFI: high $FE_{CH_4}/FE_{C_2H_4}$ at elevated *j*	– CdO@Zn@Y stable for 120 h; zeolites generally >1000 h in capture – Electrochemical systems are still mostly lab-scale – Conductivity remains a bottleneck.	Zeolites are capture-mature (TRL 8–9) with excellent stability; as ICCC catalysts, they need conductive, hierarchical GDE designs.	199–201, 221, 226 and 234
MOFs	– HKUST-1/MOF-74: up to ∼10 mmol g^{-1} at high P – CALF-20 MMM: 3.97 mmol g^{-1} with ≈4.5× selectivity *vs.* N_2/O_2 at 298 K	– High S_{BET} and open metal sites – CALF-20 stable under humid DAC-like conditions.	– Ag-MOF-NH_2: FE_{CO} 96–97% at 355–380 mA cm^{-2} from 15% CO_2 – CALF-20-PGDE: CO FE ≈ 95% from 10% CO_2 – Cu-MOF GDEs: FE_{C2H4} ≈ 49%, JC_2H_4 ≈ 220 mA cm^{-2} at 1 A cm^{-2}	– MOF GDEs reach $j \gtrsim$ 200–380 mA cm^{-2} – Bi-HHTP gives FE_{HCOOH} ≈ 90–93% with modelled cost ≈0.74 \$ kg^{-1} – hydrolysis often limits lifetime to <100 h	MOFs can deliver ICCC-level rates *via* local CO_2 enrichment but require robust, hydrophobic/conductive frameworks for long-term operation; TRL ≈ 3–4	243, 266–270 and 293
Metal oxides/ hybrids	– Amine-oxide systems capture CO_2 as carbamates/bicarbonates (DEA–SnO_x/C stable up to 50% CO_2)	– Strong chemisorption – Limited physical porosity – Capture capacity defined by amine loading	– DEA– SnO_x/C: FE_{HCOO^-} ≈ 84.2% – Solid-state oxide reactors: C_2 FEs ≈ 34–68%	– DEA–SnO_x/C: j_{HCOO^-} ≈ 6.7–7.9 mA cm^{-2} – Solid-state capture *j* up to 440 mA cm^{-2} with costs ≈33–83 \$ t^{-1} CO_2	Oxide-based DFMs clearly reduce capture energy *versus* thermal stripping but amine-based systems have low *j* and degradation; oxide solid-state reactors are closer to TE targets but face poisoning and capital-cost issues; TRL ≈ 3–5	294–299

Table 33 (*continued*)

Material class	Capture capacity (273–298 K, ∼1 bar)	Textural/binding metrics	CO_2RR selectivity (FE)	Current density & kinetics	Stability/TRL insight	Ref.
Amines	– Typical 30 wt% MEA: 0.4–0.5 mol CO_2 per mol amine – High capacities at 40–60 °C	– Carbamate formation – Regeneration energy ≈3 GJ t^{-1} CO_2; oxidative/thermal degradation above ≈100–110 °C	– MEA/Ag: FE_{CO} ≈ 72% at 50 mA cm^{-2} – AMP-based systems: FE_{HCOO^-} ≈ 40–50% – Ni–N/C in MEA: FE_{CO} ≈ 65%	– j usually ≤50 mA cm^{-2} in H-cells – Best flow systems approach ≈200 mA cm^{-2} – Integrated schemes can save up to ≈44% capture energy *versus* thermal stripping	Amines are capture-mature (TRL4) but electrochemically limited by conductivity, HER, and degradation; useful for energy savings but not yet superior in productivity to gas-fed CO_2RR	312–320
Ionic liquids	– Physical ILs: ≤0.5 mol CO_2 mol^{-1} at 1 bar Reactive ILs (*e.g.* $[P_{66614}][AA]$) up to 1.6–2.0 mol mol^{-1}	– Strong, tunable interactions but high viscosities (50–1000 cP) and cost – Non-fluorinated, heterocycle ILs show better viscosity–capacity trade-offs	– Neat imidazolium ILs: $FE_{CO/HCOO^-}$ ≥80–96% – IL additives (0.01–0.5 M [Emim][BF_4]/[TFO]): FE ≈ 75–80% – [Emim][2-CNPyrr]: FE_{CO} > 94–98%	– Strong overpotential reduction (≈0.2–0.24 V) but often limited j due to viscosity in neat Ils – Additive/surface-modifier modes maintain aqueous-like j while improving FE	ILs excel as interfacial modifiers/additives rather than bulk electrolytes; cost, viscosity, and toxicity remain barriers for large-scale ICCC; TRL ≈ 3–4	321, 330, 337, 338 and 389
DESs	– ChCl:urea/EG: ≈0.6 mol kg^{-1} – PRIDES: up to 769 mmol kg^{-1} – DEACl:DEA: 52.71 mol L^{-1} equivalent loading	– Viscosity 200–800 cP (lower than many ILs but higher than water) – H-bond network controls CO_2 speciation and transport	– DEACl:DEA: FE_{CO} ≈ 94% – ChCl:urea-based systems: FE_{CO} 90–98% at low j	– j typically 4–20 mA cm^{-2} – R_{ct} lower than in $KHCO_3$, but still limits high-rate operation – Stability is good over tens of hours	DESs offer green, low-cost, high-FE media but need GDEs/pressure and polymeric hybrids to reach ≥200 mA cm^{-2}; TRL ≈ 2–3	390, 402, 407, 408, 429–435 and 439
Molten salts	– Li_2CO_3/Li–Na–K carbonates: CO_2 solubility up to 0.835 mol CO_2 per mol Li at 723 K	– Toper 550–900 °C; fully inorganic, excellent stability; strong chemisorption *via* CO_3^{2-} species	– MSCC-ET: current efficiency >80–93% for C or CO; CNT products with near-100% carbon selectivity	– j typically 0.2–1 A cm^{-2}; SWCNT cost 0.05–0.20 \$ g^{-1} with effective profit ≈50 k\$ t^{-1} CO_2; >100 h operation demonstrated	Molten salts uniquely enable CO_2-negative carbon materials at industrial current densities and flue-gas tolerance, but high T and corrosion limit integration with low-T ICCC; TRL ≈ 4–5 for MSCC-ET	447, 470, 472 and 507

Table 34 Operating windows & flue-gas tolerance of DFMs

Material class	T (°C)	P (bar)	P_{CO_2} range	H_2O tolerance	SO_x/NO_x tolerance	Typical j_{max} (mA cm^{-2})	Ref.
POPs/CTFs	25–100	0.1–5	0.01–0.15	Moderate	Low	10–50 (up to 201 for Ni–N/CNT@CTF)	62, 82, 91 and 108
COFs	25–80	0.1–10	0.01–0.20	Poor (hydrolysis)	Low	5–100	149, 164 and 175
MOFs	25–150	0.1–40	0.01–1.0	Poor–moderate (framework-dependent)	Variable	200–380 (GDEs)	247, 261–263, 266–270 and 273
Zeolites	25–500	0.1–20	0.01–0.15	Excellent	Excellent	100–440 (in integrated cells)	183, 185, 199–201, 212 and 213
Metal oxides	25–400	1–10	0.10–1.0	Good	Moderate	6–200	294–299
Amines	40–120	0.1–2	0.01–0.15	Excellent	Poor (degradation)	20–200	305, 309, 312 and 319
ILs	25–100	0.1–93	0.01–1.0	Good (hydrophobic ILs)	Moderate	10–100	322, 323, 325, 356 and 383–388
DES	25–80	0.1–10	0.01–0.50	Excellent	Good	4–20	390, 402, 407, 408 and 429–434
Molten salts	550–900	0.1–5	0.01–0.15	Excellent	Excellent	200–1000	447, 465, 495 and 505

C deposition (molten salts), revealing an optimal ΔH_{ads} "Goldilocks window" (−40 to −60 kJ mol^{-1}) for kinetic balance. Synergy manifests quantitatively: Ag-MOF-NH_2 retains 93% j_{CO} (355 mA cm^{-2}, 15% CO_2), DESs/ILs boost FE_{CO} to 94% (R_{ct} 65 Ω *vs.* 120 Ω $KHCO_3$), molten salts achieve 93% CNT selectivity at 1 A cm^{-2}, and amines deliver 44% energy savings *versus* thermal stripping, confirming local P_{CO_2} enrichment, overpotential suppression (−240 mV IL onset), and transport optimization as validated ICCC performance drivers.

(Fig. 73) illustrates the distinct capture mechanisms, while Table 35 consolidates the associated intermediates, activation barriers, and their coupling to the rate-determining electrochemical steps across amines, ILs, and DES. While these classes differ in chemical functionality and solvation environments, they all modulate the local thermodynamics of CO_2 activation, proton availability, and electron-transfer barriers. Importantly, the comparison illustrates how capture strength (chemisorption *vs.* physisorption) does not simply correlate with performance; rather, it controls whether the apparent RDS shifts toward adsorption/desorption, first-electron transfer, or proton-coupled steps. This mechanistic synthesis provides a framework for rationally selecting capture media based on the desired catalytic pathway rather than solely on bulk absorption capacity.

The synergy between capture media and catalytic turnover is quantified by improvements in product selectivity and kinetic barriers compared to non-integrated systems. For amine-based CTCs, direct conversion of captured CO_2 has been demonstrated to bypass the energy-intensive desorption step. In an aqueous monoethanolamine capture solution, amine–CO_2 conversion to CO was achieved with a faradaic efficiency (FE) of 72% at 50 mA cm^{-2}, confirming that chemisorbed species contribute directly to the reduction pathway rather than acting merely as inert reservoirs.[312] Complementary work by Pérez-Gallent *et al.* reported the direct reduction of captured CO_2 to formate with FEs up to 50%, and to CO with efficiencies up to 45% in mixed amine media, significantly outperforming physical absorption baselines.[311] In contrast, synergy in Ionic Liquids (ILs) is primarily driven by selectivity tuning rather than raw reaction rate; functionalized imidazolium ILs have been shown to steer the reaction pathway toward formate with >85% selectivity by stabilizing the specific carboxylate intermediate, although overall turnover frequencies are often limited by viscosity.[321,330] Finally, in Deep Eutectic Solvents (DES), the hydrogen-bond network actively stabilizes the CO_2 radical anion intermediate, reducing the overpotential for CO_2 reduction by approximately 150–200 mV compared to conventional ILs while maintaining current densities above 10 mA cm^{-2}.[347,368] These quantitative results support the existence of distinct synergistic pathways: amines primarily enhance kinetic efficiency, ILs tune product selectivity, and DES networks lower the energetic overpotential.

Table 36 directly fulfills the explicit mechanistic demarcation, distinguishing settled capture paradigms OMS physisorption (MOFs, ΔH_{ads} −35 kJ mol^{-1}), zwitterion → carbamate (amines, FTIR/NMR-validated), carbonate chemisorption (molten salts), H-bonding networks (DESs), and ultramicropore confinement (COFs/CTFs/zeolites), from emerging dual-site hypotheses like Ag-cluster *COOH stabilization (amine-MOFs), DEA-SnO_x *OCHO coupling (oxides), [Emim][2-CNPyrr] carbene-anion cooperativity (ILs), and N-site/CNT *CO_2 activation (POPs). Each hypothesis is rigorously qualified by quantitative performance gaps and TRL realities: Ag-MOF-NH_2 delivers 355 mA cm^{-2} (93% retention, 15% CO_2) but hydrolyzes 80% capacity in humid cycles (TRL 3); DES HBA/HBD interfaces cut R_{ct} to 65 Ω (FE_{CO} 94%) yet cap j at 20 mA cm^{-2} due to 800 cP viscosity (TRL 2–3); molten Ni^{2+}/ZnO CNT nucleation achieves 93% carbon selectivity at 1 A cm^{-2} but demands 900 °C Ni-Cr hardware (<5000 h, TRL 4–5). Critical verdict: while capture mechanisms stand on decades of equilibrium/spectroscopic data, dual-site CO_2RR claims remain system-specific, short-term (<100 h), and sub-industrial (j < 200 mA cm^{-2}), necessitating GDE validation under impure feeds before scale-up confidence.

Porous organic polymers (POPs) exhibit structural diversity but face critical stability limitations under ICCC-relevant conditions (373 K flue gas, humid/SO_x/NO_x, oxidative potentials ±1.0 V *vs.* RHE). Table 37 quantifies thermal/oxidative resilience: CTFs demonstrate superior stability (T_{decomp} > 500 °C, stable to −1.0 V *vs.* RHE over 10 h at 201 mA cm^{-2}) due to aromatic triazine linkages, while COFs suffer hydrolysis (>50% crystallinity loss after 100 h at 80% RH). Amorphous CMPs/PIMs oxidize rapidly under anodic potentials (+0.8 V), losing 60–70% surface area

Table 35 Comparative mechanistic framework across DFMs classes

Material class	Adsorption route	ΔH_{ads} (kJ mol^{-1})	Key intermediates	Active sites	Coupling between capture mode and RDS	RDS (ΔG_{RDS})	Synergy metric	Ref.
POPs/CTFs/CMPs	Physisorption in N-rich ultramicropores	−24 to −45	*CO_2, *COOH	Triazine N, NiPor, CNT	Hydrophobic micropore confinement increases local CO_2 fugacity near catalytic sites, shifting the RDS to proton-coupled electron transfer	*COOH (0.58–0.59 eV)	Ni–N/CNT@CTF: j_{CO} 201 mA cm^{-2}, FE_{CO} 98%	62, 88 and 90–92
COFs	Pore confinement + imine/azine N-sites	−42	*CO_2, *COOH	CoPc, imine N, Cu^{2+}	Ordered 1D channels align CO_2 with functionalized linkers, lowering the entropic penalty of *COOH formation *via* cooperative host–guest interactions	*COOH (0.4–0.6 eV)	CoPc-PI-4COF: TOF 2.2 s^{-1}, FE_{CO} 97%	153 and 155
MOFs	OMS coordination + amine physisorption	−30 to −80	Metal-CO_2, *COOH	Cu^{2+} OMS, Ag-NH_2	CO_2 binds at open metal sites, lowering activation barriers, but overall ICCC rates are often limited by charge-transport resistance across non-conductive linkers	*COOH (0.4–0.6 eV)	Ag-MOF-NH_2: j_{CO} 355 mA cm^{-2} (93% retention, 15% CO_2)	243 and 293
Zeolites	Cation–π quadrupole + framework sites	−30 to −70	Formates, *COOH	Na^+/Ni^{2+}, Brønsted acid	Extra-framework cations stabilize adsorbed CO_2 and transition states, while rigid pores and intracrystalline diffusion limit the overall ICCC rate	*CO_2 activation	CdO@Zn@Y: FE_{CO} > 90% (120 h stable)	199–201 and 234
Metal Oxides/DFMs	Lewis acid–base + amine chemisorption	−50 to −90	*OCHO, carbonates	SnO_x, Ni/Co NPs	Strong surface carbonate formation facilitates capture but imposes a high energy penalty on regeneration, coupling carbonate activation with catalytic turnover	*CO_2 → *COOH (0.8 eV)	DEA-SnO_x: FE_{HCOO^-} 84% (6.7 mA cm^{-2})	294–299
Amines	Chemisorption *via* zwitterion → carbamate/bicarbonate formation ($RNH_2 + CO_2 \rightleftharpoons RNHCOO^- + RNH_3^+$)	∼20–40 kJ mol^{-1} (typically lower for sterically hindered amines)	Zwitterion, carbamate, bicarbonate	Amine N atoms (primary/secondary)	Chemisorption increases local CO_2 activity and can lower the barrier for the first electron-transfer/desorption steps; however, overly strong binding may shift the apparent RDS toward regeneration	Carbamate hydrolysis	MEA/Ag: FE_{CO} 72% (50 mA cm^{-2}, 44% energy savings)	305, 308, 310 and 312–320
ILs	Anion coordination/weak chemisorption or task-specific nucleophilic binding	∼10–30 kJ mol^{-1} (physisorption) and 40–60 kJ mol^{-1} (chemisorption)	CO_2–anion complexes, carbene-like species	Anionic functional groups; imidazolium C2–H	Strong solvation stabilizes CO_2^- and CO-forming pathways; viscosity and mass-transfer effects can shift the apparent RDS from electron transfer to diffusion control	*CO_2 (↓0.3 eV)	[Emim][2-CNPyrr]: FE_{CO} 94% (onset −240 mV)	321, 325, 330, 339, 340 and 389
DES	H-bond network stabilization leading to bicarbonate/carbonate species	∼15–35 kJ mol^{-1} (H-bond networks reduce the barrier *vs.* neat IL analogues)	H-bonded CO_2, HCO_3^-/CO_3^{2-}	HBD/HBA hydrogen-bond network (*e.g.*, urea–ChCl, glycerol–ChCl)	Hybrid chemisorption–physisorption environment promotes proton-coupled steps and often reduces overpotential (∼100–200 mV reported), without excessively penalizing desorption	*COOH (R_{ct} 65 Ω)	DEACl:DEA: FE_{CO} 94% (53 mol L^{-1})	347–349, 368, 390 and 439
Molten salts	O^{2-} nucleophilic → CO_3^{2-}	−150	CO_3^{2-}, C*	Li^+/Ni nuclei	Extra-framework cations stabilize adsorbed CO_2 and transition states, yet rigid pores and intracrystalline diffusion often govern the overall ICCC rate	C deposition ($4e^-$)	93% CNT efficiency (j 0.2–1 A cm^{-2})	447 and 507

Table 36 Settled mechanisms *vs.* emerging dual-site hypotheses across ICCC materials

Materials	Settled mechanistic understanding	Emerging dual-site/CO_2-activation hypothesis	Quantitative performance & failure mode	Ref.
MOFs	OMS-driven physisorption governs CO_2 uptake (*e.g.* HKUST-1 Type I isotherm, MOF-74 low-*P* capture; CALF-20 physisorbs CO_2 with $\Delta H_{ads} \approx -35$ kJ mol^{-1} and retains capacity under humid gas)	Amine-enriched MOFs (Ag-MOF-NH_2) proposed to couple high CO_2/N_2 selectivity with *Ag-cluster COOH stabilization for dual capture–conversion; saturation of strong sites risks *CO_2/*COOH blocking	Ag-MOF-NH_2: $CO_2/N_2 \approx 280$ and $j_{CO} \approx 355$ mA cm^{-2} from 15% CO_2; CALF-20–PGDE reaches ≈95% FE_{CO} but requires weak physisorption to avoid product trapping; typical hydrolytically sensitive MOFs lose up to 80% capacity in a few humid cycles, and many systems stay <100 mA cm^{-2}, below ≥200 mA cm^{-2} industrial target	62, 65, 66, 90–92 and 243
Metal oxides	Lewis acid–base capture: surface M–O sites and grafted amines form bicarbonate/carbamate pools; capture step is well described by chemisorption and CO_2 hydration equilibria	Dual-site view: local DEA enrichment at SnO_x combines with *Sn–OCHO stabilization (lowering ΔG for formate pathway) to enable bifunctional capture–reduction	DEA–SnO_x/C: hydration doubles uptake; $FE_{HCOO^-} \approx 84\%$ at modest $j \approx 6$–8 mA cm^{-2}; viscosity rise and amine degradation during operation limit lifetime; membrane-type oxide BGDE designs still far from ≥200 mA cm^{-2} and rarely tested *vs.* O_2/impurities	294–299
Amines	Zwitterion → carbamate mechanism is classical: $CO_2 + 2RNH_2 \rightarrow RNHCOO^- + RNH_3^+$; kinetics and speciation confirmed by FTIR/NMR and widely used in process models	Dual-site electrochemical hypothesis: amine EDL compression plus metal (Ag, Sn, *etc.*) centers create coupled capture–conversion micro-environments for *in situ* reduction of carbamate/bicarbonate	Ag/MEA and AMP/PC systems achieve ≈72–100% FE_{CO} at ≈50 mA cm^{-2}, and AMP/PC boosts formate rates ~10×; however, viscosity, HER competition, oxidative degradation and 3–5 V cell voltages prevent reaching stable ≥200 mA cm^{-2} and yield higher LCOE than gas-fed CO_2RR	312–320
ILs	Settled picture: physical solubility and specific anion–CO_2 interactions control capture; CO_2 loading and viscosity trends *vs.* anion/cation family are well mapped; bifunctional ILs like [Emim][2-CNPyrr] form carbamate adducts and shift onset by ≈ +240 mV	Dual-site hypothesis: $[Emim]^+$ carbene/$[2\text{-CNPyrr}]^-$ nucleophilic attack pre-activate CO_2 (*CO_2–IL adduct) and lower *CO_2 activation barrier *via* EDL compression	[Emim][2-CNPyrr] shifts CO_2RR onset by ≈240 mV and enables $FE_{CO} > 90$–95% for ≥10–12 h, but viscosity explosion and proton transport disruption at high IL loading limit *j* and require dilution/mixtures; fluorinated ILs remain expensive and poorly tested under flue impurities	330, 337, 338 and 389
DESs	Settled: H-bonding networks between HBA/HBD components provide bifunctional capture and conductivity; DEACl:DEA DES shows strong CO_2 affinity and supports ECO_2R with $FE_{CO} \approx 94\%$ at −1.5 V	Dual-site view: HBA/HBD cooperative binding plus interfacial structuring at the electrode create enriched CO_2 layers and tuned EDL, lowering R_{ct} and facilitating *CO_2/*COOH formation	DEACl:DEA: $FE_{CO} \approx 94\%$, $R_{ct} \approx 65\ \Omega$ *vs.* 120 Ω in $KHCO_3$, but viscosity 200–800 cP cuts D_{CO_2} and caps *j* at ≈10–20 mA cm^{-2}; $H_2O >$ 40 wt% disrupts DES structure and halves capacity	390, 407, 408 and 439
Molten salts	Settled: carbonate chemisorption ($CO_2 + O^{2-} \rightarrow CO_3^{2-}$) and high-*T* electrolysis to C or CO; molten Li_2CO_3–based systems make CNTs or carbon nano-onions directly from CO_2 with high selectivity	Dual-site hypothesis: Ni^{2+}/ZnO or other nucleation sites steer CNT *vs.* other carbon morphologies (*e.g.* onions *vs.* sheets) *via* local carbon supersaturation and metal–C interactions	Near-quantitative CNO or CNT yields (>90%) and industrial-level *j* (0.2–1 A cm^{-2}); however, 750–900 °C operation, Ni–Cr corrosion (<5000 h), and poor SO_x tolerance raise energy and materials costs *vs.* low-*T* systems	447, 470, 472 and 507
COFs/ CTFs/ CMPs/ Zeolites	Settled: pore chemistry and ultramicroporosity dictate CO_2 uptake and selectivity (*e.g.* TPE-COF-II 118.8 cm^3 g^{-1} at 273 K; N-rich CTFs and zeolite cation sites deliver high CO_2/N_2 selectivity)	Dual-site claims: coupling Lewis basic N sites or cation sites with confinement and conductive backbones (*e.g.* MWCNTs, π-systems) to facilitate *CO_2/*COOH activation in addition to capture	COFs/CTFs/CMPs deliver excellent low-P capture and FE_{CO} up to ≈80–90% in some hybrid electrodes, but imine hydrolysis, N-site oxidation, and H_2O competition in zeolites halve capacity under humid gas; most systems operate at $j <$ 100 mA cm^{-2} and TRL remains low	62, 130, 153 and 234

Table 37 Thermal/oxidative stability of porous polymer network platforms in ICCC conditions

Material class	T_{decomp} (°C)	Oxidative limit (V *vs.* RHE)	Stability in CO_2RR (h@j_{max}	Ref.
CTFs	>500	−1.0 to +0.8	≈20 h@201 mA cm^{-2} (Ni–N/CNT@CTF)	82, 86, 90–92, 104 and 108
COFs	300–400	down to ≈−0.8	≈24 h@100 mA cm^{-2} (best cases)	149 and 162–164
CMPs	350–450	up to ≈ + 0.5 (60–70% SSA loss in 24 h)	<12 h@50 mA cm^{-2}	62 and 164
Zeolites (benchmark)	>800	−1.2 to +1.5	>1000 h@440 mA cm^{-2} (integrated cells)	183, 185, 199–201, 212, 213 and 233
Molten salts (benchmark)	>1000	Wide electrochemical window	>100 h@1 A cm^{-2} (CO_2-to-C/CO)	447, 465, 495 and 505

within 24 h, whereas HCPs maintain microporosity but swell irreversibly in water vapor (20% V_{micro} loss). NiPor-CTF achieves 92.3% FECO stability over 20 h at 12.8 mA cm^{-2} with NiN_4 sites intact, but F-CTFs lose 30% activity after 50 cycles due to C-F hydrolysis. Compared to zeolites (>1000 h stability at 440 mA cm^{-2}) and molten salts (>90% efficiency at 1000 °C), POPs require protective strategies: fluorination (FCTF-1: hydrophobic, Q_{st} 24 → 40 kJ mol^{-1}), conductive backbones

Table 38 Kinetic benchmarking of dual-functional materials (DFMs), relating CO_2 adsorption/desorption dynamics to catalytic turnover frequencies to assess ICCC viability

Material	Adsorption kinetics	Desorption kinetics	Catalytic TOF (s^{-1})	Rate mismatch	Ref.
CTFs (PHCTF-1a/4)	Fast physisorption (<1 nm pores)	Moderate Q_{st} 24–45 kJ mol^{-1}	Ni-CTF: ~1–2 s^{-1} (12.8 mA cm^{-2})	Desorption > catalytic at low P_{CO_2}	82, 90–92 and 108
MEA (amines)	Carbamate formation ~40 °C (fast)	Thermal stripping 1.5–2.5 GJ $t^{-1}CO_2$ (slow)	Ag: 72% FE at 50 mA cm^{-2}	Stripping ≫ catalytic	312
MOFs (HKUST-1)	OMS binding ~30 kJ mol^{-1} (fast)	Regeneration 100–150 °C (moderate)	Ag-MOF-NH_2: 355 mA cm^{-2}	Well-matched in GDEs	273
Molten carbonates	$O^{2-} \rightarrow CO_3^{2-}$ equilibrium ~2 h	Instantaneous at 723 K	C deposition >90% at 1 A cm^{-2}	Well-matched (high T)	447

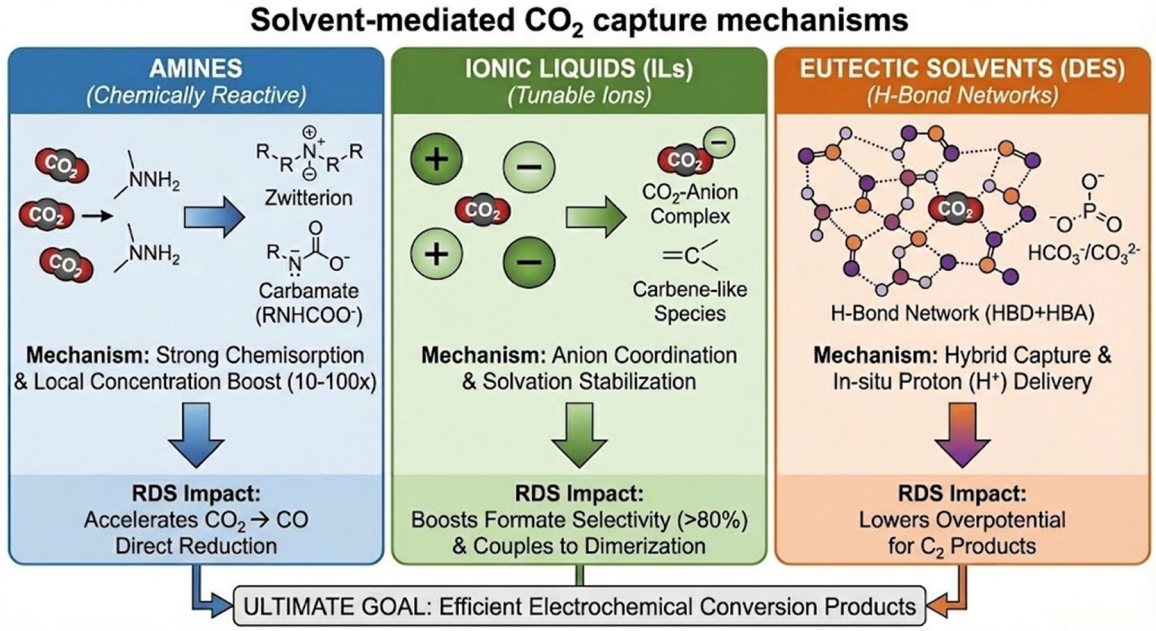

Fig. 73 Comparative mechanisms of solvent-mediated CO_2 capture and their impact on electrochemical reduction.

(Ni–N/CNT@CTF: 98% FECO, 201 mA cm^{-2}), and GDE encapsulation to shield against oxidative degradation and flue-gas impurities.

Integrated Carbon Capture and Conversion (ICCC) demand precise rate-matching between capture kinetics and electrocatalytic turnover frequencies (TOFs) to eliminate bottlenecks that plague decoupled systems. As shown in Table 38, while CTFs like PHCTF-4 exhibit rapid physisorption (52 cm^3 g^{-1} at 273 K/1 bar in minutes) with moderate desorption energies (Q_{st} 24–45 kJ mol^{-1}), Ni-CTF electrocatalysts deliver TOFs of ~1–2 s^{-1} (12.8 mA cm^{-2}), requiring continuous CO_2 supply >10× faster than flue gas delivers (0.03 mmol h^{-1} cm^{-2} at 10% CO_2). Amine systems face the opposite problem: MEA carbamate formation occurs rapidly (~40 °C), but thermal stripping demands 1.5–2.5 GJ $t^{-1}CO_2$ over hours, creating >10^3-fold mismatch *versus* Ag cathodes operating at 50 mA cm^{-2} turnover. Gas-diffusion electrode (GDE) architectures with MOF/DES interlayers elevate local P_{CO_2} >1 atm, harmonizing rates to support industrial currents ≥200 mA cm^{-2}, while molten carbonates achieve natural synchronization at 723 K (>90% efficiency, 1 A cm^{-2}). Hierarchical porosity (micropores for binding, mesopores for diffusion) further reduces LTA zeolite kinetics by 29–92 s.[82,83,90–92,273,312]

Integrated carbon capture and conversion (ICCC) case studies consistently identify adsorption thermodynamics, catalytic kinetics, and operating temperature as the dominant, tightly coupled parameters governing system cost through their combined effects on regeneration energy, reactor sizing, and heat integration. The adsorption enthalpy (ΔH_{ads}) of CO_2 defines a central thermodynamic trade-off: stronger binding enhances capture efficiency and single-pass utilization but increases regeneration or reactive release energy, whereas weaker binding lowers thermal demand at the expense of larger sorbent inventories. Process modeling and TEA of amine-based and dual-function material (DFM) ICCC systems show that variations in ΔH_{ads} of ~20–30 kJ mol^{-1} can shift total CO_2 avoidance costs by ~25–40%, depending on cycle design and heat integration, making ΔH_{ads} one of the most economically sensitive thermodynamic parameters.[511] Furthermore, catalytic turnover frequency (TOF) is a primary kinetic cost lever, as it directly determines reactor volume and catalyst loading; ICCC case studies of DFM-assisted methanation demonstrate that order-of-magnitude increases in TOF can reduce reactor-related CAPEX by ~30–50%, with limited impact on operating costs.[512] Moreover, operating temperature as mentioned in (Table 34) further couples' kinetics, adsorption

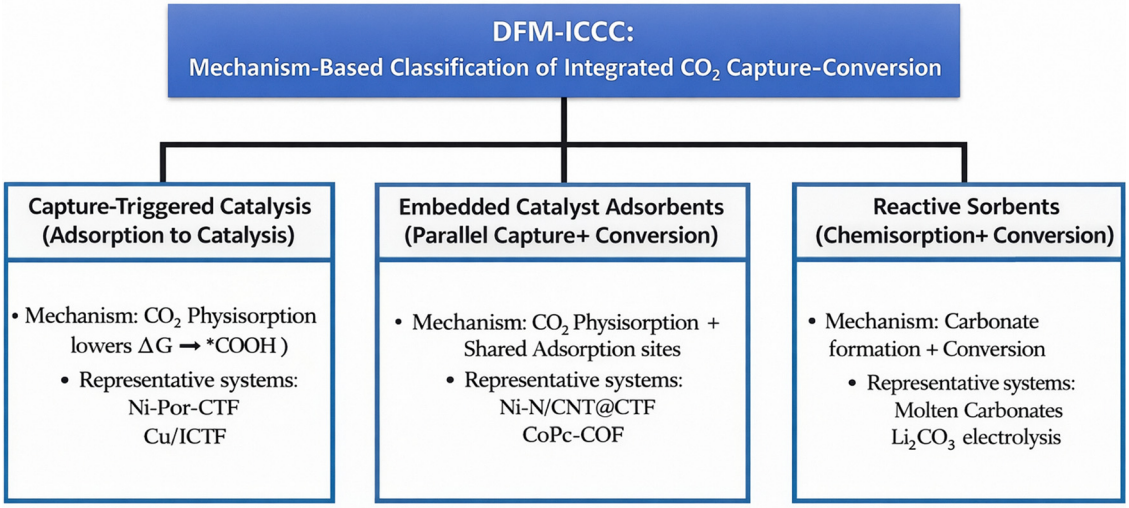

Fig. 74 Categorization of dual function materials. A breakdown of ICCC systems into three primary classes based on capture-conversion synergy.

equilibria, and heat recovery, with TEA of Ca-looping- and DFM-based ICCC systems showing that deviation from the optimal temperature window increases total system cost by ~20–35% due to inefficient heat integration and higher utility demand.[513] Collectively, these studies highlight that ICCC economics are governed by co-optimization of adsorption thermodynamics, catalytic activity, and operating temperature, underscoring the need for integrated material–process design.

The proposed classification framework in Fig. 74 categorizes DFM-ICCC platforms into three distinct strategies based on the synergy between the capture and conversion steps. Capture-Triggered Catalysis operates *via* a physisorption mechanism where the physical binding of CO_2 thermodynamically lowers the Gibbs free energy barrier (ΔG) for the critical activation step ($*CO_2 \rightarrow *COOH$), a pathway exemplified by systems such as Ni-Por-CTF. In contrast, Embedded Catalyst Adsorbents utilize the spatial integration of catalytic centers within porous frameworks (*e.g.*, CoPc-COF) to enable parallel capture and conversion at shared adsorption sites. Finally, Reactive Sorbents are distinguished by a chemisorption-driven mechanism; in these systems, such as molten carbonates or Li_2CO_3 electrolysis configurations, CO_2 is chemically fixed into stable carbonate intermediates which subsequently undergo conversion. This distinction highlights the progression from physical adsorption-assisted catalysis to chemical fixation-dependent transformation.

Techno-economic analysis of ICCC

A techno-economic analysis (TEA) can assess the feasibility of ICCC, identify economically viable products, and determine the performance metrics necessary for achieving economic viability. In terms of technological evaluation, a reference process simulation is needed to estimate the mass and energy balance, which relies on thermodynamics properties and kinetic factors for producing reliable simulation results. Regarding economic evaluation, it comprises calculating the levelized cost of CO_2 capture, power price, separation cost, product selling price, and the CO_2 electrolyzers' CAPEX and OPEX. Consequently, it is crucial to conduct a discounted and undiscounted cash flow analysis, a sensitivity analysis of different process metrics, and an uncertainty analysis to determine which factors affect the project's environmental and economic feasibility. To illustrate the practical potential of integrated CO_2 capture and conversion technologies, several case studies and techno-economic assessments (TEAs) are discussed.

Regarding the ICCC system's efficiency, Xia *et al.* conducted a techno-economic analysis (TEA) for three different electrochemical CO_2 capture and reduction processes: independent CO_2 capture and electrochemical conversion, integrated CO_2 capture and conversion in a dual electrochemical cell, and integrated CO_2 capture and conversion in a single electrochemical cell.[514] And, they concluded that the independent system has the lowest energy efficiency as it involves multiple procedures of CO_2 capture, compression, and storage; about 55.56 GJ of energy was needed to produce 1 ton of CO. However, the dual electrolytic cell system, which consists of two electrolytic cells for both capturing and reduction processes under mild conditions without a CO_2 compression process, needs 44.38 GJ of energy to produce 1 ton of CO, compared to 27.41 GJ of energy for the single electrolytic cell system (Fig. 75a). Also, both independent and dual electrolytic systems show similar cost distributions, with capture and conversion together make up nearly 60% of the total cost while electrochemical conversion exceeds 70% in single-cell system despite its overall lowest total cost, highlighting the importance of energy efficiency in both stages (Fig. 75b). Furthermore, they highlighted that under optimistic conditions, producing 1 ton of CO from the single electrolytic cell system can cost $224 with a low cell voltage of 2.1 V, while reaching $342 per 1 ton of CO with a 60% conversion rate in the dual electrolytic cell system (Fig. 75c and d).

Compared to conventional decoupled Carbon Capture and Utilization (CCU), Li *et al.*[515] Integrated Carbon Capture and Utilization (ICCU) demonstrate superior thermodynamic

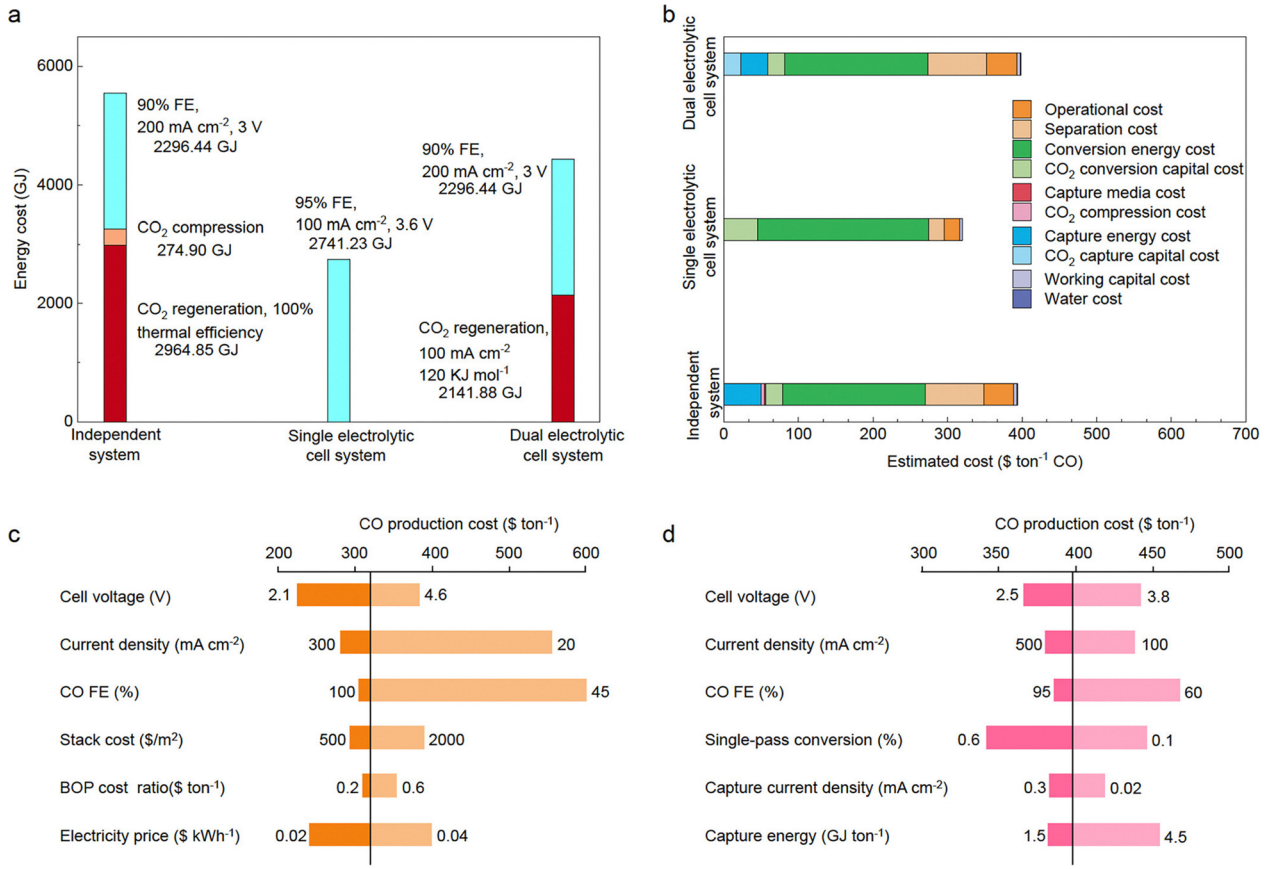

Fig. 75 (a) Comparative schematic of energy consumption for the production of 100 tons of CO across various systems. (b) Techno-economic assessment (TEA)-based estimation of CO production costs. (c) and (d). Sensitivity analysis of CO production costs for a single electrolytic cell system and a dual electrolytic cell system, respectively, based on optimistic and pessimistic parameter assumptions. Reprinted (adapted) with permission from *ACS Energy Lett.* 2023, **8**(6), 2840–2857. Copyright © 2023 American Chemical Society.

and economic performance. (Fig. 76) provides a comprehensive techno-economic and exergy comparison of four DRM-based configurations, conventional CCU, ICCU, and solar-driven direct and indirect ICCU (D-ICCU and ID-ICCU), highlighting the systemic benefits of integration and renewable energy coupling. The energy balance shows that all ICCU systems require lower reactor energy input than CCU because CO_2 capture and conversion occur in a single unit, eliminating transport-related penalties, although D-ICCU exhibits the lowest syngas output due to partial substitution of methane-derived energy with solar input as seen in (Fig. 76a). Economically in (Fig. 76b), *in situ* DRM reduces variable O&M costs from 389.03 M$ $year^{-1}$ in CCU to 322.49 M$ $year^{-1}$ in ICCU, while solar integration further lowers this value to approximately 268.7 M$ $year^{-1}$ in D/ID-ICCU, with methane feedstock remaining the dominant cost contributor (~70%), reflecting the strongly endothermic nature of $CaCO_3$ decomposition and DRM. In (Fig. 76c), exergy analysis indicates a progressive improvement from CCU (83.59%) to ICCU and solar-driven systems, with D-ICCU achieving the highest exergy efficiency (89.24%) and reducing exergy losses for CO_2 avoidance by more than 80%, while all ICCU configurations simultaneously generate high-value syngas (0.67–0.68 MWh t^{-1}). Correspondingly, CO_2 avoiding costs decrease sharply from 1464.22 $ t^{-1} in CCU to 689.32 $ t^{-1} in ICCU and further to 333–346 $ t^{-1} in solar-driven ICCU, approaching MEA-based capture benchmarks; when electricity and carbon tax benefits are included, D-ICCU and ID-ICCU achieve costs as low as 208–216 $ t^{-1}, representing nearly a 79% reduction relative to CCU as proven in (Fig. 76d). Sensitivity analysis reveals that syngas cost is most sensitive to methane price in CCU and ICCU, whereas D/ID-ICCU exhibit enhanced resilience to fuel price volatility (Fig. 76e); catalyst cost has only a marginal effect across all systems (Fig. 76f), while increasing electricity prices and carbon taxes consistently improve the competitiveness of integrated configurations, with the strongest impact observed for solar-driven ICCU owing to greater CO_2 abatement (Fig. 76g and h). Notably, although ICCU alone reduces indirect CO_2 emissions by only 17.23% relative to CCU due to the unavoidable energy demand of $CaCO_3$ decomposition and DRM, solar-driven ICCU replaces approximately half of the fossil fuel input, lowering total CO_2 emissions to 24.10 and 24.83 kg s^{-1} for D-ICCU and ID-ICCU, respectively, thereby positioning solar-assisted ICCU as a particularly promising pathway for scalable, low-carbon syngas production.

Moreover, Spurgeon *et al.* explored four different approaches for the synthesis of methyl formate ($HCOOCH_3$): a dual CH_3OH/H_2O electrolyzer equipped with a CO_2 capture unit, a dual

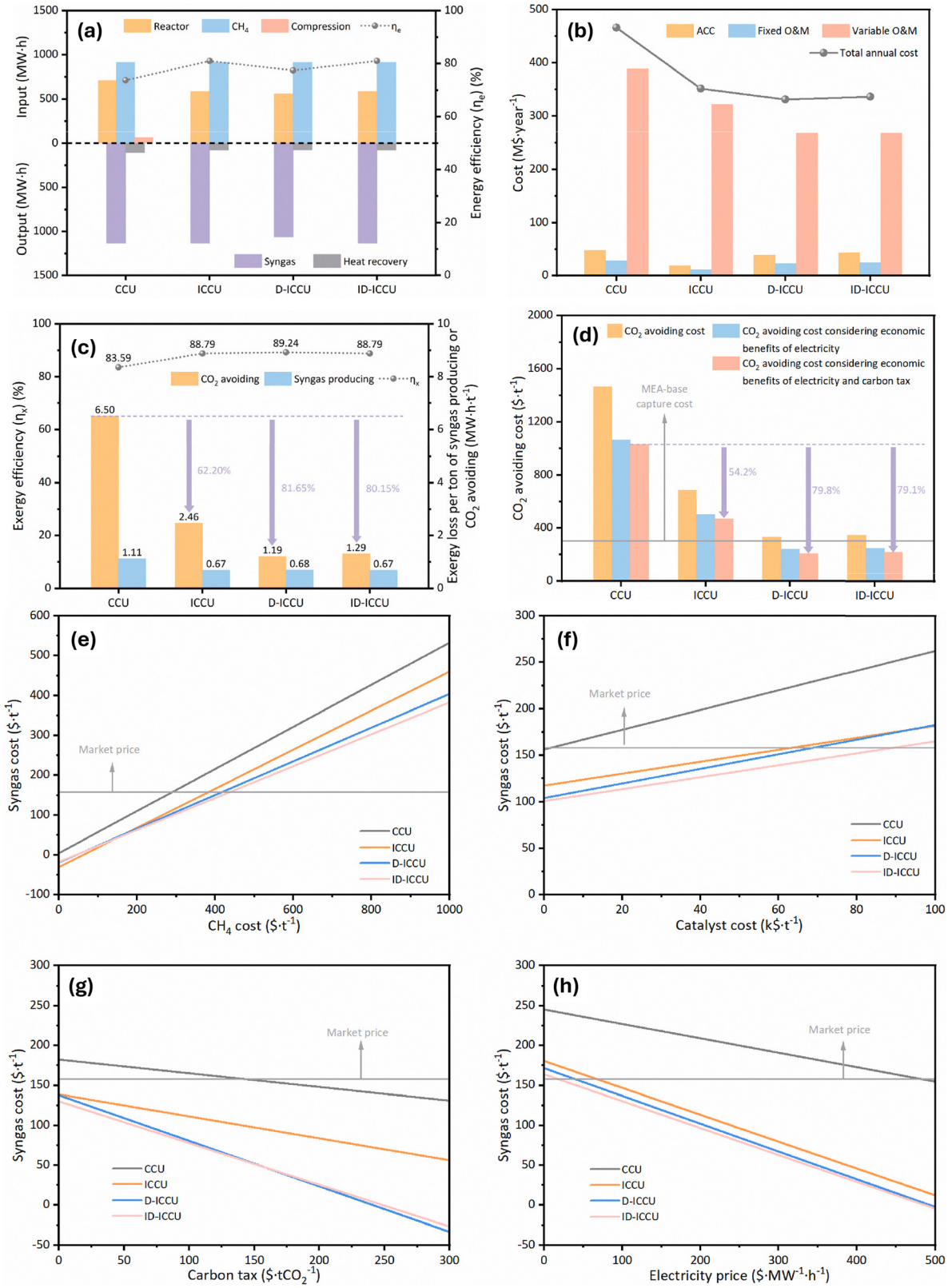

Fig. 76 Techno-economic and thermodynamic assessment of CCU, ICCU, D-ICCU, and ID-ICCU systems. (a) Total energy flows (input and output) and overall energy efficiency (η_e). (b) Economic evaluation breakdown including Annual Capital Cost (ACC), fixed and variable Operation & Maintenance (O&M) costs, and total annual cost. (c) Exergy efficiency (η_x) and exergy loss per ton of syngas produced or CO_2 avoided. (d) CO_2 avoiding cost. (e)–(h) Sensitivity analysis of syngas production cost with respect to variations in: (e) CH_4 cost, (f) Catalyst cost, (g) Electricity price, and (h) Carbon tax. The grey horizontal line in plots (e)–(h) indicates the market price. Reprinted (adapted) with permission from *Energy*, 2025, **316**, 134516. Copyright © 2025 Elsevier Ltd.

CH_3OH/H_2O electrolyzer directly fed with flue gas, a CH_3OH/CH_3OH electrolyzer with a CO_2 capture unit, and a H_2O/H_2O electrolyzer producing HCOOH with a downstream HCOOH/CH_3OH nonelectrochemical reactor.[516] And, their economic assessment revealed that the direct flue gas-fed dual CH_3OH/H_2O electrolyzer exhibited the lowest production cost at \$1.37 per kilogram (Fig. 77c), followed by the CH_3OH/CH_3OH electrolyzer with CO_2 capture at \$1.42 per kilogram (Fig. 77a), in comparison to the conventional commercial production cost of methyl formate at \$1.60 per kilogram. Then, they revealed that faradaic efficiency and the price of electricity significantly influence the production expenses of $HCOOCH_3$ while type of electrolyzers, flow rate, and current density exhibit modest impacts.

Furthermore, Nabil *et al.*[295] performed a comprehensive techno-economic analysis (TEA) for two scenarios: the conventional decoupled process and integrated/*in situ* separation and electrochemical conversion of CO_2 to ethylene from dilute streams (Fig. 78a). And, they stated that the integrated process can reduce the minimum selling price of ethylene by 20% as compared to the decoupled process by eliminating the energy-intensive capture, regeneration, compression and transportation steps. However, when they adopted stretch-target performance metrics by applying the optimistic integrated scenario of cell voltage = 1.60 V, current density = 500 mA cm^{-2}, and FE C_2H_4 = 65%, compared to the base scenario of cell voltage = 2.30 V, current density = 100 mA cm^{-2}, and FE C_2H_4 = 45%, the minimum selling price of ethylene significantly decreased by 79% compared to the decoupled process as it costed \$1.1 kg^{-1} C_2H_4, which was lower than the market price, about \$1.3 kg^{-1} C_2H_4 (Fig. 78b).

Additionally, Li *et al.* assessed the energy performance of sequential and integrated CO_2 capture and electrochemical conversion for CO generation.[511] In detail, sequential systems employ advanced gas-fed electrolyzers with either 50% or projected 100% CO_2 utilization, whereas integrated systems explore electrolysis performance under optimistic (3 V, 90% CO FE), baseline (4 V, 70% CO FE), and pessimistic (5 V, 40% CO FE) scenarios, emphasizing comparative energy demand and economic viability (Fig. 79a). In the optimistic case, where the integrated electrolyzer fully regenerates the amine, energy consumption dropped by 44% and energy costs by 22% compared to a sequential process (Fig. 79b and c). However, this energy benefit narrows to 26% if gas-fed electrolyzers without CO_2 losses to (bi)carbonate at high current densities. Under the pessimistic scenario, the integrated systems required far higher energy (2412 kJ mol^{-1} CO_2) to drive the integrated conversion.

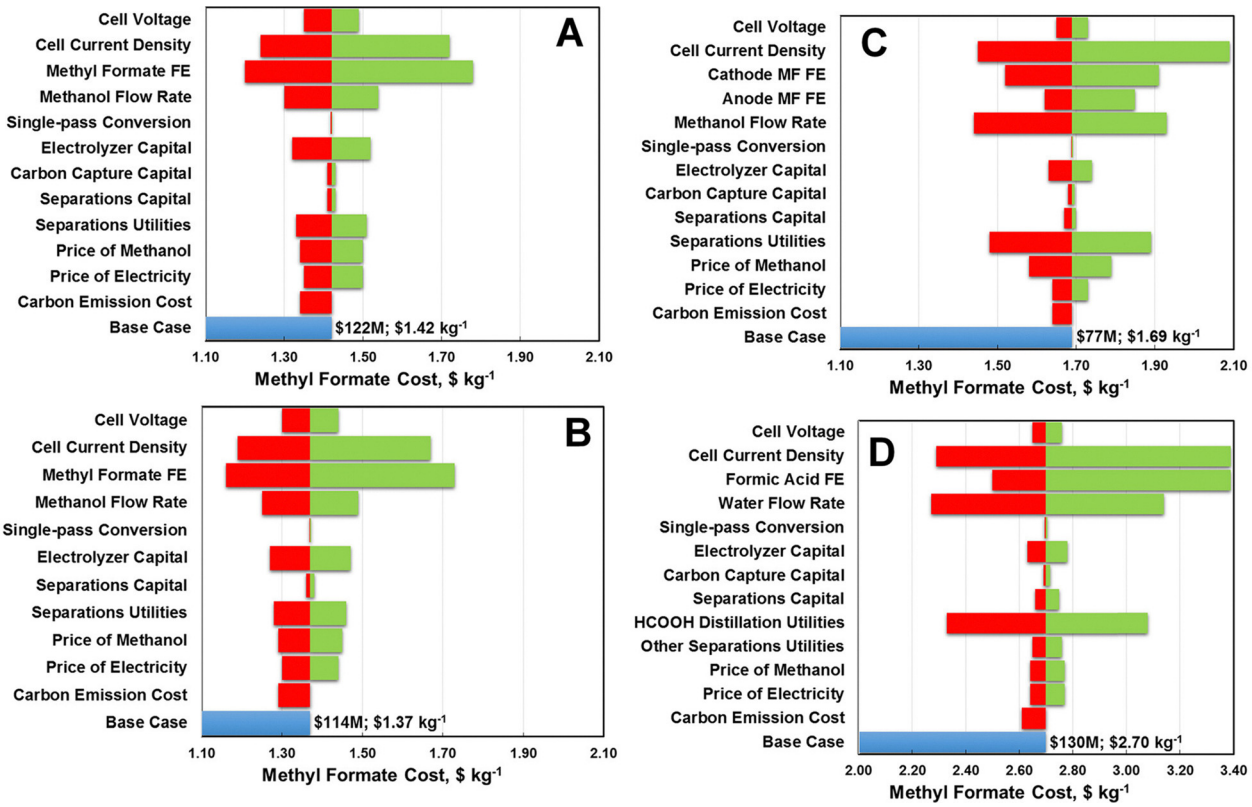

Fig. 77 Sensitivity analysis of four electrochemical systems for methyl formate production *via* CO_2 reduction, showing the impact of ±25% variation in key parameters on levelized cost (LC MF) and capital expense, with blue bars indicating base case estimates under a carbon emission cost of \$100 per tonne CO_2. (A) Electroreduction of captured CO_2 in a dual CH3OH/H_2O electrolyzer. (B) Direct electroreduction of flue gas CO_2 in a dual CH_3OH/H_2O electrolyzer. (C) Electroreduction of captured CO_2 in a CH_3OH/CH_3OH electrolyzer. (D) Electroreduction of captured CO_2 in a H_2O/H_2O electrolyzer with a downstream CH_3OH reactor. Reprinted (adapted) with permission from *ACS Sustainable Chem. Eng.* 2022, **10**, 38, 12882–12894. Copyright © 2022 American Chemical Society.

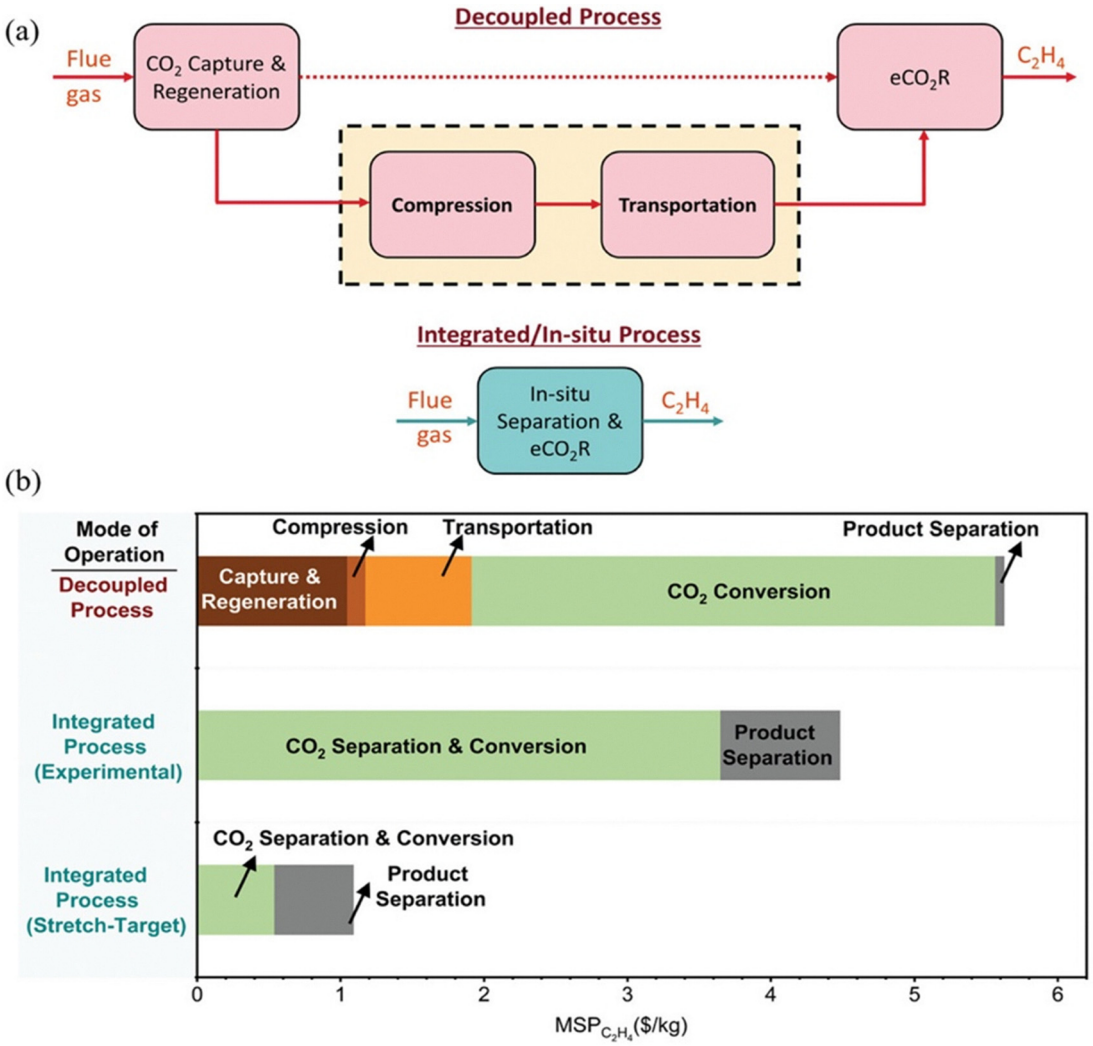

Fig. 78 (a) Comparative schematic and cost analysis of traditional decoupled *vs.* integrated CO_2 conversion processes to C_2H_4. (b) Cost analysis minimum selling price (MSP(C_2H_4)) contributors for both approaches, showing lower costs in the integrated approach. Reprinted (adapted) from *Adv. Mater.* 2023, **35**(24), 2300389. Copyrights © 2023 The Authors. Published by Wiley-VCH GmbH under the terms of CC-BY license.

Thus, they pointed out further improvement on faradaic efficiency and cell voltage at industrial current densities is essential to reduce energy consumption at least similar to the gas-fed electrolyzer performance, otherwise, the sequential method remains effective.

Moreover, Pinto *et al.* performed a techno-economic and life-cycle assessment of formate production from blast-furnace gas using either an electrocatalytic route (ER) or a biocatalytic route (BR).[517] With faradaic efficiency 81% and current density 100 mA cm^{-2}, ENaF70% and ENaF60% had a production cost between \$1.07 and \$0.71 per kg which was lower than for biocatalysis (BNaF70% and BNaF50%), about \$0.93–\$1.39 per kg, considering uncertainty analysis of electricity/power cost and H2 purchase cost which varied between 0.07 and 0.10 USD per kWh and 0.60–1.0 USD per kg respectively (Fig. 80). Life-cycle assessment reveals that biocatalysis achieved lower product carbon footprints, achieving a net-emissions reduction below petrochemical formate in 58% of simulations, compared to just 2% for electrocatalysis. Although, electrolysis can offset up to 77% of its emissions through carbon-negative credits from blast-furnace-gas valorization, its overall global warming potential (GWP) remains higher.

Kim *et al.* conducted a comprehensive technoeconomic assessment demonstrating the feasibility of an integrated ''reactive carbon capture'' system, which simultaneously captures atmospheric CO_2 and directly converts it into carbon monoxide (CO) within a single closed-loop process using a bicarbonate electrolyzer.[518] They addressed the challenge between the high pH required for efficient CO_2 capture and the lower pH preferred for electrolysis by employing chemical promoters such as piperazine to accelerate capture kinetics, enabling a cost-effective capture unit. Based on a mass-balance model of the optimized setup, the analysis estimated a break-even CO production cost of \$0.72 kg_{CO}^{-1} without separations, \$0.94 kg_{CO}^{-1} with separations, and \$0.86 kg_{CO}^{-1} with separations and a promoter (Fig. 81), thereby reinforcing the potential

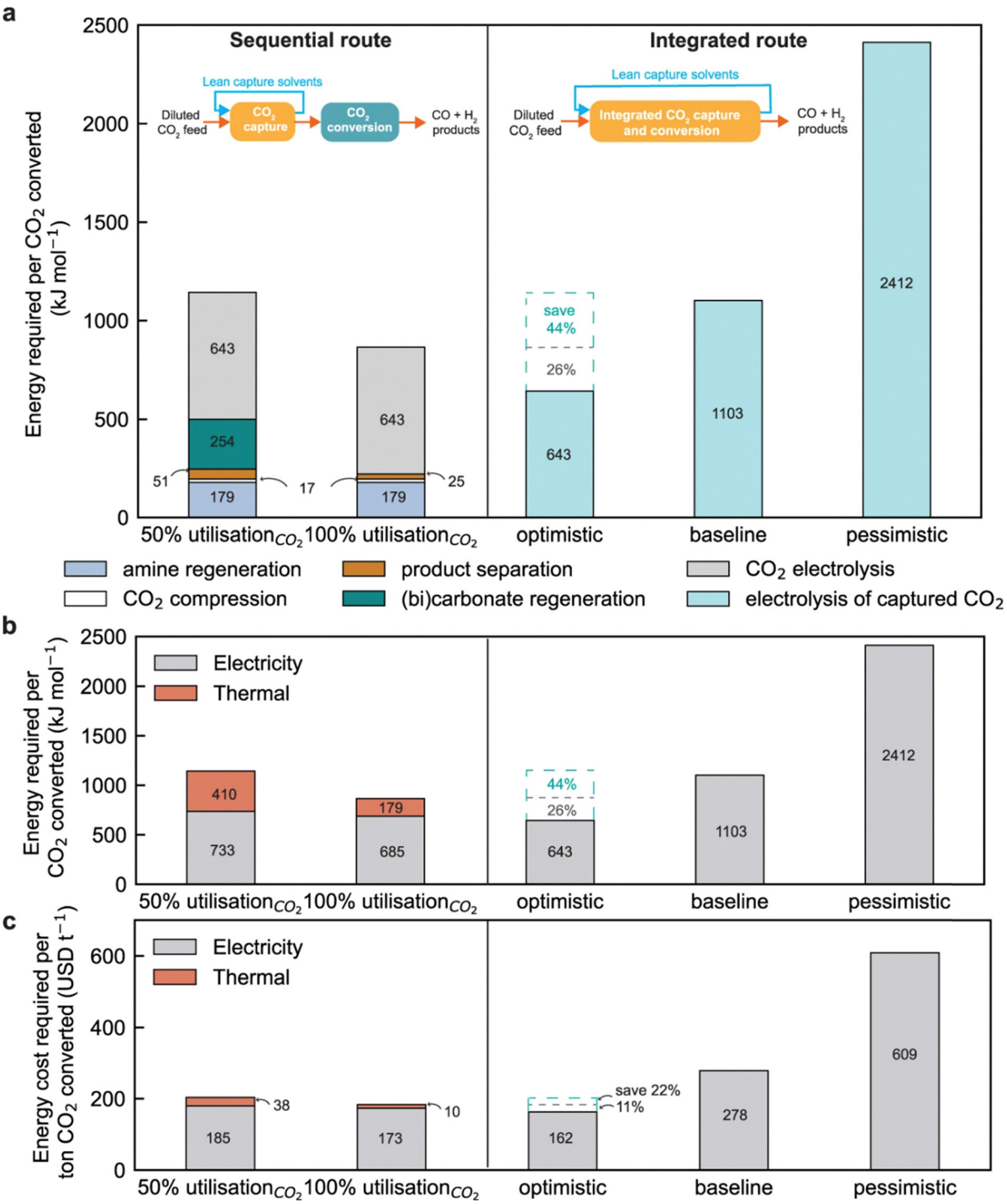

Fig. 79 Scenario analysis of (a), overall energy consumption for sequential and integrated routes. (b) Thermal energy and electricity consumption. (c) Energy cost. Reprinted (adapted) from *Nat Commun* 2022 **13**, 5398. © 2022 The Authors. Published by Springer Nature under the terms of CC-BY license.

of reactive carbon capture as a scalable and viable route for carbon utilization.

Regarding carbon capture and utilization (CCU) *versus* Carbon capture and storage (CCS), Rathore *et al.*[519] assessed the role of both pilot-scale technologies in mitigating CO_2 emissions from the highly carbon-intensive steel sector, highlighting both their technical potential and the economic and operational challenges associated with large-scale deployment. In the Blast Furnace–Basic Oxygen Furnace (BF-BOF) route, as shown in (Fig. 82a), the base production cost is INR 28 979 per tcs (~USD 350 per tcs) at an emission intensity of ~2.4 tCO_2 per tcs. When CCS is applied at USD 92 per tCO_2, costs rise to about INR 38 000 per tcs (~USD 460 per tcs) at ~0.6 tCO_2 per tcs, while near-zero steel enabled by CCU at USD 468 per tCO_2 increases costs

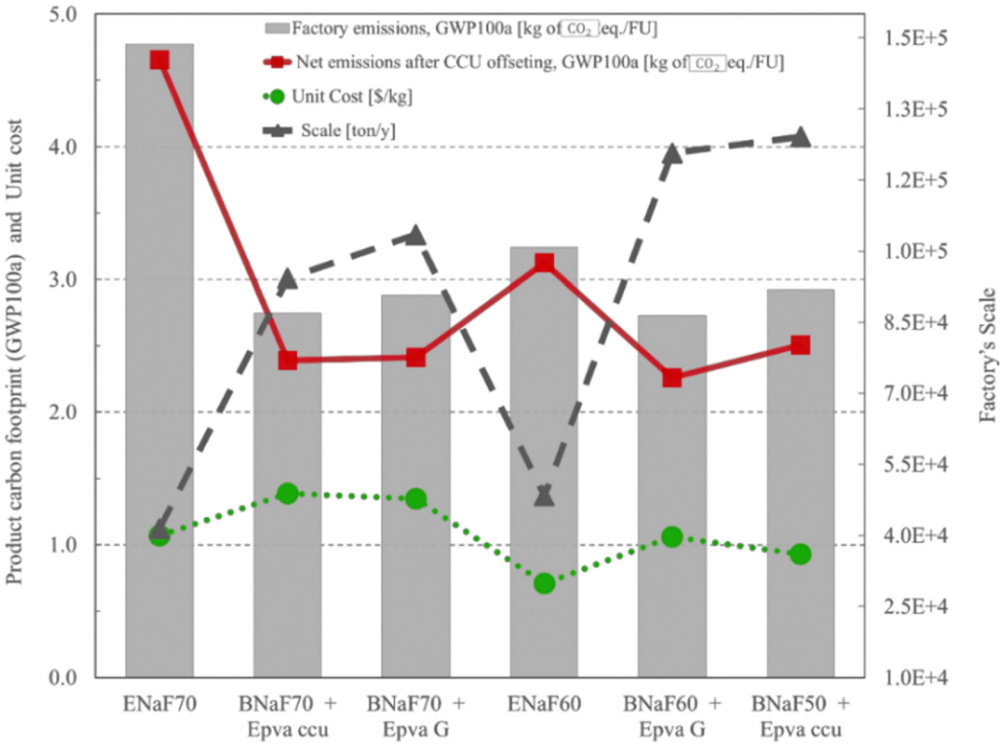

Fig. 80 Summary of TEA and LCA for formate production. Reprinted (adapted) from *ACS Sustainable Resour. Manage.* 2025, **2**(5), 733–743. Copyrights © 2025 The Authors. Published by American Chemical Society under the terms of CC-BY license.

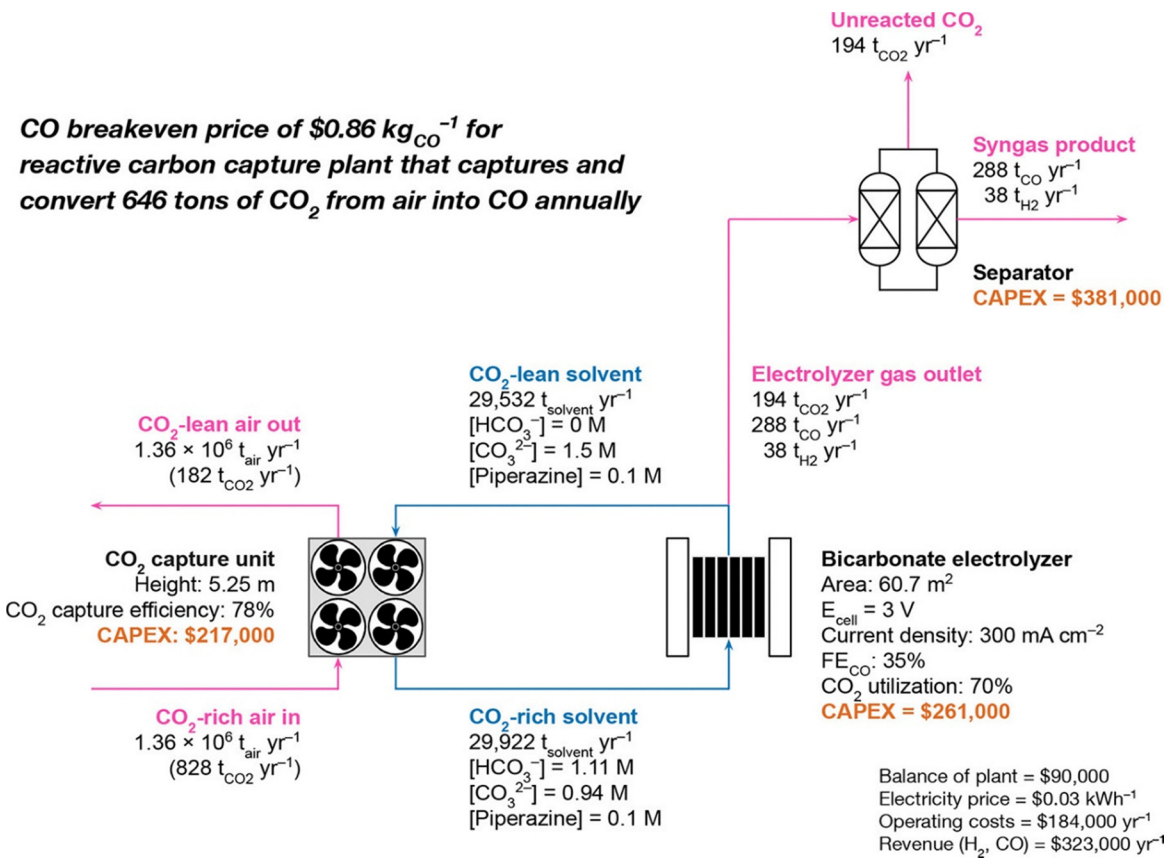

Fig. 81 Process flow diagram and techno-economic analysis of an integrated reactive carbon capture system. Reprinted (adapted) from *ACS Energy Lett.* 2025, **10**(1), 403–409. Copyright © 2025, American Chemical Society.

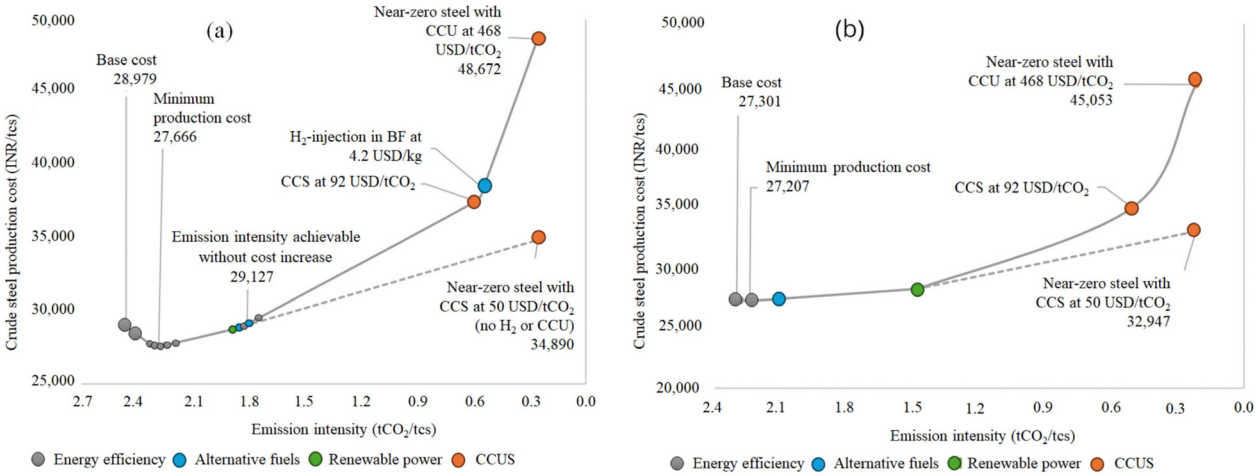

Fig. 82 Economic feasibility of steel decarbonization, highlighting initial emission reduction potentials of (a) 25% (BF-BOF) and (b) 8% (coal DRI-IF) at zero marginal cost. Reprinted (adapted) from *Energy Sustain. Dev.* 2025, **89**, 101866. Copyrights © 2025 by International Energy Initiative. Published by Elsevier Inc.

sharply to INR 48 672 per tcs (~USD 585 per tcs) at ~0.3 tCO_2 per tcs. In comparison, the Coal-based Direct Reduced Iron–Electric Arc Furnace (DRI–IF) route, as shown in (Fig. 82b), starts from a slightly lower base cost of INR 27 301 per tcs (~USD 330 per tcs) at ~2.3 tCO_2 per tcs. With CCS at USD 92 per tCO_2, costs rise to around INR 35 000 per tcs (~USD 420 per tcs) at ~0.6 tCO_2 per tcs, while near-zero steel enabled by CCU at USD 468 per tCO_2 reaches INR 45 053 per tcs (~USD 540 per tcs). Overall, although both routes exhibit strong cost sensitivity to CCS and CCU, the DRI–IF pathway consistently maintains a modest cost advantage at comparable emission intensities. They have also emphasised that, despite encouraging results from pilot-scale CCU projects such as Tata Steel India, ArcelorMittal Belgium, and HIsarna Netherlands, which report capture efficiencies of 80–90% and partial GHG reductions of 30–50%, progress is still limited by the lack of standardized monitoring, reporting, and verification (MRV) frameworks. This restricts the comparability of outcomes across different sites and technologies. CCU systems, particularly solvent-based capture, remain highly energy-intensive, requiring 3–4 GJ per ton of CO_2 captured, and face integration challenges with existing steelmaking operations, including solvent degradation, impurity management, and limited utilization of waste heat. Economic evaluations highlight that high capital expenditures ($100–300 per ton of CO_2) and operational costs ($20–50 per ton of CO_2) result in long payback periods, making the deployment of CCU heavily dependent on supportive policies such as carbon pricing, tax incentives, or subsidies. Furthermore, scale-up and replicability remain uncertain, as most pilots are tailored to site-specific conditions and lack standardized modular designs, while limited CO_2 transport and storage infrastructure further constrains widespread adoption. Finally, life-cycle assessments indicate potential environmental benefits but show wide variability due to differences in system boundaries, assumptions on energy sources, and product lifespans, underscoring the need for harmonized LCA methodologies to quantify net climate impacts reliably.

Regarding the usage of flue gas in comparison with pure CO_2, Tian *et al.* developed a 2D steady-state multi-physics model to compare Cu_xO-catalyzed CO_2 electrolysis fed with purified CO_2 to a direct-flue-gas feed containing 20% CO_2, 4% O_2, 0.5% SO_2 and balance N_2.[520] At atmospheric pressure and room temperature, the hydrogen evolution reaction (HER) dominated the electrochemical reduction of flue gas, reaching a faradaic efficiency of 91.5% at −1.17 V *vs.* RHE due to the low CO_2 partial pressure and competitive oxygen reduction. To overcome these limitations, the study proposed an effective optimization strategy by increasing the operating pressure to 20 atm and reducing the catholyte inlet temperature to 273 K, which significantly enhanced the CO_2 reduction reaction with a faradaic efficiency of 71%, compared to pure CO_2 electrolysis under standard conditions with a faradaic efficiency of 56% (Fig. 83a). Notably, the yield of valuable C_1 products from optimized flue gas became more than 2.3 times greater than pure CO_2 electrolysis, which may simplify downstream separation and improve system efficiency (Fig. 83b). The study also explained that this optimization strategy homogenized the dissolved CO_2 concentration and mitigated the high temperature in the catalyst layer caused by the increased current density and SO_2 partial pressure in the flue gas. Economically, the flue gas electrolysis system required 2 years to reach its break-even point, while the purified CO_2 system took 4 years (Fig. 83c). Also, over a 20-year lifecycle, the flue gas electrolysis had a net present value 1.5 times higher than that of purified CO_2 electrolysis, making it a more profitable and scalable solution.

To enhance the economic viability of electrochemical CO_2 reduction (eCO_2R), it can be coupled with anodic oxidation reactions that have lower thermodynamic cell potentials than the oxygen evolution reaction (OER) and yield other value-added byproducts, but it is needed to effectively design the electrolysis system, including optimized flow fields, reactant feeding rates, and integrated systems for industrial applications for efficient conversion.[521] To illustrate, Verma *et al.* stated that coupling eCO_2R with glycerol electro-oxidation reduces energy consumption

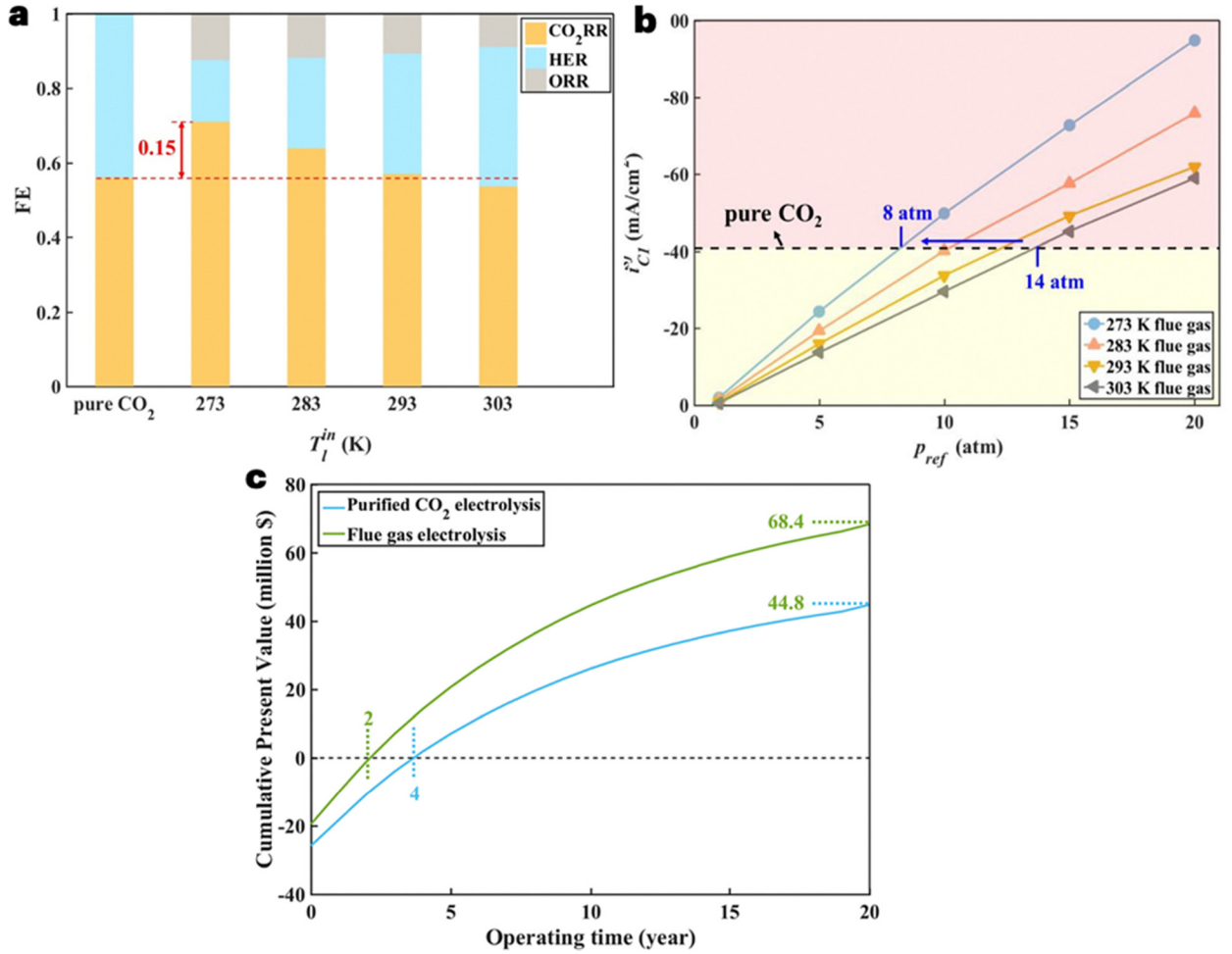

Fig. 83 (a) Effect of electrolyte inlet temperature on FE for flue gas electrolysis at P_{ref} = 20 atm, V_{app} = −1.17 *vs.* RHE. (b) Variation of current density of C1 products in flue gas electrolysis with temperature and pressure at −1.17 *vs.* RHE. (c) Cumulative present value analysis for flue gas electrolysis and purified CO_2 electrolysis. Reprinted (adapted) from *Applied Energy*, 2023 **351**, 121787. Copyrights © 2023 The Authors, Published by Elsevier Ltd.

by 37–53% compared to using OER,[522] while reducing the onset cell potentials for the production of HCOOH, C_2H_4, and C_2H_5OH to −0.9 V, −0.95 V, and −1.3 V, compared to −1.75 V, −1.8 V, and −2.1 V, respectively, when applying OER (Fig. 84a–c). Also, the onset cell potentials for CO formation reduced to −0.75 V with glycerol and −0.95 V with glucose, *versus* −1.6 V under OER conditions (Fig. 84d). Thus, these reductions in cell potential enhance both CO_2 utilization efficiency and technoeconomic viability of the process.

Additionally, Jiang *et al.* developed an H_2-integrated CO_2 reduction (CO_2RR) system that couples CO_2 electrolysis with the hydrogen oxidation reaction (HOR) in a single cell, mediated by a $Ni(OH)_2$/NiOOH redox layer that blocks carbon crossover and catalyst poisoning (Fig. 85a).[523] At a current density of 50 mA cm^{-2}, the H_2-integrated CO_2 electrolysis cell delivers CO or formate with up to 95.3% faradaic selectivity at voltages below 0.9 V and remains stable for more than 100 h. They concluded that this approach reduced the total polarization loss by up to 22% and the overall energy consumption by up to 42% compared to conventional CO_2 electrolysis, offering a scalable route to integrate CO_2 electrolysis with the hydrogen economy (Fig. 85b and c).

Besides that, Wang *et al.* paired acidic CO_2-to-CO electroreduction with allyl alcohol oxidation reaction to acrolein, achieving a faradaic efficiency of 96% for CO_2-to-CO on the cathode and 85% for allyl alcohol-to-acrolein on the anode (Fig. 86a and b).[524] And, they observed a reduction in the system's full-cell voltage by 0.7 V (Fig. 86c), leading to 1.6 times less energy usage than the most efficient CO_2-to-CO eCO_2R process (Fig. 86d). Also, the cell reached 84% single-pass CO_2 utilization with a 6 times improvement in atom efficiency by operating in acid and suppressing carbonate formation.

Regarding the feasibility assessment for the eCO_2R products, Gao *et al.* conducted a techno-economic analysis (TEA) of four main products: HCOOH, CO, C_2H_5OH and C_2H_6 while assuming CO_2 capture cost is $40 per ton of CO_2, using the post-combustion method due to its current level of maturity and technological capability.[525] And, they highlighted that, in the base scenario, formic acid at $0.468 per kg and CO at $0.449 per kg are cost-competitive, whereas ethanol at $1.872 per kg and ethylene at $2.907 per kg are not yet economically viable because FE of ethanol and ethylene (60%) is lower than that of formic acid and carbon monoxide, about 80%. For sensitivity analysis, a 25% increase in

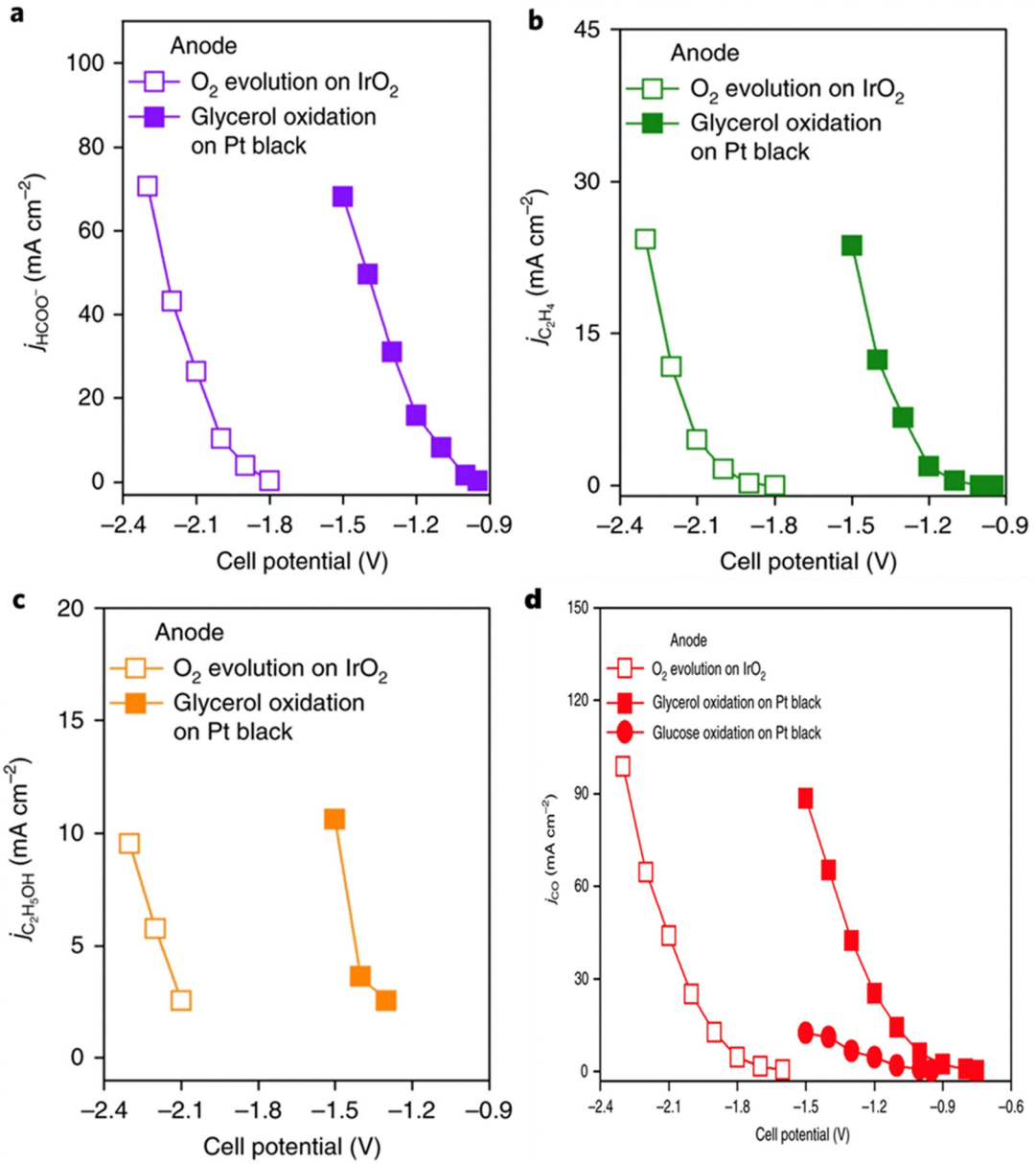

Fig. 84 Electrochemical performance for the electroreduction of CO_2, coupled to O_2 evolution, glycerol electro-oxidation or glucose electro-oxidation at the anode: Partial current densities plotted against applied cell potential for (a) formate ($HCOO^-$). (b) Ethylene (C_2H_4). (c) Ethanol (C_2H_5OH) under oxygen evolution (OER) and glycerol oxidation at the anode. (d) Carbon monoxide (CO) under OER, glycerol, and glucose oxidation at the anode. Reprinted (adapted) from *Nat Energy* 2019, **4**, 466–474. Copyrights © 2019, The Author(s), under exclusive license to Springer Nature Limited.

selectivity lowers the levelized cost by ~10.8% (HCOOH), ~16% (CO), ~18% (C_2H_5OH), and ~19% (C_2H_6), while a 25% reduction in cell voltage cuts costs by ~10.2%, ~18%, ~34%, and ~13%, respectively (Fig. 87a–d). Also, after performing a net present value (NPV) study, they found out that formic acid and CO generate positive NPVs of $89.86 million and $52.11 million, respectively, by the 20th year, while ethanol and ethylene consistently show negative NPVs, reaching −$134.88 million and −$537.79 million, which validates the advantage of C1 chemical production *via* CO_2 electrolysis (Fig. 87e). Furthermore, formic acid and carbon monoxide achieved energy conversion efficiencies (EE) values of 35.1% and 39.3%, respectively, while ethanol and ethylene recorded substantially lower efficiencies of 23.7% and 24.3%, reinforcing the viability of C_1 product formation in CO_2 electrolysis systems (Fig. 87f). Finally, they found out that as all assessed renewable energy could generate a carbon-negative effect, hydroelectricity displayed the most negative value at −1.89 kg of CO_2 equiv., followed by −1.75 kg of CO_2 equiv. for wind energy. Whereas, concentrated solar power (CSP) technology is a highly desirable renewable energy supply with −1.69 kg of CO_2 equiv. over −1.57 kg of CO_2 equiv. for PV due to CSP's direct steam generation for the electrolysis plant's downstream separation process.

In terms of solar-driven electrochemical CO_2 reduction, Chae *et al.* performed TEA study for PV-Chae *et al.* developed

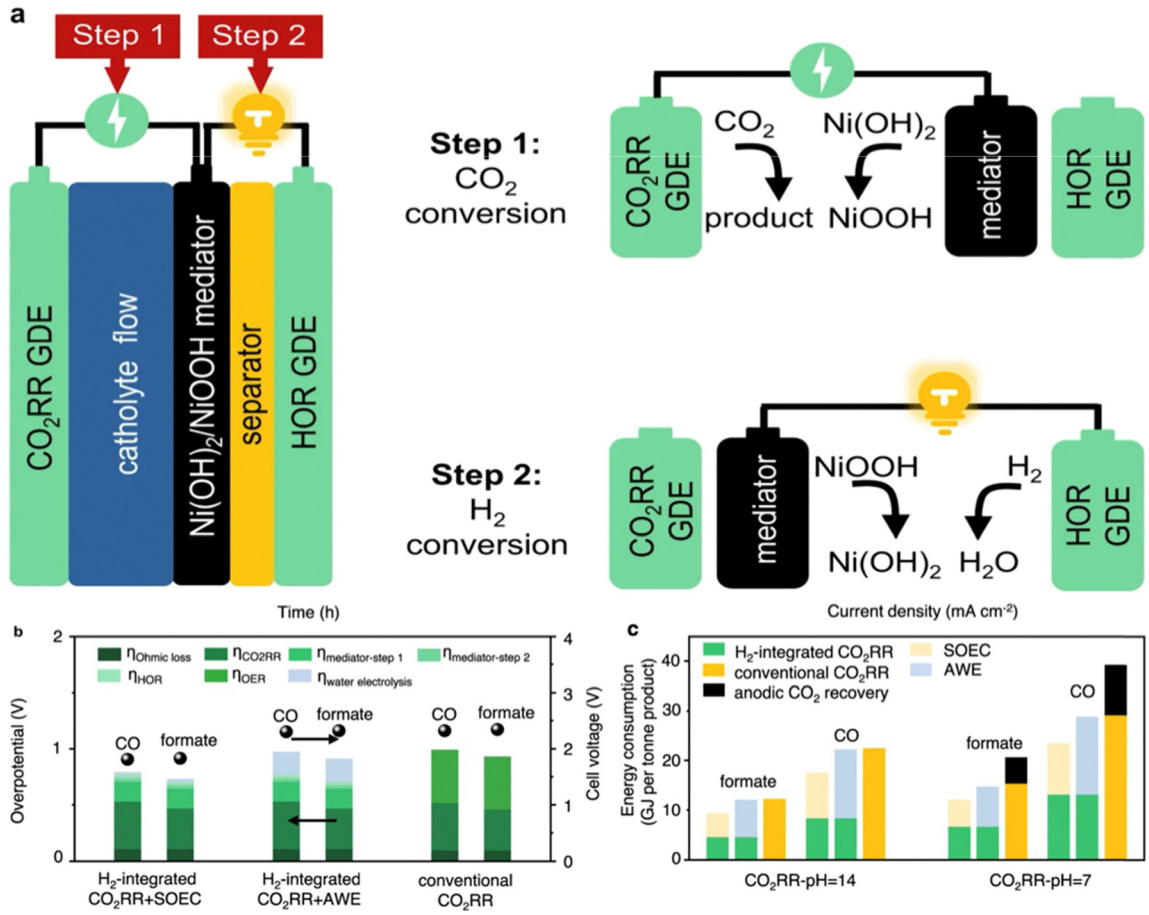

Fig. 85 (a), Schematic of the H_2-integrated CO_2 electrolysis cell architecture. (b) Polarization loss analysis for H_2-integrated CO_2 electrolysis. (c) Energy consumption analysis. Reprinted (adapted) from *Nat Commun*, 2024 **15**, 1427. Copyrights © 2024 The Authors. Published by Springer Nature under the terms of CC-BY license.

a solar-powered device for CO_2-to-CO conversion, achieving 8.03% solar-to-CO efficiency and estimating a base-case production cost of $10.94 per kg CO at a 4 MW scale (Fig. 88a and b).[526] To compete with the traditional CO price of $0.6 per kg, a sensitivity analysis revealed that the current density must be improved to >80 mA cm^{-2} and the CO_2 one-path conversion must reach 22% or boosting solar-to-CO efficiency to 20% while halving the membrane cost (Fig. 88c and d). Finally, the study estimated a required carbon tax of $6.6/kg CO_2 to bridge the gap with fossil-derived CO pricing.

Furthermore, Agliuzza *et al.* demonstrated that solar-driven CO_2 electroreduction to CO, powered by dye-sensitized solar cells (DSSCs), achieved a faradaic efficiency of 73.85% at a current density of 3.35 mA cm^{-2} under 1 sun illumination (Fig. 89a). These results were validated by a mathematical model and sustained efficiencies of 68.5% and 64.1% under reduced light intensities of 0.8 and 0.6 suns, respectively (Fig. 89b), which reproduced by the experimental chronoamperometry and simulated data (Fig. 89c and d). The study highlights the need to address the performance decline of CO_2RR under lower incident power for effective PV-EC optimization systems for real-world deployment.[527]

While techno-economic assessments provide valuable initial insights, it is crucial to recognize that most of these analyses are typically conducted under idealized laboratory conditions, presenting best-case scenarios that may not fully account for the complexities of industrial application. Although laboratory prototypes may perform well, demonstrating durability over thousands of hours and scaling from small single cells (1–25 cm^2) to industrial stacks (0.01–1 m^2) introduces major challenges such as catalyst degradation, mass transport limitations, Ohmic losses, and more. And, addressing these barriers requires multidisciplinary approaches, so the following section will provide a detailed analysis of the key Performance Indicators, challenges, opportunities, and future prospects for ICCC.

Key performance indicators for ICCC

The key performance indicators for CO_2 capture and electrochemical conversion to consider in the TEA study when developing electrocatalysts for the final product are stability, cell voltage, faradaic efficiency, and current density, with carbon efficiency, product purity, productivity, capacity, and more for both industrial

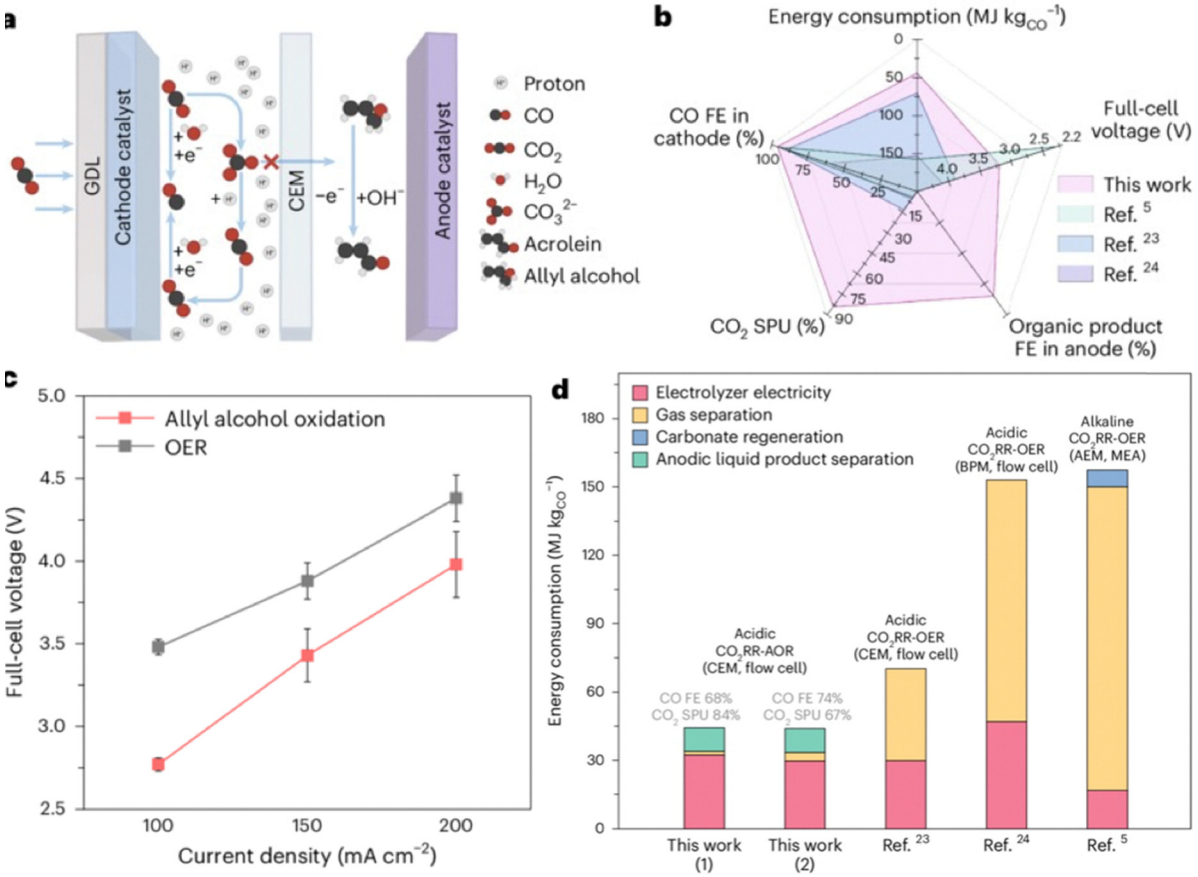

Fig. 86 (a) Schematic of the paired electrolysis system coupling acidic CO_2 reduction with alkaline allyl alcohol oxidation. (b) Performance benchmark comparing paired electrolysis to state-of-the-art systems. (c) Full-cell voltage comparison for CO_2RR-AOR and CO_2RR-OER systems across current densities. (d) Energy consumption analysis across different CO_2 electrolysis systems. Reprinted (adapted) from *Nat Sustain*, 2024, **7**, 931–937. Copyrights © 2024 The Authors, under exclusive license to Springer Nature Limited.

and laboratory settings, as detailed in (Table 39). For instance, Segets *et al.* pointed out that some key operational criteria that need to be met for eCO_2R-derived products to become economically viable include current densities over 300 mA cm^{-2}, cell voltages under 2.5 V, faradaic efficiencies over 80%, and system lifetimes over 50 000 hours.[528]

Furthermore, (Table 40) critically analyzes the four requested industrial feasibility factors, explicitly linking DFM structural features to quantitative performance limitations and mitigation strategies across all material classes. Diffusional resistances arise from microporous architectures (MOFs HKUST-1 PLD $>$ 8 Å halves D_{eff}, COFs PLD 4.5–6 Å limit $j < 100$ mA cm^{-2},[153,182,243,293] requiring meso/macropore hierarchies and monolithic shaping to optimize Thiele modulus under industrial GHSV. Competitive adsorption reflects sorbent chemistry where hydrophilic amines/carbonates risk pore flooding (HKUST-1 H_2O blocks OMS) while hydrophobic CALF-20 retains 4 mmol g^{-1} at 80% RH, demanding site-specific tuning for humid flue tolerance.[294] Temperature-pressure constraints emerge from ΔH_{ads}-catalytic kinetics mismatch—strong chemisorption (CaO/amines) favors low-*T*/high-*P* capture but demands severe regeneration conflicting with methanation kinetics, whereas weaker physisorption reduces flue capacity, necessitating heat-conductive supports for *T*–*P* overlap. Cyclic deactivation is structure-intrinsic: COF imine hydrolysis causes 80% capacity loss in 5 humid cycles,[153,158] molten salt Ni-Cr corrosion limits lifetimes $<$5000 h,[447,507] and amine oxidative degradation above 110 °C requires basic supports/tethered motifs targeting $>$1000 cycles, confirming robust structure-function design must integrate all four factors for industrial viability.

Challenges and opportunities of ICCC

Despite clear conceptual advantages and encouraging case studies, ICCC technologies are still at early to mid-technology readiness levels (typically TRL 3–5), with demonstrations largely confined to laboratory or small pilot reactors processing gram- to kilogram-scale sorbent inventories. Thus, as the ICCC process is a new emerging technology, many considerable gaps must be addressed for its industrial applications such as material degradation under realistic flue-gas impurities (SO_x, NO_x, H_2O, O_2) and understanding the synergies between catalysts and adsorbents in addition to reaction intermediates, and comprehensive considerations from an engineering perspective such as process design, especially for ICCC-Met, ICCC-RWGS,

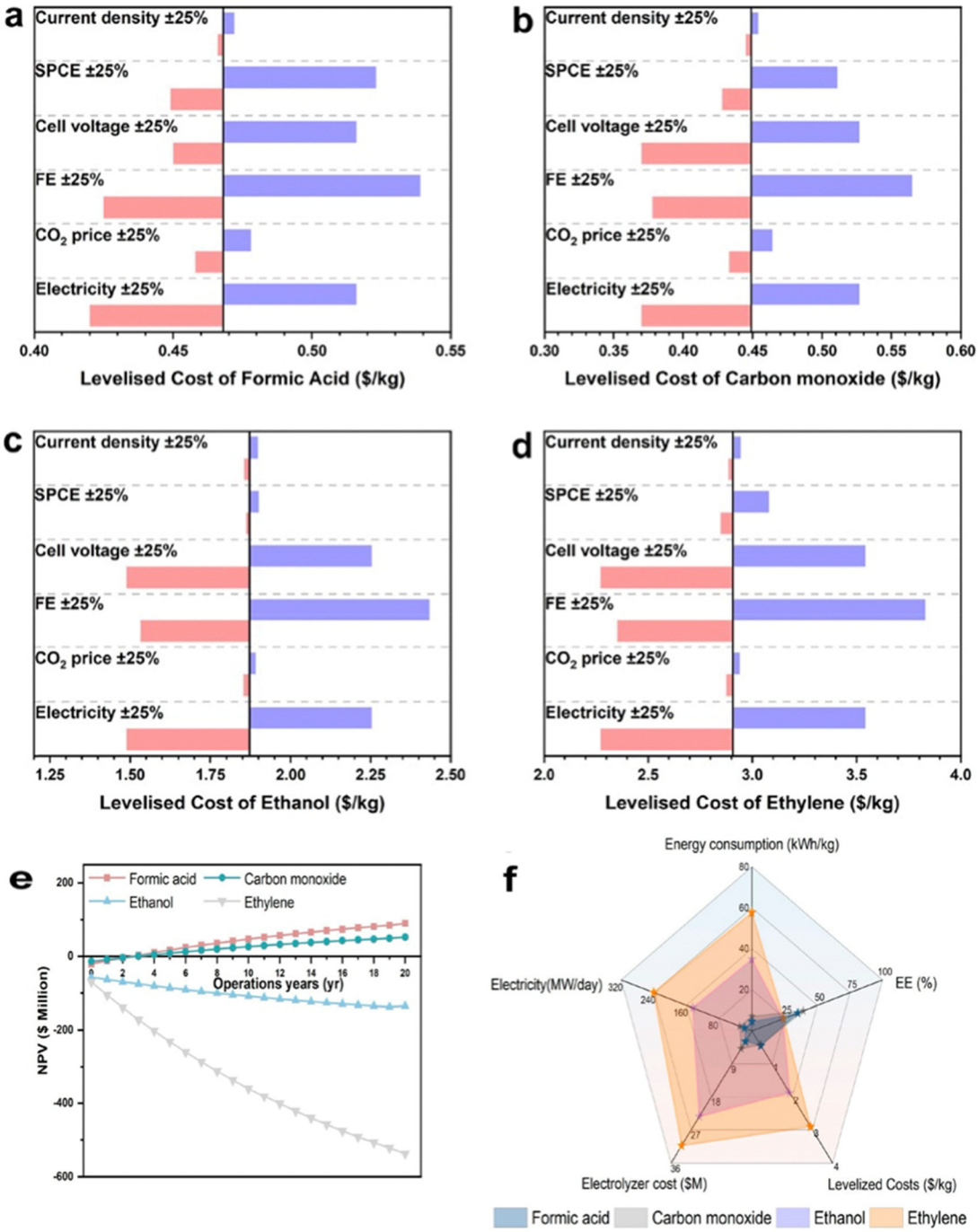

Fig. 87 Sensitivity analysis of the levelized cost for eCO_2RR products: (a) formic acid. (b) Carbon monoxide. (c) Ethanol. (d) Ethylene as a function of cell voltage, selectivity, current density, prices of CO_2 and electricity, and SPCE. (e) Net Present Value (NPV) analysis over a 20-year horizon, revealing economic feasibility of formic acid and CO but persistent deficits for ethanol and ethylene. (f) Key energy conversion indicators. Reprinted (adapted) with permission from *Energy Fuels* 2023, **37**, 23, 17997–18008. Copyright © 2023 American Chemical Society.

and ICCC-DR.[14] While ICCC presents promising opportunities, there are ongoing challenges:[530,531]

• Although CO_2 can be captured from flue gas streams, its use in producing energy and synthesizing materials is still relatively underdeveloped due to the high expected costs and the efficiency constraints of current techniques as well as the technological immaturity of green hydrogen production which is inevitably used in the ICCC-Met and ICCC-RWGS processes.

• It is challenging to match the operation conditions of both CO_2 capture and conversion reactions such as reaction rates, temperatures, duration, heat management, and continuous operation close to industrially relevant conditions which

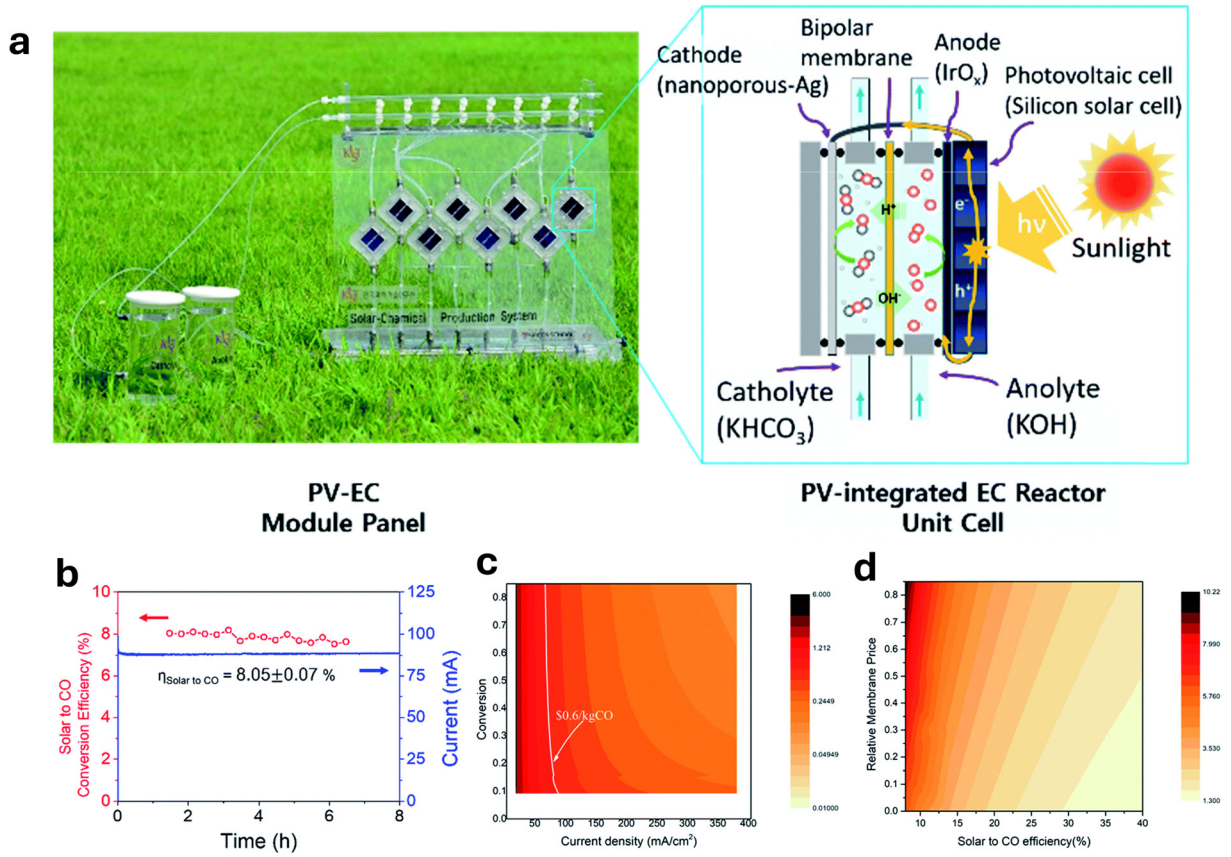

Fig. 88 (a) PV-EC device and schematic of the unit cell structure. (b) Solar to chemical conversion efficiency during PV-EC device operation. (c) and (d) Contour plots of CO cost *vs.* current density, CO_2 conversion, relative membrane price, and solar-to-CO efficiency. Reprinted (adapted) from *Sustainable Energy Fuels*, 2020, **4**, 199. Copyrights © 2020 The Authors. Published by Royal Society of Chemistry (RSC).

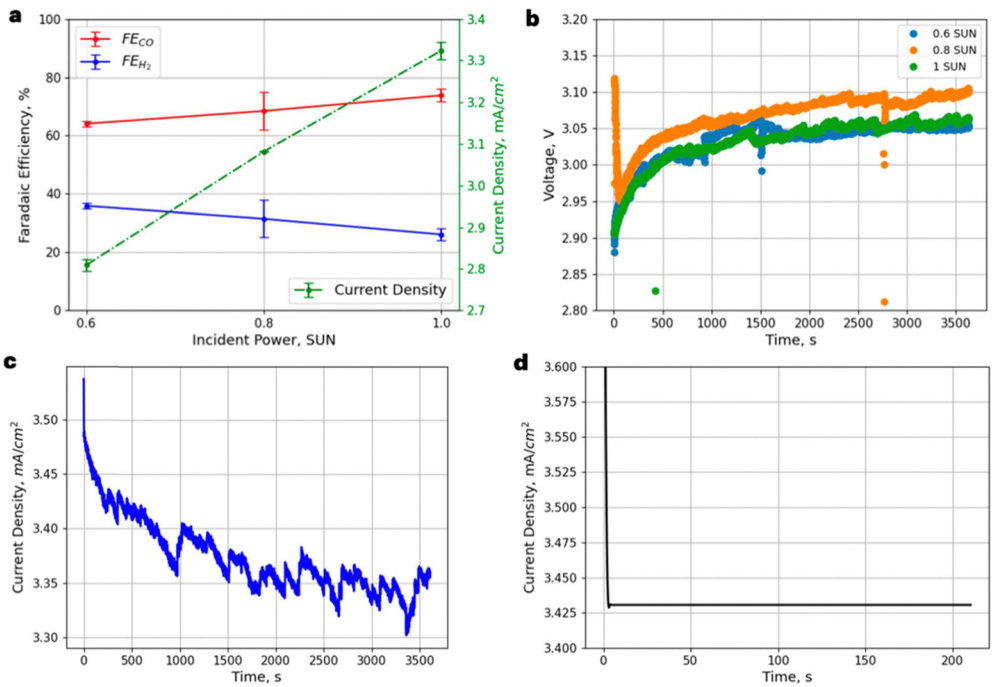

Fig. 89 (a) The performance of the integrated solar-powered CO_2 reduction device under different levels of solar irradiance. (b) Cell-voltage stabilization under different light intensities. (c) Experimental chronoamperometry at 1 sun. (d) Modelled current-density response at 1 sun. Reprinted (adapted) from *Appl. Sci.* 2025, **15**(2), 549. Copyrights © 2025 by the Authors. Published by MDPI under the terms of CC-BY license.

Table 39 Key performance indicators for CO_2 electrochemical conversion[277,529]

Indicators	Definition	Impact
Faradaic efficiency	A measure of the selectivity in an electrochemical process FE = $(I \times t/z \times F \times n) \times 100$, where: I is the current (in amperes) t is the time (in seconds) z is the number of required electrons to produce the given product. F is Faraday's constant n is the number of moles of the product theoretically produced	High faradaic efficiency (FE) is advantageous for reducing both the capital and operating costs of the system, because it is directly proportional to the energy efficiency and inversely proportional to the electrode area of the electrolyzers, which should exceed 80% for most products
Energy efficiency	The energy input per unit mass product EE = $(\Delta E^{\circ}/\Delta E_{applied}) \times$ FE, where: ΔE° is the equilibrium full cell potential $\Delta E_{applied}$ is the applied full cell voltage FE is the average faradaic efficiency	High energy efficiency leads to lower energy losses, better process performance, and hence lower operating costs of the system
Partial current density	The fraction of the total current density is specifically used for forming that particular product $J_x = (I/A) \times$ FE, where: I is the current passed by the electrode A is the area of the electrode FE is faradaic efficiency	High partial current density is essential for a higher production rate, resulting in the requirement of a smaller electrode area for the CO_2 electrolyzers, which reduces the capital costs of the system
Cell voltage	The total applied voltage to a CO_2 electrolyzer $P_x = j \times A \times E_{cell}$, where: P_x is the power required to produce component x J is the partial current density of component x $\sum$ A is the electrode area E_{cell} is the cell voltage	Low cell voltage means less energy consumption to drive the electrochemical reaction by reducing internal resistances and overpotentials for a more energy-efficient and cost-effective system
Stability	The time retention of a performance metric (*e.g.*, FE, partial current, or voltage) within an interval while the system's deterioration must be below 10 μV per hour or exceed 10 000 hours	Low catalyst stability means more frequent replacements over the plant's operational lifetime, thereby increasing the capital costs of the system
Cycling stability (Capture)	Number of adsorption/desorption cycles without >10% capacity loss	>100 cycles
Catalyst durability (Electrolysis)	Continuous operation time without >10% drop in FE or activity	>100 h
Carbon efficiency	The ratio of CO_2 concentrations in the pre- and post-eCO_2R process. carbon eff. = $(\sum C_x \times n_x)/nCO_2$, where: C_x is the number of carbons in product x n_x is the number of moles of product x produced nCO_2 is the number of moles of CO_2 that entered the system	For successful commercialization of the eCO_2R process, carbon eff > 50% is recommended to optimize process efficiency and minimize costs
CO_2 uptake capacity	The amount of CO_2 a material can adsorb per unit mass under specified conditions, reflects total capacity	Up to 7–8 mmol g^{-1} at 273 K, 1 bar
Internal CO_2 utilization rate	Captured CO_2 converted *vs.* total captured	>85%
Mass transport limitation index	Measure of CO_2 diffusion efficiency (*e.g.*, *via* limiting current or impedance)	Minimal diffusion loss; >90% active site accessibility
Pressure/flow compatibility	Operates under typical flue gas or DAC conditions	1–2 atm (flue gas); 400 ppm (air)
Resistance to impurities (SO_x, NO_x)	Tolerance to flue gas contaminants	Minimal loss of capacity (<10%)
Scalability index	Scalability of synthesis method and electrode fabrication	>10 g batch synthesis; compatibility with commercial supports
Energy consumption per mol CO_2 converted	Includes electrolysis energy and capture regeneration	<200 kJ mol^{-1}
Carbon intensity (LCA)	Net CO_2 avoided per kg of product	Positive CO_2 balance (>90%)
Product purity	The percentage of purity of a substance, indicating the absence of impurities or contaminants. Purity = (specific product 'n_x'/$(\sum C_x \times n_x)$) × 100%	High product purity means better conversion, lower separation costs, less energy required, and fewer risks associated with impurities
Capacity/productivity	Capacity refers to a system's maximum production (t per day), whereas productivity assesses resource efficiency (MWh t^{-1})	Higher productivity and properly scaled capacity result in higher economic viability, accelerated return on investment, and a cheaper cost per unit

Table 40 Critical analysis of industrial feasibility factors limiting dual-functional materials (DFMs) in ICCC

Feasibility factor	Structural determinants	Quantitative metrics & limitations	Mitigation strategies	Material examples	Ref.
Diffusional resistances	Pore hierarchy (micro/meso/macropores) tortuosity, particle size shaping (pellets/monoliths/foams)	Thiele modulus (φ), effectiveness factor (η) Microporous DFMs: slow intraparticle diffusion at high GHSV CALF-20 GDE: 355–380 mA cm^{-2} *vs.* HKUST-1 half-D_{eff}	Meso/macropore networks Short diffusion paths Hierarchical architectures	MOFs (HKUST-1 PLD >8 Å), Zeolites (LTA 3.8 Å), COFs (PLD 4.5–6 Å)	243, 293
Competitive adsorption	Sorbent site chemistry (amine/carbonate/oxide/carbon) surface hydrophilicity functionalization density	CO_2/H_2O co-adsorption isotherms hydrophilic: pore flooding *vs.* cooperative binding CALF-20 : 4 mmol g^{-1} (RH 80%) *vs.* HKUST-1 blocking	Hydrophobic tuning Site-specific functionalization Humid flue-gas testing	Hydrophilic amines/carbonates *vs.* hydrophobic CALF-20/POPs	
T–P operating window	Binding strength (ΔH_{ads}) catalyst-support thermal overlap heat conduction	ΔH_{ads} 40–80 kJ mol^{-1} optimal strong chemisorption: severe regeneration *T* weak physisorption: low flue capacity	Heat-conductive supports Proximal sorbent-catalyst *T–P* overlap optimization	Amines (40–60 °C), Zeolites (25–200 °C), Molten salts (550–900 °C)	312–320
Cyclic deactivation	Pore architecture, metal dispersion support acidity/basicity phase stability	Coking (Ni/Cu), amine degradation COF imine hydrolysis (80% loss/5 cycles) Molten Ni-Cr corrosion <5 kh	Basic supports (anti-coking) tethered amines corrosion-resistant alloys	COFs (imine fragility), Molten salts (Ni-Cr), Amines (oxidative)	153–158

should be considered in further studies as performance tests and process simulation.

• Some challenges with electrochemical conversion are its energy-intensive fuel production process, making it unfeasible, and the need for a comprehensive understanding of highly efficient and selective catalysts, including their mechanisms, degradation, morphological variations, and active site characteristics.

• The absence of a global, consistent carbon pricing system makes it challenging to predict potential revenues from ICCC's projects which prevents developers and investors from accurately assessing the long-term financial assessments due to the lack of economies of scale coupled with high-risk perception while other low-carbon technologies like renewable energy become more affordable.

• The adoption of ICCC technologies is influenced by policy and regulatory challenges including the lack of financial incentives such as grants, tax credits, or feed-in tariffs, the absence of consistent regulations, and public concerns about safety, environmental impact, and long-term viability.

Recent advances and future prospects

The future development of ICCC technologies will be shaped by efficiently addressing these challenges and leveraging opportunities. Nonetheless, to make ICCC technologies more economically viable and attractive from a sustainable point of view, the following factors should be considered:[11,532,533]

• Reducing the energy costs associated with large-scale CO_2 capture through adopting more efficient, innovative CO_2 capture technologies and improving process energy efficiency could enhance the economic viability of CO_2 capture and conversion.

• Integrating CO_2 conversion systems with other clean energy sources like nuclear, solar, wind, and geothermal can address both CO_2 emissions and energy supply challenges while enhancing the economic feasibility of the ICCC process, which is challenging and requires significant global governmental support for large-scale and widespread adoption.

• Enhancing material stability and activity, optimizing reactor designs and exploring innovative reactor types are crucial for improving performance. In the context of electrochemical processes, adopting novel solid oxide cell (SOC) configurations can reduce ohmic and polarization resistances, thereby boosting the power densities of SOC stacks.

• To enhance CO_2 conversion efficiency, product selectivity, and stability, it is vitally important to address the CO_2 conversion process at intermediate temperatures (300–700 °C) as a promising trend where materials such as catalysts, electrodes, and electrolyte materials need to be developed to fulfill the requirements for the conversion process.

• The implementation of emission-based carbon taxes could play a crucial role in accelerating the development of CO_2 capture and conversion technologies, given their proven effectiveness in curbing greenhouse gas emissions. And, converting a fraction of the captured CO_2 into marketable products would create additional economic value, thereby further supporting the financial sustainability and economic feasibility of the ICCC process.

• ICCC's potential applications across multiple sectors are vast, providing a flexible solution to meet energy demands sustainably and open up new opportunities beyond traditional carbon capture and storage approaches. However, the variety of products and processes from ICCC technologies emphasizes the importance of conducting thorough life cycle assessments, including techno-economic, social, and market evaluations, when considering industrial-scale implementation and the commercial future of CO_2-derived products.

• Despite growing interest in the research and development efforts required to assess the technical and economic viability of Integrated Carbon Capture and Conversion (ICCC) in scientific and industrial contexts, there has been little field-based research exploring the public's understanding and perceptions

of the ICCC technology. Thus, there should be communication strategies that prioritize the practical applications of ICCC products, rather than focusing exclusively on Carbon Capture and Storage (CCS).

• Future progress in ICCC will depend on tightly coupled computational–experimental co-design, where multiscale modeling (DFT, microkinetics, and process simulations) is used not only to screen adsorbents and catalysts but to co-optimize capture thermodynamics, reaction pathways, and reactor operating windows.[534] Integrating these models with high-throughput synthesis and automated testing will enable rational tuning of binding energies, site proximity, and transport properties specifically for integrated capture–conversion rather than standalone capture or catalysis.[12]

• There is an urgent need for in-*operando* spectroscopy and microscopy (*e.g.*, DRIFTS, ambient-pressure XPS, XAS, Raman/IR under flow, *operando* TEM) to resolve CO_2 speciation, intermediate formation, and active-site evolution under realistic flue-gas and cycling conditions.[535] Such tools are essential to disentangle adsorption, activation, and deactivation (SO_x/NO_x/H_2O/O_2 poisoning) in ICCC materials and to validate mechanistic hypotheses that currently rely heavily on *ex situ* characterization and DFT alone.[26]

• Reactor engineering and heat/mass management remain major bottlenecks for scale-up: exothermic hydrogenation and carbonate formation must be balanced against endothermic desorption and pre-heating, while minimizing temperature gradients, hot spots, and diffusion limitations in packed or structured beds.[27]

• Future work should focus on intensified reactor concepts (*e.g.*, structured monoliths, microchannel and rotating beds, periodic reactors) and robust thermal integration strategies that allow rate-matched capture and conversion under cyclic operation at industrial scales.[536]

Summary

The integrated carbon capture and conversion (ICCC) process is rapidly emerging as a pivotal research focus in both academia and industry, driven by its potential to provide a promising economic incentive for CO_2 mitigation, enhanced energy security, and industrial growth. This review paper discusses the latest ICCC developments, focusing on electrochemical conversion coupled with solvent-based and sorbent-based CO_2 capture approaches for flue gas. The review primarily highlights key adsorbent and absorbent materials used in this context, including Porous Organic Polymers (POPs), Covalent Organic Frameworks (COFs), Metal–Organic Frameworks (MOFs), Zeolites, Carbon Materials, Amines, Ionic liquids, Eutectics, and Molten Salts, as concluded below.

• In terms of Porous Organic Polymers (POPs), especially covalent triazine frameworks (CTFs) and conjugated microporous polymers (CMPs), they are a flexible group of crystalline or amorphous organic materials that have long chain of π-conjugation, a large specific surface area, and adjustable heteroatom functionalities. This makes them very useful for capturing CO_2 and converting it to electricity. CTFs are prepared *via* different methods such as iono-thermal or acid-catalyzed trimerization of nitrile monomers. They have stiff, nitrogen-rich structures that allow CO_2 to be strongly physiosorbed through Lewis's base–acid interactions and provide coordination sites for anchoring metal centers that are catalytically active. CMPs, which are synthesized by cross-coupling approach, have intrinsic characteristics represented in semiconductivity and hierarchical porosity. This makes it suitable materials for charge and mass transfer in electrochemical systems. CTFs can be modified by molecular catalysts, metal nanoparticles, or single-atom sites to these frameworks makes them even better at electrocatalysis by encouraging selective CO_2 activation and multi-electron transfer processes. CTFs and CMPs work together to create a flexible platform for producing new materials that combine selective CO_2 adsorption with effective, long-lasting electrocatalytic CO_2 reduction (CO_2RR) activity.

• With respect to Covalent Organic Frameworks (COFs), they are distinguished as promising materials for integrated CO_2 capture and conversion owing to their adjustable porosity, structural adaptability, and chemical stability. Their design enables precise functionalization, improving selectivity and catalytic efficacy. COFs, capable of hosting metal centers and conductive units, effectively facilitate electrocatalytic CO_2 reduction, rendering them suitable for sustainable carbon utilization strategies and prospective clean energy applications.

• Considering Zeolites for ICCC, they are shown to be a good and dependable substitute for integrated carbon capture and utilization systems when metal-loaded or nanoconfined zeolites are used to make electrochemical reduction more efficient due to their crystalline microporous structures and adjustable acidity. Also, Zeolites are good at separating and activating CO_2 molecules because they are very thermally stable, have a high ion-exchange capacity, and can selectively adsorb certain shapes.

• In the context of Metal–Organic Frameworks (MOFs), they have emerged as a highly promising category of materials for the simultaneous collection and electrochemical reduction of CO_2. Their modular structures, which integrate adjustable porosity, elevated surface area, and functionalizable metal–organic linkers, enable the simultaneous enrichment of CO_2 and the provision of catalytic conditions for selective conversion. Essential tactics encompass the creation of metal–organic framework (MOF)-based gas diffusion electrodes to augment local CO_2 concentration, the design of permselective membranes for targeted CO_2 transport, and the incorporation of functional groups, such as amines, to boost capture from dilute gas streams. Moreover, metal–organic frameworks (MOFs) can be engineered to influence product selectivity, such as methane, ethylene, or formate, by altering pore chemistry, metal centers, or interfacial environments. The advancement of conductive MOFs or MOF-derived composites mitigates inherent conductivity constraints, facilitating effective electron transfer and stability in electrochemical environments. These advancements collectively illustrate the adaptability of MOFs as dual-function adsorbent-catalyst systems, establishing a basis for sustainable and scalable carbon usage. Their versatility renders them crucial to contemporary initiatives

in merging CO_2 collection with CO_2RR, providing significant insights for the design of next-generation electrocatalysts.

Regarding Metal Oxides, they have garnered considerable interest as multifunctional materials that can combine CO_2 collection with electrochemical CO_2 reduction (CO_2RR). Their plentifulness, robust basicity, and structural adaptability facilitate excellent CO_2 adsorption, especially when altered with amine groups or integrated into porous substrates. In addition to capture, metal oxides are essential in catalysis by activating CO_2 molecules, stabilizing critical intermediates, and inhibiting competing hydrogen evolution. Modifying oxide composition and nanostructure has enhanced selectivity for formate (*e.g.*, SnO_2, Bi_2O_3, In_2O_3) or multi-carbon compounds (oxide-derived Cu). Recent integrated techniques, including amine-functionalized oxides, bifunctional gas diffusion electrodes, and hybrid oxide-metal systems, illustrate the capability of oxides to combine capture and conversion in a singular process, even in dilute flue gas environments. Notwithstanding limitations such as restricted adsorption capacity, stability of functional groups, and the attainment of industrially pertinent current densities, the versatility and scalability of oxide-based systems render them formidable contenders for practical CO_2 usage. These advancements collectively underscore the potential of metal oxides as effective, economical materials for enhancing integrated CO_2 capture and conversion technologies.

• Regarding Amines electrolytes, Amine electrolytes have served as the pillars of post-combustion CO_2 capture (PCC) and early integrated capture-conversion systems because of their cost advantages and chemical reactivity. Nevertheless, their inherent disadvantages, like low ionic conductivity, hydrogen evolution reaction (HER) interference, solvent degradation, and moderate current densities, are significant barriers to long-term sustainability and efficiency. Accordingly, there is a growing tendency toward novel next-generation solvents such as ionic liquids (ILs) and deep eutectic solvents (DESs), with higher CO_2 solubility, better electrochemical stability, and tunable physicochemical properties. Such novel solvent systems have promise to enable more efficient, sustainable, and scalable integrated CO_2 capture and electrochemical valorization under low-temperature processes such as direct air capture (DAC). Therefore, while amines remain best suited for mature, large-scale systems where cost and reactivity are most important, the future of carbon management is becoming more directed towards ILs, DESs, and hybrid approaches better suited for future generations of carbon capture and conversion technology.

• For Ionic Liquid, Due to their distinct structural features, high CO_2 solubility, large ionic conductivity, and broad electrochemical windows, ionic liquids (ILs) are quickly becoming a promising class of solvents for CO_2 capture and electrochemical reduction (CO_2ER). Researchers can adjust the properties of ILs to achieve the best CO_2 capture and conversion performance because of their great diversity, which results from the ability to customize both cations and anions. Recent developments have demonstrated that important limitations of previous IL designs can be addressed by modifying the interactions between ILs and CO_2 to further increase absorption capacities and decrease viscosities. While supported ILs, in which ILs are immobilized on solid substrates, offer high capacities, faster adsorption rates, and lower costs, making them appealing for industrial applications, conventional ILs, amino-functionalized ILs, and non-amino functionalized ILs each offer unique mechanisms and performance profiles for CO_2 capture. As electrolytes, additives, and electrode modifiers in CO_2ER, ILs' potent interactions with CO_2 facilitate effective dissolution, activation, and catalytic conversion, frequently improving process efficiency and product selectivity. Future studies should concentrate on methods to maintain the catalytic advantages of ILs while reducing dosage, as this is crucial for industrial scalability due to their comparatively high cost. A deeper mechanistic understanding of IL–CO_2 interactions, electric double-layer structures, and co-catalytic effects remains required despite tremendous advancements. This can be accomplished through *in situ* characterization, molecular simulations, and quantum chemical calculations. Furthermore, machine learning is a promising approach for screening and designing high-performance ILs for CO_2 capture and conversion. Overall, ILs offer a versatile and potent platform for sustainable carbon management, and their full potential in useful, large-scale applications will depend on continued innovation in material design, mechanistic understanding, and process integration.

• Referring to deep eutectic solvents (DESs), due to their high CO_2 solubility, low toxicity, and environmental friendliness, deep eutectic solvents (DESs) are quickly gaining attention as effective, sustainable alternatives for CO_2 capture and conversion. DESs are simple to create from low-cost, bio-based ingredients and have adjustable characteristics that can be tailored for chemical and physical CO_2 absorption as well as for incorporation into electrochemical reactions. Recent developments, such as the use of co-solvents, immobilization techniques, and functionalized DESs, are improving performance and scalability, even though issues like high viscosity and limited conductivity still exist. DESs are positioned as a promising platform for upcoming carbon capture and utilization technologies due to their adaptability and environmental credentials.

• In the context of Molten Salts, it combines capturing CO_2 and converting it into functional carbon nanomaterials. This process uses carbonate-based electrolytes to directly reduce CO_2 at the cathode, producing carbon structures such as nano-tubes, nano-onions, and nano-coils. It has high current efficiency, minimizes byproducts, and offers long-lasting economy. The composition of the electrodes, the chemistry of the electrolyte, and the additives all have a significant impact on the morphology and yield of the product. This makes this method a scalable, CO_2-negative way to use carbon and make advanced materials.

Besides that, this comprehensive review consolidates literature to assess the techno-economic analysis and key performance indicators of the ICCC process. Despite recent progress in improving ICCC technologies, there are still considerable challenges: technical limitations such as energy consumption and system efficiency, and non-technical barriers such as high capital costs, lack of economic incentives, public awareness, and inadequate government regulations. Thus, scaling up ICCC from laboratory settings to industrial deployment necessitates

further research into cost-effective syntheses of dual-function materials, the development of reactor and separation apparatus design, and holistic evaluations through integrated system-level modeling, life cycle assessment, and techno-economic analysis for performance optimization and economic feasibility.

Author contributions

Mohamed A. Elokl: writing – original draft, data curation, visualization, writing – review & editing, investigation, validation, and methodology. Ahmed G. Ali: writing – original draft, investigation, data curation, and visualization. Abdelrahman Mohsen: writing – original draft, investigation, data curation, and visualization. Ahmed Taha: writing – original draft, investigation, data curation, and visualization. Abdelrahman Ashor: writing – original draft, investigation; data curation, and visualization. Salma Elshabrawy: writing – original draft, investigation, data curation; and visualization. Nageh K. Allam: conceptualization, investigation, validation, writing – review & editing, supervision, and funding acquisition.

Conflicts of interest

The authors declare that they have no conflict of interest.

Abbreviations

AEM	Anion-exchange membrane
AFIL	Amino-functionalized Ionic Liquid
BET	Brunauer–Emmett–Teller (method for surface area measurement)
BGDE	Bifunctional gas diffusion electrode
CCUS	Carbon capture, utilization, and storage
CMP	Conjugated microporous polymer
CNC	Carbon nanocoil
DFT	Density functional theory
DFM	Dual functional material
eCO_2R	Electrochemical CO_2 reduction
EDS	Energy-dispersive X-ray spectroscopy
EGR	Enhanced gas recovery
EMAR	Electrochemically mediated amine regeneration
EOR	Enhanced oil recovery
EPRI	Electric power research institute
EXAFS	Extended X-ray absorption fine structure
FE	Faradaic efficiency
GDE	Gas diffusion electrode
GPU	Gas permeation unit
GWP	Global warming potential
HAADF-STEM	High-angle annular dark-field scanning transmission electron microscopy
HBA	Hydrogen bond acceptor
HBD	Hydrogen bond donor
HCP	Hyper-cross linked polymer
HER	Hydrogen evolution reaction
HOR	Hydrogen oxidation reaction
HPC	High-density polyethylene-derived porous carbon
HRTEM	High-resolution transmission electron microscopy
ICCC	Integrated CO_2 capture and conversion
ICCU	Integrated carbon capture and utilization
ICP	Inductively coupled plasma
IEA	International energy agency
SBU	Secondary building unit
SMR	Steam methane reforming
SOC	Solid oxide cell
SWCNT	Single-walled carbon nanotube
TEA	Techno-economic analysis
TOF	Turnover frequency
TON	Turnover number
TPP	Tetraphenyl porphyrin
TRL	Technology readiness level
US GAO	US Government Accountability Office
NO_x	Nitrogen oxides
CNS	Carbon nano-scaffold
CNT	Carbon nanotube
COF	Covalent organic framework
CO_2RR	CO_2 reduction reaction
CTF	Covalent triazine framework
CVD	Chemical vapor deposition
DEA	Diethanolamine
DES	Deep eutectic solvent
IGCC	Integrated gasification combined cycle
IL	Ionic liquid
IPCC	Intergovernmental panel on climate change
LCA	Life cycle assessment
LIB	Lithium-ion battery
MDEA	Methyl diethanolamine
MFI	Mobil composition of matter no. five (zeolite framework type)
MMM	Mixed matrix membrane
MOF	Metal–organic framework
NPV	Net present value
OER	Oxygen evolution reaction
OMS	Open metal site
ORR	Oxygen reduction reaction
PAF	Porous aromatic framework
PCP	Porous coordination polymer
PEM	Polymer electrolyte membrane
PGDE	Permselective gas diffusion electrode
PIM	Polymer of intrinsic microporosity
POP	Porous organic polymer
PTFE	Polytetrafluoroethylene
PV	Photovoltaic
RCC	Reactive capture of CO_2
RDF	Radial distribution function
RWGS	Reverse water–gas shift reaction
WGSR	Water–gas shift reaction
XPS	X-ray Photoelectron Spectroscopy
C_2H_4	Ethylene
CH_4	Methane

CO	Carbon monoxide
CO_2	Carbon dioxide
H_2	Hydrogen
H_2O	Water
$HCOO^-$	Formate
N_2	Nitrogen
SO_x	Sulfur oxides

Data availability

The data supporting this article have been included in the manuscript.

Acknowledgements

This work is supported by the American University in Cairo.

References

1 W. Gao, S. Liang, R. Wang, Q. Jiang, Y. Zhang, Q. Zheng, B. Xie, C. Y. Toe, X. Zhu, J. Wang, L. Huang, Y. Gao, Z. Wang, C. Jo, Q. Wang, L. Wang, Y. Liu, B. Louis, J. Scott, A. C. Roger, R. Amal, H. He and S. E. Park, *Chem. Soc. Rev.*, 2020, **49**, 8584–8686.
2 D. Sallam, B. S. Shaheen and N. K. Allam, *Green Chemistry*, 2026, **28**, 1286–1315.
3 IEA, *Global Energy Review 2025*, IEA, Paris, 2025.
4 M. Pathak, R. Slade, P. R. Shukla, J. Skea, R. Pichs-Madruga and D. Ürge-Vorsatz, in *Climate Change 2022: Mitigation of Climate Change. Contribution of Working Group III to the Sixth Assessment Report of the Intergovernmental Panel on Climate Change*, ed. P. R. Shukla, J. Skea, R. Slade, A. Al Khourdajie, R. van Diemen, D. McCollum, M. Pathak, S. Some, P. Vyas, R. Fradera, M. Belkacemi, A. Hasija, G. Lisboa, S. Luz and J. Malley, Cambridge University Press, Cambridge, UK and New York, NY, USA, 2022.
5 M. Abdallah and R. Farrauto, *Catal. Today*, 2023, **423**, 113923.
6 S. Chen, J. Liu, Q. Zhang, F. Teng and B. C. McLellan, *Renewable Sustainable Energy Rev.*, 2022, **167**, 112537.
7 IEA, *Net Zero Roadmap: A Global Pathway to Keep the 1.5 °C Goal in Reach*, IEA, Paris, 2023.
8 F. Marocco Stuardi, F. MacPherson and J. Leclaire, *Green Sustainable Chem.*, 2019, **16**, 71–76.
9 K. T. de campos Roseno, R. M. de b. Alves, R. Giudici and M. Schmal, Syngas Production Using Natural Gas from the Environmental Point of View, in *Biofuels – State of Development*, InTech, 2018.
10 G. Leonzio and N. Shah, *Green Sustainable Chem.*, 2024, **46**, 100895.
11 M. A. Sabri, S. Al Jitan, D. Bahamon, L. F. Vega and G. Palmisano, *Sci. Total Environ.*, 2021, **790**, 148081.
12 R. E. Siegel, S. Pattanayak and L. A. Berben, *ACS Catal.*, 2023, **13**, 766–784.
13 M. Bhattacharya, S. Sebghati, R. T. Vanderlinden and C. T. Saouma, *J. Am. Chem. Soc.*, 2020, **142**, 17589–17597.
14 S. Sun, H. Sun, P. T. Williams and C. Wu, *Sustainable Energy Fuels*, 2021, **5**, 4546–4559.
15 Y. Qiao, W. Liu, R. Guo, S. Sun, S. Zhang, J. J. Bailey, M. Fang and C. Wu, *Fuel*, 2023, **332**, 125972.
16 Z. Lv, H. Du, S. Xu, T. Deng, J. Ruan and C. Qin, *Appl. Energy*, 2024, **355**, 122242.
17 H. Wang, Z. Yu, J. Zhou, C. Li, A. Jayanarasimhan, X. Zhao and H. Zhang, *Energies.*, 2023, **16**, 616.
18 M. M. F. Hasan, R. C. Baliban, J. A. Elia and C. A. Floudas, *Ind. Eng. Chem. Res.*, 2012, **51**, 15665–15682.
19 M. Bui, I. Gunawan, T. V. Verheyen and E. Meuleman, in *Absorption-Based Post-Combustion Capture of Carbon Dioxide*, Elsevier Inc., 2016, pp. 589–621.
20 J. Z. Y. Tan, J. M. Uratani, S. Griffiths, J. M. Andresen and M. M. Maroto-Valer, *Nat. Rev. Chem.*, 2025, **9**, 656–671.
21 Z. Kapetaki, O. Eulaerts, A. Georgakaki, M. D. R. Gonzalez Sanchez, M. Grabowska, E. Ince, G. Joanny Ordonez, A. Kuokkanen, S. Letout, A. Mountraki and D. Shtjefni, Clean Energy Technology Observatory: Carbon Capture Utilisation and Storage in the European Union – 2022 Status Report on Technology Development, Trends, Value Chains and Markets, Publications Office of the European Union, 2022.
22 S. Hughes, A. Zoelle, M. Woods, S. Henry, S. Homsy, S. Pidaparti, N. Kuehn, H. Hoffman, K. Forrest, A. Sheriff, T. Fout, W. Summers and S. Herron, *Cost of Capturing CO2 from Industrial Sources*, 2022.
23 J. Gao, S. Choo Sze Shiong and Y. Liu, *Chem. Eng. J.*, 2023, **472**, 145033.
24 A. P. Hallenbeck and J. R. Kitchin, *Ind. Eng. Chem. Res.*, 2013, **52**, 10788–10794.
25 B. H. Ko, B. Hasa and H. Shin, *et al.*, *Nat. Commun.*, 2020, **11**, 5856.
26 M. Sardo, R. Afonso, J. Juźków, M. Pacheco, M. Bordonhos, M. L. Pinto, J. R. B. Gomes and L. Mafra, *J. Mater. Chem. A.*, 2021, **9**, 5542–5555.
27 A. Porta, R. Matarrese, C. G. Visconti, L. Castoldi and L. Lietti, *Ind. Eng. Chem. Res.*, 2021, **60**, 6706–6718.
28 M. Namdari, Y. Kim, D. J. D. Pimlott, A. M. L. Jewlal and C. P. Berlinguette, *Chem. Soc. Rev.*, 2025, **54**, 590–600.
29 D. Bhattacharyya and D. C. Miller, *Chem. Eng*, 2017, **17**, 78–92.
30 D. Jansen, M. Gazzani, G. Manzolini, E. Van Dijk and M. Carbo, *Int. J. Greenhouse Gas Control*, 2015, **40**, 167–187.
31 R. Stanger, T. Wall, R. Spörl, M. Paneru, S. Grathwohl, M. Weidmann, G. Scheffknecht, D. McDonald, K. Myöhänen, J. Ritvanen, S. Rahiala, T. Hyppänen, J. Mletzko, A. Kather and S. Santos, *Int. J. Greenhouse Gas Control*, 2015, **40**, 55–125.
32 B. Dziejarski, R. Krzyżyńska and K. Andersson, *Fuel*, 2023, **342**, 127776.
33 W. Y. Hong, *Carbon Capture Sci. Technol*, 2022, **3**, 100044.
34 J. C. Abanades, B. Arias, A. Lyngfelt, T. Mattisson, D. E. Wiley, H. Li, M. T. Ho, E. Mangano and S. Brandani, *Int. J. Greenhouse Gas Control*, 2015, **40**, 126–166.
35 J. Serafin and B. Dziejarski, *Microporous Mesoporous Mater.*, 2023, **354**, 112513.

36 Y. Chang, S. Gao, Q. Ma, Y. Wei and G. Li, *Renewable Sustainable Energy Rev.*, 2024, **199**, 114550.
37 E. De Lena, M. Spinelli, M. Gatti, R. Scaccabarozzi, S. Campanari, S. Consonni, G. Cinti and M. C. Romano, *Int. J. Greenhouse Gas Control.*, 2019, **82**, 244–260.
38 G. M. Castilla, D. C. Guío-Pérez, S. Papadokonstantakis, F. Johnsson and D. Pallarès, *Energies*, 2021, **14**, 3211.
39 A. Akinmoladun and O. S. Tomomewo, *Carbon Capture Sci. Technol*, 2025, **16**, 100461.
40 A. Karayil, A. Elseragy and A. M. Aliyu, *Energies.*, 2024, **17**, 1460.
41 H. Hekmatmehr, A. Esmaeili, M. Pourmahdi, S. Atashrouz, A. Abedi, M. Ali Abuswer, D. Nedeljkovic, M. Latifi, S. Farag and A. Mohaddespour, *Fuel*, 2024, **363**, 130898.
42 IEA, *CCUS in Clean Energy Transitions*, IEA, Paris, 2020.
43 D. Kearns, H. Liu and C. Consoli, *Technology Readiness and Costs of CCS, Global CCS Institute*, 2021.
44 C. Font-Palma, D. Cann and C. Udemu, *C—J. Carbon Res.*, 2021, **7**, 58.
45 Y. Zhang, H. Han, N. Zhu, Y. Che, X. Zhang, Y. Xue, J. Deng, C. Wu, H. Wang, Y. Chen and S. Yi, *Ind. Eng. Chem. Res*, 2025, **64**(4), 1933–1967.
46 B. Arias, Y. Alvarez Criado, A. Méndez, P. Marqués, I. Finca and J. C. Abanades, *Energy Fuels*, 2024, **38**, 14757–14764.
47 A. A. Ashour, A. M. Abdelmohsen, G. E. Khedr, K. E. Salem, I. M. Badawy and N. K. Allam, *ACS Appl. Mater. Interfaces*, 2025, **17**, 64687–64698.
48 F. Wang, Y. Dai, Y. Zhang, S. Ren, Y. Hou and W. Wu, *Sep. Purif. Technol.*, 2025, **359**, 130462.
49 C. I. Melo, D. Rente, M. Nunes Da Ponte, E. Bogel-Łukasik and L. C. Branco, *ACS Sustainable Chem. Eng.*, 2019, **7**, 11963–11969.
50 A. Dhakshinamoorthy, S. Navalón, A. Primo and H. García, *Angew. Chem., Int. Ed.*, 2024, **63**, e202311241.
51 I. M. Badawy, G. E. Khedr, A. Hafez, E. A. Ashour and N. K. Allam, *Chem. Commun.*, 2023, **59**, 7974–7977.
52 Y. Lei, Z. Wang, A. Bao, X. Tang, X. Huang, H. Yi, S. Zhao, T. Sun, J. Wang and F. Gao, *Chem. Eng. J.*, 2023, **453**, 139663.
53 S. Kumar De, D. Il Won, J. Kim and D. H. Kim, *Chem. Soc. Rev.*, 2023, **52**, 5744–5802.
54 Z. Liu, J. Qian, G. Zhang, B. Zhang and Y. He, *Sep. Purif. Technol*, 2024, **330**, 125177.
55 X. M. Hu, H. Q. Liang, A. Rosas-Hernández and K. Daasbjerg, *Chem. Soc. Rev.*, 2025, **54**, 1216–1250.
56 R. Küngas, *J. Electrochem. Soc.*, 2020, **167**, 044508.
57 M. Songolzadeh, M. Soleimani, M. Takht Ravanchi and R. Songolzadeh, *Sci. World J.*, 2014, **2014**, 828131.
58 U. Khan, C. C. Ogbaga, O. A. O. Abiodun, A. A. Adeleke, P. P. Ikubanni, P. U. Okoye and J. A. Okolie, *Carbon Capture Sci. Technol*, 2023, **8**, 100125.
59 P. A. Saenz Cavazos, E. Hunter-Sellars, P. Iacomi, S. R. McIntyre, D. Danaci and D. R. Williams, *Front. Energy Res*, 2023, **11**, 1167043.
60 D. Panda, E. A. Kumar and S. K. Singh, *J. CO2 Util.*, 2020, **40**, 101223.
61 Z. Zhang, Z. P. Cano, D. Luo, H. Dou, A. Yu and Z. Chen, *J. Mater. Chem. A.*, 2019, **7**, 20985–21003.
62 D.-H. Yang, Y. Tao, X. Ding and B.-H. Han, *Chem. Soc. Rev.*, 2022, **51**, 761–791.
63 H. Wang, G. Wang, L. Hu, B. Ge, X. Yu and J. Deng, *Materials*, 1630, **2023**, 16.
64 G. Singh, J. Lee, A. Karakoti, R. Bahadur, J. Yi, D. Zhao, K. AlBahily and A. Vinu, *Chem. Soc. Rev.*, 2020, **49**, 4360–4404.
65 W. Song, Y. Tang, B. Y. Moon, Q. Liao, H. Xu, Q. Hou, H. Zhang, D.-G. Yu, Y. Liao and I. Kim, *Green Chem*, 2024, **26**, 2476–2504.
66 K. Cai, P. Liu, Z. Chen, P. Chen, F. Liu, T. Zhao and D.-J. Tao, *Chem. Eng. J.*, 2023, **451**, 138946.
67 C. Chakravarty, B. Mandal and P. Sarkar, *J. Phys. Chem. C*, 2018, **122**, 3245–3255.
68 T. Sick, A. G. Hufnagel, J. Kampmann, I. Kondofersky, M. Calik, J. M. Rotter, A. Evans, M. Döblinger, S. Herbert, K. Peters, D. Böhm, P. Knochel, D. D. Medina, D. Fattakhova-Rohlfing and T. Bein, *J. Am. Chem. Soc.*, 2018, **140**, 2085–2092.
69 H. Vardhan, A. Nafady, A. M. Al-Enizi and S. Ma, *Nanoscale*, 2019, **11**, 21679–21708.
70 L. P. Tang, S. Yang, D. Liu, C. Wang, Y. Ge, L. M. Tang, R. L. Zhou and H. Zhang, *J. Mater. Chem. A.*, 2020, **8**, 14356–14383.
71 Y. Xin, D. Wang, W. Zhang, F. Su, Y. Liu, Y. Lu, W. Fan, D. Yao and Y. Zheng, *Ind. Eng. Chem. Res.*, 2025, **64**(13), 7044–7055.
72 A. Mehtab and T. Ahmad, *ACS Catal.*, 2024, **14**, 691–702.
73 B. Chen, M. Dong, S. Liu, Z. Xie, J. Yang, S. Li, Y. Wang, J. Du, H. Liu and B. Han, *ACS Catal.*, 2020, **10**, 8557–8566.
74 J. K. Tang, C. Y. Zhu, T. W. Jiang, L. Wei, H. Wang, K. Yu, C. L. Yang, Y. B. Zhang, C. Chen, Z. T. Li, D. W. Zhang and L. M. Zhang, *J. Mater. Chem. A.*, 2020, **8**, 18677–18686.
75 J. Li, D. Jia, Z. Guo, Y. Liu, Y. Lyu, Y. Zhou and J. Wang, *Green Chem.*, 2017, **19**, 2675–2686.
76 Z. Zhong, X. Wang and B. Tan, *Chem. Eur. J.*, 2025, **31**, e202404089.
77 T. Ben and S. Qiu, *CrystEngComm*, 2013, **15**, 17–26.
78 N. B. McKeown and P. M. Budd, *Chem. Soc. Rev.*, 2006, **35**, 675–683.
79 Y. Xu, S. Jin, H. Xu, A. Nagai and D. Jiang, *Chem. Soc. Rev.*, 2013, **42**, 8012–8031.
80 T. Ben, H. Ren, M. Shengqian, D. Cao, J. Lan, X. Jing, W. Wang, J. Xu, F. Deng, J. M. Simmons, S. Qiu and G. Zhu, *Angew. Chem., Int. Ed.*, 2009, **48**, 9457–9460.
81 T. X. Wang, H. P. Liang, D. A. Anito, X. Ding and B. H. Han, *J. Mater. Chem. A.*, 2020, **8**, 7003–7034.
82 P. Puthiaraj, Y. R. Lee, S. Zhang and W. S. Ahn, *J. Mater. Chem. A.*, 2016, **4**, 16288–16311.
83 C. Krishnaraj, H. S. Jena, K. Leus and P. Van Der Voort, *Green Chem.*, 2020, **22**, 1038–1071.
84 J. Artz, *ChemCatChem*, 2018, **10**, 1753–1771.
85 N. Tahir, C. Krishnaraj, K. Leus and P. Van Der Voort, *Polymers*, 2019, **11**, 1326.
86 P. Kuhn, M. Antonietti and A. Thomas, *Angew. Chem., Int. Ed.*, 2008, **47**, 3450–3453.

87 R. Luo, W. Xu, M. Chen, X. Liu, Y. Fang and H. Ji, *ChemSusChem*, 2020, **13**, 6509.
88 P. Su, K. Iwase, T. Harada, K. Kamiya and S. Nakanishi, *Chem. Sci.*, 2018, **9**, 3941–3947.
89 L. Shao, Y. Li, J. Huang and Y. N. Liu, *Ind. Eng. Chem. Res.*, 2018, **57**, 2856–2865.
90 G. Liu, S. Liu, C. Lai, L. Qin, M. Zhang, Y. Li, M. Xu, D. Ma, F. Xu, S. Liu, M. Dai and Q. Chen, *Small*, 2024, **20**, 2307853.
91 C. Lu, J. Yang, S. Wei, S. Bi, Y. Xia, M. Chen, Y. Hou, M. Qiu, C. Yuan, Y. Su, F. Zhang, H. Liang and X. Zhuang, *Adv. Funct. Mater.*, 2019, **29**, 1806884.
92 H. Wang, D. Jiang, D. Huang, G. Zeng, P. Xu, C. Lai, M. Chen, M. Cheng, C. Zhang and Z. Wang, *J. Mater. Chem. A.*, 2019, **7**, 22848–22870.
93 Y. Fu, Z. Wang, S. Li, X. He, C. Pan, J. Yan and G. Yu, *ACS Appl. Mater. Interfaces*, 2018, **10**, 36002–36009.
94 Y. Xiong, Y. Qin, L. Su and F. Ye, *Chem. Eur. J.*, 2017, **23**, 11037–11045.
95 T. Liu, X. Hu, Y. Wang, L. Meng, Y. Zhou, J. Zhang, M. Chen and X. Zhang, *J. Photochem. Photobiol. B*, 2017, **175**, 156–162.
96 K. Scanda, Y. Avila, L. Sánchez, R. Mojica, B. Portales-Martínez, M. González, M. Ávila and E. Reguera, *J. Phys. Chem. C*, 2023, **127**, 21777–21787.
97 J. Wei, D. Zhou, Z. Sun, Y. Deng, Y. Xia and D. Zhao, *Adv. Funct. Mater.*, 2013, **23**, 2322–2328.
98 B. Guo, C. Wu, Q. Su, Z. Liu, X. Li, G. Li and Q. Wu, *Mater. Lett.*, 2018, **221**, 236–239.
99 K. Yuan, C. Liu, L. Zong, G. Yu, S. Cheng, J. Wang, Z. Weng and X. Jian, *ACS Appl. Mater. Interfaces*, 2017, **9**, 13201–13212.
100 D. M. D'Alessandro, B. Smit and J. R. Long, *Angew. Chem., Int. Ed.*, 2010, **49**, 6058–6082.
101 C. Hu, Y. Xiao, Y. Zou and L. Dai, *Electrochem. Energy Rev.*, 2018, **1**, 84–112.
102 K. P. Kuhl, T. Hatsukade, E. R. Cave, D. N. Abram, J. Kibsgaard and T. F. Jaramillo, *J. Am. Chem. Soc.*, 2014, **136**, 14107–14113.
103 X. Zhu, C. Tian, H. Wu, Y. He, L. He, H. Wang, X. Zhuang, H. Liu, C. Xia and S. Dai, *ACS Appl. Mater. Interfaces*, 2018, **10**, 43588–43594.
104 Y. Wang, J. Chen, G. Wang, Y. Li and Z. Wen, *Angew. Chem., Int. Ed*, 2018, **57**, 13120–13124.
105 A. Laemont, S. Abednatanzi, P. G. Derakshandeh, F. Verbruggen, E. Fiset, Q. Qin, K. Van Daele, M. Meledina, J. Schmidt, M. Oschatz, P. Van Der Voort, K. Rabaey, M. Antonietti, T. Breugelmans and K. Leus, *Green Chem.*, 2020, **22**, 3095–3103.
106 S. Kato, T. Hashimoto, K. Iwase, T. Harada, S. Nakanishi and K. Kamiya, *Chem. Sci.*, 2023, **14**, 613–620.
107 L. Gong, X. Wang, T. Zheng, J. Liu, J. Wang, Y. C. Yang, J. Zhang, X. Han, L. Zhang and Z. Xia, *J. Mater. Chem. A.*, 2021, **9**, 3555–3566.
108 K. Ao, P. Zhao, Q. Zhang, X. Fan, Q. Fang, G. Wang and Y. Zhu, *Small Struct.*, 2024, **5**, 2300500.
109 S. Feng, W. Zheng, J. Zhu, Z. Li, B. Yang, Z. Wen, J. Lu, L. Lei, S. Wang and Y. Hou, *Appl. Catal., B*, 2020, **270**, 118908.
110 A. Jana, A. Maity, A. Sarkar, B. Show, P. A. Bhobe and A. Bhunia, *J. Mater. Chem. A.*, 2024, **12**, 5244–5253.
111 M. J. Mao, M. Di Zhang, D. L. Meng, J. X. Chen, C. He, Y. B. Huang and R. Cao, *ChemCatChem*, 2020, **12**, 3530–3536.
112 J. X. Jiang, F. Su, A. Trewin, C. D. Wood, N. L. Campbell, H. Niu, C. Dickinson, A. Y. Ganin, M. J. Rosseinsky, Y. Z. Khimyak and A. I. Cooper, *Angew. Chem., Int. Ed.*, 2007, **46**, 8574–8578.
113 A. Giri, Y. Khakre, G. Shreeraj, T. K. Dutta, S. Kundu and A. Patra, *J. Mater. Chem. A.*, 2022, **10**, 17077–17121.
114 M. Rose, *ChemCatChem*, 2014, **6**, 1166–1182.
115 T. D. Hoang, S. A. Bandh, F. A. Malla, I. Qayoom, S. Bashir, S. B. Peer and A. Halog, *Recycling*, 2023, **8**, 53.
116 S. L. Hou, J. Dong, X. Y. Zhao, X. S. Li, F. Y. Ren, J. Zhao and B. Zhao, *Angew. Chem., Int. Ed.*, 2023, **62**, e202305213.
117 Y. Xie, T. T. Wang, X. H. Liu, K. Zou and W. Q. Deng, *Nat. Commun.*, 2013, **4**, 1960.
118 R. Wang, X. Wang, W. Weng, Y. Yao, P. Kidkhunthod, C. Wang, Y. Hou and J. Guo, *Angew. Chem., Int. Ed.*, 2022, **61**, e202115503.
119 C. Zhang, X. Yang, W. Ren, Y. Wang, F. Su and J. X. Jiang, *J. Power Sources*, 2016, **317**, 49–56.
120 F. Qiu, C. Li, X. Xuan, S. Huang, C. Lu, H. Lin, S. Han, X. Zhuang and W. Y. Wong, *J. Mater. Chem. A.*, 2024, **12**, 33572–33580.
121 C. L. Smith, R. Clowes, R. S. Sprick, A. I. Cooper and A. J. Cowan, *Sustainable Energy Fuels*, 2019, **3**, 2990–2994.
122 X. M. Hu, Z. Salmi, M. Lillethorup, E. B. Pedersen, M. Robert, S. U. Pedersen, T. Skrydstrup and K. Daasbjerg, *Chem. Commun.*, 2016, **52**, 5864–5867.
123 A. B. Soliman, R. R. Haikal, Y. S. Hassan and M. H. Alkordi, *Chem. Commun.*, 2016, **52**, 12032–12035.
124 U. Karatayeva, S. A. Al Siyabi, B. Brahma Narzary, B. C. Baker and C. F. J. Faul, *Adv. Sci.*, 2024, **11**, 2308228.
125 Y. Song, J. J. Zhang, Z. Zhu, X. Chen, L. Huang, J. Su, Z. Xu, T. H. Ly, C. S. Lee, B. I. Yakobson, B. Z. Tang and R. Ye, *Appl. Catal., B*, 2021, **284**, 119750.
126 C. Ampelli, C. Genovese, M. Errahali, G. Gatti, L. Marchese, S. Perathoner and G. Centi, *J. Appl. Electrochem.*, 2015, **45**, 701–713.
127 D. Jiang, R. Bu, W. Xia, Y. Hu, M. Zhou, E. Gao, T. Asahi, Y. Yamauchi and J. Tang, *Materials Reports: Energy*, 2023, **3**, 100176.
128 B. B. Narzary, B. C. Baker and C. F. J. Faul, *Adv. Mater.*, 2023, **35**, 2211795.
129 B. B. Narzary, U. Karatayeva, J. Mintah, M. Villeda-Hernandez and C. F. J. Faul, *Mater. Chem. Front.*, 2023, **7**, 4473–4481.
130 K. S. Song, P. W. Fritz and A. Coskun, *Chem. Soc. Rev.*, 2022, **51**, 9831–9852.
131 G. Ji, Y. Zhao and Z. Liu, *Green Chem. Eng.*, 2022, **3**, 96–110.
132 S. Bin Ren, P. X. Li, A. Stephenson, L. Chen, M. E. Briggs, R. Clowes, A. Alahmed, K. K. Li, W. P. Jia and D. M. Han, *Ind. Eng. Chem. Res.*, 2018, **57**, 9254–9260.
133 I. Khan, A. Altaf, S. Sadiq, S. Khan, A. Khan, S. Khan, M. Humayun, A. Khan, R. A. Abumousa and M. Bououdina, *Chem. Eng. J. Adv.*, 2025, **21**, 100691.

134 K. Wang, H. Huang, D. Liu, C. Wang, J. Li and C. Zhong, *Environ. Sci. Technol.*, 2016, **50**, 4869–4876.
135 S. Hug, M. B. Mesch, H. Oh, N. Popp, M. Hirscher, J. Senker and B. V. Lotsch, *J. Mater. Chem. A.*, 2014, **2**, 5928–5936.
136 S. Raja, G. T. S. T. da Silva, E. A. Reis, J. C. da Cruz, A. Brunca Silva, M. B. Andrade, G. Periyasami, P. Karthikeyan, I. F. Perepichka, L. H. Mascaro and C. Ribeiro, *Energy Fuels*, 2023, **37**, 19113–19123.
137 X. Feng, X. Ding and D. Jiang, *Chem. Soc. Rev.*, 2012, **41**, 6010–6022.
138 P. W. Anderson, W. F. Brinkman and D. A. Huse, *Science.*, 2005, **310**, 1164–1166.
139 A. P. Cote, A. I. Benin, N. W. Ockwig, M. O'Keeffe, A. J. Matzger and O. M. Yaghi, *Science.*, 2005, **310**, 1166–1170.
140 W. T. Chung, I. M. A. Mekhemer, M. G. Mohamed, A. M. Elewa, A. F. M. EL-Mahdy, H. H. Chou, S. W. Kuo and K. C. W. Wu, *Coord. Chem. Rev.*, 2023, **483**, 215066.
141 W. K. Fan and M. Tahir, *Energy Convers. Manag*, 2022, **253**, 115180.
142 U. Shahzad, H. M. Marwani, M. Saeed, A. M. Asiri, M. R. Repon, R. H. Althomali and M. M. Rahman, *Chem. Rec.*, 2024, **24**, e202300285.
143 M. H. Alenazi, A. Helal, M. Y. Khan, A. Khalil, A. Khan, M. Usman and M. H. Zahir, *Carbon Capture Sci. Technol.*, 2025, **14**, 100365.
144 X. Cui, S. Lei, A. C. Wang, L. Gao, Q. Zhang, Y. Yang and Z. Lin, *Nano Energy*, 2020, **70**, 104525.
145 F. J. Uribe-Romo, J. R. Hunt, H. Furukawa, C. Klöck, M. O'Keeffe and O. M. Yaghi, *J. Am. Chem. Soc.*, 2009, **131**, 4570–4571.
146 Y. Fan, M. Chen, N. Xu, K. Wang, Q. Gao, J. Liang and Y. Liu, *Front.chem.*, 2022, **10**, 942492.
147 H. Dong, M. Lu, Y. Wang, H. L. Tang, D. Wu, X. Sun and F. M. Zhang, *Appl. Catal., B*, 2022, **303**, 120897.
148 B. Han, X. Ding, B. Yu, H. Wu, W. Zhou, W. Liu, C. Wei, B. Chen, D. Qi, H. Wang, K. Wang, Y. Chen, B. Chen and J. Jiang, *J. Am. Chem. Soc.*, 2021, **143**, 7104–7113.
149 M. Dogru and T. Bein, *Chem. Commun.*, 2014, **50**, 5531–5546.
150 C. Y. Lin, D. Zhang, Z. Zhao and Z. Xia, *Adv. Mater.*, 2018, **30**, 1703646.
151 L. Ma, W. Hu, B. Mei, H. Liu, B. Yuan, J. Zang, T. Chen, L. Zou, Z. Zou, B. Yang, Y. Yu, J. Ma, Z. Jiang, K. Wen and H. Yang, *ACS Catal.*, 2020, **10**, 4534–4542.
152 C. P. Wan, J. D. Yi, R. Cao and Y. B. Huang, *Chin. J. Struct. Chem.*, 2022, **41**, 2205001–2205014.
153 H. M. El-Kaderi, J. R. Hunt, J. L. Mendoza-Cortés, A. P. Côté, R. E. Taylor, M. O'Keeffe and O. M. Yaghi, *Science.*, 2007, **316**, 268–272.
154 M. Lu, M. Zhang, J. Liu, Y. Chen, J. Liao, M. Yang, Y. Cai, S. Li and Y. Lan, *Angew. Chem.*, 2022, **134**, e202200003.
155 J. F. Kurisingal, H. Kim, J. H. Choe and C. S. Hong, *Coord. Chem. Rev.*, 2022, **473**, 214835.
156 G. Singh and C. M. Nagaraja, *J. CO2 Util.*, 2021, **53**, 101716.
157 K. Xu, Y. Dai, B. Ye and H. Wang, *Dalton Trans.*, 2017, **46**, 10780–10785.
158 Q. Gao, X. Li, G.-H. Ning, H.-S. Xu, C. Liu, B. Tian, W. Tang and K. P. Loh, *Chem. Mater.*, 2018, **30**, 1762–1768.
159 Y. B. Zhang, J. Su, H. Furukawa, Y. Yun, F. Gándara, A. Duong, X. Zou and O. M. Yaghi, *J. Am. Chem. Soc.*, 2013, **135**, 16336–16339.
160 R. Wang, J. Zhao, Q. Fang and S. Qiu, *Chem. Synth.*, 2024, **4**, 29.
161 D. Zhu, Y. Zhu, Y. Chen, Q. Yan, H. Wu, C. Y. Liu, X. Wang, L. B. Alemany, G. Gao, T. P. Senftle, Y. Peng, X. Wu and R. Verduzco, *Nat. Commun.*, 2023, **14**, 2865.
162 X. Huang, C. Sun and X. Feng, *Sci. China Chem.*, 2020, **63**, 1367–1390.
163 T. Saeed, A. Naeem, B. Ahmad, S. Ahmad, S. Afridi, F. Khan, I. U. Din and N. H. Khan, *J. Porous Mater.*, 2024, **31**, 33–48.
164 H. A. Patel, J. Byun and C. T. Yavuz, *ChemSusChem*, 2017, **10**, 1303–1317.
165 G. Kumar, M. Singh, R. Goswami and S. Neogi, *ACS Appl. Mater. Interfaces*, 2020, **12**, 48642–48653.
166 H. Furukawa and O. M. Yaghi, *J. Am. Chem. Soc.*, 2009, **131**, 8875–8883.
167 S. B. Alahakoon, C. M. Thompson, A. X. Nguyen, G. Occhialini, G. T. McCandless and R. A. Smaldone, *Chem. Commun.*, 2016, **52**, 2843–2845.
168 S. Wei, H. Xin, M. Wang, S. Xu, W. Zhai, S. Liu, L. Wang, S. Liu, Z. Wang and X. Lu, *Adv. Theory Simul.*, 2022, **5**, 2200588.
169 G. Lin, H. Ding, R. Chen, Z. Peng, B. Wang and C. Wang, *J. Am. Chem. Soc.*, 2017, **139**, 8705–8709.
170 A. Paparo and J. Okuda, *Coord. Chem. Rev.*, 2017, **334**, 136–149.
171 S. Vijay, W. Ju, S. Brückner, S.-C. Tsang, P. Strasser and K. Chan, *Nat. Catal.*, 2021, **4**, 1024–1031.
172 S. Lin, C. S. Diercks, Y.-B. Zhang, N. Kornienko, E. M. Nichols, Y. Zhao, A. R. Paris, D. Kim, P. Yang and O. M. Yaghi, *Science.*, 2015, **349**, 1208–1213.
173 D. Wu, J. Wu, P. Lv, H. Li, K. Chu and D. Ma, *Small Struct*, 2023, **4**, 2200358.
174 F. W. Dagnaw, K. Harrath, T. Zheng, X. D. Wu, Y. Z. Liu, R. Q. Li, L. H. Xie, Z. Li, X. He, Q. X. Tong and J. X. Jian, *Adv. Sci.*, 2024, **11**, 2408152.
175 H.-J. Zhu, M. Lu, Y.-R. Wang, S.-J. Yao, M. Zhang, Y.-H. Kan, J. Liu, Y. Chen, S.-L. Li and Y.-Q. Lan, *Nat. Commun.*, 2020, **11**, 497.
176 G. Liu, X. Li, M. Liu, S. Yang, X. Yang, X. Chen, W. Wei, Q. Xu and G. Zeng, *ACS Catal.*, 2024, **14**, 11076–11086.
177 X. Yang, X. Li, M. Liu, S. Yang, Q. Xu and G. Zeng, *Angew. Chem., Int. Ed.*, 2024, **63**, e202317785.
178 X. Wang, X. Ding, T. Wang, K. Wang, Y. Jin, Y. Han, P. Zhang, N. Li, H. Wang and J. Jiang, *ACS Appl. Mater. Interfaces*, 2022, **14**, 41122–41130.
179 Y. Wang, H. Ding, X. Ma, M. Liu, Y. Yang, Y. Chen, S. Li and Y. Lan, *Angew. Chem., Int. Ed.*, 2022, **61**, e202114648.
180 P. Guan, J. Qiu, Y. Zhao, H. Wang, Z. Li, Y. Shi and J. Wang, *Chem. Commun.*, 2019, **55**, 12459–12462.
181 S. An, T. Xu, C. Peng, J. Hu and H. Liu, *RSC Adv.*, 2019, **9**, 21438–21443.

182 W. Zhou, Q. W. Deng, G. Q. Ren, L. Sun, L. Yang, Y. M. Li, D. Zhai, Y. H. Zhou and W. Q. Deng, *Nat. Commun.*, 2020, **11**, 4481.
183 Q. Zhang, S. Gao and J. Yu, *Chem. Rev.*, 2022, **123**, 6039–6106.
184 B. Yue, S. Liu, Y. Chai, G. Wu, N. Guan and L. Li, *J. Energy Chem.*, 2022, **71**, 288–303.
185 Y. Li and J. Yu, *Nat. Rev. Mater.*, 2021, **6**, 1156–1174.
186 X. Deng, R. Bai, Y. Chai, Z. Hu, N. Guan and L. Li, *CCS Chemistry*, 2022, **4**, 949–962.
187 Y. Li and J. Yu, *Chem. Rev.*, 2014, **114**, 7268–7316.
188 C. S. Cundy and P. A. Cox, *Chem. Rev.*, 2003, **103**, 663–702.
189 G. T. M. Kadja, M. D. Rukmana, R. R. Mukti, M. H. Mahyuddin, A. G. Saputro and T. D. K. Wungu, *Mater. Lett.*, 2021, **290**, 129501.
190 M. A. Keane, *Colloids Surf. A Physicochem. Eng. Asp.*, 1998, **138**, 11–20.
191 W. W. Lestari, L. Yunita, T. E. Saraswati, E. Heraldy, M. A. Khafidhin, Y. K. Krisnandi, U. S. F. Arrozi and G. T. M. Kadja, *Chem. Pap.*, 2021, **75**, 3253–3263.
192 J. Gao, C. Jia and B. Liu, *Catal. Sci. Technol.*, 2017, **7**, 5602–5607.
193 J. Wei, Q. Ge, R. Yao, Z. Wen, C. Fang, L. Guo, H. Xu and J. Sun, *Nat. Commun.*, 2017, **8**, 15174.
194 S. Bhatia, *Zeolite Catalysts: Principles and Applications*, 1st edn, CRC Press, 1989.
195 R. P. Townsend and E. N. Coker, in *Studies in surface science and catalysis*, Elsevier, 2001, vol. 137, pp. 467–524.
196 N. J. Azhari, N. Nurdini, S. Mardiana, T. Ilmi, A. T. N. Fajar, I. G. B. N. Makertihartha, S. Subagjo and G. T. M. Kadja, *J. CO2 Util.*, 2022, **59**, 101969.
197 B. Dziejarski, J. Serafin, K. Andersson and R. Krzyżyńska, *Mater. Today Sustain.*, 2023, **24**, 100483.
198 M. W. Ackley, S. U. Rege and H. Saxena, *Microporous Mesoporous Mater.*, 2003, **61**, 25–42.
199 D. G. Boer, J. Langerak and P. P. Pescarmona, *ACS Appl. Energy Mater*, 2023, **6**(5), 2634–2656.
200 Q. Zhang, J. Li, L. Li and J. Yu, *Sci. China Chem*, 2025, **68**, 1703–1716.
201 H. J. Choi, D. Jo, J. G. Min and S. B. Hong, *Angew. Chem., Int. Ed.*, 2021, **60**, 4307–4314.
202 Q. Jiang, J. Rentschler, G. Sethia, S. Weinman, R. Perrone and K. Liu, *Chem. Eng. J.*, 2013, **230**, 380–388.
203 M. R. Hudson, W. L. Queen, J. A. Mason, D. W. Fickel, R. F. Lobo and C. M. Brown, *J. Am. Chem. Soc.*, 2012, **134**, 1970–1973.
204 M. Mofarahi and F. Gholipour, *Microporous Mesoporous Mater.*, 2014, **200**, 1–10.
205 M. M. Lozinska, E. Mangano, J. P. S. Mowat, A. M. Shepherd, R. F. Howe, S. P. Thompson, J. E. Parker, S. Brandani and P. A. Wright, *J. Am. Chem. Soc.*, 2012, **134**, 17628–17642.
206 J. Shang, G. Li, R. Singh, Q. Gu, K. M. Nairn, T. J. Bastow, N. Medhekar, C. M. Doherty, A. J. Hill and J. Z. Liu, *J. Am. Chem. Soc.*, 2012, **134**, 19246–19253.
207 M. P. S. Santos, C. A. Grande and A. E. Rodrigues, *Ind. Eng. Chem. Res.*, 2011, **50**, 974–985.
208 Z. Song, Y. Huang, W. L. Xu, L. Wang, Y. Bao, S. Li and M. Yu, *Sci. Rep.*, 2015, **5**, 13981.
209 Database of Zeolite Structures, International Zeolite Association, https://www.iza-structure.org/databases/, accessed July 2025.
210 R. Krishna, *Chem. Soc. Rev.*, 2012, **41**, 3099–3118.
211 E. Beerdsen, D. Dubbeldam and B. Smit, *Phys. Rev. Lett.*, 2006, **96**, 044501.
212 M. C. Verbraeken, R. Mennitto, V. M. Georgieva, E. L. Bruce, A. G. Greenaway, P. A. Cox, J. G. Min, S. B. Hong, P. A. Wright and S. Brandani, *Sep. Purif. Technol.*, 2021, **256**, 117846.
213 B. Ilić and S. G. Wettstein, *Microporous Mesoporous Mater.*, 2017, **239**, 221–234.
214 V. M. Georgieva, E. L. Bruce, R. G. Chitac, M. M. Lozinska, A. M. Hall, C. A. Murray, R. I. Smith, A. Turrina and P. A. Wright, *Chem. Mater.*, 2021, **33**, 1157–1173.
215 O. Cheung and N. Hedin, *RSC Adv.*, 2014, **4**, 14480–14494.
216 G. Calleja, J. Pau and J. A. Calles, *J. Chem. Eng. Data*, 1998, **43**, 994–1003.
217 H. Chen, W. Wang, J. Ding, X. Wei and J. Lu, *Energy Procedia*, 2017, **105**, 4370–4376.
218 R. A. Schoonheydt, P. Geerlings, E. A. Pidko and R. A. Van Santen, *J. Mater. Chem.*, 2012, **22**, 18705–18717.
219 D. Barthomeuf, *J. Phys. Chem.*, 1984, **88**, 42–45.
220 M. Palomino, A. Corma, F. Rey and S. Valencia, *Langmuir*, 2010, **26**, 1910–1917.
221 D. Newsome, S. Gunawan, G. Baron, J. Denayer and M.-O. Coppens, *Adsorption*, 2014, **20**, 157–171.
222 H. J. Choi and S. B. Hong, *Chem. Eng. J.*, 2022, **433**, 133800.
223 D. Barthomeuf, *Microporous Mesoporous Mater.*, 2003, **66**, 1–14.
224 J. C. Lavalley, *Catal. Today*, 1996, **27**, 377–401.
225 Z. Tao, Y. Tian, S. Y. Ou, Q. Gu and J. Shang, *AIChE J.*, 2023, **69**, e18139.
226 E. B. Clatworthy, S. Ghojavand, R. Guillet-Nicolas, J.-P. Gilson, P. L. Llewellyn, N. Nesterenko and S. Mintova, *Chem. Eng. J.*, 2023, **471**, 144557.
227 A. A. Dabbawala, I. Ismail, B. V. Vaithilingam, K. Polychronopoulou, G. Singaravel, S. Morin, M. Berthod and Y. Al Wahedi, *Microporous Mesoporous Mater.*, 2020, **303**, 110261.
228 J. Shen, Q. Sun, J. Cao, P. Wang, W. Jia, S. Wang, P. Zhao and Z. Wang, *New J. Chem.*, 2022, **46**, 6720–6728.
229 J. Al Atrach, A. Aitblal, A. Amedlous, E. B. Clatworthy, D. Honorato Piva, Y. Xiong, R. Guillet-Nicolas and V. Valtchev, *ACS Appl. Mater. Interfaces*, 2025, **17**, 7119–7130.
230 L. Xu, Y. Xiu, F. Liu, Y. Liang and S. Wang, *Molecules*, 2020, **25**, 3653.
231 M. Usman, A. S. Ghanem, S. Niaz Ali Shah, M. D. Garba, M. Yusuf Khan, S. Khan, M. Humayun and A. Laeeq Khan, *Chem. Rec.*, 2022, **22**, e202200039.
232 M. Zhu, Q. Ge and X. Zhu, *Trans. Tianjin Univ.*, 2020, **26**, 172–187.
233 Z. Zhang, M. Li, R. Gao, S. Yang, Q. Ma, R. Feng, H. Dou, J. Dang, G. Wen, Z. Bai, D. Liu, M. Feng and Z. Chen, *J. Am. Chem. Soc.*, 2024, **146**, 6397–6407.

234 Y. Zhu, P. Li, X. Yang, M. Wang, Y. Zhang, P. Gao, Q. Huang, Y. Wei, X. Yang, D. Wang, Y. Shen and M. Wang, *Adv. Energy Mater.*, 2023, **13**, 2204143.
235 L. Li, H. S. Jung, J. W. Lee and Y. T. Kang, *Renewable Sustainable Energy Rev.*, 2022, **162**, 112441.
236 X. Lin, S. Wang, W. Tu, Z. Hu, Z. Ding, Y. Hou, R. Xu and W. Dai, *Catal. Sci. Technol.*, 2019, **9**, 731–738.
237 T. Qiu, S. Gao, Z. Liang, D. Wang, H. Tabassum, R. Zhong and R. Zou, *Angew. Chem.*, 2021, **133**, 17455–17477.
238 V. A. Tran, H. H. Do, V. T. Le, Y. Vasseghian, V. Vo, S. H. Ahn, S. Y. Kim and S. W. Lee, *Int. J. Hydrogen Energy*, 2022, **47**, 19590–19608.
239 M. A. Nazir, N. A. Khan, C. Cheng, S. S. A. Shah, T. Najam, M. Arshad, A. Sharif, S. Akhtar and A. ur Rehman, *Appl. Clay Sci.*, 2020, **190**, 105564.
240 H. Zhang, X. Liu, Y. Wu, C. Guan, A. K. Cheetham and J. Wang, *Chem. Commun.*, 2018, **54**, 5268–5288.
241 S. S. A. Shah, T. Najam, M. K. Aslam, M. Ashfaq, M. M. Rahman, K. Wang, P. Tsiakaras, S. Song and Y. Wang, *Appl. Catal., B*, 2020, **268**, 118570.
242 Z. Zeng, X. Fang, W. Miao, Y. Liu, T. Maiyalagan and S. Mao, *ACS Sens*, 2019, **4**, 1934–1941.
243 H. Zhang, J. Li, Q. Tan, L. Lu, Z. Wang and G. Wu, *Chem. Eur. J.*, 2018, **24**, 18137.
244 S. Bose, D. Sengupta, T. M. Rayder, X. Wang, K. O. Kirlikovali, A. K. Sekizkardes, T. Islamoglu and O. K. Farha, *Adv. Funct. Mater.*, 2024, **34**, 2307478.
245 S. Mahajan and M. Lahtinen, *J. Environ. Chem. Eng.*, 2022, **10**, 108930.
246 J. Wang, Z. Jiang, S. Wen, Y. Wei, P. Ning and Y. Zhang, *J. Mater. Chem. A.*, 2025, **13**, 11185–11209.
247 A. R. Millward and O. M. Yaghi, *J. Am. Chem. Soc.*, 2005, **127**, 17998–17999.
248 C. A. Trickett, A. Helal, B. A. Al-Maythalony, Z. H. Yamani, K. E. Cordova and O. M. Yaghi, *Nat. Rev. Mater.*, 2017, **2**, 17045.
249 S. Gao, Y. Lin, X. Jiao, Y. Sun, Q. Luo, W. Zhang, D. Li, J. Yang and Y. Xie, *Nature*, 2016, **529**, 68–71.
250 F. Li, H. Yang, W. Li and L. Sun, *Joule*, 2018, **2**, 36–60.
251 A. Banerjee and C. G. Morales-Guio, *EES Catal*, 2025, **3**, 205–234.
252 X. Zhang, Z. Wu, X. Zhang, L. Li, Y. Li, H. Xu, X. Li, X. Yu, Z. Zhang, Y. Liang and H. Wang, *Nat. Commun.*, 2017, **8**, 1.
253 L. Zhang, Z. J. Zhao and J. Gong, *Angew. Chem., Int. Ed.*, 2017, **56**, 11326–11353.
254 R. Hinogami, S. Yotsuhashi, M. Deguchi, Y. Zenitani, H. Hashiba and Y. Yamada, *ECS Electrochem. Lett.*, 2012, **1**, H17.
255 R. Senthil Kumar, S. Senthil Kumar and M. Anbu Kulandainathan, *Electrochem. Commun.*, 2012, **25**, 70–73.
256 M. Cheng, X. Zheng, F. Ma, Z. Zhu and Q. Xu, *ChemCatChem*, 2024, **16**, e202400438.
257 R. Chen, L. Cheng, J. Liu, Y. Wang, W. Ge, C. Xiao, H. Jiang, Y. Li and C. Li, *Small*, 2022, **18**, 2200720.
258 C. P. Wan, H. Guo, D. H. Si, S. Y. Gao, R. Cao and Y. B. Huang, *JACS Au*, 2024, **4**, 2514–2522.
259 H. Li, R. Li, J. Niu, K. Gan and X. He, *Front. Chem.*, 2022, **10**, 1067327.
260 C. Li, Y. Ji, Y. Wang, C. Liu, Z. Chen, J. Tang, Y. Hong, X. Li, T. Zheng, Q. Jiang and C. Xia, *Nano-Micro Lett.*, 2023, **15**, 1–44.
261 C. Li, H. Yan and H. Yang, *et al.*, *Sci. China Mater.*, 2025, **68**, 21–38.
262 M. Ding, R. W. Flaig, H. L. Jiang and O. M. Yaghi, *Chem. Soc. Rev.*, 2019, **48**, 2783–2828.
263 J. M. Huang, X. Da Zhang, J. Y. Huang, D. S. Zheng, M. Xu and Z. Y. Gu, *Coord. Chem. Rev.*, 2023, **494**, 215333.
264 D. Kim, W. Choi, H. W. Lee, S. Y. Lee, Y. Choi, D. K. Lee, W. Kim, J. Na, U. Lee, Y. J. Hwang and D. H. Won, *ACS Energy Lett.*, 2021, **6**, 3488–3495.
265 J. Wang, Y. Zhang, Y. Ma, J. Yin, Y. Wang and Z. Fan, *ACS Mater. Lett.*, 2022, **4**, 2058–2079.
266 Y. Belmabkhout, V. Guillerm and M. Eddaoudi, *Chem. Eng. J.*, 2016, **296**, 386–397.
267 Q. Yang, C. Xue, C. Zhong and J. F. Chen, *AIChE J.*, 2007, **53**, 2832–2840.
268 H. M. Polat, S. Kavak, H. Kulak, A. Uzun and S. Keskin, *Chem. Eng. J.*, 2020, **394**, 124916.
269 W. Liang, P. M. Bhatt, A. Shkurenko, K. Adil, G. Mouchaham, H. Aggarwal, A. Mallick, A. Jamal, Y. Belmabkhout and M. Eddaoudi, *Chem*, 2019, **5**, 950–963.
270 C. Y. Gao, J. Ai, H. R. Tian, D. Wu and Z. M. Sun, *Chem. Commun.*, 2017, **53**, 1293–1296.
271 J. S. Yan, R. T. Guo, L. Q. Yu, H. Liu, S. H. Guo and W. G. Pan, *Energy Fuels*, 2023, **37**, 15453–15475.
272 Y.-Y. Liu, J.-R. Huang, H.-L. Zhu, P.-Q. Liao and X.-M. Chen, *Angew. Chem.*, 2023, **135**, e202311265.
273 T. Al-Attas, S. K. Nabil, A. S. Zeraati, H. S. Shiran, T. Alkayyali, M. Zargartalebi, T. Tran, N. N. Marei, M. A. Al Bari, H. Lin, S. Roy, P. M. Ajayan, D. Sinton, G. Shimizu and M. G. Kibria, *ACS Energy Lett.*, 2023, **8**, 107–115.
274 Y. L. Qiu, H. X. Zhong, T. T. Zhang, W. Bin Xu, P. P. Su, X. F. Li and H. M. Zhang, *ACS Appl. Mater. Interfaces*, 2018, **10**, 2480–2489.
275 S. Nitopi, E. Bertheussen, S. B. Scott, X. Liu, A. K. Engstfeld, S. Horch, B. Seger, I. E. L. Stephens, K. Chan, C. Hahn, J. K. Nørskov, T. F. Jaramillo and I. Chorkendorff, *Chem. Rev.*, 2019, **119**, 7610–7672.
276 D.-H. Nam, O. Shekhah, A. Ozden, C. McCallum, F. Li, X. Wang, Y. Lum, T. Lee, J. Li, J. Wicks, A. Johnston, D. Sinton, M. Eddaoudi and E. H. Sargent, *Adv. Mater.*, 2022, **34**, 2207088.
277 B. Kumar, B. Muchharla, M. Dikshit, S. Dongare, K. Kumar, B. Gurkan and J. M. Spurgeon, *Environ. Sci. Technol. Lett.*, 2024, **11**(11), 1161–1174.
278 Z. H. Zhao, J. R. Huang, D. S. Huang, H. L. Zhu, P. Q. Liao and X. M. Chen, *J. Am. Chem. Soc.*, 2024, **146**, 14349–14356.
279 E. M. Johnson, S. Ilic and A. J. Morris, *ACS Cent. Sci.*, 2021, **7**, 445–453.
280 C. Cammarere, J. Cortés, T. G. Glover, R. Q. Snurr, J. T. Hupp and J. Liu, *Front. Chem.*, 2025, **13**, 1634637.
281 D. Bohra, J. H. Chaudhry, T. Burdyny, E. A. Pidko and W. A. Smith, *Energy Environ. Sci.*, 2019, **12**, 3380–3389.
282 X. Zhang, D. Xue, S. Jiang, H. Xia, Y. Yang, W. Yan, J. Hu and J. Zhang, *InfoMat*, 2022, **4**, e12257.

283 K. Yang, M. Li, T. Gao, G. Xu, D. Li, Y. Zheng, Q. Li and J. Duan, *Nat. Commun.*, 2024, **15**, 7060.
284 D. Bůžek, S. Adamec, K. Lang and J. Demel, *Inorg. Chem. Front.*, 2021, **8**, 720–734.
285 X. Zhao, C. Y. Zhu, J. S. Qin, H. Rao, D. Y. Du, M. Zhang, P. She, L. Li and Z. M. Su, *Mater. Chem. Front.*, 2024, **8**, 2439–2446.
286 W. Wang, H. Yan, U. Anand and U. Mirsaidov, *J. Am. Chem. Soc.*, 2021, **143**, 1854–1862.
287 B. Han, K. A. Stoerzinger, V. Tileli, A. D. Gamalski, E. A. Stach and Y. Shao-Horn, *Nat. Mater.*, 2017, **16**, 121–126.
288 N. Gholampour, C. I. Ezugwu, H. A. Younus, D. P. Debecker, M. Al Abri, R. Alhajri, C. M. Kao and F. Verpoort, *J. Mater. Chem. A.*, 2024, **12**, 27825–27854.
289 S. Yuan, L. Feng, K. Wang, J. Pang, M. Bosch, C. Lollar, Y. Sun, J. Qin, X. Yang, P. Zhang, Q. Wang, L. Zou, Y. Zhang, L. Zhang, Y. Fang, J. Li and H. C. Zhou, *Adv. Mater.*, 2018, **30**, 1704303.
290 S. Yuan, J. S. Qin, C. T. Lollar and H. C. Zhou, *ACS Cent. Sci.*, 2018, **4**, 440–450.
291 S. Dou, X. Li and X. Wang, *ACS Mater. Lett.*, 2020, **2**, 1251–1267.
292 M. Ding, X. Cai and H.-L. Jiang, *Chem. Sci.*, 2019, **10**, 10209–10230.
293 M. A. Abdelkareem, Q. Abbas, E. T. Sayed, N. Shehata, J. B. M. Parambath, A. H. Alami and A. G. Olabi, *Energy*, 2024, **299**, 131127.
294 Y. Cheng, J. Hou and P. Kang, *ACS Energy Lett.*, 2021, **6**, 3352–3358.
295 S. K. Nabil, S. Roy, W. A. Algozeeb, T. Al-Attas, M. A. Al Bari, A. S. Zeraati, K. Kannimuthu, P. G. Demingos, A. Rao, T. N. Tran, X. Wu, P. Bollini, H. Lin, C. V. Singh, J. M. Tour, P. M. Ajayan and M. G. Kibria, *Adv. Mater.*, 2023, **35**, 2300389.
296 T. Yan, S. Liu, Z. Liu, J. Sun and P. Kang, *Adv. Funct. Mater.*, 2024, **34**, 1–8.
297 Y. Xu, J. P. Edwards, J. Zhong, C. P. O'Brien, C. M. Gabardo, C. McCallum, J. Li, C. T. Dinh, E. H. Sargent and D. Sinton, *Energy Environ. Sci.*, 2020, **13**, 554–561.
298 P. Zhu, Z. Y. Wu, A. Elgazzar, C. Dong, T. U. Wi, F. Y. Chen, Y. Xia, Y. Feng, M. Shakouri, J. Y. (Timothy) Kim, Z. Fang, T. A. Hatton and H. Wang, *Nature*, 2023, **618**, 959–966.
299 M. B. Li, M. Li, F. Luo, L. Zhou and H. Li, *Energy Fuels*, 2024, **38**, 10390–10393.
300 X. Y. D. Soo, J. J. C. Lee, W. Y. Wu, L. Tao, C. Wang, Q. Zhu and J. Bu, *J. CO2 Util.*, 2024, **81**, 102727.
301 G. Zhang, J. Liu, J. Qian, X. Zhang and Z. Liu, *J. Ind. Eng. Chem.*, 2024, **134**, 28–50.
302 J. Hack, N. Maeda and D. M. Meier, *ACS Omega*, 2022, **7**(44), 39520–39530.
303 S. Hafizi Yazdabadi, D. Mihrin, K. L. Feilberg and R. Wugt Larsen, *Molecules*, 2024, **29**, 5521.
304 K. Gottschling, L. Stegbauer, G. Savasci, N. A. Prisco, Z. J. Berkson, C. Ochsenfeld, B. F. Chmelka and B. V. Lotsch, *Chem. Mater.*, 2019, **31**, 1946–1955.
305 X. Yang, R. J. Rees, W. Conway, G. Puxty, Q. Yang and D. A. Winkler, *Chem. Rev.*, 2017, **117**(14), 9524–9593.
306 B. Yoon and G. A. Voth, *J. Am. Chem. Soc.*, 2023, **145**, 15663–15667.
307 D. Loachamin, J. Casierra, V. Calva, A. Palma-Cando, E. E. Ávila and M. Ricaurte, *Chem. Eng.*, 2024, **8**, 129.
308 H. Yu and P. H. M. Feron, in *Absorption-Based Post-Combustion Capture of Carbon Dioxide*, Elsevier Inc., 2016, pp. 283–301.
309 B. K. Choi, S. M. Kim, K. M. Kim, U. Lee, J. H. Choi, J. S. Lee, I. H. Baek, S. C. Nam and J. H. Moon, *Chem. Eng. J.*, 2021, **419**, 129517.
310 M. Caplow, *J. Am. Chem. Soc.*, 1968, **90**, 6795–6803.
311 E. Pérez-Gallent, C. Vankani, C. Sánchez-Martínez, A. Anastasopol and E. Goetheer, *Ind. Eng. Chem. Res.*, 2021, **60**, 4269–4278.
312 G. Lee, Y. C. Li, J. Y. Kim, T. Peng, D. H. Nam, A. Sedighian Rasouli, F. Li, M. Luo, A. H. Ip, Y. C. Joo and E. H. Sargent, *Nat. Energy*, 2021, **6**, 46–53.
313 M. Abdinejad, Z. Mirza, X. A. Zhang and H. B. Kraatz, *ACS Sustainable Chem. Eng.*, 2020, **8**, 1715–1720.
314 L. Chen, F. Li, Y. Zhang, C. L. Bentley, M. Horne, A. M. Bond and J. Zhang, *ChemSusChem*, 2017, **10**, 4109–4118.
315 N. Ahmad, Y. Chen, X. Wang, P. Sun, Y. Bao and X. Xu, *Renew. Energy*, 2022, **189**, 444–453.
316 J. H. Kim, H. Jang, G. Bak, W. Choi, H. Yun, E. Lee, D. Kim, J. Kim, S. Y. Lee and Y. J. Hwang, *Energy Environ. Sci.*, 2022, **15**, 4301–4312.
317 M. N. Hossain, S. Ahmad, I. S. da Silva and H. B. Kraatz, *Chem. Eur. J.*, 2021, **27**, 1346–1355.
318 S. Akhter, T. Palai, L. M. Aeshala and A. M. Kannan, *Carbon Capture Sci. Technol*, 2024, **13**, 100289.
319 J. Lin, Y. Zhang, P. Xu and L. Chen, *Materials Reports: Energy.*, 2023, **3**, 100194.
320 X. Zhu, Z. Chen and H. Ai, *J. Mol. Model.*, 2020, **26**, 345.
321 J. P. Hallett and T. Welton, *Chem. Rev*, 2011, **111**(5), 3508–3576.
322 L. Sun, H. Xia, O. Morales-Collazo and J. F. Brennecke, *ECS Trans.*, 2016, **75**, 469–487.
323 S. Hussain, A. Ali, S. Foorginezhad, Y. Chen and X. Ji, *Sep. Purif. Technol.*, 2025, **360**, 130997.
324 B. E. Gurkan, T. R. Gohndrone, M. J. McCready and J. F. Brennecke, *Phys. Chem. Chem. Phys.*, 2013, **15**, 7796–7811.
325 J. Cheng, Y. Li, L. Hu, J. Zhou and K. Cen, *Energy Fuels*, 2016, **30**, 3251–3256.
326 S. Seo, M. A. Desilva, H. Xia and J. F. Brennecke, *J. Phys. Chem. B*, 2015, **119**, 11807–11814.
327 L. A. Blanchard, Z. Gu and J. F. Brennecke, *J. Phys. Chem. B*, 2001, **105**, 2437–2444.
328 A. Shariati and C. J. Peters, *J. Supercrit. Fluids*, 2005, **34**, 171–176.
329 S. G. Kazarian, B. J. Briscoe and T. Welton, *Chem. Commun.*, 2000, 2047–2048.
330 C. Cadena, J. L. Anthony, J. K. Shah, T. I. Morrow, J. F. Brennecke and E. J. Maginn, *J. Am. Chem. Soc.*, 2004, **126**, 5300–5308.
331 J. L. Anthony, J. L. Anderson, E. J. Maginn and J. F. Brennecke, *J. Phys. Chem. B*, 2005, **109**, 6366–6374.

332 X. Zhang, K. Jiang, Z. Liu, X. Yao, X. Liu, S. Zeng, K. Dong and S. Zhang, *Ind. Eng. Chem. Res.*, 2019, **58**, 1443–1453.
333 R. Zhang, Q. Ke, Z. Zhang, B. Zhou, G. Cui and H. Lu, *Int. J. Mol. Sci.*, 2022, **23**, 11401.
334 S. K. Shukla, S. G. Khokarale, T. Q. Bui and J. P. T. Mikkola, *Front. Mater*, 2019, **6**, 42.
335 S. Onofri and E. Bodo, *J. Phys. Chem. B*, 2021, **125**, 5611–5619.
336 S. Saravanamurugan, A. J. Kunov-Kruse, R. Fehrmann and A. Riisager, *ChemSusChem*, 2014, **7**, 897–902.
337 J. Ma, Y. Du, M. Liu, Y. Zhou, X. Wang, B. Wang, J. Zhu and M. Zhu, *J. Phys. Chem. B*, 2025, **129**, 372–384.
338 J. Ma, Y. Zhou, M. Liu, Y. Du, X. Wang, B. Wang, M. Zhu and J. Zhu, *Carbon Capture Sci. Technol.*, 2024, **12**, 100222.
339 H. Huang, R. Peters, R. C. Samsun, D. Stolten, C. He and X. Zhou, *Energy*, 2024, **301**, 131670.
340 E. D. Bates, R. D. Mayton, I. Ntai and J. H. Davis, *J. Am. Chem. Soc.*, 2002, **124**, 926–927.
341 W. Faisal Elmobarak, F. Almomani, M. Tawalbeh, A. Al-Othman, R. Martis and K. Rasool, *Fuel*, 2023, **344**, 128102.
342 H. Zhao and G. A. Baker, *Green Chem. Lett. Rev.*, 2023, **16**, 1.
343 H. Ohno and K. Fukumoto, *Acc. Chem. Res.*, 2007, **40**, 1122–1129.
344 G. Yu, D. Zhao, L. Wen, S. Yang and X. Chen, *AIChE J.*, 2012, **58**, 2885–2899.
345 R. Macchieraldo, L. Esser, R. Elfgen, P. Voepel, S. Zahn, B. M. Smarsly and B. Kirchner, *ACS Omega*, 2018, **3**, 8567–8582.
346 T. Numpilai, L. K. H. Pham and T. Witoon, *Ind. Eng. Chem. Res.*, 2024, **63**(46), 19865–19915.
347 S. J. Grabowski, *Crystals.*, 2020, **10**, 460.
348 T. B. Lee, S. Oh, T. R. Gohndrone, O. Morales-Collazo, S. Seo, J. F. Brennecke and W. F. Schneider, *J. Phys. Chem. B*, 2016, **120**, 1509–1517.
349 S. F. R. Taylor, C. McCrellis, C. McStay, J. Jacquemin, C. Hardacre, M. Mercy, R. G. Bell and N. H. De Leeuw, *J. Solution Chem.*, 2015, **44**, 511–527.
350 Q. R. Sheridan, W. F. Schneider and E. J. Maginn, *J. Phys. Chem. B*, 2016, **120**, 12679–12686.
351 O. Palumbo, A. Cimini, F. Trequattrini, J. B. Brubach, P. Roy and A. Paolone, *Int. J. Mol. Sci.*, 2021, **22**, 6155.
352 T. Koishi, *J. Phys. Chem. B*, 2018, **122**, 12342–12350.
353 F. Ju, J. Zhang and W. Lu, *Catalysts*, 2020, **10**, 1–14.
354 A. Senocrate and C. Battaglia, *J. Energy Storage*, 2021, **36**, 102373.
355 B. A. Rosen, A. Salehi-Khojin, M. R. Thorson, W. Zhu, D. T. Whipple, P. J. A. Kenis and R. I. Masel, *Science.*, 2011, **334**, 643–644.
356 B. Kumar, M. Asadi, D. Pisasale, S. Sinha-Ray, B. A. Rosen, R. Haasch, J. Abiade, A. L. Yarin and A. Salehi-Khojin, *Nat. Commun.*, 2013, **4**, 2819.
357 E. E. L. Tanner, C. Batchelor-McAuley and R. G. Compton, *J. Phys. Chem. C*, 2016, **120**, 26442–26447.
358 S. Yu and P. K. Jain, *Nat. Commun.*, 2019, **10**, 2022.
359 A. Kemna, N. García Rey and B. Braunschweig, *ACS Catal.*, 2019, **9**, 6284–6292.
360 Y. Wang, M. Hatakeyama, K. Ogata, M. Wakabayashi, F. Jin and S. Nakamura, *Phys. Chem. Chem. Phys.*, 2015, **17**, 23521–23531.
361 L. Yuan, L. Zhang, J. Feng, C. Jiang, J. Feng, C. Li, S. Zeng and X. Zhang, *Chem. Eng. J.*, 2022, **450**, 138378.
362 S. S. Neubauer, R. K. Krause, B. Schmid, D. M. Guldi and G. Schmid, *Adv. Energy Mater.*, 2016, **6**, 1502231.
363 T. N. Huan, P. Simon, G. Rousse, I. Génois, V. Artero and M. Fontecave, *Chem. Sci.*, 2016, **8**, 742–747.
364 J. L. Dimeglio and J. Rosenthal, *J. Am. Chem. Soc.*, 2013, **135**, 8798–8801.
365 H. K. Lim, Y. Kwon, H. S. Kim, J. Jeon, Y. H. Kim, J. A. Lim, B. S. Kim, J. Choi and H. Kim, *ACS Catal.*, 2018, **8**, 2420–2427.
366 A. Leal-Duaso, Y. Adjez and C. M. Sánchez-Sánchez, *ChemElectroChem*, 2024, **11**, e202300771.
367 Y. Li, F. Li, A. Laaksonen, C. Wang, P. Cobden, P. Boden, Y. Liu, X. Zhang and X. Ji, *Ind. Chem. Mater.*, 2023, **1**, 410–430.
368 X. Tan, X. Sun and B. Han, *Natl. Sci. Rev.*, 2022, **9**, nwab022.
369 A. Verma, J. P. Stoppelman and J. G. McDaniel, *Int. J. Mol. Sci.*, 2020, **21**, 403.
370 X. Li, W. Han, S. Yu and F. Zou, *Chem. Eng. Trans.*, 2018, **66**, 223–228.
371 W. A. Parada, D. V. Vasilyev, K. J. J. Mayrhofer and I. Katsounaros, *ACS Appl. Mater. Interfaces*, 2022, **14**(12), 14193–14201.
372 Y. Sha, J. Zhang, X. Cheng, M. Xu, Z. Su, Y. Wang, J. Hu, B. Han and L. Zheng, *Angew. Chem., Int. Ed.*, 2022, **61**, e202200039.
373 G. Iijima, T. Kitagawa, A. Katayama, T. Inomata, H. Yamaguchi, K. Suzuki, K. Hirata, Y. Hijikata, M. Ito and H. Masuda, *ACS Catal*, 2018, **8**, 1990–2000.
374 J. Tamura, A. Ono, Y. Sugano, C. Huang, H. Nishizawa and S. Mikoshiba, *Phys. Chem. Chem. Phys.*, 2015, **17**, 26072–26078.
375 P. Tamilarasan and S. Ramaprabhu, *J. Mater. Chem. A.*, 2015, **3**, 797–804.
376 S. Kamalakannan, K. Rudharachari Maiyelvaganan, K. Palanisamy, A. Thomas, R. Ben Said, M. Prakash and M. Hochlaf, *Chemosphere*, 2022, **286**, 131612.
377 D. Faggion, W. D. G. Gonçalves and J. Dupont, *Front. Chem.*, 2019, **7**, 102.
378 S. Dongare, O. K. Coskun, E. Cagli, K. Y. C. Lee, G. Rao, R. D. Britt, L. A. Berben and B. Gurkan, *ACS Catal.*, 2023, **13**, 7812–7821.
379 Y. Zhao, X. Wang, Z. Li, H. Wang, Y. Zhao and J. Qiu, *J. Phys. Chem. B*, 2024, **128**, 1079–1090.
380 X. An, P. Wang, X. Ma, X. Du, X. Hao, Z. Yang and G. Guan, *Carbon Resources Conversion*, 2023, **6**, 85–97.
381 M. M. Wan, H. Y. Zhu, Y. Y. Li, J. Ma, S. Liu and J. H. Zhu, *ACS Appl. Mater. Interfaces*, 2014, **6**, 12947–12955.
382 N. L. Ho, J. Perez-Pellitero, F. Porcheron and R. J. M. Pellenq, *J. Phys. Chem. C*, 2012, **116**, 3600–3607.
383 S. Supasitmongkol and P. Styring, *Energy Environ. Sci.*, 2010, **3**, 1961–1972.
384 D. Yang, Q. Zhu, C. Chen, H. Liu, Z. Liu, Z. Zhao, X. Zhang, S. Liu and B. Han, *Nat. Commun.*, 2019, **10**, 677.

385 M. H. Barecka, J. W. Ager and A. A. Lapkin, *Energy Environ. Sci.*, 2021, **14**, 1530–1543.
386 M. Rumayor, A. Dominguez-Ramos, P. Perez and A. Irabien, *J. CO2 Util.*, 2019, **34**, 490–499.
387 J. Baier, G. Schneider and A. Heel, *Front. Energy Res.*, 2018, **6**, 5.
388 Y. Li, CO_2 electrochemical reduction to CO with ionic liquids: evaluation and technology exploration, *Luleå University of Technology*, 2025, ISBN: 978-91-8048-831-0.
389 B. B. Hansen, S. Spittle, B. Chen, D. Poe, Y. Zhang, J. M. Klein, A. Horton, L. Adhikari, T. Zelovich, B. W. Doherty, B. Gurkan, E. J. Maginn, A. Ragauskas, M. Dadmun, T. A. Zawodzinski, G. A. Baker, M. E. Tuckerman, R. F. Savinell and J. R. Sangoro, *Chem. Rev.*, 2021, **121**(3), 1232–1285.
390 Q. Zhang, K. De Oliveira Vigier, S. Royer and F. Jérôme, *Chem. Soc. Rev.*, 2012, **41**, 7108–7146.
391 M. F. H. Ismail, A. N. Masri, N. Mohd Rashid, I. M. Ibrahim, S. A. S. Mohammed and W. Z. N. Yahya, *J. Mol. Liq.*, 2024, **4**, 100114.
392 A. Paiva, R. Craveiro, I. Aroso, M. Martins, R. L. Reis and A. R. C. Duarte, *ACS Sustainable Chem. Eng*, 2014, **2**(5), 1063–1071.
393 L. I. N. Tomé, V. Baião, W. da Silva and C. M. A. Brett, *Appl. Mater. Today*, 2018, **10**, 30–50.
394 A. P. Abbott, D. Boothby, G. Capper, D. L. Davies and R. K. Rasheed, *J. Am. Chem. Soc.*, 2004, **126**, 9142–9147.
395 O. E. Plastiras and V. Samanidou, *Molecules*, 2022, **27**, 7699.
396 R. Urvika and R. Kataria, Deep Eutectic Solvents, in *ACS Symposium Series*, vol. 1504, American Chemical Society, 2025, pp. 1–29.
397 S. P. Ijardar, V. Singh and R. L. Gardas, *Molecules*, 2022, **27**, 1368.
398 M. Freemantle, *Chem. Eng. News*, 2005, **83**(37), 33–38.
399 V. Agieienko and R. Buchner, *J. Chem. Eng. Data*, 2021, **66**, 780–792.
400 A. Umar, M. Munir, M. Murtaza, R. Sultana, M. A. Riaz, G. R. Srinivasan, A. Firdous and M. Saeed, *Egypt. J. Chem.*, 2020, **63**, 59–69.
401 H. Wang, X. Kang and B. Han, *Chem. Sci.*, 2024, **15**, 9949–9976.
402 X. Meng, K. Ballerat-Busserolles, P. Husson and J. M. Andanson, *New J. Chem.*, 2016, **40**, 4492–4499.
403 V. Alizadeh, L. Esser and B. Kirchner, *J. Chem. Phys.*, 2021, **154**, 094503.
404 B. Bohlen, D. Wastl, J. Radomski, V. Sieber and L. Vieira, *Electrochem. commun.*, 2020, **110**, 106597.
405 T. J. Trivedi, J. H. Lee, H. J. Lee, Y. K. Jeong and J. W. Choi, *Green Chem.*, 2016, **18**, 2834–2842.
406 S. Foorginezhad and X. Ji, *Results Eng.*, 2025, **26**, 105162.
407 Q. Shi, K. Jia, X. Zhang, C. Wang, P. Cobden, A.-M. B. Amnéus, D. Muren and X. Ji, *Chem. Eng. J.*, 2025, **522**, 167866.
408 Z. Coin, S. Dangwal, M. H. Irwin, T. Knight, R. Bhave, G. Rother, R. Sacci, M. Arifuzzaman, V. Bocharova, I. Ivanov, D. S. Sholl and S. Z. Islam, *ACS Omega*, 2025, **10**, 3407–3417.
409 S. Sarmad, Y. Xie, J. P. Mikkola and X. Ji, *New J. Chem.*, 2016, **41**, 290–301.
410 A. A. Manafpour, F. Feyzi and M. Rezaee, *Sci. Rep.*, 2024, **14**, 19744.
411 H. Wibowo, L. Zhong, Q. Huan, Q. Hu, D. A. Rahim and M. Yan, *Biomass Convers. Biorefin.*, 2022, **12**, 61–71.
412 S. Bhattacharjee and R. Getman, Effect of Water On Deep Eutectic Solvents: Structural Properties and Interactions with CO2, *ChemRxiv*, 2023, DOI: 10.26434/chemrxiv-2023-bqj91.
413 M. Chen and J. Xu, *Molecules*, 2023, **28**, 5461.
414 S. K. Shukla and J. P. Mikkola, *Phys. Chem. Chem. Phys.*, 2018, **20**, 24591–24601.
415 T. Umecky, A. Goto, N. Hayashi and K. Eguchi, *ACS Omega*, 2023, **8**, 14694–14698.
416 X. Liu, Q. Ao, S. Shi and S. Li, *Mater. Res. Express*, 2022, **9**, 015504.
417 Q. Shi, Z. Zuo and X. Ji, *Sep. Purif. Technol.*, 2025, **367**, 132877.
418 L. L. Bezerra, A. N. Correia, P. de Lima-Neto, N. de and K. V. Monteiro, *J. Mol. Graphics Modell.*, 2024, **126**, 108649.
419 A. Al-Bodour, N. Alomari, S. K. Liew, S. Aparicio, J. Springstead and M. Atilhan, *ACS Omega*, 2025, **10**, 24675–24696.
420 M. Heydari Dokoohaki and A. R. Zolghadr, *J. Phys. Chem. B*, 2021, **125**, 10035–10046.
421 B. Jiang, C. Zhang, Q. Zhou, L. Zhang, J. Li, X. Tantai, Y. Sun and L. Zhang, *ACS Sustainable Chem. Eng.*, 2024, **12**, 14109–14118.
422 I. Cichowska-Kopczyńska, D. Warmińska and B. Nowosielski, *Materials*, 2021, **14**, 1–14.
423 K. Xin, F. Gallucci and M. Van Sint Annaland, *ACS Sustainable Chem. Eng.*, 2022, **10**, 15284–15296.
424 M. B. Haider, P. Maheshwari and R. Kumar, *J. Environ. Chem. Eng.*, 2021, **9**, 106727.
425 C. Ma, S. Sarmad, J. P. Mikkola and X. Ji, in *Energy Procedia*, Elsevier Ltd, 2017, vol. 142, pp. 3320–3325.
426 H. Sang, L. Su, W. Han, F. Si, W. Yue, X. Zhou, Z. Peng and H. Fu, *J. CO2 Util.*, 2022, **65**, 102201.
427 N. Ahmad, X. Lin, X. Wang, J. Xu and X. Xu, *Fuel*, 2021, **293**, 120466.
428 N. Noorani and A. Mehrdad, *J. Mol. Liq.*, 2022, **357**, 119078.
429 A. Alnajjar and S. A. Onaizi, *J. Mol. Liq.*, 2025, **421**, 126832.
430 S. Dongare, M. Zeeshan, A. S. Aydogdu, R. Dikki, S. F. Kurtoglu-Oztulum, O. K. Coskun, M. Munoz, A. Banerjee, M. Gautam, R. D. Ross, J. S. Stanley, R. S. Brower, B. Muchharla, R. L. Sacci, J. M. Velazquez, B. Kumar, J. Y. Yang, C. Hahn, S. Keskin, C. G. Morales-Guio, A. Uzun, J. M. Spurgeon and B. Gurkan, *Chem. Soc. Rev*, 2024, **53**, 8563–8631.
431 K. K. Maniam and S. Paul, *Materials*, 2021, **14**, 4519.
432 M. Gilmore, M. Swadzba-Kwasny and J. D. Holbrey, *J. Chem. Eng. Data*, 2019, **64**, 5248–5255.
433 F. Li and X. Ji, *Sci. Talks*, 2025, **16**, 100495.
434 P. J. Smith, C. B. Arroyo, F. Lopez Hernandez and J. C. Goeltz, *J. Phys. Chem. B*, 2019, **123**, 5302–5306.

435 A. Halilu, M. K. Hadj-Kali, M. A. Hashim, R. Yusoff and M. K. Aroua, *ACS Omega*, 2022, **7**, 37764–37773.
436 S. Imteyaz, C. M. Suresh, T. Kausar and P. P. Ingole, *J. CO2 Util.*, 2023, **68**, 102349.
437 S. Verma, X. Lu, S. Ma, R. I. Masel and P. J. A. Kenis, *Phys. Chem. Chem. Phys.*, 2016, **18**, 7075–7084.
438 S. Garg, M. Li, Y. Wu, M. Nazmi Idros, H. Wang, A. J. Yago, L. Ge, G. G. X. Wang and T. E. Rufford, *ChemSusChem*, 2021, **14**, 2601–2611.
439 D. V. Vasilyev, A. V. Rudnev, P. Broekmann and P. J. Dyson, *ChemSusChem*, 2019, **12**, 1635–1639.
440 V. Bušić, S. Roca and D. Gašo-Sokač, *Separations*, 2023, **10**, 551.
441 D. Yu, Z. Xue and T. Mu, *Cell Rep. Phys. Sci.*, 2022, **3**, 100809.
442 D. C. Nunes, *Development of PRIDES – PolymeRIc Deep Eutectic Solvents – for CO_2 capture, NOVA School of Science and Technology (FCT NOVA), 2021.*
443 F. P. García de Arquer, C. T. Dinh, A. Ozden, J. Wicks, C. McCallum, A. R. Kirmani, D. H. Nam, C. Gabardo, A. Seifitokaldani, X. Wang, Y. C. Li, F. Li, J. Edwards, L. J. Richter, S. J. Thorpe, D. Sinton and E. H. Sargent, *Science*, 2020, **367**, 661–666.
444 C. T. Dinh, T. Burdyny, M. G. Kibria, A. Seifitokaldani, C. M. Gabardo, F. P. García de Arquer, A. Kiani, J. P. Edwards, P. De Luna, O. S. Bushuyev, C. Zou, R. Quintero-Bermudez, Y. Pang, D. Sinton and E. H. Sargent, *Science*, 2018, **360**, 783–787.
445 S. Zong, A. Chen, M. Wiśniewski, L. Macheli, L. L. Jewell, D. Hildebrandt and X. Liu, *Carbon Capture Sci. Technol*, 2023, **8**, 100133.
446 J. Resasco, L. D. Chen, E. Clark, C. Tsai, C. Hahn, T. F. Jaramillo, K. Chan and A. T. Bell, *J. Am. Chem. Soc.*, 2017, **139**, 11277–11287.
447 H. Yin, X. Mao, D. Tang, W. Xiao, L. Xing, H. Zhu, D. Wang and D. R. Sadoway, *Energy Environ. Sci.*, 2013, **6**, 1538–1545.
448 H. Yamada, *Polym. J.*, 2021, **53**, 93–102.
449 E. S. Rubin, J. E. Davison and H. J. Herzog, *Int. J. Greenhouse Gas Control.*, 2015, **40**, 378–400.
450 S. Licht, *J. CO2 Util.*, 2017, **18**, 378–389.
451 V. Khanna, B. R. Bakshi and L. J. Lee, *J. Ind. Ecol.*, 2008, **12**, 394–410.
452 H. Y. Teah, T. Sato, K. Namiki, M. Asaka, K. Feng and S. Noda, *ACS Sustainable Chem. Eng.*, 2020, **8**, 1730–1740.
453 M. Yin, X. Bai, D. Wu, F. Li, K. Jiang, N. Ma, Z. Chen, X. Zhang and L. Fang, *Chem. Eng. J.*, 2022, **433**, 134441.
454 Q. Yu, J. Liu, Y. Liang, T. Liu, Y. Zheng, Z. Lai, X. Liu, J. Chen, Q. Zhang and X. Li, *Electrochim. Acta*, 2022, **422**, 140515.
455 I.-N. Tano, E. Rasouli, T. Ziev, Z. Wu, N. Lamprinakos, J. Seo, L. S. Balhorn, P. Vaishnav, A. Rollett and V. Narayanan, *Solar Energy*, 2022, **234**, 152–169.
456 Y. Zuo, Y. Li and H. Zhou, *Energy*, 2022, **251**, 123893.
457 Z. Xie, X. Tang, J. Shi, Y. Wang, G. Yuan and J.-M. Liu, *Nano Energy*, 2022, **98**, 107247.
458 H. Hua, K. Yasuda and T. Nohira, *ACS Sustainable Chem. Eng.*, 2022, **10**, 9225–9231.
459 Z. Wang, J. Ban, K. Su, H. Cheng, Q. Geng, H. Wang, J. Shen, Q. Jia, Z. Zhang and X. Liu, *Ceram. Int.*, 2022, **48**, 12342–12349.
460 F. Yuan, Y.-L. He, M.-J. Li and X.-Y. Li, *Sol. Energy Mater. Sol. Cells*, 2022, **238**, 111631.
461 A. Yu, G. Ma, J. Ren, P. Peng and F. Li, *ChemSusChem*, 2020, **13**, 6229–6245.
462 A. Yu, S. Liu, W. Zhang and Y. Yang, *ACS Appl. Nano Mater.*, 2024, **7**, 27960–27978.
463 X. Wang, F. Sharif, X. Liu, G. Licht, M. Lefler and S. Licht, *J. CO_2* Util., 2020, **40**, 101218.
464 I. A. Novoselova, N. F. Oliinyk, S. V. Volkov, A. A. Konchits, I. B. Yanchuk, V. S. Yefanov, S. P. Kolesnik and M. V. Karpets, *Phys. E*, 2008, **40**, 2231–2237.
465 S. Licht, *J. Phys. Chem. C*, 2009, **113**, 16283–16292.
466 R. Jiang, M. Gao, X. Mao and D. Wang, *Curr. Opin. Electrochem.*, 2019, **17**, 38–46.
467 B. Deng, Z. Chen, M. Gao, Y. Song, K. Zheng, J. Tang, W. Xiao, X. Mao and D. Wang, *Faraday Discuss.*, 2016, **190**, 241–258.
468 E. Sada, S. Katoh, H. Yoshii, I. Takemoto and N. Shiomi, *J. Chem. Eng. Data*, 1981, **26**, 279–281.
469 Y. Kanai, K. Fukunaga, K. Terasaka and S. Fujioka, *Chem. Eng. Sci.*, 2013, **100**, 153–159.
470 X. Chen, Z. Zhao, J. Qu, B. Zhang, X. Ding, Y. Geng, H. Xie, D. Wang and H. Yin, *ACS Sustainable Chem. Eng.*, 2021, **9**, 4167–4174.
471 S. Licht, B. Wang, S. Ghosh, H. Ayub, D. Jiang and J. Ganley, *J. Phys. Chem. Lett.*, 2010, **1**, 2363–2368.
472 H. Wu, Z. Li, D. Ji, Y. Liu, L. Li, D. Yuan, Z. Zhang, J. Ren, M. Lefler and B. Wang, *Carbon*, 2016, **106**, 208–217.
473 X. Wang, G. Licht, X. Liu and S. Licht, *Sci. Rep.*, 2020, **10**, 21518.
474 J. Ren, F.-F. Li, J. Lau, L. González-Urbina and S. Licht, *Nano Lett.*, 2015, **15**, 6142–6148.
475 X. Liu, G. Licht, X. Wang and S. Licht, *Catalysts*, 2022, **12**, 137.
476 X. Wang, G. Licht, X. Liu and S. Licht, *Adv. Sustain. Syst.*, 2022, **6**, 2100481.
477 G. A. Mutch, L. Qu, G. Triantafyllou, W. Xing, M.-L. Fontaine and I. S. Metcalfe, *J. Mater. Chem. A.*, 2019, **7**, 12951–12973.
478 N. Prasongthum, A. Suemanotham, Y. Thanmongkhon, P. Khowattana, P. Butniam, N. Khoduangklang, C. Samart and L. Attanatho, in *Journal of Physics: Conference Series*, IOP Publishing, 2023, vol. 2602, p. 012002.
479 H. V. Ijije, R. C. Lawrence and G. Z. Chen, *RSC Adv.*, 2014, **4**, 35808–35817.
480 H. Yin and D. Wang, in *Electrochemical Society Meeting Abstracts 243*, The Electrochemical Society, Inc., 2023, p. 2737.
481 L. Zhang, B. Geng, Y. Gao, H. Kang, P. Wang, C. Liu, H. Xiao, M. Zhao, J. Jia and H. Wu, *Chem. Eng. J.*, 2024, **481**, 148086.
482 S. Arcaro, F. A. Berutti, A. K. Alves and C. P. Bergmann, *Appl. Surf. Sci.*, 2019, **466**, 367–374.

483 J. Cao, S. Jing, H. Wang, W. Xu, M. Zhang, J. Xiao, Y. Peng, X. Ning, Z. Wang and W. Xiao, *Angew. Chem., Int. Ed.*, 2023, **62**, e202306877.
484 V. Kaplan, E. Wachtel, K. Gartsman, Y. Feldman and I. Lubomirsky, *J. Electrochem. Soc.*, 2010, **157**, B552.
485 R. Yu, B. Deng, K. Zheng, X. Wang, K. Du and D. Wang, *Composites Communications*, 2020, **22**, 100464.
486 W. Weng, B. Jiang, Z. Wang and W. Xiao, *Sci. Adv.*, 2020, **6**, eaay9278.
487 D. Tang, Y. Dou, H. Yin, X. Mao, W. Xiao and D. Wang, *J. Energy Chem.*, 2020, **51**, 418–424.
488 X. Liu, X. Wang, G. Licht and S. Licht, *J. CO2 Util.*, 2020, **36**, 288–294.
489 D. Ji, Q. Jia, C. Zhu, W. Dong, H. Wu and G. Wang, *Appl. Sci.*, 2022, **12**, 8874.
490 X. Chen, H. Zhao, H. Xie, J. Qu, X. Ding, Y. Geng, D. Wang and H. Yin, *Electrochim. Acta*, 2019, **324**, 134852.
491 B. P. Thapaliya, A. S. Ivanov, H.-Y. Chao, M. Lamm, H. M. Meyer III, M. Chi, X.-G. Sun, T. Aytug, S. Dai and S. M. Mahurin, *ACS Appl. Mater. Interfaces*, 2024, **16**, 2251–2262.
492 K. Otake, H. Kinoshita, T. Kikuchi and R. O. Suzuki, *Electrochim. Acta*, 2013, **100**, 293–299.
493 M. Gao, B. Deng, Z. Chen, M. Tao and D. Wang, *Electrochem. Commun.*, 2019, **100**, 81–84.
494 B. Deng, M. Gao, R. Yu, X. Mao, R. Jiang and D. Wang, *Appl. Energy*, 2019, **255**, 113862.
495 X. Liu, J. Ren, G. Licht, X. Wang and S. Licht, *Adv. Sustain. Syst.*, 2019, **3**, 1900056.
496 X. Wang, X. Liu, G. Licht and S. Licht, *Sci. Rep.*, 2020, **10**, 15146.
497 L. Hu, B. Deng, Z. Yang and D. Wang, *Electrochem. commun.*, 2020, **121**, 106864.
498 L. Hu, B. Deng, K. Du, R. Jiang, Y. Dou and D. Wang, *iScience.*, 2020, **23**, 101607.
499 R. Yu, B. Deng, K. Du, D. Chen, M. Gao and D. Wang, *Carbon*, 2021, **184**, 426–436.
500 X. Wang, G. Licht and S. Licht, *Sep. Purif. Technol.*, 2021, **255**, 117719.
501 E. Laasonen, V. Ruuskanen, M. Niemelä, T. Koiranen and J. Ahola, *J. Environ. Chem. Eng.*, 2022, **10**, 106933.
502 B. P. Thapaliya, A. S. Ivanov, H.-Y. Chao, M. Lamm, M. Chi, H. M. Meyer III, X.-G. Sun, T. Aytug, S. Dai and S. M. Mahurin, *Carbon*, 2023, **212**, 118151.
503 T. Giannakopoulou, N. Todorova, E. Sakellis, N. Plakantonaki and C. Trapalis, *Carbon*, 2025, **238**, 120179.
504 H. Shi, M. Cai, W. Li, X. Chen, K. Du, L. Guo, P. Wang, P. Li, B. Deng and H. Yin, *Chem. Eng. J.*, 2023, **462**, 142240.
505 S. Licht, A. Douglas, J. Ren, R. Carter, M. Lefler and C. L. Pint, *ACS Cent. Sci.*, 2016, **2**, 162–168.
506 P. Wang, Y. Liu, Z. Li, D. Ji, Z. Qiao, J. Zhang, Q. Jia and H. Wu, *J. Electrochem. Soc.*, 2021, **168**, 083501.
507 R. Yu, J. Xiang, K. Du, B. Deng, D. Chen, H. Yin, Z. Liu and D. Wang, *Nano Lett.*, 2021, **22**, 97–104.
508 M. M. A. Rafique and J. Iqbal, *J. Encapsulation Adsorpt. Sci.*, 2011, **1**, 29–34.
509 A. Rezaei and A. R. Kamali, *Diam. Relat. Mater.*, 2018, **83**, 146–161.
510 I. D. Rahatwan, P. P. D. K. Wulan and M. Solahudin, in *AIP Conference Proceedings*, AIP Publishing, 2020, vol. 2230.
511 M. Li, E. Irtem, H. P. Iglesias van Montfort, M. Abdinejad and T. Burdyny, *Nat. Commun.*, 2022, **13**, 5398.
512 M. A. Arellano-Treviño, N. Kanani, C. W. Jeong-Potter and R. J. Farrauto, *Chem. Eng. J.*, 2019, **375**, 121953.
513 D. P. Hanak, E. J. Anthony and V. Manovic, *Energy Environ. Sci.*, 2015, **8**, 2199–2249.
514 Q. Xia, K. Zhang, T. Zheng, L. An, C. Xia and X. Zhang, *ACS Energy Lett.*, 2023, **8**(6), 2840–2857.
515 J. Li, C. Qin, Z. Lv, C. Gao, L. Chen and S. Xu, *Energy*, 2025, **316**, 134516.
516 J. M. Spurgeon, N. Theaker, C. A. Phipps, S. S. Uttarwar and C. A. Grapperhaus, *ACS Sustainable Chem. Eng.*, 2022, **10**, 12882–12894.
517 A. Silveira Sbrice Pinto, N. Gulpinar, F. Liu, E. Gibson, L. Fuller and P. Souter, *ACS Sustainable Resour. Manage.*, 2025, **2**, 733–743.
518 Y. Kim, M. Namdari, A. M. L. Jewlal, Y. Chen, D. J. D. Pimlott, M. Stolar and C. P. Berlinguette, *ACS Energy Lett.*, 2025, **10**, 403–409.
519 D. Rathore, *Energy Sustain. Dev.*, 2025, **89**, 101866.
520 D. Tian, Z. Qu and J. Zhang, *Appl. Energy*, 2023, **351**, 121787.
521 Y. Li and T. B. Lu, *Mater. Chem. Front*, 2024, **8**, 341–353.
522 S. Verma, S. Lu and P. J. A. Kenis, *Nat. Energy*, 2019, **4**, 466–474.
523 X. Jiang, L. Ke, K. Zhao, X. Yan, H. Wang, X. Cao, Y. Liu, L. Li, Y. Sun, Z. Wang, D. Dang and N. Yan, *Nat. Commun*, 2024, **15**, 1427.
524 X. Wang, P. Li, J. Tam, J. Y. Howe, C. P. O'Brien, A. Sedighian Rasouli, R. K. Miao, Y. Liu, A. Ozden, K. Xie, J. Wu, D. Sinton and E. H. Sargent, *Nat. Sustainable*, 2024, **7**, 931–937.
525 T. Gao, B. Xia, K. Yang, D. Li, T. Shao, S. Chen, Q. Li and J. Duan, *Energy Fuels*, 2023, **37**, 17997–18008.
526 S. Y. Chae, S. Y. Lee, S. G. Han, H. Kim, J. Ko, S. Park, O. S. Joo, D. Kim, Y. Kang, U. Lee, Y. J. Hwang and B. K. Min, *Sustainable Energy Fuels*, 2019, **4**, 199–212.
527 M. Agliuzza, R. Speranza, A. Lamberti, C. F. Pirri and A. Sacco, *Appl. Sci.*, 2025, **15**, 549.
528 D. Segets, C. Andronescu and U. P. Apfel, *Nat. Commun.*, 2023, **14**, 7950.
529 B. Belsa, L. Xia and F. P. García de Arquer, *ACS Energy Lett*, 2024, **9**, 4293–4305.
530 K. Zhao, C. Jia, Z. Li, X. Du, Y. Wang, J. Li, Z. Yao and J. Yao, *Fuel*, 2023, **351**, 128913.
531 J. Chen, Y. Xu, P. Liao, H. Wang and H. Zhou, *Carbon Capture Sci. Technol*, 2022, **4**, 100052.
532 K. Armstrong, *Carbon Dioxide Utilisation: Closing the Carbon Cycle*, Elsevier, 2015, pp. 237–251, ISBN: 9780444627469.
533 Y. Zheng, W. Zhang, Y. Li, J. Chen, B. Yu, J. Wang, L. Zhang and J. Zhang, *Nano Energy*, 2017, **40**, 512–539.
534 I. S. Omodolor, H. O. Otor, J. A. Andonegui, B. J. Allen and A. C. Alba-Rubio, *Ind. Eng. Chem. Res.*, 2020, **59**, 17612–17631.
535 Y. Zhang, S. Zhao, L. Li, J. Feng, K. Li, Z. Huang and H. Lin, *Catal. Sci. Technol.*, 2024, **14**, 790–819.
536 S. Sarmad, D. Lu, S. Gao, Z. Sun, Z. Zhou, A. Ali and L. Duan, *J. Environ. Chem. Eng.*, 2024, **12**, 114562.